

**“Soft-soft nanocomposite
coating materials produced by
emulsion polymerisation”**

A thesis submitted to the University of Manchester for
the degree of Doctor of Philosophy in the Faculty of
Engineering and Physical Sciences

2015

Elizabeth M. Eaves

School of Materials

The University of Manchester

Table of Contents

Table of Contents.....	2
List of Tables	18
List of Abbreviations	22
Abstract.....	24
Declaration.....	25
Copyright statement	26
1 Project background and aims	29
1.1 Project aims.....	29
2 Literature Review	31
2.1 Introduction to Polymers	31
2.1.1 Types of polymerisation process	31
2.2 Emulsion polymerisation – Mechanism and Kinetics	33
2.2.1 Interval I – Particle nucleation	33
2.2.2 Intervals II/III – Particle growth.....	38
2.2.3 Emulsion polymerisation processes.....	39
2.3 Nanocomposite latex particles	41
2.3.1 Particle Morphologies.....	42
2.3.2 Properties of core-shell latexes	44
2.3.3 Control of core-shell nanocomposite morphology.....	45
2.4 Film formation of polymer latexes.....	49
2.4.1 Mechanism of Film Formation	50
2.4.2 Crosslinking and Film Formation.....	52
2.4.3 Elastomers.....	54
2.4.4 Crosslinking Chemistries	55
2.4.5 Advantages of core-shell nanoparticles with respect to film formation	59
2.5 Applications of core-shell nanocomposite particles.....	61
2.5.1 Pressure-sensitive adhesives	61
2.5.2 Coatings.....	64
2.6 Summary	68
3 Experimental Methods.....	69
3.1 Materials	69
3.2 Emulsion polymerisation processes.....	69

3.2.1	Preparation of a standard AkzoNobel latex.....	69
3.2.2	Preparation of a core-shell soft-soft nanocomposite latex	70
3.2.3	Determination of coagulum levels.....	71
3.3	Film formation processes.....	71
3.3.1	Post-polymerisation addition of ADH	71
3.3.2	Film casting	71
3.4	Characterisation methods.....	71
3.4.1	Latex characterisation.....	71
3.4.2	Mechanical and morphological characterisation of films.....	81
3.4.3	Thermal characterisation of latexes and films.....	93
3.4.4	Industrial test methods.....	97
4	Establishing a framework formulation for the synthesis of soft-soft nanocomposite latexes.....	99
4.1	Introduction	99
4.2	Preliminary investigations.....	101
4.3	Development of a latex formulation to produce core-shell latexes.....	102
4.3.1	Evaluation of original AkzoNobel formulation.....	102
4.3.2	Initial changes to formulation to fit the project brief.....	107
4.4	Addition of a non-ionic surfactant	109
4.4.1	Effect of surfactant degree of ethoxylation upon coagulum levels.....	110
4.4.2	Confirmation by ¹ H NMR of Lutensol TO7 structure	111
4.4.3	Establishing the optimum level of Lutensol TO7	112
4.4.4	Establishing the effect of Lutensol TO7 in latexes containing functional monomers.....	113
4.5	Adjustments made to formulation to compensate for discrepancies between predicted and observed T _g values.....	114
4.6	Conclusions	118
5	Establishing the effect of keto-hydrazide crosslinking	120
5.1	Introduction	120
5.2	Synthesis of soft-soft nanocomposite latexes containing latent crosslinking functionalities	125
5.3	Effect of crosslinking upon mechanical properties.....	127
5.4	Visual differences between crosslinked and non-crosslinked films investigated by AFM	131
5.4.1	Investigating film surfaces using AFM	131

5.4.2	Investigations of film cross-sections using AFM	136
5.4.3	Visualising keto-hydrazide crosslinks using AFM-IR.....	139
5.5	Effect of crosslinking upon 'paint' film properties.....	145
5.5.1	Minimum film formation temperature (MFT)	145
5.5.2	Viscosity testing – high and low shear rheology.....	146
5.6	Conclusions	147
6	Effect of core:shell ratio and crosslinker content on soft-soft nanocomposite film properties.....	149
6.1	Introduction	149
6.2	Effect of core:shell ratio on soft-soft nanocomposites	154
6.2.1	Hysteresis and stress relaxation mechanical testing of soft-soft nanocomposites with varying core:shell ratio.....	158
6.2.2	Effect of core:shell ratio on copolymer molar mass	162
6.2.3	Visualisation of soft-soft nanocomposite films with varying core:shell ratio.....	164
6.3	Effect of crosslinker content on film properties	168
6.3.1	Unstructured particles of uniform composition	169
6.3.2	Structured core-shell particle latexes	170
6.4	Effect of DAAM-ADH stoichiometric ratio	176
6.5	Conclusions	179
7	Effect of core and shell phase polymer T_g on film properties.....	181
7.1	Introduction	181
7.2	Investigating the effect of core T_g upon film properties.....	183
7.2.1	70:30 core:shell ratio	184
7.2.2	80:20 core:shell ratio	187
7.2.3	90:10 core:shell ratio	189
7.2.4	Effect of core phase copolymer T_g on minimum film formation temperature (MFT)	192
7.3	Effect of crosslinker content at higher core T_g	193
7.4	Investigating the effect of shell T_g upon film properties	201
7.5	Effect of the average T_g upon Young's modulus.....	206
7.6	Conclusions	210
8	Effect of methacrylic acid on film properties.....	211
8.1	Introduction	211
8.2	Effect of adding methacrylic acid to the shell phase copolymer of soft-soft nanocomposites.....	213

8.2.1	Systems with lower core T_g	214
8.2.2	Systems with higher core T_g	215
8.2.3	AFM imaging of MAA-containing films	218
8.3	Effect of type of neutralisation on the film properties of MAA-containing soft-soft nanocomposites.....	220
8.4	Conclusions	224
9	Comparing soft-soft nanocomposite systems with commercial water-based paint binders	226
9.1	Introduction	226
9.2	Wet latex characterisation.....	227
9.3	Thermal and mechanical characterisation.....	229
9.3.1	Thermal properties	229
9.3.2	Mechanical (tensile) properties	230
9.4	Mechanical property comparisons to a wider range of AkzoNobel binder systems 231	
9.5	Conclusions	233
10	Conclusions	235
11	Recommendations for further work	239
12	References	242
	Appendix (i) – Characterisation plots for soft-soft nanocomposite latexes discussed in Chapter 4.....	251
	Appendix (ii) – Characterisation plots for soft-soft nanocomposite latexes discussed in Chapter 5.....	258
	Appendix (iii) – Characterisation plots for soft-soft nanocomposite latexes discussed in Chapter 6.....	260
	Appendix (iv) – Characterisation plots for soft-soft nanocomposite latexes discussed in Chapter 7.....	269
	Appendix (v) – Characterisation plots for soft-soft nanocomposite latexes discussed in Chapter 8.....	283

TOTAL WORD COUNT: 79,918

List of Figures

Figure 2.1 Simple schematic plot showing the relationship between monomer conversion and time with respect to Intervals I, II and III of emulsion polymerisation ²⁹	34
Figure 2.2 Structure of sodium lauryl sulphate (SLS), a commonly used surfactant in emulsion polymerisation	34
Figure 2.3 Cross-sectional structure of a surfactant micelle, where the circular and linear sections represent hydrophilic and hydrophobic moieties, respectively	35
Figure 2.4 Representation of micellar nucleation, where R· = initiator molecule. M = monomer molecule and P = polymer chain. Adapted from Odian ¹⁶	37
Figure 2.5 Examples of nanocomposite latex particle morphology - (a) core-shell; (b) inverted core-shell, (c) hemisphere, (d) raspberry ⁵²	43
Figure 2.6 TEM images showing the formation of core-shell morphology in a nanocomposite latex particle. (a) shows the poly[(n-butyl acrylate) -co- (methacrylic acid) - co -{ ethylene glycol dimethacrylate}]core, and (b) shows the final particle morphology after addition of the poly[styrene -co- (methyl methacrylate)] shell ⁵⁵	44
Figure 2.7 TEM images of core-shell nanocomposites formed at a reaction temperature of 70°C. (a) Poly[(MMA)-co-(MA)] seed polymer with $T_g = 88\text{ }^\circ\text{C}$ and (b) Poly[(MMA)-co-(MA)] seed polymer with $T_g = 52\text{ }^\circ\text{C}$ ⁵⁷ , where MA is methyl acrylate.	47
Figure 2.8 TEM images of PMMA core- PSty shell nanoparticles produced in a surfactant-free polymerisation using (a) 2,2'-Azobis[2-methyl-N-(2-hydroxyethyl)propionamide] (non-ionic) initiator and (b) potassium persulphate (anionic) initiator ⁶⁵ . Scale bars represent 300 nm....	48
Figure 2.9 (a) formation of film at above shell polymer T_g leads to deformation of particles and hence honeycomb structure in film; (b) Formation of film below shell polymer T_g leads to spherical particle structure in film ³²	52
Figure 2.10 Simple schematic diagram to show the formation of films with both pre- and postcoalescence crosslinking	54
Figure 2.11 Structure of allyl methacrylate	55
Figure 2.12 Self-crosslinking of n-MA-containing polymer chains by condensation of the alcohol functionality ¹⁰³	56
Figure 2.13 Structure of diacetone acrylamide (DAAM).....	56
Figure 2.14 Structure of adipic acid dihydrazide (ADH).....	56
Figure 2.15 Keto-hydrazide crosslinking mechanism of DAAM and ADH ⁹⁵	58
Figure 2.16 Crosslinked network of polymer chains with hydrazone linkages.....	58

Figure 2.17 Nominal strain (σ_N) vs extension ratio (λ) plot showing the tensile behaviour of soft-soft nanocomposites with different shell/core ratios, showing the effect of a crosslinked shell phase on the extensibility of the material ⁵	64
Figure 2.18 'Blend'-type strategy used by Overbeek <i>et al.</i> to form a water-borne zero-VOC paint binder ¹³⁷ . The light blue, large domains represent the hard particles, and the purple, smaller domains the soft particles.....	66
Figure 3.1 Schematic diagram representing the fluctuation of light intensity with time observed in dynamic light scattering measurements, where $x\Delta t$ is the sample time after x measurements and τ is the correlation time ¹⁵⁷	73
Figure 3.2 Parabolic-type flow velocity conditions in HDC columns ¹⁵⁹ . The lengths of the arrows indicate relative flow velocities.	76
Figure 3.3 Schematic representation of particle size separation in HDC as a consequence of parabolic-type flow velocity conditions. The orange shape represents a large analyte, and the green shape a smaller one. ¹⁵⁹	76
Figure 3.4 Schematic representation of polymer chain separation in GPC ¹⁵⁷	78
Figure 3.5 Typical GPC calibration curves for polystyrene in THF ¹⁷ , obtained using six different columns with the following pore sizes: (a) 10^5 nm, (b) 10^4 nm, (c) 10^3 nm, (d) 10^2 nm, (e) 50 nm and (f) 5 nm.....	79
Figure 3.6 Dumbbell-shaped stress-strain tensile testing samples, with the parallel-sided section of length l_0 indicated.	83
Figure 3.7 Characteristic stress-strain curves for different types of polymers ¹⁷	83
Figure 3.8 Plot of strain versus time demonstrating viscoelastic behaviour during both loading and unloading processes ¹⁶⁵	84
Figure 3.9 Schematic representation of a Maxwell material ¹⁶⁸	85
Figure 3.10 Mechanical hysteresis loop showing complete recovery of strain upon the removal of load ¹⁷	86
Figure 3.11 Schematic diagram of an atomic force microscope (AFM).....	88
Figure 3.12 Schematic representation of AFM-IR equipment, showing (a) traditional 'bottom-up' IR irradiation ¹⁸¹ and (b) novel 'top down' IR irradiation ¹⁸²	92
Figure 3.13 Representations of measurements possible using AFM-IR ¹⁸² . (a) shows point IR spectrum, and (b) shows the surface mapping of a single wavelength	93
Figure 3.14 Thermal transitions that can be seen from heat-flux DSC, including glass transition (T_g), melting (T_m) and cold crystallisation (T_{cc}) ¹⁷	95
Figure 3.15 Illustration showing how T_g was determined in this PhD project.....	95

Figure 3.16 Test geometries available in DMTA testing ¹⁶⁵	96
Figure 4.1 ¹ H NMR spectrum of Rhodafac RK-500A in D ₂ O. The peak assignments are given in Table 4.1.....	101
Figure 4.2 Rhodafac RK500A (IUPAC name poly(oxy-1,2-ethanediyl), α,α' -phosphinicobis(ω -hexyloxy)] ammonium salt) with protons labelled to aid NMR spectrum peak analysis.	102
Figure 4.3 Plot of conversion against time for a preparation of the latex formulation given in Table 4.2.....	104
Figure 4.4 Plot of theoretical and actual particle diameter against time for the latex formulation given in Table 4.2	105
Figure 4.5 Plot of d_z^3 (average particle diameter ³ , red points) and total number of particles (blue points) against conversion for a preparation of the latex formulation given in Table 4.2	106
Figure 4.6 Particle size distribution for the latex formulation given in Table 4.2.....	106
Figure 4.7 Chemical structure of Lutensol TOx non-ionic surfactants, where X indicates the degree of ethoxylation.....	110
Figure 4.8 ¹ H NMR spectrum of Lutensol TO7 in DMSO-d ₆ , assignments of the peaks are given in Table 4.6.....	111
Figure 4.9 Lutensol TO7 (IUPAC name poly(oxy-1,2-ethanediyl) α -isodridecyl- ω -hydroxy ether) with protons labelled to aid NMR spectrum peak analysis	112
Figure 4.10 Characterisation plots for samples removed from the repeat preparation containing 20 wt% Lutensol TO7 relative to Rhodafac RK-500A – (a) conversion vs time, (b) z-average particle diameter vs time, (c) (z-average particle diameter) ³ (red points) and number of particles (blue points) vs conversion and (d) particle size distribution	113
Figure 4.11 DSC traces for (a) poly[(BA)-co-(BMA)] core and shell with theoretical $T_{gs} = 0$ °C, (b) poly[(BA)-co-(BMA)] core and poly[(BA)-co-(BMA)-co-(MAA)] shell with theoretical $T_{gs} = 0$ °C and (c) poly[(BA)-co-(BMA)] core and poly[(BA)-co-(BMA)-co-(MAA)-co-(DAAM)] shell with theoretical $T_{gs} = 0$ °C.....	115
Figure 4.12 Plot showing the linear relationships between theoretical and actual T_g values for unstructured poly[(BA)-co-(BMA)] latexes	117
Figure 4.13 DSC trace for poly[(BA)-co-(BMA)] copolymer with theoretical $T_g = 0$ °C as predicted from Equation 4.3.....	117
Figure 5.1 Chemical structures of (a) DAAM and (b) ADH	120
Figure 5.2 Structures of possible (a) imine/hydrazone and (b) enamine products from the DAAM-ADH crosslinking reaction	121

Figure 5.3 Stress-strain profiles for poly[(MMA)- <i>co</i> -(BA)- <i>co</i> -(AAEM)- <i>co</i> -(MAA)] latex films with (a) no diamine and (b) HMDA incorporated at a 2:1 AAEM:HMDA molar stoichiometric ratio 107	122
Figure 5.4 Nominal stress (σ_N) vs extension ratio (λ) profiles for soft-soft nanocomposite PSAs with a poly[(2-EHA)- <i>co</i> -(EA)- <i>co</i> -(BA)- <i>co</i> -Sty- <i>co</i> -(AA)] core phase and a poly[(2-EHA)- <i>co</i> -(EA)- <i>co</i> -(BA)- <i>co</i> -Sty- <i>co</i> -(DAAM)- <i>co</i> -(MAA)] shell. The percentage labels for each line identify the stoichiometric percentage of DAAM units that are crosslinked with ADH, and 'Classic' refers to the performance of a commercial water-borne PSA with no internal particle morphology and crosslinking throughout the particle ⁵	123
Figure 5.5 Tensile behaviour of soft-soft nanocomposites ($T_g = -38$ °C) with varying core-shell ratios and therefore degrees of crosslinking (ratio = non-crosslinked/crosslinked) ⁵	123
Figure 5.6 AFM height images of low T_g poly[(BA)- <i>co</i> -(MAA)- <i>co</i> -(MA)- <i>co</i> -(DAAM)] copolymers with (a) ADH added and (b) no ADH ⁹⁵	124
Figure 5.7 (a) Stress-strain curves for film with poly[(BA)- <i>co</i> -(BMA)] core and shell phase copolymer presented in triplicate; (b) Section of stress-strain curves from (a) with strains of 0-4% used to calculate Young's modulus (as the coefficient of first order term in a polynomial fit expression; order of fit = 6)	128
Figure 5.8 (a) Stress-strain curves for film with a poly[(BA)- <i>co</i> -(BMA)] core phase copolymer and poly[(BA)- <i>co</i> -(BMA)- <i>co</i> -(DAAM)] shell phase copolymer presented in triplicate; (b) Section of stress-strain curves from (a) with strains of 0-4% used to calculate Young's modulus (as the coefficient of first order term in a polynomial fit expression; order of fit = 6)	128
Figure 5.9 (a) Stress-strain curves for film with poly[(BA)- <i>co</i> -(BMA)] core phase copolymer and poly[(BA)- <i>co</i> -(BMA)- <i>co</i> -(DAAM)] shell phase copolymer with ADH added presented in triplicate; (b) Section of stress-strain curves from (a) with strains of 0-4% used to calculate Young's modulus (as the coefficient of first order term in a polynomial fit expression; order of fit = 6)	129
Figure 5.10 Comparison of stress-strain curves for soft-soft nanocomposite systems detailed in Table 5.1, where:	129
Figure 5.11 DMT Modulus AFM image of a soft-soft nanocomposite film surface with 70:30 core:shell ratio, comprising poly[(BA)- <i>co</i> -(BMA)] core and shell phase copolymers with T_g s of 5 °C. Image size = 5 μ m square	132
Figure 5.12 DMT Modulus AFM image of a soft-soft nanocomposite film surface with 70:30 core:shell ratio, comprising poly[(BA)- <i>co</i> -(BMA)] core and poly[(BA)- <i>co</i> -(BMA)- <i>co</i> -(DAAM)] shell phase copolymers with T_g s of 5 °C. Image size = 5 μ m square	132
Figure 5.13 DMT Modulus AFM image of a soft-soft nanocomposite film surface with 70:30 core:shell ratio, comprising poly[(BA)- <i>co</i> -(BMA)] core and poly[(BA)- <i>co</i> -(BMA)- <i>co</i> -(DAAM)] shell phase copolymers with T_g s of 5 °C and ADH added. Image size = 5 μ m square	133

- Figure 5.14 DMT Modulus AFM image of a soft-soft nanocomposite film surface with 70:30 core:shell ratio, comprising poly[(BA)-co-(BMA)] core and shell phase copolymers with T_g s of 5 °C. Image size = 20 μ m square 133
- Figure 5.15 DMT Modulus AFM image of a soft-soft nanocomposite film surface with 70:30 core:shell ratio, comprising poly[(BA)-co-(BMA)] core and poly[(BA)-co-(BMA)-co-(DAAM)] shell phase copolymers with T_g s of 5 °C. Image size = 20 μ m square..... 133
- Figure 5.16 DMT Modulus AFM image of a soft-soft nanocomposite film surface with 70:30 core:shell ratio, comprising poly[(BA)-co-(BMA)] core and poly[(BA)-co-(BMA)-co-(DAAM)] shell phase copolymers with T_g s of 5 °C and ADH added. Image size = 20 μ m square 134
- Figure 5.17 3D height images of systems with (a) poly[(BA)-co-(BMA)] core and shell, (b) poly[(BA)-co-(BMA)] core and poly[(BA)-co-(BMA)-co-(DAAM)] shell, and (c) poly[(BA)-co-(BMA)] core and poly[(BA)-co-(BMA)-co-(DAAM)] shell with ADH. Image sizes 2 μ m square.....136
- Figure 5.18 AFM phase image of the cross-section of a soft-soft nanocomposite PSA film⁶. 137
- Figure 5.19 DMT Modulus AFM image of an uncrosslinked soft-soft nanocomposite film cross-section with 70:30 core:shell ratio, comprising poly[(BA)-co-(BMA)] core and poly[(BA)-co-(BMA)-co-(DAAM)] shell phase copolymers with T_g s of 25 and 5 °C, respectively. Image size = 1 μ m square 138
- Figure 5.20 DMT Modulus AFM image of a lightly crosslinked soft-soft nanocomposite film cross-section with 70:30 core:shell ratio, comprising poly[(BA)-co-(BMA)] core and poly[(BA)-co-(BMA)-co-(DAAM)] shell phase copolymers with T_g s of 25 and 5 °C, respectively. ADH added at a 2:1 DAAM:ADH molar stoichiometric ratio. Image size = 1 μ m square..... 139
- Figure 5.21 Simplified reaction schematic for keto-hydrazide crosslinking, with the imine crosslinks highlighted..... 140
- Figure 5.22 Targeted section of the FTIR spectrum of selected soft-soft nanocomposite film with and without ADH added 141
- Figure 5.23 AFM-IR array over particle interfaces in a soft-soft nanocomposite film with 70:30 core:shell ratio, comprising poly[(BA)-co-(BMA)] core and poly[(BA)-co-(BMA)-co-(DAAM)] shell phase copolymers with T_g s of 25 and 5 °C and ADH added at a 2:1 DAAM:ADH molar stoichiometric ratio. Spectra 1-4 and 7-10 are of the particle cores, Spectrum 5 is of the percolating phase and Spectrum 6 is of the core-percolating phase boundary..... 142
- Figure 5.24 Zoomed-in AFM-IR array of a soft-soft nanocomposite film with 70:30 core:shell ratio, comprising poly[(BA)-co-(BMA)] core and poly[(BA)-co-(BMA)-co-(DAAM)] shell phase copolymers with T_g s of 25 and 5 °C, respectively, and ADH added at a 2:1 DAAM:ADH molar stoichiometric ratio, showing specific areas of interest. Spectra 1-4 and 7-10 are of the particle cores, Spectrum 5 is of the percolating phase and Spectrum 6 of the core-percolating phase boundary. 143
- Figure 5.25 AFM-IR height (L) and map of IR absorption at 1684 cm^{-1} (R) images of an uncrosslinked soft-soft nanocomposite film cross-section with 70:30 core:shell ratio,

poly[(BA)-*co*-(BMA)] core and poly[(BA)-*co*-(BMA)-*co*-(DAAM)] shell phase copolymers with T_g s of 25 and 5 °C, respectively. Image sizes = 5 μ m square..... 143

Figure 5.26 AFM-IR height (L) and map of IR absorption at 1684 cm^{-1} (R) images of a lightly crosslinked soft-soft nanocomposite film cross-section with 70:30 core:shell ratio, poly[(BA)-*co*-(BMA)] core and poly[(BA)-*co*-(BMA)-*co*-(DAAM)] shell phase copolymers with T_g s of 5 °C and ADH added at a 2:1 DAAM:ADH stoichiometric ratio. Image sizes = 5 μ m square 144

Figure 5.27 Plot of temperature against MFT bar marking 146

Figure 6.1 Nominal stress (σ_N)-extension ratio (λ) profiles showing (a) the effect of core/shell ratio on soft-soft nanocomposite PSAs with 2-EHA-based core and shell phase copolymers, where DAAM level is 0.4 wt% of the total particle; and (b) close-up of the boxed low-strain area of (a)..... 150

Figure 6.2 Plot showing the effect of DAAM content upon both coagulum levels and particle sizes for a poly[(MMA)-*co*-(BA)-*co*-(AA)-*co*-(HPMA)-*co*-(DAAM)] copolymer¹³¹..... 151

Figure 6.3 Stress-strain profiles showing the effect of DAAM in low T_g poly[(BMA)-*co*-(BA)-*co*-(MAA)-*co*-(DAAM)] films using the notation 'EL-x', where x is the wt% of DAAM incorporated into the copolymer⁹⁶ 152

Figure 6.4 Stress-strain profiles showing the independent effect of DAAM content on tensile performance for 50:50 poly[Sty-*co*-(2-EHA)-*co*-(1,6-HDDA)]: poly[(MMA)-*co*-(BA)-*co*-(MAA)-*co*-(DAAM)] interpenetrating polymer networks²⁰⁸ 153

Figure 6.5 Nominal stress (σ_N)-extension ratio (λ) profiles showing the effect of DAAM:ADH stoichiometric ratio in soft-soft nanocomposite PSAs with an 80:20 core:shell ratio, 2-EHA-based core and shell phase copolymers. DAAM level is 0.4 wt% of the total particle, and 100% ADH represents a 2:1 (DAAM:ADH) ratio⁵ 153

Figure 6.6 (a) Stress-strain curves for films with varying core:shell ratio. Film composition is poly[(BA)-*co*-(BMA)] core phase copolymer and poly[(BA)-*co*-(BMA)-*co*-(DAAM)] shell phase copolymer with ADH added at 2:1 molar stoichiometric ratio; (b) Section of stress-strain curves from (a) with strains of 0-4% used to calculate Young's modulus (coefficient of first order term in a polynomial fit expression; order of fit = 6)..... 157

Figure 6.7 Mechanical hysteresis profiles for soft-soft nanocomposites with 2 wt% DAAM in the shell phase copolymer and (a) 70:30; (b) 90:10 and (c) 0:100 core:shell mass ratios. Samples extended to 12.5% strain before retraction to 0% strain, 10 minutes left between cycles 1 and 2 160

Figure 6.8 Stress relaxation profiles for soft-soft nanocomposites of varying core:shell ratio. All variants contain 2 wt% DAAM in the shell phase copolymer 161

Figure 6.9 GPC traces for soft-soft nanocomposite systems 163

Figure 6.10 DMT Modulus AFM image of a lightly crosslinked soft-soft nanocomposite film cross-section with 70:30 core:shell ratio, comprising poly[(BA)-*co*-(BMA)] core and poly[(BA)-

co-(BMA)-*co*-(DAAM)] shell phase copolymers with T_g s of 25 and 5 °C, respectively. ADH added at a 2:1 DAAM:ADH molar stoichiometric ratio. Image size = 2 μ m square 165

Figure 6.11 DMT Modulus AFM image of a lightly crosslinked soft-soft nanocomposite film cross-section with 70:30 core:shell ratio, comprising poly[(BA)-*co*-(BMA)] core and poly[(BA)-*co*-(BMA)-*co*-(DAAM)] shell phase copolymers with T_g s of 25 and 5 °C, respectively. ADH added at a 2:1 DAAM:ADH molar stoichiometric ratio. Image size = 1 μ m square 165

Figure 6.12 DMT Modulus AFM image of a lightly crosslinked soft-soft nanocomposite film cross-section with 80:20 core:shell ratio, comprising poly[(BA)-*co*-(BMA)] core and poly[(BA)-*co*-(BMA)-*co*-(DAAM)] shell phase copolymers with T_g s of 25 and 5 °C, respectively. ADH added at a 2:1 DAAM:ADH molar stoichiometric ratio. Image size = 2 μ m square 166

Figure 6.13 DMT Modulus AFM image of a lightly crosslinked soft-soft nanocomposite film cross-section with 80:20 core:shell ratio, comprising poly[(BA)-*co*-(BMA)] core and poly[(BA)-*co*-(BMA)-*co*-(DAAM)] shell phase copolymers with T_g s of 25 and 5 °C, respectively. ADH added at a 2:1 DAAM:ADH molar stoichiometric ratio. Image size = 1 μ m square 166

Figure 6.14 DMT Modulus AFM image of a lightly crosslinked soft-soft nanocomposite film cross-section with 90:10 core:shell ratio, comprising poly[(BA)-*co*-(BMA)] core and poly[(BA)-*co*-(BMA)-*co*-(DAAM)] shell phase copolymers with T_g s of 20 and 5 °C, respectively. ADH added at a 2:1 DAAM:ADH molar stoichiometric ratio. Image size = 2 μ m square 167

Figure 6.15 DMT Modulus AFM image of a lightly crosslinked soft-soft nanocomposite film cross-section with 90:10 core:shell ratio, comprising poly[(BA)-*co*-(BMA)] core and poly[(BA)-*co*-(BMA)-*co*-(DAAM)] shell phase copolymers with T_g s of 20 and 5 °C, respectively. ADH added at a 2:1 DAAM:ADH molar stoichiometric ratio. Image size = 1 μ m square 167

Figure 6.16 (a) Stress-strain curves for 0:100 core:shell ratio films with varying DAAM contents. Film composition is poly[(BA)-*co*-(BMA)] core phase copolymer and poly[(BA)-*co*-(BMA)-*co*-(DAAM)] shell phase copolymer with ADH added at 2:1 molar stoichiometric ratio; (b) Section of stress-strain curves from (a) with strains of 0-4% used to calculate Young's modulus (coefficient of first order term in a polynomial fit expression; order of fit = 6) 170

Figure 6.17 (a) Stress-strain curves for 70:30 core:shell ratio films with varying DAAM contents. Film composition is poly[(BA)-*co*-(BMA)] core phase copolymer and poly[(BA)-*co*-(BMA)-*co*-(DAAM)] shell phase copolymer with ADH added at 2:1 molar stoichiometric ratio; (b) Section of stress-strain curves from (a) with strains of 0-4% used to calculate Young's modulus (coefficient of first order term in a polynomial fit expression; order of fit = 6) 172

Figure 6.18 (a) Stress-strain curves for 80:20 core:shell ratio films with varying DAAM contents. Film composition is poly[(BA)-*co*-(BMA)] core phase copolymer and poly[(BA)-*co*-(BMA)-*co*-(DAAM)] shell phase copolymer with ADH added at 2:1 molar stoichiometric ratio; (b) Section of stress-strain curves from (a) with strains of 0-4% used to calculate Young's modulus (coefficient of first order term in a polynomial fit expression; order of fit = 6) 173

Figure 6.19 (a) Stress-strain curves for 90:10 core:shell ratio films with varying DAAM contents. Film composition is poly[(BA)-*co*-(BMA)] core phase copolymer and poly[(BA)-*co*-

(BMA)-*co*-(DAAM)] shell phase copolymer with ADH added at 2:1 molar stoichiometric ratio; (b) Section of stress-strain curves from (a) with strains of 0-4% used to calculate Young's modulus (coefficient of first order term in a polynomial fit expression; order of fit = 6) 175

Figure 6.20 (a) Stress-strain curve for 70:30 core:shell ratio films with poly[(BA)-*co*-(BMA)] core phase copolymer and poly[(BA)-*co*-(BMA)-*co*-(DAAM)] shell phase copolymer with 2 wt% of DAAM. ADH added at various stoichiometric ratios, as can be seen in the legend; (b) Section of stress-strain curve from (a) with strains of 0-4% used to calculate Young's modulus (coefficient of first order term in a polynomial fit expression; order of fit = 6) 177

Figure 7.1 Plot of $\log(\text{modulus})$ versus temperature for polystyrene and polyisobutylene.²²¹ The rapid change in gradient, and hence the modulus of a polymer film, represents the glass transition..... 182

Figure 7.2 Structure of (a) polystyrene repeat unit and (b) polyisobutylene repeat unit 182

Figure 7.3 DSC traces for (a) unstructured poly[(BA)-*co*-(BMA)] particle and (b) structured particle with poly[(BA)-*co*-(BMA)] core and poly[(BA)-*co*-(BMA)-*co*-(DAAM)] shell phase copolymers and a core:shell ratio of 70:30. ΔT_g is the glass transition temperature width. . 186

Figure 7.4(a) Stress-strain curves for 70:30 core:shell ratio films with varying core phase T_g . Film composition is poly[(BA)-*co*-(BMA)] core phase copolymer and poly[(BA)-*co*-(BMA)-*co*-(DAAM)] shell phase copolymer with ADH added at 2:1 molar stoichiometric ratio; (b) Section of stress-strain curves from (a) with strains of 0-4% used to calculate Young's modulus (coefficient of first order term in a polynomial fit expression; order of fit = 6) 186

Figure 7.5(a) Stress-strain curves for 80:20 core:shell ratio films with varying core phase T_g . Film composition is poly[(BA)-*co*-(BMA)] core phase copolymer and poly[(BA)-*co*-(BMA)-*co*-(DAAM)] shell phase copolymer with ADH added at 2:1 molar stoichiometric ratio; (b) Section of stress-strain curves from (a) with strains of 0-4% used to calculate Young's modulus (coefficient of first order term in a polynomial fit expression; order of fit = 6) 188

Figure 7.6(a) Stress-strain curves for 80:20 core:shell ratio films with varying core phase T_g . Film composition is poly[(BA)-*co*-(BMA)] core phase copolymer and poly[(BA)-*co*-(BMA)-*co*-(DAAM)] shell phase copolymer with ADH added at 2:1 molar stoichiometric ratio; (b) Section of stress-strain curves from (a) with strains of 0-4% used to calculate Young's modulus (coefficient of first order term in a polynomial fit expression; order of fit = 6) 191

Figure 7.7(a) Stress-strain curves for 80:20 core:shell ratio films with varying core phase T_g and DAAM content. Film composition is poly[(BA)-*co*-(BMA)] core phase copolymer and poly[(BA)-*co*-(BMA)-*co*-(DAAM)] shell phase copolymer with ADH added at 2:1 molar stoichiometric ratio; (b) Section of stress-strain curves from (a) with strains of 0-4% used to calculate Young's modulus (coefficient of first order term in a polynomial fit expression; order of fit = 6)..... 196

Figure 7.8 Optical images of film cross-sections for (a) Core copolymer $T_g = 25^\circ\text{C}$; 5 wt% DAAM in shell and (b) Core copolymer $T_g = 25^\circ\text{C}$; 7.5 wt% DAAM in shell..... 197

Figure 7.9 DMT Modulus AFM image of a lightly crosslinked soft-soft nanocomposite film cross-section with 80:20 core:shell ratio, comprising poly[(BA)-*co*-(BMA)] core and poly[(BA)-*co*-(BMA)-*co*-(DAAM)] shell phase copolymers with T_g s of 25 and 5 °C, respectively and 5 wt% DAAM in the shell phase. ADH added at a 2:1 DAAM:ADH molar stoichiometric ratio. Image size = 2 μ m square 198

Figure 7.10 DMT Modulus AFM image of a lightly crosslinked soft-soft nanocomposite film cross-section with 80:20 core:shell ratio, comprising poly[(BA)-*co*-(BMA)] core and poly[(BA)-*co*-(BMA)-*co*-(DAAM)] shell phase copolymers with T_g s of 25 and 5 °C, respectively and 5 wt% DAAM in the shell phase. ADH added at a 2:1 DAAM:ADH molar stoichiometric ratio. Image size = 10 μ m square 198

Figure 7.11 DMT Modulus AFM image of a lightly crosslinked soft-soft nanocomposite film cross-section with 80:20 core:shell ratio, comprising poly[(BA)-*co*-(BMA)] core and poly[(BA)-*co*-(BMA)-*co*-(DAAM)] shell phase copolymers with T_g s of 25 and 5 °C, respectively and 7.5 wt% DAAM in the shell phase. ADH added at a 2:1 DAAM:ADH molar stoichiometric ratio. Image size = 2 μ m square..... 199

Figure 7.12 DMT Modulus AFM image of a lightly crosslinked soft-soft nanocomposite film cross-section with 80:20 core:shell ratio, comprising poly[(BA)-*co*-(BMA)] core and poly[(BA)-*co*-(BMA)-*co*-(DAAM)] shell phase copolymers with T_g s of 25 and 5 °C, respectively and 7.5 wt% DAAM in the shell phase. ADH added at a 2:1 DAAM:ADH molar stoichiometric ratio. Image size = 10 μ m square..... 199

Figure 7.13 Height AFM images of a lightly crosslinked soft-soft nanocomposite film cross-section with 80:20 core:shell ratio, comprising poly[(BA)-*co*-(BMA)] core and poly[(BA)-*co*-(BMA)-*co*-(DAAM)] shell phase copolymers with (a) T_g s of 25 and 5 °C, respectively, and 5 wt% DAAM in the shell phase and (b) T_g s of 25 and 5 °C, respectively, and 7.5 wt% DAAM in the shell phase . ADH added at a 2:1 DAAM:ADH molar stoichiometric ratio. Image sizes = 10 μ m square 200

Figure 7.14 Height profiles for a lightly crosslinked soft-soft nanocomposite film cross-sections with 80:20 core:shell ratio, comprising poly[(BA)-*co*-(BMA)] core and poly[(BA)-*co*-(BMA)-*co*-(DAAM)] shell phase copolymers with T_g s of 25 and 5 °C, respectively, and 5 wt% and 7.5 wt% DAAM in the shell phase. 201

Figure 7.15 (a) Stress-strain curves for 70:30 core:shell ratio films with varying shell phase T_g . Film composition is poly[(BA)-*co*-(BMA)] core phase copolymer with T_g = 10 °C and poly[(BA)-*co*-(BMA)-*co*-(DAAM)] shell phase copolymer with ADH added at 2:1 molar stoichiometric ratio; (b) Section of stress-strain curves from (a) with strains of 0-4% used to calculate Young's modulus (coefficient of first order term in a polynomial fit expression; order of fit = 6) 204

Figure 7.16(a) Stress-strain curves for 80:20 core:shell ratio films with varying shell phase T_g . Film composition is poly[(BA)-*co*-(BMA)] core phase copolymer with T_g = 10 °C and poly[(BA)-*co*-(BMA)-*co*-(DAAM)] shell phase copolymer with ADH added at 2:1 molar stoichiometric ratio; (b) Section of stress-strain curves from (a) with strains of 0-4% used to calculate

Young's modulus (coefficient of first order term in a polynomial fit expression; order of fit = 6)	204
Figure 7.17(a) Stress-strain curves for 90:10 core:shell ratio films with varying shell phase T_g . Film composition is poly[(BA)-co-(BMA)] core phase copolymer with $T_g = 10\text{ }^\circ\text{C}$ and poly[(BA)-co-(BMA)-co-(DAAM)] shell phase copolymer with ADH added at 2:1 molar stoichiometric ratio; (b) Section of stress-strain curves from (a) with strains of 0-4% used to calculate Young's modulus (coefficient of first order term in a polynomial fit expression; order of fit = 6)	205
Figure 7.18 Variation of Young's modulus with observed T_g for soft-soft nanocomposite films with a poly[(BA)-co-(BMA)] core phase copolymer and a poly[(BA)-co-(BMA)-co-(DAAM)] shell phase copolymer with fixed $T_g = 5\text{ }^\circ\text{C}$. ADH was added to each film at a 2:1 DAAM:ADH molar stoichiometry	206
Figure 7.19 Variation of Young's modulus values with core phase T_g for soft-soft nanocomposite films with a poly[(BA)-co-(BMA)] core phase copolymer and a poly[(BA)-co-(BMA)-co-(DAAM)] shell phase copolymer with fixed $T_g = 5\text{ }^\circ\text{C}$. ADH was added to each film at a 2:1 DAAM:ADH molar stoichiometry	207
Figure 7.20 DMTA profiles for soft-soft nanocomposite films with a poly[(BA)-co-(BMA)] core phase copolymer and a poly[(BA)-co-(BMA)-co-(DAAM)] shell phase copolymer with (a) fixed core and shell $T_g = 5\text{ }^\circ\text{C}$ and (b) core $T_g = 25\text{ }^\circ\text{C}$ and shell $T_g = 5\text{ }^\circ\text{C}$. ADH was added to the films at a 2:1 DAAM:ADH molar stoichiometry	208
Figure 7.21 Zoomed portion of Storage modulus vs. adjusted temperature plot for soft-soft nanocomposite films with a poly[(BA)-co-(BMA)] core phase copolymer and a poly[(BA)-co-(BMA)-co-(DAAM)] shell phase copolymer with fixed core and shell $T_g = 5\text{ }^\circ\text{C}$ and core $T_g = 25\text{ }^\circ\text{C}$ and shell $T_g = 5\text{ }^\circ\text{C}$. ADH was added to the films at a 2:1 DAAM:ADH molar stoichiometry	209
Figure 7.22 Variation of Young's modulus with V_c , T_g , where V_c is the core phase volume fraction, for soft-soft nanocomposite films with a poly[(BA)-co-(BMA)] core phase copolymer and a poly[(BA)-co-(BMA)-co-(DAAM)] shell phase copolymer with fixed $T_g = 5\text{ }^\circ\text{C}$. ADH was added to each film at a 2:1 DAAM:ADH molar stoichiometry	209
Figure 8.1 Structures of (a) acrylic acid (AA) and (b) methacrylic acid (MAA).....	211
Figure 8.2 Schematic diagram showing the incorporation of ionic crosslinking into soft-soft nanocomposite nitrile rubber films using MAA and Zn species ⁹	212
Figure 8.3 (a) Stress-strain curves for 80:20 core:shell ratio films with core copolymer $T_g = 10\text{ }^\circ\text{C}$ and varying levels of MAA in the shell phase copolymer. Film composition is poly[(BA)-co-(BMA)] core phase copolymer and poly[(BA)-co-(BMA)-co-(DAAM)-co-(MAA)] shell phase copolymer with ADH added at 2:1 molar stoichiometric ratio; (b) Section of stress-strain curves from (a) with strains of 0-4% used to calculate Young's modulus (coefficient of first order term in a polynomial fit expression; order of fit = 6)	215

Figure 8.4 (a) Stress-strain curves for 80:20 core:shell ratio films with core copolymer $T_g = 25$ °C and varying levels of MAA in the shell phase copolymer. Film composition is poly[(BA)-co-(BMA)] core phase copolymer and poly[(BA)-co-(BMA)-co-(DAAM)-co-(MAA)] shell phase copolymer with ADH added at 2:1 molar stoichiometric ratio; (b) Section of stress-strain curves from (a) with strains of 0-4% used to calculate Young's modulus (coefficient of first order term in a polynomial fit expression; order of fit = 6)..... 216

Figure 8.5 DMT Modulus AFM image of a lightly-crosslinked soft-soft nanocomposite film cross-section with 80:20 core:shell ratio, comprising poly[(BA)-co-(BMA)] core and poly[(BA)-co-(BMA)-co-(DAAM)-co-(MAA)] shell phase copolymers with T_{gs} of 25 and 5 °C, respectively, with 2 wt% MAA present in the shell phase only. ADH was added at a 2:1 DAAM:ADH molar stoichiometric ratio. Image size = 5 μ m square 219

Figure 8.6 DMT Modulus AFM image of a lightly-crosslinked soft-soft nanocomposite film cross-section with 80:20 core:shell ratio, comprising poly[(BA)-co-(BMA)] core and poly[(BA)-co-(BMA)-co-(DAAM)-co-(MAA)] shell phase copolymers with T_{gs} of 25 and 5 °C, respectively, with 5 wt% MAA present in the shell phase. ADH was added at a 2:1 DAAM:ADH molar stoichiometric ratio. Image size = 5 μ m square 219

Figure 8.7 Stress-strain curves for 80:20 core:shell ratio films with core copolymer $T_g = 25$ °C and 2 wt% MAA in the shell phase copolymer. Film composition is poly[(BA)-co-(BMA)] core phase copolymer and poly[(BA)-co-(BMA)-co-(DAAM)-co-(MAA)] shell phase copolymer with ADH added at 2:1 molar stoichiometric ratio; (b) Section of stress-strain curves from (a) with strains of 0-4% used to calculate Young's modulus (coefficient of first order term in a polynomial fit expression; order of fit = 6) 222

Figure 8.8 DMT Modulus AFM image of a lightly crosslinked soft-soft nanocomposite film cross-section with 80:20 core:shell ratio, comprising poly[(BA)-co-(BMA)] core and poly[(BA)-co-(BMA)-co-(DAAM)-co-(MAA)] shell phase copolymers with T_{gs} of 25 and 5 °C, respectively, with 2 wt% MAA present in the shell phase and latex neutralised with NaOH. ADH was added at a 2:1 DAAM:ADH molar stoichiometric ratio. Image size = 5 μ m square 223

Figure 8.9 DMT Modulus AFM image of a lightly crosslinked soft-soft nanocomposite film cross-section with 80:20 core:shell ratio, comprising poly[(BA)-co-(BMA)] core and poly[(BA)-co-(BMA)-co-(DAAM)-co-(MAA)] shell phase copolymers with T_{gs} of 25 and 5 °C, respectively, with 2 wt% MAA present in the shell phase and latex neutralised with NH_3 . ADH added at a 2:1 DAAM:ADH molar stoichiometric ratio. Image size = 5 μ m square 223

Figure 8.10 DMT Modulus AFM image of a lightly crosslinked soft-soft nanocomposite film cross-section with 80:20 core:shell ratio, comprising poly[(BA)-co-(BMA)] core and poly[(BA)-co-(BMA)-co-(DAAM)-co-(MAA)] shell phase copolymers with T_{gs} of 25 and 5 °C, respectively, with 2 wt% MAA present in the shell phase and latex unneutralised. No ADH was added. Image size = 5 μ m square 224

Figure 9.1 (a) Comparative particle size distribution curves for the latexes described in Table 9.1; (b) zoomed section of (a) from 0-500 nm 228

Figure 9.2 DSC traces for (a) NeoCryl XK-98 and (b) Linear acrylic 1 229

Figure 9.3 (a) Stress-strain curves for films from selected water-borne binder latexes described in Table 9.1; (b) Section of stress-strain curves from (a) with strains of 0-4% used to calculate Young's modulus (coefficient of first order term in a polynomial fit expression; order of fit = 6)..... 230

Figure 9.4 (a) Stress-strain curves for films from selected water-borne binder latexes described in Table 9.1 compared to soft-soft nanocomposites; (b) Section of stress-strain curves from (a) (minus NeoCryl XK-98) with strains of 0-4% used to calculate Young's modulus (coefficient of first order term in a polynomial fit expression; order of fit = 6) 232

Figure 9.5 Plot of Young's modulus vs extension to break for a range of AkzoNobel binders and four soft-soft nanocomposite variants. 233

List of Tables

Table 4.1 Summary of the assignments of peaks from the NMR spectrum shown in Figure 4.1 in relation to the structure of the surfactant shown in Figure 4.2.	102
Table 4.2 Original poly[(MMA)- <i>co</i> -(BA)- <i>co</i> -(MAA)] latex formulation provided by AkzoNobel	103
Table 4.3 Table of monomer feed compositions to form a copolymer with a specified theoretical T_g	108
Table 4.4 Characterisation data for latexes synthesised to investigate the effect of functional and crosslinking monomers	109
Table 4.5 Coagulum produced by preparations using Lutensol TOx non-ionic surfactants ...	110
Table 4.6 Summary of the assignments of peaks from the NMR spectrum shown in Figure 4.8 in relation to the structure of the surfactant shown in Figure 4.9	112
Table 4.7 Kinetics data for preparations including Lutensol TO7	114
Table 4.8 DSC data for films from the latex variants discussed in Table 4.7	114
Table 4.9 Levels of residual monomer in soft-soft nanocomposite latexes analysed by GC..	116
Table 4.10 Table showing difference between theoretical and actual T_g values for poly[(BA)- <i>co</i> -(BMA)] latexes.....	116
Table 5.1 Latex compositions and theoretical T_g values discussed in Section 5.2.....	125
Table 5.2 Kinetics data for the latexes discussed in Section 5.2.....	126
Table 5.3 Actual T_g values for soft-soft nanocomposites discussed in Section 5.2	127
Table 5.4 Mechanical property data for films from the systems defined in Table 5.1.....	130
Table 5.5 Relative mass of surfactant and ADH in 100 g of the latexes discussed in Section 5.3	134
Table 5.6 Composition of latexes discussed in Section 5.5.....	145
Table 5.7 Results from MFT testing	146
Table 5.8 High- and low-shear viscosity testing results	147
Table 6.1 Composition of soft-soft nanocomposite systems with varying core:shell ratios ..	155
Table 6.2 Kinetics data for the soft-soft nanocomposite systems detailed in Table 6.1.....	155
Table 6.3 Mechanical property data for variants discussed in Section 6.2	157
Table 6.4 Films used for hysteresis and stress relaxation testing discussed in Section 6.2.1	159

Table 6.5 Stress relaxation property data for the films detailed in Table 6.4	161
Table 6.6 Soft-soft nanocomposite latexes used for GPC analysis	162
Table 6.7 GPC analysis data for soft-soft nanocomposite polymers with varying core:shell ratios	163
Table 6.8 Latex characterisation data for the synthesis of 0:100 core:shell latexes	169
Table 6.9 Mechanical property data for 0:100 core:shell latexes with varying levels of DAAM	170
Table 6.10 Latex characterisation data for the synthesis of 70:30 core:shell latexes with varying levels of DAAM	171
Table 6.11 Mechanical property data for 70:30 core:shell latexes with varying levels of DAAM in the shell phase	172
Table 6.12 Latex characterisation data for the synthesis of 80:20 core:shell latexes with varying levels of DAAM	173
Table 6.13 Mechanical property data for 80:20 core:shell latexes with varying levels of DAAM in the shell phase	174
Table 6.14 Latex characterisation data for the synthesis of 90:10 core:shell latexes with varying levels of DAAM	174
Table 6.15 Mechanical property data for 90:10 core:shell latexes with varying levels of DAAM in the shell phase	175
Table 6.16 Variants tested to deduce the effect of DAAM:ADH molar stoichiometry	176
Table 6.17 Mechanical property data for systems discussed in Section 3.2.5	178
Table 7.1 List of parameters kept constant for work detailed in Section 7.2	184
Table 7.2 Kinetics characterisation data for the synthesis of 70:30 core:shell latexes with varying core phase T_g values	184
Table 7.3 DSC data for 70:30 core:shell ratio films with variable core phase copolymer T_g ..	185
Table 7.4 Mechanical property data for 70:30 core:shell latexes with varying core phase T_g	187
Table 7.5 Latex characterisation data for the synthesis of 80:20 core:shell latexes with varying core phase T_g values	187
Table 7.6 Mechanical property data for 80:20 core:shell latexes with varying core phase T_g	188
Table 7.7 DSC data for 80:20 core:shell ratio films with variable core phase copolymer T_g ..	189

Table 7.8 Latex characterisation data for the synthesis of 90:10 core:shell latexes with varying core phase T_g values.....	190
Table 7.9 Mechanical property data for 80:20 core:shell latexes with varying core phase T_g	191
Table 7.10 DSC data for 90:10 core:shell ratio films with variable core phase T_g	192
Table 7.11 MFT analysis of soft-soft nanocomposite latexes described in Section 7.2	192
Table 7.12 Synthesis matrix to investigate the effect of crosslinker content at higher poly[(BA)-co-(BMA)] core phase T_g	194
Table 7.13 Characterisation data for syntheses detailed in Table 7.12.....	194
Table 7.14 DSC data for films with high core phase T_g and crosslinker content	195
Table 7.15 Mechanical property data for soft-soft nanocomposite films with 80:20 core:shell ratio, fixed shell T_g of 5 °C, high core copolymer T_g and variable DAAM content	197
Table 7.16 Parameters kept constant throughout Section 7.4.....	201
Table 7.17 Synthesis characterisation data for preparations detailed in Table 7.16	202
Table 7.18 DSC data for films with varying shell phase T_g	203
Table 7.19 Mechanical property data for films with fixed core T_g of 10 °C and varying shell phase T_g	205
Table 8.1 Synthesis matrix of variants to evaluate the effect of adding MAA	213
Table 8.2 Synthesis characterisation data for preparations described in Table 8.1.....	214
Table 8.3 Mechanical property data for the lower core T_g systems with varying amounts of MAA in the shell phase	214
Table 8.4 DSC data for low core T_g systems with varying amounts of MAA in the shell phase	215
Table 8.5 Mechanical property data for high core T_g systems with varying amounts of MAA in the shell phase	216
Table 8.6 DSC data for high core T_g systems with varying amounts of MAA in the shell phase	216
Table 8.7 Details of latex used for the investigation discussed in Section 8.3.	221
Table 8.8 Mechanical property data for MAA-containing latex with varying methods of neutralisation.....	222
Table 9.1 Technical information for systems discussed in Chapter 9.....	226

Table 9.2 Characterisation data for the binder systems in the wet state	228
Table 9.3 Summary of DSC data for latexes described in Table 9.1	229
Table 9.4 Mechanical property data for AkzoNobel comparison binder systems.....	230
Table 9.5 Soft-soft nanocomposite systems of interest discussed in Section 9.4	231

List of Abbreviations

1,6-HDDA	1,6-hexanediol diacrylate
2-EHA	2-ethylhexyl acrylate
AA	Acrylic acid
AAEM	Acetoacetoxy methacrylate
ADH	Adipic acid dihydrazide
AFM	Atomic force microscopy
AFM-IR	Atomic force microscopy-infrared spectroscopy
APEO	Alkylphenyl ethoxylate
ASR	Alkali-soluble resin
BA	n-Butyl acrylate
Bd	1,4-butadiene
BDDA	1,4-butanediol diacrylate
BMA	Butyl methacrylate
DAAM	Diacetone acrylamide
DET	Direct energy transfer
DMT	Derjagurin-Muller-Toporov modulus
DMTA	Dynamic mechanical thermal analysis
DSC	Differential scanning calorimetry
EGDMA	Ethylene glycol dimethacrylate
EA	Ethyl acrylate
FID	Flame ionization detector
FTIR	Fourier transform infrared spectroscopy
GC	Gas chromatography
GPC	Gel permeation chromatography
HDC	Hydrodynamic chromatography
HDMA	Hexamethylene diamine
IPN	Interpenetrating polymer network
IR	Infrared
MA	Methyl acrylate
MAA	Methacrylic acid
MFT	Minimum film formation temperature
MMA	Methyl methacrylate
MWD	Molecular weight distribution
n-DDM	n-Dodecyl mercaptan
n-MA	n-Methylol acrylamide
NMR	Nuclear magnetic resonance spectroscopy
PBA	Poly(n-butyl acrylate)
PCS	Photon correlation spectroscopy
PMMA	Poly(methyl methacrylate)
PSA	Pressure-sensitive adhesive
PSDA	Particle size distribution analysis
PSty	Polystyrene
PVC	Poly(vinyl chloride)
QNM	Quantitative Nanomechanical mapping

SANS	Small angle neutron scattering
SEC	Size exclusion chromatography
SEM	Scanning electron microscopy
SLS	Sodium lauryl sulphate
Sty	Styrene
TEM	Transmission electron microscopy
THF	Tetrahydrofuran
TMS	Tetramethylsilane
T_g	Glass transition temperature
T_m	Melting temperature
VOC	Volatile organic compound

Abstract

Elizabeth Eaves

The University of Manchester

PhD Polymer Science and Engineering

“Soft-soft nanocomposite coating materials produced by emulsion polymerisation”

March 2015

This thesis reports on the challenge of applying an innovative ‘soft-soft nanocomposite’ design strategy to establish synthesis parameters that affect the performance of coatings based upon water-borne latexes, which is driven by the environmental and legislative need to develop feasible alternatives to solvent-borne coatings. A framework emulsion polymerisation formulation to synthesise core-shell latexes with (poly[(butyl acrylate)-*co*-(butyl methacrylate)]) core and (poly[(butyl acrylate)-*co*-(butyl methacrylate)-*co*-(diacetone acrylamide)]) shell copolymer phases in a controlled manner was established, with high monomer conversions and approximately constant particle numbers. Retention of particle morphology in the films was confirmed using atomic force microscopy (AFM).

The effect of adding adipic acid dihydrazide to the latex post-polymerisation to facilitate crosslinking of the shell phase during film formation was found to have a significant effect on the stress-strain properties of latex films. A core:shell mass ratio of 80:20 was found to be optimum in all crosslinked systems tested. Increasing the amount of crosslinking in the shell phase of the particles was found to have an effect on the large strain tensile properties of films, leading to strain hardening with reduced extension to break and higher failure stresses at higher crosslinker levels.

Core phase copolymer T_g had a very significant effect upon the low strain mechanical properties, with Young’s modulus values of 5-180 MPa being accessible in the range of core T_g s from 5 – 25 °C, although little difference in mechanical behaviour was seen when varying the shell phase T_g from 5 – 15 °C. Adding 2 wt% methacrylic acid (MAA) to the shell phase copolymer gave an additional improvement in the low strain tensile region, with a Young’s modulus of 425 MPa being realised. However, it was found that additional amounts of MAA (up to 5 wt% in the shell phase) were deteriorious to film properties, with low Young’s modulus and poor extensibility. This was interpreted as being due to an increased concentration of ionic crosslinks restricting interparticle chain diffusion and keto-hydrazide crosslinking. Studies to evaluate the mechanical performance of soft-soft nanocomposite films compared to binder latexes used in commercial products were favourable, and showed that a high level of versatility with regards to mechanical properties is possible.

Declaration

I declare that no portion of the work referred to in the thesis has been submitted in support of an application for another degree or qualification of this or any other university or other institute of learning.

Elizabeth Eaves
March 2015

Copyright statement

- i. The author of this thesis (including any appendices and/or schedules to this thesis) owns certain copyright or related rights in it (the “Copyright”) and s/he has given The University of Manchester certain rights to use such Copyright, including for administrative purposes.
- ii. Copies of this thesis, either in full or in extracts and whether in hard or electronic copy, may be made **only** in accordance with the Copyright, Designs and Patents Act 1988 (as amended) and regulations issued under it or, where appropriate, in accordance with licensing agreements which the University has from time to time. This page must form part of any such copies made.
- iii. The ownership of certain Copyright, patents, designs, trademarks and other intellectual property (the “Intellectual Property”) and any reproductions of copyright works in the thesis, for example graphs and tables (“Reproductions”), which may be described in this thesis, may not be owned by the author and may be owned by third parties. Such Intellectual Property and Reproductions cannot and must not be made available for use without the prior written permission of the owner(s) of the relevant Intellectual Property and/or Reproductions.
- iv. Further information on the conditions under which disclosure, publication and commercialisation of this thesis, the Copyright and any Intellectual Property and/or Reproductions described in it may take place is available in the University IP Policy (see <http://documents.manchester.ac.uk/DocuInfo.aspx?DocID=487>), in any relevant Thesis restriction declarations deposited in the University Library, The University Library’s regulations (see <http://www.manchester.ac.uk/library/aboutus/regulations>) and in The University’s policy on Presentation of Theses

*This thesis is dedicated to my grandmother, Molly Garland,
who may well get her wish to see me become a doctor granted after all.*

Acknowledgements

The completion of this thesis would not have been possible without the contributions, both professional and personal, of many people. I would like to take this opportunity to thank those that have helped me over the past three and a half years for all of their efforts.

Firstly to my supervisor, Professor Pete Lovell, who gave me the opportunity to work with him and has been a constant source of both academic and pastoral support. The lessons that I have learned from Pete about being thorough and rigorous with my work will stay with me throughout the rest of my career.

I would also like to thank EPSRC and AkzoNobel Decorative Coatings for funding the project. I am grateful to all of those from AkzoNobel who have helped me, most notably Simon Emmett, Neal Williams and Martin Murray for their insight and help with my work. Big thanks also go to Cathy Stevens, Juan Zhou and Beth Green who have all organised and lobbied for things on my behalf throughout this PhD.

In Manchester, the biggest thanks go to Polly Greensmith, who has always been there with both technical and personal support. Another person whose contribution to my PhD is extremely valued is Ivan Easdon, although his contribution to my expanded waistline is not!

All of my various office, pub and lunch friends deserve a mention too. Katy Gibson, Margaret Wegrzyn, Judith McCann, Colin Norman, Robbie Farley, Alice Nelson, Tom Jansen, Shicheng Li, Jane Bramhill, Mary Zhang and Sirikarn Khansumled – you have all made my time in the School of Materials an absolute pleasure, although some of the mornings-after-the-nights-before haven't been.

Last, but certainly not least are the thanks to my very closest friends and family. To Richard, who will yet have more tired, stressed and hungry Lizzie Eaves-anger to deal with in his usual admirable style before the ink is dry on this thesis. To my parents, who always have an interest in my day's activities and an encouraging bit of advice or a stern word when I need it. To my sister, who is always pleased for my successes and gives the best advice about power dressing. To both my grandparents, who proudly tell all and sundry "*She's going to be a doctor, you know*". Your love and dedication means the world to me.

1 Project background and aims

To form a film from latex polymer particles, it is often necessary to add a coalescing aid, which is typically a volatile organic compound (VOC). The role of a coalescing aid is to plasticise the polymer particles during film formation, therefore lowering the minimum film forming temperature (MFT) of a latex before evaporating slowly to leave a rigid and water resistant film¹. However, due to environmental concerns the use of such additives is being discouraged so it is desirable to investigate alternative ways of forming mechanically-strong films.

The EU VOC Solvents Emission Directive 1999/13/EC was first introduced in 1999² and covers a large number of VOC-utilising processes, including manufacturing, printing and dry cleaning. Successively stricter amendments³ to this directive have increasingly limited the VOC content of paints, which are split into categories depending on their intended application and physical properties such as solids content.

1.1 Project aims

This project sought to evaluate the feasibility of developing robust and durable high-performance coatings based upon water-borne latexes by building upon the principles underlying an innovative soft-soft nanocomposite strategy for the design and synthesis of high-performance water-borne pressure-sensitive adhesives (PSAs) that evolved from an EC FP6 project led by Prof. Lovell in 2009⁴⁻⁶. This set of principles have recently been applied successfully to enhancing properties of nitrile rubber films through controlled particle synthesis⁷⁻⁹, but had yet to be explored for polymer films with glass transition temperatures (T_g) much closer to room temperature, as is the case for those utilised in coating materials. The strategy requires the synthesis of colloiddally-stable dispersions of polymer particles with diameters of 100-300 nm, control of the radial particle morphology at the nanometre scale and the inclusion of latent crosslinkable functional groups, such as diacetone acrylamide (DAAM) and adipic acid dihydrazide (ADH) in an outer shell phase. These crosslinkable functional groups react only when polymer particles coalesce during film formation, which gives a film that has a honeycomb-like retained morphology with a percolating phase that crosslinks and controls the elastic properties of the film. This percolating phase should deliver the enhancement in film properties that is traditionally achieved by the evaporation of VOC coalescing solvents, but also should be tuneable to achieve greater improvements in film properties, particularly toughness. The control of particle composition, reactivity and morphology required is non-trivial and the key challenges involved in this project were to

understand the design and controlled synthesis of particle composition and morphology and the extent of crosslinking that is required to achieve the necessary balance between easy film formation and build up in film properties/performance.

This thesis contains a full review of the existing literature that discusses the underpinning theories of the project in Chapter 2, followed by a section that describes the materials, synthesis and characterisation methods. Six chapters that discuss the results of investigations into establishing a synthesis method for soft-soft nanocomposite coating materials, structure-property relationships and comparisons to existing water-borne coating systems are then presented. The thesis will conclude with an overview of the conclusions that can be drawn from the work discussed and recommendations for further work.

2 Literature Review

2.1 Introduction to Polymers

Synthetic polymers were first developed and commercialised in the early 20th century with the production of Bakelite in 1910, a phenol-formaldehyde resin that was the first fully synthetic polymer material. However, the scientific understanding of polymers and the quality of commercially produced synthetic polymers were poor until the 1930's, when the outbreak of international conflict necessitated the development of alternatives to natural resources, the supply of which became restricted in the years of World War II¹⁰.

There are two distinct mechanisms by which polymerisation may occur, namely 'step growth' and 'chain growth' polymerisations. Step polymerisation refers to monomer units initially combining to form low molar mass oligomers, before further combination to form a higher molar mass polymer chain. This may happen with the loss of a low-molar mass condensate, as the molar mass of the resulting polymer chain repeat unit is often contains less molecules than that of the monomer species. These reactions are characterised by a very slow initial increase in molar mass with monomer conversion, followed by a steep growth in molar mass at high conversions.

Polymers produced by chain polymerisation are typically of a higher molar mass than those from step-growth polymerisation, with molar masses of $10^5 - 10^7 \text{ g mol}^{-1}$ being easily achievable¹⁰. This is due to the polymer being formed by the subsequent addition of monomer units onto a polymer chain by means of an 'active centre', which is most commonly either an ionic or free radical species. Due to the polymer growth proceeding by the successive addition of units to a chain, the molar mass of the polymer increases extremely rapidly as the reaction proceeds.

The most widely used form of chain-growth polymerisation is free radical polymerisation, which is used to polymerise unsaturated monomers of the form $\text{CH}_2=\text{CR}_1\text{R}_2$ ¹¹. Free radical polymerisation occurs in three distinct mechanistic stages – initiation, propagation and termination. A fourth mechanism, chain transfer, can occur and has a significant effect on the properties of the polymer produced. All four have been extensively investigated, and detailed descriptions of each can be found in the literature¹²⁻¹⁶.

2.1.1 Types of polymerisation process

Unlike other polymerisation methods, such as ionic or non-radical methods, which are usually performed in bulk or solution¹⁷, there are 4 principal processes by which free-radical polymerisation can be conducted: bulk, solution, suspension and emulsion. Each represents

unique advantages and disadvantages over the other methods, and has appropriate applications that are often related to the desired end use for the polymer. As the soft-soft nanocomposites that will be discussed in this thesis will be intended for use as a water-borne medium, emulsion polymerisation will be used for their synthesis.

The first patent relating to an emulsion polymerisation process was granted in 1912 to F. Bayer & Co. for the preparation of synthetic rubber, caoutchouc¹⁸. Large amounts of research relating to synthetic rubber were subsequently conducted, with the outbreak of the First and Second World Wars and the associated restriction in the supply of natural products being the driving force behind it. The first commercialised polymer produced from an emulsion polymerisation, a styrene and butadiene copolymer, was introduced by Dow Chemical in 1946¹⁹.

The most kinetically complex of the four principal polymerisation processes, emulsion polymerisation differs from suspension polymerisation in one main way, which is that the initiator used is soluble in the aqueous phase and insoluble in the monomer²⁰. It is due to this that the polymerisation is heterogeneous rather than homogenous, which complicates the reaction kinetics by introducing terms to acknowledge diffusion of the initiating radical species from the aqueous phase to the monomer-saturated regions by the mechanism discussed in Section 2.2.1.

The use of oil-soluble initiators in emulsion polymerisation has been extensively researched, and findings indicate that the kinetic behaviour with an oil-soluble initiator is very similar to that of a water-soluble initiated equivalent²¹⁻²³. In work carried out in 1992 by Nomura *et al.*, it was found that for the emulsion polymerisation of styrene initiated by 2, 2'-azoisobutyronitrile (AIBN), polymerisation takes place in both the monomer droplets and polymer particles, although the polymerisation in droplets was only significant in the early stages of the polymerisation and represented only a few percent of the total amount of polymer produced by the reaction. During the same work it was also found that only radicals produced in the aqueous medium initiate polymerisation, as radicals formed within the polymer particles terminate by recombination immediately upon formation due to the small volume of the particles in which they are constrained²⁴. However, even though the polymerisations of oil- and water-soluble initiators are very similar in kinetics, water-soluble initiators are employed industrially as they give more stable latexes than those produced by an oil-soluble initiator²⁵.

Monomer droplets, which are smaller than those present in a suspension polymerisation²⁶, are dispersed in the aqueous phase and stabilized by surfactants, which are most commonly anionic in character. These surfactants provide sites for initial particle formation and stabilise the resulting colloids. The product of an emulsion polymerisation is a latex – a colloidal dispersion of polymer particles in an aqueous medium.

The method was first commercially utilized in the early 20th century and significantly developed during the Second World War as a route to making a synthetic replacement for natural rubber. Emulsion polymerisations are faster and yield a higher molar mass polymer product than bulk, solution or suspension polymerisation, which has led to the widespread use of the emulsion process in industrial production¹⁷. Other advantages of this polymerisation process include efficient heat transfer and a low viscosity of the polymer latex, even at high (50-60%) polymer content. As opposed to suspension polymerisation, stable low T_g polymers may be formed from emulsion polymerisation due to the stabilization of the particles by surfactant which reduces the occurrence of particle agglomeration.

In order for an olefinic monomer to be successfully polymerised using an emulsion process, there are three conditions that must be met. The polymer must be insoluble in an aqueous medium, and the monomer must be polymerisable at temperatures of below 100 °C at ambient pressures (i.e. the heating range of the aqueous medium before boiling occurs) and not easily hydrolysable¹⁸.

2.2 Emulsion polymerisation – Mechanism and Kinetics

The mechanism and kinetics of free-radical emulsion polymerisation have been investigated very widely, with one of the most important mechanistic and kinetics theories being developed by Harkins in 1947²⁷ and expanded upon by Smith and Ewart in 1948²⁸. This theory divides the process of emulsion polymerisation into three stages: Interval I (particle nucleation) and Intervals II and III (particle growth). The relationship of these 3 stages with monomer conversion and time can be seen in Figure 2.1.

2.2.1 Interval I – Particle nucleation

Interval I represents the initial formation of the latex particles. The monomer, which is insoluble in the aqueous phase, initially exists in two main forms – mostly as large droplets (approximately 1-10 μm in diameter) but with a small amount present within surfactant

micelles. A very small proportion of the monomer is dissolved in the aqueous phase as individual molecules.

The surfactant molecules, which in emulsion polymerisation are most commonly anionic and at a concentration of 1-5%w/w to monomer¹⁷, consist of a hydrophilic and a hydrophobic section, quite commonly as an ionic head group and a long hydrocarbon chain as can be seen in Figure 2.2 which shows sodium lauryl sulphate, a very common surfactant with a wide range of uses.

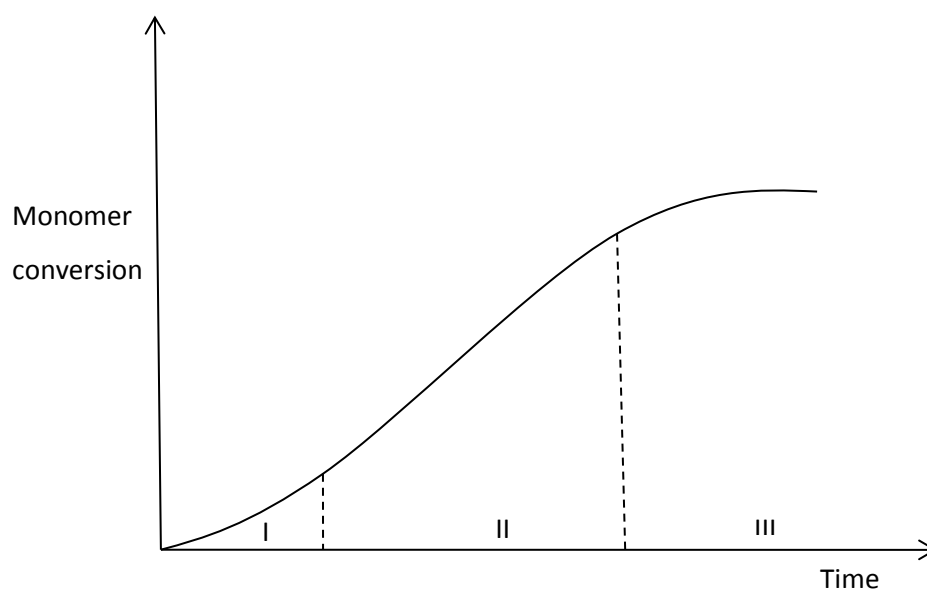


Figure 2.1 Simple schematic plot showing the relationship between monomer conversion and time with respect to Intervals I, II and III of emulsion polymerisation²⁹

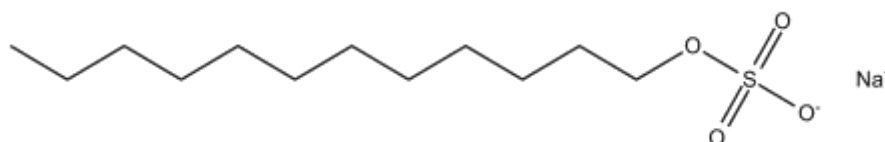


Figure 2.2 Structure of sodium lauryl sulphate (SLS), a commonly used surfactant in emulsion polymerisation

In addition to both cationic and the more commonly used anionic surfactants, uncharged species can also be used to impart colloidal stability. These non-ionic surfactants are commonly composed of long-chain fatty alcohols, and provide steric stabilisation due to their bulky character³⁰.

When added to an aqueous solution at a concentration above the 'critical micelle concentration' (CMC) the surfactant molecules will collect into spherical aggregates known

as 'micelles', with the hydrophilic head groups interacting with the aqueous phase and the hydrocarbon tails forming a hydrophobic 'pocket' within the micelle. Monomer can then diffuse into this lipophilic core. Figure 2.3 shows the cross-sectional structure of a micelle.

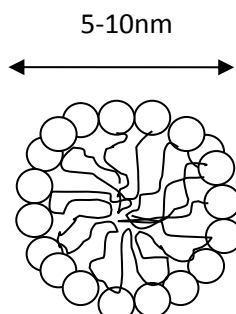


Figure 2.3 Cross-sectional structure of a surfactant micelle, where the circular and linear sections represent hydrophilic and hydrophobic moieties, respectively

The number density of the micelles in a typical emulsion polymerisation is 10^{17} - 10^{18} cm^{-3} , whereas the monomer droplets exist in a density of 10^9 - 10^{11} cm^{-3} . Hence, there are approximately 10^6 times more micelles than monomer droplets per unit volume.

The polymerisation is initiated by the decomposition of the water-soluble initiator, the reaction of the resulting radicals with individual monomer molecules dissolved in the aqueous medium, and the subsequent diffusion of the oligoradicals (typical degree of polymerisation = 2-5 for a hydrophobic monomer)¹¹ into a micelle. This mechanism is shown in Figure 2.4. It is the diffusion of the radical from the aqueous phase to the monomer-swollen core of the micelle that starts the formation of a new latex particle.

According to Smith-Ewart theory, the number of particles formed per unit volume in a polymer latex, N , is given by Equation 2.1:

$$N = k \left(\frac{\rho}{\mu} \right)^z (a_s S)^{(1-z)} \quad (2.1)$$

Where N is the number of particles formed per unit volume, ρ is the rate of radical generation, μ is the rate of particle volume growth, z has a value of 0.6 – 1 and takes into account chain transfer reactions, a_s is the area occupied by a single surfactant molecule and S represents the total amount of surfactant molecules.

However, due to the low concentration of monomer dispersed as individual molecules in the aqueous phase, there is a greater chance of the active radical species undergoing spurious side reactions such as recombination with another radical species before reaching the desired degree of polymerisation to be able to penetrate a micelle. This leads to the

initiator efficiency in emulsion polymerisation often being lower than those of bulk, solution and suspension processes³¹.

There are 3 principal mechanisms by which particle nucleation has been proposed to occur: micellar, homogenous and droplet. All three mechanisms can theoretically occur simultaneously during a polymerisation but depending on the reaction conditions, for example the concentration of surfactant and the solubility of the monomer in the aqueous phase, one mechanism will tend to predominate over the others. A fourth mechanism, coagulative nucleation, is possible and may be a key determining factor of particle size distribution^{32, 33}.

2.2.1.1 Micellar nucleation

Micellar nucleation occurs by the mechanism of initiation referred to in Section 2.2.1. During this mechanism, up to 1% of micelles will be entered by an active radical centre and initiated to form a propagating polymer particle²⁰. The remaining micelles will become disrupted, with the excess surfactant diffusing to stabilise the propagating micelles which will grow in size as monomer conversion continues. After the excess micelles have disappeared, the number of particles per volume will generally remain constant but may decrease due to particle agglomeration resulting from colloidal instability of growing polymer particles³⁴. As can be seen in Figure 2.4, as the monomer inside the micelles polymerises, the large droplets act as reservoirs with monomer molecules diffusing through the aqueous medium and into the hydrophobic core of the newly-formed particles. These droplet reservoirs will disappear at approximately 30-40% conversion, when all remaining monomer is accommodated within the micelles²⁰.

Micellar nucleation is the predominant mechanism of particle formation when the monomer is sparingly soluble in the aqueous phase, more specifically when the concentration of monomer dissolved in the aqueous phase is below 15 mmol dm^{-3} ¹¹. For most emulsion polymerisation processes this is the predominant mechanism of particle nucleation.

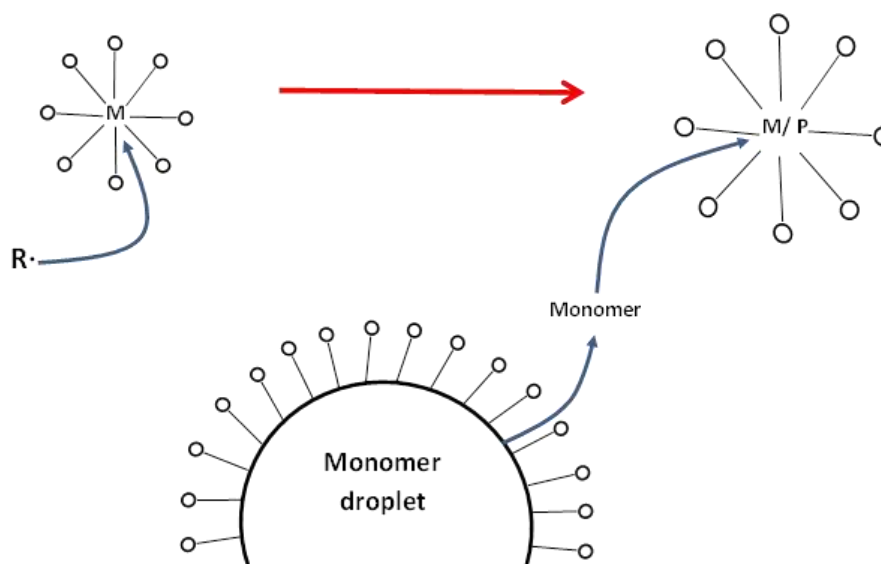


Figure 2.4 Representation of micellar nucleation, where R· = initiator molecule. M = monomer molecule and P = polymer chain. Adapted from Odian¹⁶.

2.2.1.2 Homogenous nucleation

The mechanism of homogenous nucleation tends to predominate for monomers with a higher solubility in the aqueous phase and for surfactant-free systems or when the concentration of surfactant is below the CMC, i.e. when no micelles are present within the polymerisation medium.

In this case, the oligoradicals formed by the initiation stage continue to propagate with monomer molecules dissolved in the aqueous phase. Once these chains reach a certain degree of polymerisation they will become insoluble and precipitate out of the aqueous phase. These 'primary particles' then grow by propagation by the absorption of monomer molecules and stabilisation by surfactant molecules adsorbed onto their surface.

2.2.1.3 Coagulative nucleation

Coagulative nucleation proceeds by a mechanism similar to that of homogenous nucleation, as the small primary particles formed in the aqueous phase will grow by coagulating together to form larger latex particles³⁵. These particles are colloiddally unstable and polymerise very slowly which is due to the very small size of the primary particles resulting in a low concentration of monomer being absorbed. This leads to the growth of the particles produced by coagulative nucleation being much slower by polymer chain propagation than by particle coagulation³⁶. In 2011, Sood *et al.* showed that coagulative nucleation occurs only during Interval I, not throughout the entire polymerisation as had been previously theorised³⁷. The extent to which coagulative nucleation influences particle size distribution can be affected by surfactant, monomer and electrolyte concentration^{33, 38},

³⁹, as it is heavily dependent upon the colloidal stability of particles initially formed by micellar or homogenous nucleation.

2.2.1.4 Droplet nucleation

Droplet nucleation is a mechanism of particle formation that is associated with miniemulsion processes, and is usually considered to be insignificant in standard emulsion polymerisations. It occurs when the oligoradicals generated in the aqueous phase enter into the monomer droplets and propagate. The resulting colloidal particles are stabilised by the surfactant adsorbed onto the surface of the droplet, although an additional 'co-surfactant' is often required in order to suppress Ostwald ripening, which is the transfer of monomer from a smaller droplet to a larger one⁴⁰.

2.2.2 Intervals II/III – Particle growth

The end of Interval I is marked by the disappearance of micelles as the polymer particles are formed by radical entry events, which occurs at up to 10% monomer conversion¹¹. Intervals II and III describe the growth of the monomer-swollen polymer particles once they have been created by one of the particle nucleation mechanisms detailed in Section 2.2.1.1, and represent distinct stages in the particle growth. The rate of polymerisation in all three intervals can be described using the following equation:

$$R_p = \frac{k_p [M]_p \bar{n} N}{N_A} \quad (2.2)$$

Where R_p is the rate of polymerisation, k_p is the rate coefficient for propagation, $[M]_p$ is the concentration of monomer in the polymer particles, \bar{n} is the average number of radicals per particle, N is the number of latex particles per unit volume and, N_A is the Avogadro constant.

The average number of radicals per latex particle, \bar{n} , is very important in terms of defining the kinetics of an emulsion polymerisation. It is a function of many physical factors including the rate of radical generation and is not constant throughout the polymerisation. The value of \bar{n} is used to calculate both the rate of polymerisation and the number-average degree of polymerisation, x_n , of the polymer produced assuming that chain transfer effects are negligible and that the propagating chains terminate only by combination with small radical species.

$$x_n = \frac{k_p [M] \bar{n} N}{R_i} \quad (2.3)$$

R_i is the rate of radical generation, and during Interval I $[M]_p$ is constant due to the constant diffusion of monomer molecules from the droplets into the micelles as polymer is formed. However, the number of particles present per unit volume, N , continually increases which corresponds to a continual increase in the rate of polymerisation.

2.2.2.1 Interval II

During Interval II, $[M]_p$ is constant as the polymer particles are constantly fed by monomer molecules diffusing from the monomer droplet reservoirs. The number of latex particles, N , also remains constant, leading to a constant rate of polymerisation during this stage, which typically continues until approximately 30-40% monomer conversion. However, the transition between Intervals II and III is dependent upon monomer conversion, and varies for different monomers⁴¹.

2.2.2.2 Interval III

The start of Interval III corresponds with the disappearance of the monomer droplets. This leads to a decrease in $[M]_p$ in the particles, and consequently the rate of polymerisation also decreases as propagation continues with the residual monomer within the micelles. This decrease in rate continues until approximately 80-85%, when factors such as autoacceleration can start to dominate the polymerisation depending on the monomer. The increase in viscosity associated with autoacceleration leads to a decrease in the rate of termination. After the gel effect occurs in Interval III, the rate of polymerisation finally decreases as all monomer molecules are consumed when the polymerisation reaches full conversion.

2.2.3 Emulsion polymerisation processes

There are several different processes by which an emulsion polymerisation can be conducted. The method used will depend on several factors, such as the desired properties of the end polymer product, the quantity of polymer to be made and the ease and versatility with which the reactor system would be required to switch to produce different polymers.

2.2.3.1 Batch

A batch emulsion polymerisation involves all components of the reaction (monomer, initiator, surfactant and any additives) being added to the reaction vessel at the start of the polymerisation. Little control can be gained over the reaction as the polymerisation begins, as soon as the temperature is sufficiently high for the initiator to decompose and produce active radical species. As for all emulsion polymerisations this leads to both particle

nucleation and particle growth being able to occur at the same time, but it is difficult to reproduce the latex properties from batch to batch. The polymerisation is said to be 'monomer-flooded' as an excess of monomer is present in the system, which leads to detrimental effects such as copolymer composition drift⁴². Seed latexes (i.e. pre-formed latex particles) can be used to help improve this by giving a constant particle number per unit volume. Due to the lack of control available, batch processes are not particularly versatile and are not widely used in the large-scale manufacture of latexes.

2.2.3.2 Continuous

Continuous processes refer to the simultaneous addition of reagents and removal of polymer latex product from a reaction vessel at the same rate as the polymerisation proceeds. This process represents several advantages over batch and semi-batch processes, including constant efficient heat transfer. It is due to this efficiency that continuous processes are usually used when large volumes of a specific product (e.g. certain grades of synthetic rubber) are required, but the reactors cannot be easily switched to make different polymer products, unlike batch or semi-batch processes which are more versatile in this respect.

2.2.3.3 Semi-Batch

Semi-batch processes involve the addition of reaction components, including monomer and surfactant, into the reaction vessel at a controlled rate as the polymerisation proceeds. This gives a high degree of control over several factors including the morphology of particles, rate of polymerisation and heat transfer. Due to this versatility, semi-batch processes are widely used in both industry and academic research.

The polymerisation typically begins with approximately 5-10% of the total amount of monomer being polymerised in a pseudo-batch method to produce a 'seed latex', which enables control over the particle size distribution of the final latex product. Undesirable secondary nucleation during monomer addition can be eliminated by controlling the concentration of surfactant present in the reaction vessel.

Monomer and surfactant can be added as 'shots', or continually fed into the vessel during the polymerisation. These can be added either as separate feeds at individual predetermined rates, or together as an 'emulsion feed'. The method of addition of monomer affects the properties of the latex formed, such as the number of particles formed during the seed stage¹¹.

The rate of addition of monomer also affects the polymerisation. In order to exploit the versatility and control that can be afforded from a semi-batch process, it is necessary to use 'monomer starved' conditions. This describes a system whereby the rate of addition of monomer, R_m , is slower than the maximum potential rate of polymerisation, $R_{p, \max}$, under the given conditions. The actual rate of polymerisation, R_p , can be described by:

$$R_p = \phi_p R_m \quad (2.4)$$

Where ϕ_p is the volume fraction of polymer in monomer-swollen latex particles, typically $\phi_p > 0.8$ for a steady-state system under monomer starved conditions²⁴.

Due to the rate of polymerisation being controlled by the rate of monomer addition, copolymer composition can also be tightly controlled as the instantaneous monomer conversion at any point will be very high, typically greater than 90%⁴³. This will lead to copolymers with a uniform composition being formed, as composition drift due to differences in monomer reactivity will be eliminated.

Another significant advantage to using a semi-batch process with monomer-starved conditions is that no monomer droplets are present, so droplet nucleation cannot occur. This prevents the formation of large (>10 μm in diameter) particles of coagulum which affect the useful yield of particle latex and can necessitate the lengthy cleaning of the reaction vessels¹¹.

Using monomer-starved conditions with successive different monomers gives control over the particle growth and can therefore aid the formation of nanocomposite latex particles with defined morphologies, such as 'core-shell' latex particles.

2.3 Nanocomposite latex particles

It is possible to produce nanocomposite particles that have a well-defined set of physical properties, the simplest of which have a 'core-shell' structure. Nanocomposite materials are defined as consisting of two or more immiscible phases that are mixed but not chemically bonded at the nanometre scale⁴⁴. The development of such materials is an extremely broad area of research, with polymer-polymer nanocomposite particles being just one of many different subsections of the genre.

Core-shell latexes are prepared by successive emulsion polymerisation processes, with immiscible polymer layers being formed around a 'seed' particle. Many different

morphologies can be gained by using different monomers and processing methods, which leads to a versatility in properties that cannot be gained by other polymer systems such as random copolymers or polymer blends⁴⁵.

2.3.1 Particle Morphologies

In order for a nanocomposite particle to be formed, the constituent polymers must phase separate, which is caused by incompatibility between the two phases and driven by a minimisation of the interfacial free energy and therefore a reduction in surface area of interaction⁴⁶. This creates areas of macroscopic segregation, leading to internal structure being formed within the particle. The presence and the geometry of such a structure can be described by the term 'morphology'.

Many factors are known to control phase separation – examples include the choice of monomer species, the molecular architecture of the polymer chain (for example linear or branched), the number-average degree of polymerisation of the chains and the overall volume fractions of each polymer¹⁵.

There are many different morphologies that can be gained by successive emulsion polymerisation processes to form a nanocomposite latex particle. The particle morphology that is adopted will determine the physical properties that it exhibits and hence what application it is suitable for. The most common examples of latex particle morphology are shown in Figure 2.5.

The morphology that a core-shell nanocomposite particle adopts is influenced by many factors, including the hydrophilicity of the monomer and polymer species, the molar masses of the polymer species and the polymer-polymer and polymer-aqueous phase interfacial tensions. However, morphology is not just determined by the physical and chemical properties of the component polymers, but also by the polymerisation conditions under which the nanocomposite particles are synthesised⁴⁷. This includes the feeding method for the co-monomers, the type of initiating species and rate of initiation. The use of a semi-batch seeded emulsion polymerisation to produce core-shell nanoparticles is much more effective than using a monomer-flooded batch process (as defined in Section 2.2.3.1), and will lead to much better separation between the core and shell phases^{7, 48, 49}. As the instantaneous monomer conversion during monomer-starved polymerisation conditions is typically very high (>95% for methacrylates⁵⁰), a change in composition of the monomer feed will lead to an immediate change in composition of the polymer formed. Thus, the second polymer phase can be formed within the particle, and the occurrence of phase separation will lead to

the formation of a structured nanocomposite particle. A crosslinking agent, such as ethylene glycol dimethacrylate (EGDMA) can be incorporated into the second polymer in order to bind the core and shell polymers together within the nanocomposite particle⁴⁸. However, the particle morphology is very sensitive to the level of crosslinking that occurs, as elastic forces are created that may compete with the interfacial free energy to determine the morphology that is adopted by a particle⁵¹. This competition may lead to the nanocomposite particle adopting a non-equilibrium morphology, as is discussed further in Section 2.3.3.

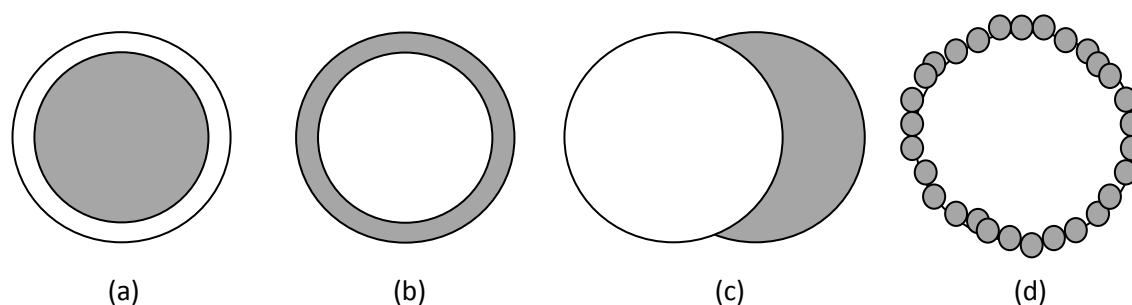


Figure 2.5 Examples of nanocomposite latex particle morphology - **(a)** core-shell; **(b)** inverted core-shell, **(c)** hemisphere, **(d)** raspberry⁵²

It is possible to observe the internal structure of a latex particle using transmission electron microscopy (TEM). The particles can also be chemically stained to enhance the natural contrast between phases, most often using ruthenium tetroxide (RuO_4 ; reacts with all polymers at differing rates) or osmium tetroxide (OsO_4 ; reacts with olefinically unsaturated polymers)⁴³. The development of defined core-shell morphology upon the addition of a second polymer phase can be seen from the images shown in Figure 2.6. The lighter coloured core phase polymer, shown as a solitary phase in Figure 2.6(a), becomes surrounded by the darker shell phase polymer. It can be seen that the morphology of these nanocomposite particles in Figure 2.6(b) is not perfectly spherical, which can be attributed to the effects of minimisation of the interfacial tension between the core and shell phases.

Core-shell particle latexes are often made by seeded emulsion polymerisation. This process has numerous advantages including the process being safer due to the efficient heat transfer of the reaction medium and lack of volatile solvents, and easier handling of the material due to the low viscosity of the latex⁵³. In order to successfully grow a core-shell particle using emulsion polymerisation, it is necessary to avoid secondary nucleation during the polymerisation of the second monomer. Secondary particle nucleation may occur due to the differing kinetics and physical properties of different monomers, for example the rate at which each polymerises, relative hydrophobicities or hydrophilicities and glass transition temperatures⁵⁴. Seeded emulsion polymerisation is often used to avoid this occurring, and

proceeds by the initial formation of a core particle with a reactive groups that allow the second stage monomer to 'anchor' onto the core, preventing secondary nucleation and forming a core-shell morphology.

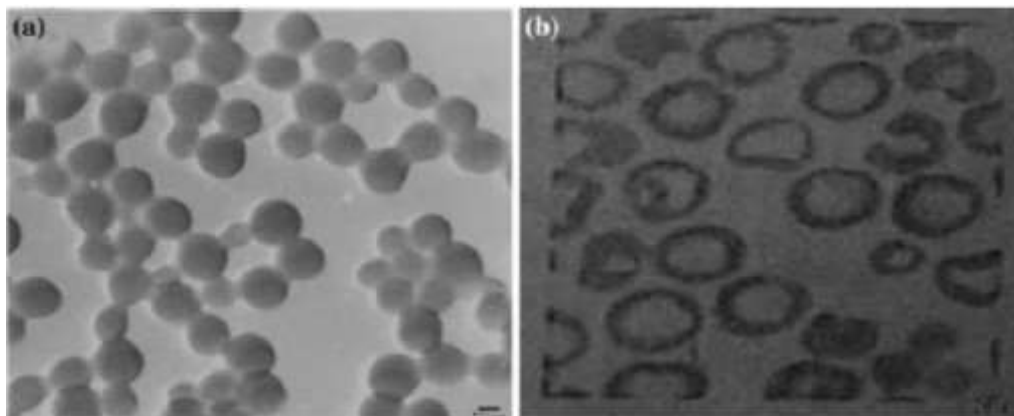


Figure 2.6 TEM images showing the formation of core-shell morphology in a nanocomposite latex particle. **(a)** shows the poly[(n-butyl acrylate) -co- (methacrylic acid) -co- { ethylene glycol dimethacrylate}] core, and **(b)** shows the final particle morphology after addition of the poly[styrene -co- (methyl methacrylate)] shell⁵⁵

2.3.2 Properties of core-shell latexes

Polymers that are incorporated into core-shell nanocomposite particles can be classified as 'soft' or 'hard', depending on their thermal properties. Those with a high glass transition temperature (T_g) are described as 'hard' as they are usually glassy at the application temperature, for example poly(methyl methacrylate), which has a T_g of 105 °C. Conversely, low T_g polymers such as poly(n-butyl acrylate), the T_g of which is -54 °C⁵⁶, are said to be 'soft'⁵⁷. Thus, nanocomposite latex particles that are composed of two low T_g polymers can be described as 'soft-soft nanocomposites'.

The properties of a core-shell nanocomposite particle are largely determined by its morphology, and usually results in an enhancement of properties compared to the respective individual core and shell components. The dynamic mechanical properties of a film or moulding cast from the latex particles directly depends upon such factors as the nature of the rubbery core polymer, the thickness of the hard polymer shell and the particle size distribution of the latex. For example, for use in toughening materials, the thickness of the shell phase is the most important factor - if the shell is too thin, the rubbery core will not be protected during manufacturing processing but if it is too thick the rubbery properties of the core will be lost and the properties of the shell polymer will predominate⁵⁸. Hence, it is important to be able to control the morphology of core-shell nanocomposite particles in order to tailor them for a specific application.

2.3.3 Control of core-shell nanocomposite morphology

The morphology of a core-shell nanocomposite is controlled by both thermodynamic and kinetic parameters. The thermodynamic factors determine the stability of a particular morphology, and the kinetic factors determine how easily a particular morphology will be formed. The equilibrium morphology of the nanocomposite particle is thermodynamically determined, and will be the arrangement of phases with the lowest surface free energy, ΔG . However, whether this equilibrium morphology is reached or not will often be controlled by kinetic factors⁵⁹.

The lowest surface free energy is determined by the respective interfacial tensions between the two polymer phases and the aqueous phase that the particles are dispersed in, and is given by:

$$\Delta G = \sum (\gamma_{ij} A_{ij}) - \gamma_{1w} A_0 \quad (2.5)$$

Where ΔG is the free energy change for phase arrangement, γ_{ij} is the interfacial tension between i and j , A_{ij} is the interfacial area between i and j , γ_{1w} is the interfacial tension between seed polymer 1 swollen with monomer 2 and aqueous phase, A_0 is the interfacial area between polymer 1 swollen with monomer 2 and aqueous phase^{59, 60}.

The polymer phase with the higher polymer-aqueous interfacial tension will be engulfed by the other polymer in order to minimise the value of ΔG . Polymer-aqueous phase interfacial tensions are affected by several factors, including the hydrophilicity of the polymer, the chain-end groups from the initiator species and the concentration and type of surfactant present⁶¹.

However, the final morphology of the particle depends heavily upon kinetics, which determine whether the particle attains the equilibrium morphology at minimum surface free energy or assumes a kinetically metastable non-equilibrium structure. The most important of these kinetic factors is the rate of diffusion of the second phase radicals through the seed particle, which in turn depends on the viscosity of the seed polymer. During monomer-starved conditions when the instantaneous conversion is very high, the polymer viscosity within the seed particle will also be very high. This leads to the diffusion of the second phase polymer being impaired, and hence a kinetically stable non-equilibrium morphology being formed⁴⁸. The need for mobility of the second phase radical also leads to a soft seed polymer being favoured over a hard seed. A soft seed polymer would have a T_g such that it would be in a rubbery state at the reaction temperature, with the mobile seed polymer chains allowing diffusion of a second stage polymer and hence an equilibrium morphology to be achieved.

Conversely, a hard seed polymer would be in a glassy state at reaction temperature, with immobile chains which would restrict the movement and diffusion of the radical, leading to a core-shell morphology being formed regardless of which equilibrium morphology would be favoured for the system⁴⁸.

The major processes that are most important in terms of controlling the morphology of a nanocomposite particle are the penetration of the second phase radical into the seed particle, the phase separation of the two polymer species and 'phase consolidation', which represents the rearrangement of the morphology within the particle⁶². As all three processes are diffusion controlled, the morphology adopted by the nanocomposite particle is dependent upon the viscosity within the particle.

There are a number of reaction conditions that can affect the kinetics and thermodynamic parameters and hence the morphology that is adopted by a nanocomposite particle. A series of five papers was published by Sundberg *et al.* between 1999 and 2006 that investigated the effect of varying these conditions on the non-equilibrium morphology observed.

2.3.3.1 Effect of monomer feed rate during second stage polymerisation

As was already discussed in Section 2.3.1, semi-batch emulsion polymerisation with monomer-starved conditions can be used to gain a greater control of the morphology of a core-shell nanocomposite particle. Sundberg *et al.* found that at a slow monomer feed rate, the concentration of monomer in the polymer particles was lower, which affected the internal viscosity of the particles. However, the main conclusion drawn from the study was that truly 'starved' conditions were only achievable for seed polymers with a high T_g , due to the second stage radical species being restricted to the outer edges of the seed particle only^{51, 53}. This would result in the diffusion of the second monomer into the seed polymer being severely restricted, and hence have a large effect on the morphology adopted by the particle.

2.3.3.2 Effect of seed polymer properties

Following on from the findings discussed in Section 2.3.3.1, the next reaction parameter investigated by Sundberg *et al.* was how the properties, namely the T_g and polarity, of the seed polymer affected the morphology of the nanocomposite particle. It was found that with a polar seed polymer (e.g. poly(methyl methacrylate) (PMMA)) and a non-polar second phase polymer (e.g. poly(n-butyl acrylate)), the equilibrium particle morphology was that of

inverted core-shell. It was also noted that when the T_g of the seed polymer was more than 15 °C below the reaction temperature that the second stage radicals could penetrate the seed particle, even at very high instantaneous conversions and hence higher polymer viscosities. Thus, it was deduced that the T_g of the seed polymer is a very important variable in the determination of nanocomposite particle morphology⁶³. Figure 2.7 shows TEM images of nanocomposite latex particles formed using seed particles with different T_g values at a reaction temperature of 70 °C. It can be seen that the nanocomposite particles in Figure 2.7(b) have a core-shell morphology which is more defined than those in Figure 2.7(a). This can be attributed to the seed polymer of Figure 2.7(b) having a T_g more than 15 °C below the reaction temperature ($T_g = 52$ °C; reaction temperature = 70 °C). This allows the second stage oligoradicals to penetrate into the core particle much more easily than for the seed particle in Figure 2.7(a) due to increased chain mobility resulting from the polymer being in its rubbery state at reaction temperature.

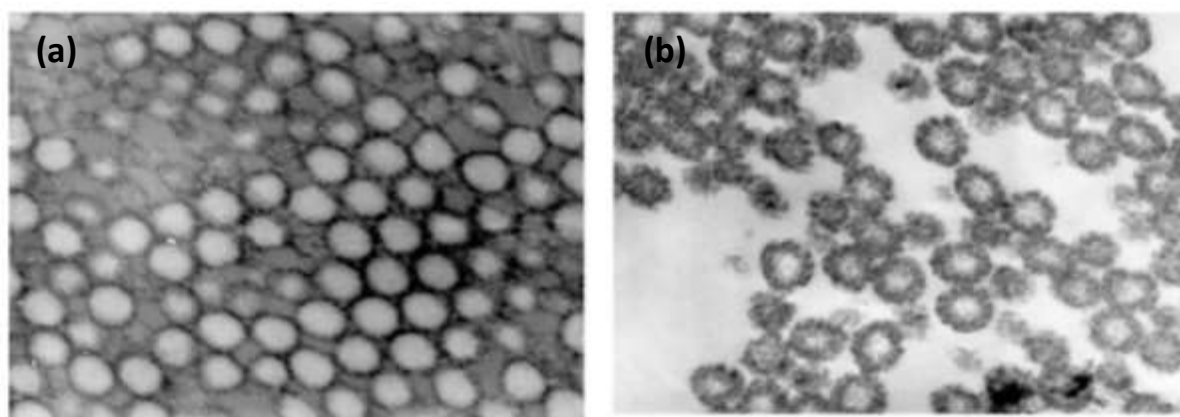


Figure 2.7 TEM images of core-shell nanocomposites formed at a reaction temperature of 70 °C. (a) Poly[(MMA)-*co*-(MA)] seed polymer with $T_g = 88$ °C and (b) Poly[(MMA)-*co*-(MA)] seed polymer with $T_g = 52$ °C⁵⁷, where MA is methyl acrylate.

2.3.3.3 Effect of initiator end-groups

It was found by Tornell *et al.* in 1994 that the surface composition and shell morphology of a core-shell nanocomposite depended upon the type of initiator used. For a PMMA core and polystyrene (PSty) shell, it was found that with the use of an organic peroxide initiator (t-butyl hydroperoxide), a thin PSty shell was formed with a well-defined boundary between the shell and core phases. Conversely, the use of a persulphate initiator produced a thick shell with a blurred boundary between shell and core and a significant particle surface concentration of PMMA⁴⁸. However, Sundberg *et al.* concluded that although the type of initiator used affected the particle morphology under some reaction conditions, it was not a

key factor in determining the kinetically-controlled morphology unlike the monomer feed rate or seed polymer T_g ⁶⁴.

Further investigation into how the nature of the initiating species affects the morphology of a core-shell nanoparticle was conducted in 2010 by Wang *et al.*, who found that in a surfactant-free polymerisation PMMA/polystyrene (PSty) system it was possible to control the kinetically-determined morphology of both the core and shell phases using water-soluble initiators with different charge properties. Both non-ionic (2,2'-azobis[2-methyl-N-(2-hydroxyethyl)propionamide]) and anionic (potassium persulphate) initiators were tested during this work, and it can be seen from the TEM images in Figure 2.8 how the choice of initiator affects the structure of the particle phases⁶⁵.

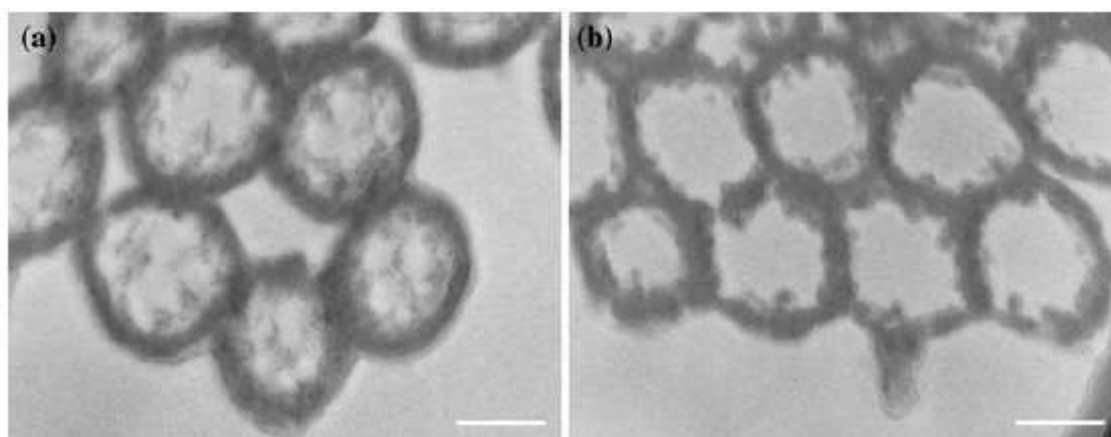


Figure 2.8 TEM images of PMMA core- PSty shell nanoparticles produced in a surfactant-free polymerisation using (a) 2,2'-Azobis[2-methyl-N-(2-hydroxyethyl)propionamide] (non-ionic) initiator and (b) potassium persulphate (anionic) initiator⁶⁵. Scale bars represent 300 nm.

The use of an uncharged initiator (Figure 2.8(a)) led to a much thicker and more continuous PSty shell phase than that formed by the use of the anionic initiator (Figure 2.8(b)), as well as more inclusions of the shell phase PSty in the core domain. As no difference was seen in the molecular weight of the polymer chains produced using the two initiators, the inclusions and the more continuous shell phase can be attributed to the lack of an electrostatic interaction between the persulphate initiator and the polymer chains, which allows the chains to diffuse further into the PMMA core phase.

2.3.3.4 Effect of chain transfer agents

The effect of adding a chain transfer agent, *n*-dodecyl mercaptan (*n*-DDM), at concentrations of up to 1.4% wt on the core-shell nanocomposite morphology was investigated by Sundberg *et al.* in 2006. This concentration of *n*-DDM is sufficient to reduce

the molar mass of the polymer by tenfold. The work was undertaken with a view to investigating how a chain transfer agent would affect the development of the second-stage polymer, and thus which non-equilibrium morphology is adopted by the particle. The effect of chain transfer to monomer and n-DDM was investigated, but chain transfer to polymer was not considered. It was found that chain transfer to the n-DDM, either in the seed or second stage polymerisations, resulted in less penetration of the second stage radicals into the seed particles due to the increased molar mass of the radicals created from chain transfer events restricting diffusion through the seed polymer phase. Due to this effect, chain transfer to polymer was not considered during this study, as the vast increase in molar mass of the radical would cause the diffusion motion into the seed particle to be negligible. However, the effect of a chain transfer agent on particle morphology was deemed to be a 'weak' effect that did not significantly affect the phase separation of the core and shell polymers, or affect the resulting morphology⁶⁶.

2.3.3.5 Effect of crosslinking agents

The final reaction variable investigated by Sundberg *et al.* in the series of publications was the effect of adding a crosslinking agent to the second-stage polymerisation. Crosslinking in the seed polymer would create a 3D-network that would restrict the penetration of the second-stage radical into the seed particle, promoting the formation of a core-shell structure. It was found that the occurrence of crosslinking in the second-stage polymer has little effect on the particle morphology as it doesn't restrict the diffusion of radicals into the seed particle, but that it may affect the degree of phase separation that occurs between the two polymers and prevent phase consolidation occurring⁶⁷.

It is a consequence of the many factors that affect which morphology is adopted by a nanocomposite particle that there are numerous individual structures, many of which can be utilised for different practical applications.

2.4 Film formation of polymer latexes

Many applications of nanocomposite particles are only possible when a film is cast from the polymer, for example when it is necessary to coat a surface. Due to the extremely high interfacial area between latex particles in a film ($>10 \text{ m}^2 \text{ g}^{-1}$ for particles 250nm in diameter) it is possible to use this connectivity between particles to tailor the bulk mechanical properties of a film cast from nanocomposite particles⁵. Two main categories of property will affect the process of film formation, namely the properties of the polymer latex, for example

the T_g , and the physical properties of the environment, e.g. temperature and humidity, in which the film is cast.

2.4.1 Mechanism of Film Formation

Investigations of the mechanism of film formation were first reported by Dillon *et al.* in 1951⁶⁸ and were subsequently expanded upon by Brown⁶⁹ and Voyutskii⁷⁰, with the latter author presenting the first theory regarding a three-step film formation process.

These three experimentally-observed stages that describe the mechanistic process of film formation from generic particle latexes can be described as water evaporation, coalescence and the formation of a homogenous film⁷¹.

2.4.1.1 Stage one – Water evaporation

The first stage to occur in the process of film formation is the bulk evaporation of water, which can occur at ambient temperatures and results in the polymer colloids approaching each other and the interfacial area between them increasing. Hence, at the end of this stage the colloid spheres are densely packed.

During this stage there is a linear loss in mass of the latex with time⁷², the rate of which is dependent on the temperature and humidity of the environment in which the film is being formed, and the concentration of any electrolytes within the water phase⁷¹. The effect of polymer latex composition and properties upon the rate of evaporation during film formation has been extensively investigated since the early 1980's. Winnik *et al.* found that water evaporated from a latex with a minimum film forming temperature (MFT) above the casting temperature at a much faster rate than a latex with MFT below casting temperature⁷³. This was attributed to the higher MFT particles being harder and undergoing less deformation, which therefore increased the capillary size of the interstitial spaces and facilitated evaporation. This observation that water evaporates faster from harder latexes than softer ones was also reported by Keddie *et al.*^{71, 74}. Other physical factors that influence the rate of evaporation of water from a polymer latex film include pH⁷⁵, particle size⁷⁶ and latex viscosity⁷⁷.

The end of the linear evaporation stage of film formation was found by Okubo *et al.* to be due to the formation of a 'skin' of dried material overlying the wet latex⁷⁸. This finding was later supported by AFM imaging studies of film formation performed by Butt *et al.*^{79, 80}.

2.4.1.2 Stage two – Coalescence

Stage two, often called 'coalescence', refers to the physical deformation of the closely-packed polymer particles that result from the evaporation of water during stage one. Any water tightly bound to the colloids, e.g. by an attraction to the stabilising surfactant, is also lost during this stage. The minimum film-forming temperature (MFT) of the polymer greatly influences this stage and the properties of the film that it produces. The MFT of a polymer is typically close, but not identical, to its T_g ⁸¹, and is related to the chemical composition and molecular structure of the polymer particles. Other factors known to influence the MFT include the viscosity and surface tension⁸² of a latex, and the type and amount of surfactant and other colloidal stabilisers present⁸³. The morphology of polymer particles will also seriously affect the MFT of a latex⁸⁴. The degree of particle deformation that occurs during coalescence is determined by the elastic moduli of the polymer particle and the forces, such as surface tension, that are present to facilitate or resist the deformation process⁸⁵.

In order for a film to be formed successfully, the application temperature of the latex must be above the MFT. For a core-shell nanocomposite particle, if the film is formed at a temperature above the T_g of the shell polymer phase then deformation of the particles will occur and a stable, strong film composed of honeycomb-shaped particles will result, as can be seen in Figure 2.9(a), whereby the harder, higher T_g core phase polymer is isolated as discrete regions in a percolating phase formed from the softer, lower T_g shell phase. This arises from the surface tension both between the particles, and between the particles and its surrounding medium, which is most commonly air or water⁸⁶. If core phase copolymers with higher T_g than application temperature are used, this can represent a distinct improvement in the mechanical properties of the film, as it can be considered to be a biphasic system whereby areas of higher modulus are dispersed in a lower modulus, and therefore more flexible, medium⁸⁷. The application potential of such systems will be discussed in Section 2.5.

Conversely, if the shell phase polymer has a T_g above the application temperature, the resulting film will be composed of spherical particles that have not undergone deformation (see Figure 2.9(b)) and be mechanically weaker than that of the honeycomb-structured film⁴⁴. This is due to the polymer chains within the shell being rigid and immobile, and causes voids to be present within the medium.

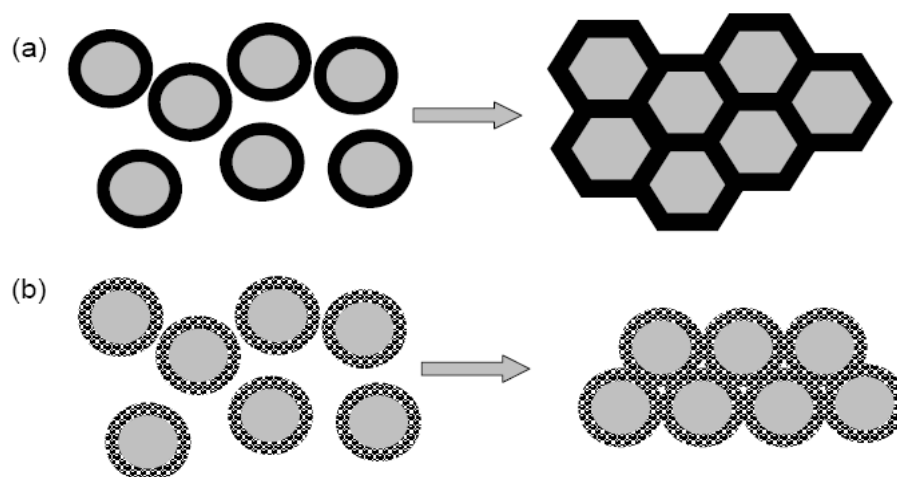


Figure 2.9 (a) formation of film at above shell polymer T_g leads to deformation of particles and hence honeycomb structure in film; (b) Formation of film below shell polymer T_g leads to spherical particle structure in film³²

2.4.1.3 Stage three – Further coalescence and interdiffusion

During the final stage of film formation the deformed honeycomb-shaped particles will undergo further coalescence, whereupon the polymer chains will diffuse across the particle boundaries to form a homogeneous film. The diffusion of polymer chains across the particle-particle interface is driven by thermal energy in the particles, and will continue until eventually the original particle boundaries cannot be discerned⁸⁵, but is restricted by the conformation of polymer chains at the particle-particle interface⁸⁸. It is this third stage of film formation that is the most influential upon the final mechanical properties of the film^{89,90}.

As discussed in Section 2.4.1.2, for a film formed from a core-shell nanoparticle, the core phase will remain isolated in a homogenous matrix that is composed of the shell polymer. This demonstrates that a ‘memory’ of the particle morphology is retained in the final film⁴⁴. The film formation behaviour of a core-shell latex is highly dependent on the relative proportions of core and shell copolymer, and their respective properties⁹¹.

2.4.2 Crosslinking and Film Formation

The cohesive strength of the polymer film may be enhanced by crosslinking reactions that occur between the polymer chains after particle interdiffusion (i.e. after stage three of film formation occurs)⁹⁰. Crosslinking refers to the linking together of pre-existing polymer chains to form a 3D network, which can greatly alter the properties of a polymeric material. Incorporating crosslinking into a polymer film can enhance the mechanical strength, chemical stability and solvent resistance compared to an un-crosslinked equivalent⁹². It is not just the

occurrence of crosslinking that can affect the properties of a polymer but also the extent to which it occurs, as a sample of natural rubber with a low crosslink density will be flexible, whereas one with a high crosslink density will be hard and rigid¹⁷. A crosslinked material will also be able to absorb large quantities of solvent without dissolving, forming a swollen gel which exhibits elastic rather than plastic behaviour⁹³.

The proportion of the polymer that has been crosslinked can be investigated by determining the gel fraction of a sample. This refers to the fraction of a polymer sample that is insoluble in a solvent that will typically dissolve the corresponding linear polymer, and can take a value of between 0 and 1, with 0 representing no crosslinking present and 1 representing a totally crosslinked sample¹⁹. The homogeneity of crosslinking in a cured polymer can be deduced by comparing the gel fraction with the swelling ratio, which describes the volume of a dry polymer compared to that in its equilibrium swollen state and is defined in Equation 2.6. A sample with a gel fraction of 0.8 indicates that 80% of the polymer chains are crosslinked into a network.

$$Q = \frac{V_{eq}}{V_{dry}} \quad (2.6)$$

Where Q is the swelling ratio, V_{et} is the equilibrium volume of the polymer swollen with solvent and V_{dry} is the dry volume of the polymer⁹³.

With regards to film formation, it is important that crosslinking reactions occur after particle interdiffusion occurs (known as 'postcoalescence crosslinking') otherwise the diffusion of polymer chains within the film will be restricted and a brittle film with poor cohesive strength formed. Figure 2.10 illustrates the effect of crosslinking rate versus interparticle diffusion rate.

Intramolecular (i.e. precoalescence) crosslinking will generate stiffness and strength within each particle but will severely restrict interparticle diffusion⁹⁴. This lack of particle-particle boundary chain entanglement leads to a lack of cohesion within the film, with the particle boundaries being particularly weak areas prone to fracture⁹⁵. Films formed with postcoalescence crosslinking will tend to have a higher gel fraction than those formed with precoalescence, due to interparticle diffusion occurring to a further extent and hence a more homogeneously crosslinked film existing⁹⁶.

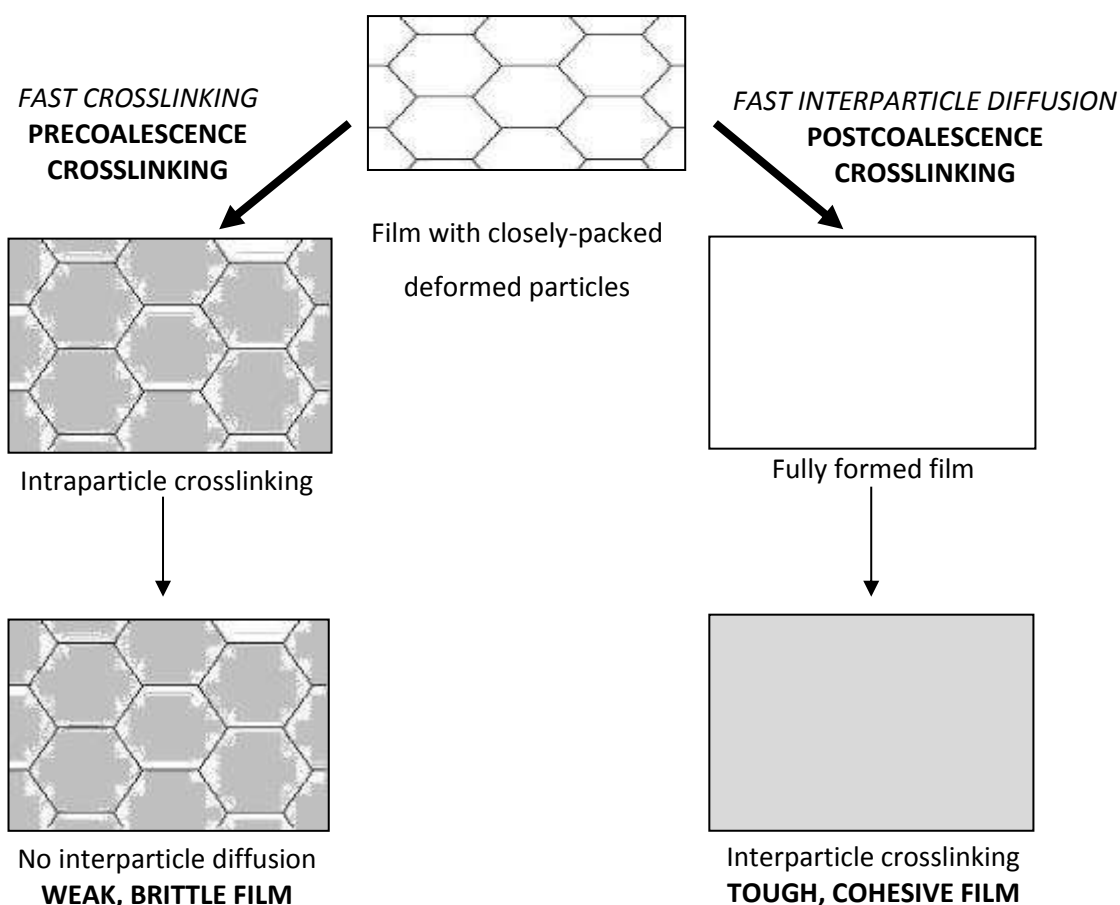


Figure 2.10 Simple schematic diagram to show the formation of films with both pre- and postcoalescence crosslinking

2.4.3 Elastomers

Knowledge of the network structure formed by a crosslinked polymer is very important, as it can affect the application potential of a film⁹⁷. One such class of polymers for which such knowledge of network structure is important are elastomers.

An elastomer is defined as being a polymer that “*displays rubber-like elasticity*”⁹⁸, and is composed of a lightly-crosslinked polymer network that is above its T_g so hence is permanently in the rubbery state, and which has a zero or negligible degree of crystallinity¹⁷. Elastomers are extremely versatile materials that find a wide range of practical applications⁹⁹, due to their ability to undergo large (> 500% strain) deformations and rapidly retract to their original size when the deforming stress is removed. This recovery of strain is entropically driven, and only occurs due to crosslinking restricting the translational motion of the polymer chains. It is possible to predict the stress-strain mechanical behaviour of elastomers using simple statistical analysis, and although the agreement between theoretical and

experimental results is good at low (> 150%) strains, it does not hold at higher strains as crystallisation of the material may occur¹⁰⁰.

The use of elastomeric behaviour to enhance the mechanical behaviour of core-shell latex films will be discussed further in Section 2.5.

2.4.4 Crosslinking Chemistries

There are a vast range of different chemistries that can be used to promote crosslinking in latex films. Two main types of chemistries are utilised - those that promote crosslinking after film formation, and those that introduce a crosslinked network during polymerisation. Both involve the addition of functional monomers into the latex particles, with those monomers with delayed crosslinking ability being typically more costly than the monomers that are used to form the polymer backbone or introduce crosslinks during polymerisation¹⁹.

Multifunctional monomers, such as dimethacrylates, are often used to crosslink polymer chains during polymerisation, forming materials such as dental fillers which polymerise after having been applied to the target substrate. However since the polymerisation temperatures for such applications tend to be fairly low (body temperature (37 °C) for dental uses) the crosslinking efficiency tends to be fairly low, typically 40-75%¹⁰¹.

Methods of promoting delayed-onset crosslinking into a polymer include melamine-formaldehyde derivatives and the use of organometallic zinc and zirconium compounds to induce ionomer-like crosslinks by Coulombic attraction with carboxylate anions¹⁹. The addition of allyl methacrylate, the structure of which is shown in Figure 2.11, as a latently functional group to induce unsaturation crosslinking is another method that has been extensively researched. It is possible to incorporate un-polymerised allyl groups into the polymer backbone due to their low reactivity ratio compared to other co-monomers. Research conducted by Lovell *et al.* showed that the reactivity ratios of allyl methacrylate were approximately 10^4 times smaller than those of MMA, BA and styrene, which led to the allyl group remaining unreacted until all other C=C groups present in the polymerisation had reached high conversions¹⁰². These pendant allyl groups will then react with other monomers to form a grafted or crosslinked polymer.

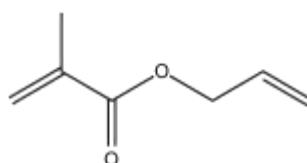


Figure 2.11 Structure of allyl methacrylate

A more hydrophilic class of crosslinking monomers are alcohol-containing acrylamides, which are known to self-crosslink at high temperatures by self-condensation of the hydroxyl groups. This mechanism is shown in Figure 2.12 with n-methylol acrylamide (n-MA), a commonly used crosslinking monomer. It is possible to reduce the temperature required for this self-crosslinking so it occurs at ambient temperature by adding a catalyst such as aluminium chloride or a strong organic acid, although this results in formaldehyde as a by-product and is therefore undesirable^{103, 104}.

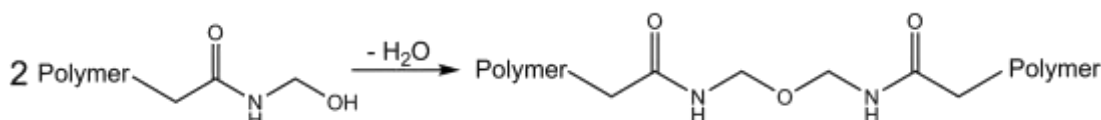


Figure 2.12 Self-crosslinking of n-MA-containing polymer chains by condensation of the alcohol functionality¹⁰³

There are however acrylamide species that will crosslink polymer chains at ambient temperature with no undesirable side products. N-(1, 1-dimethyl-3-oxobutyl) acrylamide, commercially known as diacetone acrylamide (DAAM), is a vinyl monomer that was first synthesised and evaluated as to its suitability for use in polymerisations in 1965¹⁰⁵. The structure of this monomer is shown in Figure 2.13. Due to its multiple hydrophilic functionalities, DAAM has excellent stability in water and is therefore suitable for incorporation into water-borne latexes in order to impart a post-film coalescence crosslinking. Pendant DAAM groups attached to a polymer backbone will form crosslinks between polymer chains by reaction of the ketone groups with an amine moiety such as adipic acid dihydrazide (ADH; Figure 2.14) via a keto-hydrazide reaction mechanism. The amine moiety is typically dissolved in the aqueous phase of the polymer latex, which enables crosslinking to occur post-coalescence as the crosslinking reaction is inhibited by the presence of water⁹⁵. The hydrophilic DAAM side groups preferentially migrate to the surface of the polymer particles, and it is at this interface that the reaction with ADH can occur¹⁰⁶.

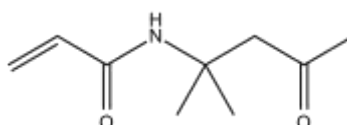


Figure 2.13 Structure of diacetone acrylamide (DAAM)

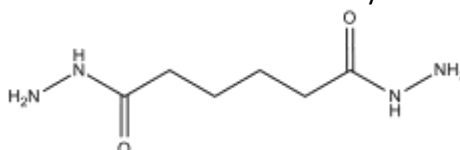


Figure 2.14 Structure of adipic acid dihydrazide (ADH)

2.4.4.1 Keto-Hydrazide crosslinking

The keto-hydrazide crosslinking mechanism is widely used in water-borne coating systems as it occurs rapidly at ambient temperatures. It has been extensively reported in the literature^{92, 95, 107}, and was most recently utilised in 2015 by Thongnuanchan *et al.* to crosslink natural rubber adhesives¹⁰⁸. The fast rate of reaction that is observed enables the water resistance of a film crosslinked using keto-hydrazide chemistry to be built up very quickly during the curing process, and provides a huge advantage over non-crosslinked films¹⁰⁹.

The reaction mechanism shown in Figure 2.15 proceeds via the reaction of pendant carbonyl functionalities attached to the polymer backbone with amine moieties dispersed in the aqueous phase of the polymer latex. This reversible reaction results in a hydrazone linkage between polymer chains, which is shown in Figure 2.16, and is driven by the loss of a water molecule.

As discussed in Section 2.4.3, the most common reagents employed in this crosslinking reaction between polymer chains are DAAM (representing the 'keto' functionality) and ADH (as the amine moiety). The reaction can occur under both acidic, as shown in Figure 2.15, and basic conditions.

As the reaction is driven by the loss of a water molecule¹¹⁰, it will not occur until water has evaporated from the film during coalescence. Conducting the reaction under basic conditions will further retard the reaction as the initial step is acid catalysed, as can be seen from Figure 2.15. The addition of ammonia or another volatile base is most commonly used for this purpose, as it will evaporate from the film during the first stage of film formation, therefore raising the pH of the film⁹². Weak non-volatile hydroxides, such as dilute solutions of ammonium and sodium hydroxide, have also previously been used to adjust the pH of latexes to above 8.5 before the addition of ADH^{6, 95}.

A thorough study into the mechanism of the keto-hydrazide reaction reported by Kessel *et al.* in 2008 found that the rate was increased by almost 2000% when conducted at film pH 4 compared to film pH 8.5⁹⁵. Regardless of the pH of the film, the keto-hydrazide reaction reaches irreversible completion after 7 days provided no residual water is present within the film matrix^{19, 92, 111}.

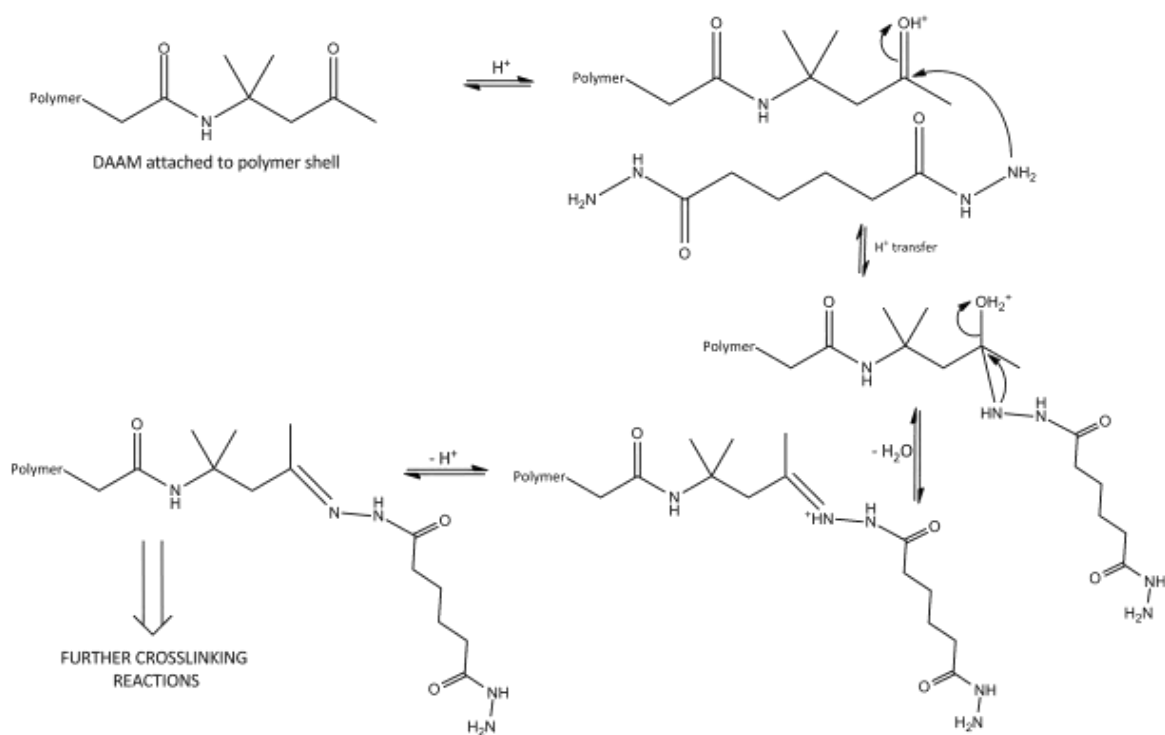


Figure 2.15 Keto-hydrazone crosslinking mechanism of DAAM and ADH⁹⁵

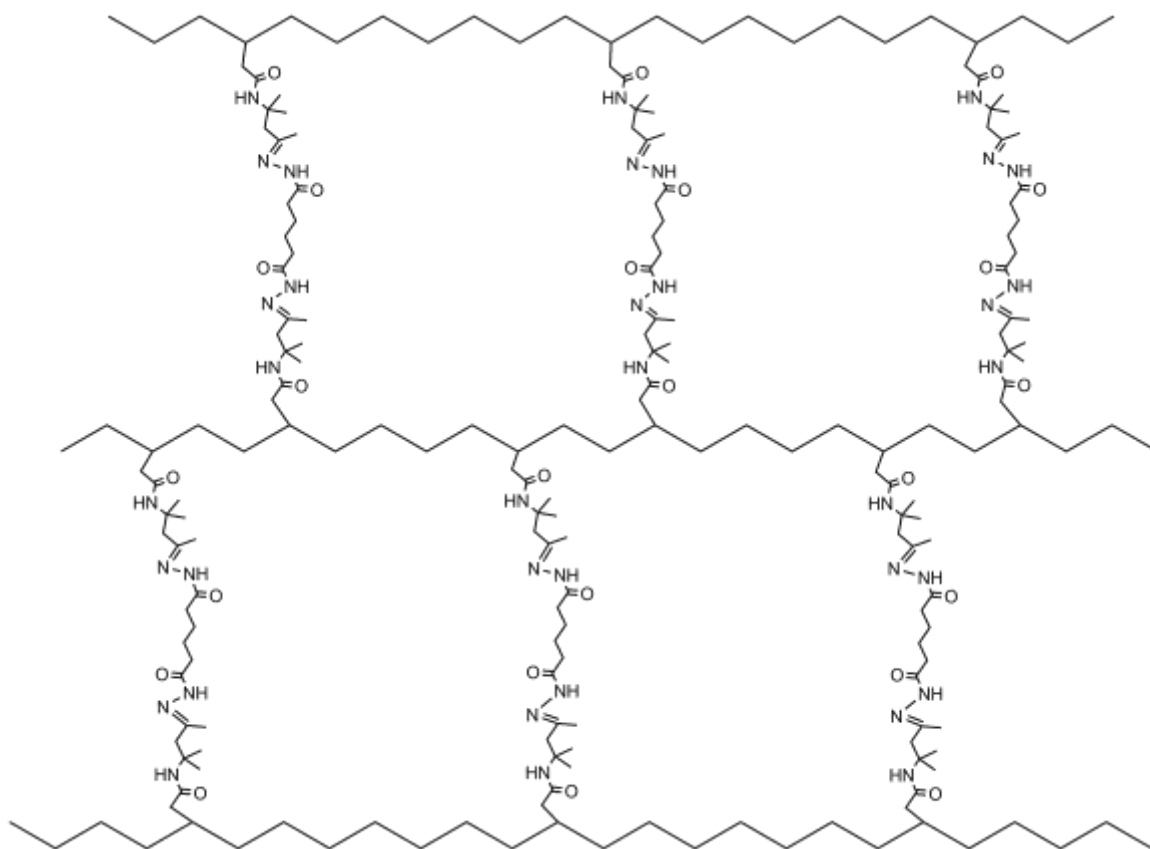


Figure 2.16 Crosslinked network of polymer chains with hydrazone linkages

The delayed onset of the keto-hydrazide reaction allows interparticle chain diffusion to occur before the crosslinking reaction, therefore enabling the formation of a tough, cohesive film as illustrated by Figure 2.10. This inhibition effect also allows the system to be stably stored for long periods of time before use, provided that the levels of DAAM within the system do not exceed 5 wt%⁹². However with time a slight elevation of the MFT of the polymer will be observed, due to unavoidable contact of the functional groups at domain interfaces¹⁰⁹. Due to imine functionalities being particularly vulnerable to hydrolysis, it is important that they are formed in an environment where the excess water (see Figure 2.15) produced by the reaction can be removed, such as occurs during film formation¹¹².

ADH and DAAM react in a stoichiometric ratio of 1:2 due to the di-functional nature of the dihydrazide molecule. This will lead to two polymer chains becoming 'bridged' by one ADH molecule, which will further contribute to the formation of a crosslinked network of polymer chains, a representation of which is shown in Figure 2.16. In order for the ADH to be successfully incorporated into a latex, it must be added as an aqueous solution, commonly at a concentration of 10 wt%, as adding solid ADH directly to a latex results in colloidal instability and subsequent coagulation of particles¹⁰⁹.

It is due to technologies like this keto-hydrazide crosslinking chemistry that water-borne latexes have been able to be developed to give films with improved tensile and mechanical strength and chemical and solvent resistance¹¹³. However in order for such films to begin to be formed from homogenous polymer particles, additional components must be incorporated into the latex which may negate the environmental benefits of switching from a solvent-based to a water-borne film. This is due to high T_g particles not being able to film form at ambient temperature, so the presence of an organic solvent plasticises the particle surface and facilitates the film formation. One possible way to overcome this is the use of structured multiphase polymer particles, such as core-shell nanoparticles.

2.4.5 Advantages of core-shell nanoparticles with respect to film formation

To form a film from homogenous polymer particles (i.e. without any internal morphology), it is often necessary to add a coalescing aid, which is typically a volatile organic compound (VOC). Amongst the most widely used are 2,2,4-trimethyl-1,3-pentanediol monoisobutyrate (commercially known as Texanol) and ethylene glycol monobutyl ether¹¹⁴. The role of a coalescing aid is to plasticise the polymer particles during film formation,

therefore accelerating particle-particle interdiffusion and lowering the MFT of a latex by increasing the diffusion coefficients of the polymer chains^{115, 116} before evaporating slowly to leave a rigid and water resistant film¹. However, due to environmental concerns the use of such additives is being discouraged so it is desirable to investigate alternative ways of forming mechanically-strong films.

In work conducted by Juhue and Lang in 1995⁸⁹, it was found that a nanostructured latex consisting of particles with a poly(BMA) core and a poly[(BMA)-*co*-(BA)] shell with no additives exhibited better film forming properties than that of a homogenous poly(BMA) latex with an added coalescing aid. It was found that the volume fraction of mixing, f_m , which is an indication of the extent to which the polymer chains have diffused across particle boundaries¹¹⁷, after 2 weeks at 70 °C was 0.9 for the nanostructured latex compared to 0.75 for poly(BMA) with a coalescing aid and 0.7 for poly(BMA) without any additives. An increased value of f_m indicates that a greater degree of polymer diffusion has taken place between particles in the film, and suggests that nanostructured latexes could be a feasible replacement for homogenous latexes which require coalescing aids.

2.4.5.1 Factors affecting core-shell nanocomposite film formation

The mechanism of the transfer from particle morphology to film morphology was poorly understood for many years. In 2012, Keddie and Asua *et al.* reported studies of phase migration in heterogeneous films and found that several factors contributed to the formation of 'aggregates', of which the discrete core phases shown in Figure 2.9(a) can be considered an example¹¹⁸. Enhanced phase migration, and hence the retention of particle morphology in a film, resulted when a higher fraction of low molecular weight polymer was present, when the two polymer phases became less compatible, hence increasing phase separation, and when the mobility of the polymer chains in the outermost (i.e. shell) phase was increased. These observations were made for water-borne acrylic-alkyd hybrid systems, but the concepts regarding film morphology are broadly applicable to a much wider range of polymer-polymer nanocomposites.

It has been widely reported that the thickness of the shell phase of a core-shell nanocomposite latex particle affects the MFT of the material^{91, 119-121}. As part of a study into the film formation process of these core-shell particles, Devon *et al.* found that particles with comparatively thinner shells required a higher temperature to form a cohesive film, which can be attributed to the smaller volume of shell polymer needing to deform more around the core phase in order to form a homogenous matrix. It was also found that for a decrease in

MFT to be observed with an increase in shell polymer T_g there was a minimum shell thickness required. For a nanocomposite particle with both core and shell phases consisting of poly[(BA)-co-(MMA)] copolymers with a core radius of 170nm, this minimum shell radius was 80nm.

This finding regarding the relationship between shell thickness and MFT was also reported by Price *et al.* in 2014, who found that film formation was enhanced for core-shell nanocomposites consisting of poly[(BA)-co-(MMA)-co-(MAA)] core and shell copolymers when thinner, harder shells were present¹²². This was attributed to the greater influence of the soft core phase copolymer predominating the film formation behaviour, and was substantiated by a rise in MFT when a larger proportion of harder, higher T_g shell phase copolymer was present. It was also reported in the same publication that film formation is further enhanced by the T_g values of the core and shell copolymers being very similar to each other, as a large difference in T_g between soft core and hard shell phases had a negative effect upon MFT.

2.5 Applications of core-shell nanocomposite particles

Due to their extremely versatile properties, core-shell nanocomposite particles have a wide range of applications including impact modifiers¹²³, adhesives and high-performance architectural and automotive coatings. Benefits of their use include the ability to create a material that has two contradictory properties, for example in impact modifiers a hard shell gives rigidity and hardness to the material, whilst the soft core of the particle is rubbery in nature. This contrast in properties has also been utilised in the design of biocompatible materials such as acrylic bone cements, for which a rubbery core phase copolymer surrounded by a hard shell phase imparts additional fracture resistance and therefore increases the durability of the cement¹²⁴. Two areas of application that have been extensively researched are pressure-sensitive adhesives and water-borne paint systems. For both of these applications, it is necessary for the nanocomposite latex particles to form a film.

2.5.1 Pressure-sensitive adhesives

The term 'pressure-sensitive adhesives' is defined by Lovell *et al.* as referring to '*viscoelastic materials which adhere to substrates on the application of slight pressure over short periods of time*'⁶. Amongst the most common uses for pressure-sensitive adhesives (PSA's) are tapes, labels and protective films¹²⁵.

PSA's were traditionally composed of a solvent-borne acrylic polymer, but they have been mostly replaced by high-solids water-borne latex systems due to environmental, safety and transport concerns. By combining one material that aids adhesion and one that aids cohesion into a nanocomposite particle, it is possible to produce very effective adhesives^{4, 5, 126, 127}. Materials utilized for this application usually have very low T_g s, in order to exploit the tacky properties of such polymers. Common polymers that have been used in publications relating to PSA performance are derived from BA, 2-ethylhexyl acrylate (2-EHA) and ethyl acrylate (EA)^{4, 48}, all of which have T_g values of below -20°C ⁵⁶.

In 2009, Lovell *et al.* showed that by relating the mechanical process of adhesion to the structure of the nanocomposite particles an effective high-performance PSA could be formulated⁶. The core-shell nanocomposites synthesised and tested in this study incorporated a low T_g ('soft') core with chain branching or a low degree of crosslinking which promoted adhesion, with a soft copolymer shell with DAAM added to give a higher degree of crosslinking during film formation, which imparted shear resistance into the adhesive film. It was found that the best adhesive performance was gained from a particle with a viscoelastic 2-EHA-based core copolymer with a high level of chain transfer agent (n-DDM) and a virtually identical shell phase copolymer with a low level of n-DDM but with a crosslinking agent, DAAM, incorporated. ADH was added to the latex post-polymerisation. This resulted in an adhesive film consisting of a very viscoelastic core phase encapsulated in a continuous crosslinked shell phase, which gave the optimum balance between adhesive and cohesive properties.

2.5.1.1 Soft-soft nanocomposite design strategy

Two routes of investigation often used to develop functional latexes such as water-borne pressure sensitive adhesives are those of controlling particle structure¹²⁸ and controlling behaviour at the particle interface¹²⁹. The 'soft-soft nanocomposite' design strategy developed by Lovell *et al.* as a route to producing high-performance water-borne PSA's utilises both of these routes in tandem, and also led to well defined structure-property relationships being identified, a novel achievement⁵.

It was found that the adhesive properties of a soft polymer on a rigid surface could be greatly improved by alternating soft viscous domains with soft elastic domains, which combined the properties of the extensible but extremely tacky viscous polymer with that of the much less extensible and crosslinked elastic polymer¹³⁰. This can be achieved by incorporating crosslinking with a varying crosslink density throughout the material⁵, and is utilised to great effect in soft-soft nanocomposites, developing particles with a defined core-

shell morphology comprising a viscoelastic core phase (taking into consideration the ‘controlling particle structure’ tool of material design) and a crosslinked shell phase from the ‘controlling behaviour at the particle interface’ tool. The addition of a crosslinked phase into the material leads to a modification in the finite extensibility of the polymer chains. Figure 2.17 shows the stress-strain behaviour of soft-soft nanocomposites with differing core-shell proportions.

A material with a core: shell ratio of 80:20, represented by the green line, moves through a yield point after the initial strain has been applied, with the decrease in $\frac{d\sigma}{d\lambda}$ representing a softening of the material as the newly-aligned polymer chains of the viscoelastic core phase continue to stretch easily. As the strain continues to increase, the gradient $\frac{d\sigma}{d\lambda}$ begins to also increase corresponding to a hardening of the material as the chains in the crosslinked percolating phase reach their finite extensibility. The behaviour of a soft-soft nanocomposite with a greater proportion of shell phase (core: shell ratio of 45:55; represented by blue line) shows similar characteristics, with a clear yield point being observed but with the changes in $\frac{d\sigma}{d\lambda}$ not being so marked. Conversely, a soft-soft nanocomposite with a core: shell ratio of 0:100 (i.e. a material that is completely crosslinked) does not show a yield point or softening of the material. These differences in mechanical behaviour can be attributed to the localisation of the crosslink density towards the outer region of the particles consisting of the crosslinked continuous phase, which enhances the adhesive strength of the soft-soft nanocomposite as determined by Majumder *et al.*¹³⁰, and are discussed in more detail in Section 6.1.

This benefit to the mechanical properties of soft-soft nanocomposite PSAs, as shown in Figure 2.17, is delivered by having both the viscoelastic core- and the crosslinked shell phase copolymers in the rubbery state at ambient temperature. The core and shell copolymers are very closely related in terms of their chemical composition, but the shell phase copolymer has latently crosslinkable DAAM groups polymerised into its backbone. These hydrophilic DAAM functionalities will preferentially migrate to the polymer-aqueous phase interface, and as such will promote crosslinking within the percolating shell phase upon coherent film formation^{96, 131}.

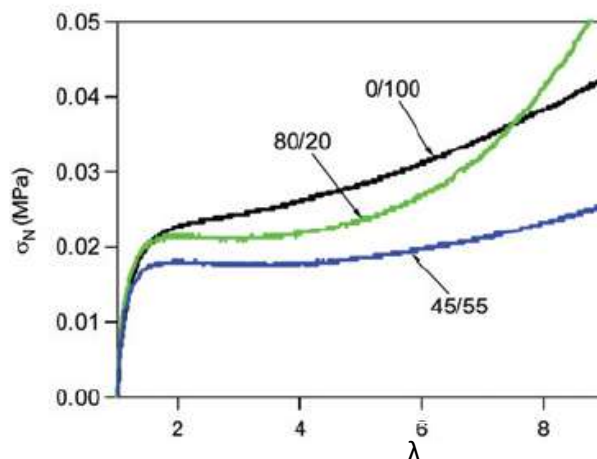


Figure 2.17 Nominal strain (σ_N) vs extension ratio (λ) plot showing the tensile behaviour of soft-soft nanocomposites with different shell/core ratios, showing the effect of a crosslinked shell phase on the extensibility of the material⁵

This set of design principles, namely the formation of particles with a soft viscoelastic core and a crosslinkable shell phase, were recently successfully applied to enhancing the properties of polybutadiene films using ionic crosslinking⁷⁻⁹, but until the work discussed in this thesis had not been investigated for polymers with T_g values of closer to ambient temperature, as are utilized in coating materials.

2.5.2 Coatings

Coatings can be considered to be adhesives that stick to a substrate on only one side¹³². As opposed to PSA's which require very tacky, low T_g polymers in order to gain good adhesion, polymers with T_g values closer to room temperature are required for coatings.

Traditionally, water-borne latexes form films with inferior chemical and solvent resistance and lower tensile strength and hardness than solvent-borne equivalents¹³²⁻¹³⁴. These adverse effects may be due to hydrophilic functionalities within the latex polymer chains, or surfactants added to enhance colloidal stability¹¹⁰ that may plasticise the films formed from water-borne latexes¹³⁵. However, due to the development of crosslinking chemistries (see Section 2.4.3) to incorporate crosslinks into the films during film formation, the physical properties of these latex films can be improved such that they can give performance on a par with solvent-borne alkyd coatings⁹⁵. Some inherent advantages of water-borne over solvent-borne coatings include fast drying and good weather durability, the latter of which originates from the high molar mass of polymers produced by emulsion polymerisation¹⁰⁹.

The morphology of a nanocomposite latex particle will determine the properties of a paint formulated from it⁴⁴. A film formed from nanocomposite particles comprising both hard

and soft phases, for example a PBA core and PMMA shell, will contain properties derived from each phase. The hard, high T_g shell can impart hardness and good blocking resistance into the film, and the soft shell a good degree of elasticity and high film gloss⁵².

As was discussed in Section 2.4.1.1.2, core-shell nanocomposite latexes do not require a coalescing aid to promote effective film formation. This also aids the replacement of traditional volatile organic solvents (VOC's) in paint formulations, which is required due to environmental legislation for reducing the emission of these VOC's into the environment⁵ and is a driving force for the development of core-shell nanocomposites specifically designed for use in coatings which may consolidate for the loss of VOC's from the formulation. The EU VOC Solvents Emission Directive 1999/13/EC was first introduced in 1999² and covers a large number of VOC-utilising processes, including manufacturing, printing and dry cleaning. Directive 2004/42/CE was issued on 21st April 2004 and amends the VOC Solvents Emission directive with specific reference to paints and coatings, stating '*The purpose of this Directive is to limit the total content of VOCs in certain paints and varnishes and vehicle refinishing products in order to prevent or reduce air pollution resulting from the contribution of VOCs to the formation of tropospheric ozone*'. The directive also dictates the technical specifications for such coatings with regards to VOC content³. Successively stricter amendments to this directive have increasingly limited the VOC content of paints, which are split into categories depending on their intended application and physical properties such as solids content. A limit of 400g/l VOC content for solvent-borne trim paints was implemented on 1st January 2007, which was then succeeded by a limit of 300g/l on 1st January 2010¹³⁶.

Another strategy to eliminate the use of VOCs in paints was reported by Overbeek *et al.* in 2008. Using a 'blend'-type system, a 'zero-VOC' water-borne paint binder that combined low MFT with good hardness and tensile properties was described¹³⁷. This was achieved using a bimodal distribution of both hard and soft acrylic polymer particles, where the diameter of the softer particles was 17% of their hard equivalent. The chemical composition of the polymers used was not disclosed in the publication. The weight ratio of hard: soft particles in the binder was 30:70 in order to enhance the film formation at low temperatures but retain the toughness and dirt pickup resistance that is a key property of a paint film. Figure 2.18 shows a schematic representation of this approach to forming a zero-VOC binder. A general advantage of core-shell nanocomposite latexes over blends such as those used by Overbeek *et al.* is that the overall T_g of the latex tends to be a few degrees lower¹³⁸, and hence more beneficial to film formation.

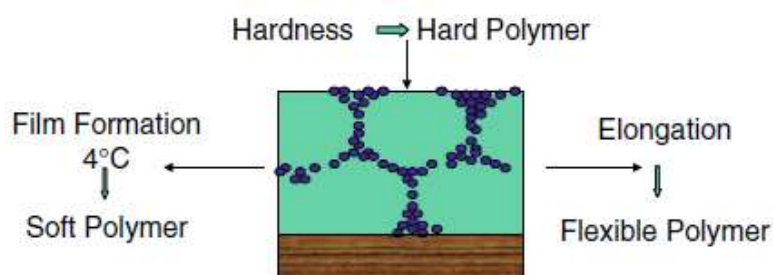


Figure 2.18 ‘Blend’-type strategy used by Overbeek *et al.* to form a water-borne zero-VOC paint binder¹³⁷. The light blue, large domains represent the hard particles, and the purple, smaller domains the soft particles.

Nanocomposite latexes have other beneficial applications regarding coatings, such as the possible use of these materials as a replacement for traditional mineral pigments such as titanium dioxide (TiO₂). Due to the two polymer phases contained within the nanocomposite having different refractive indexes and being entangled, the nanocomposite latex particles could contribute to opacity reducing the need for non-renewable mineral pigments⁵⁵. It is also possible for these materials to be used as rheological modifiers, as the incorporation of acid functional monomers into the polymer shell phases can yield an alkali thickening effect¹³⁹.

Typical polymer species used in core-shell nanocomposite latexes designed specifically for use in coatings are composed of BA, MMA, BMA, styrene and methacrylic acid (MAA)⁵⁵. These polymers have a range of T_g values, from -54 °C for PBA to 105 °C for PMMA⁵⁶, which represents their respective uses in either the rubbery core or hard shell components of the nanocomposite latex particles.

Multiple strategies for the use of core-shell nanocomposites in water-borne coatings have been both reported in the literature and patented, many to improve the properties of water-borne coatings relative to their solvent borne equivalents. However due to the nature of patents it is difficult to discern a great amount of technical detail regarding these systems, their composition and their performance mechanisms. In 1996 Eastman patented a styrene-acrylic copolymer with a core: shell volume ratio of approximately 65:35. Pendant allyl groups were incorporated into the shell phase which would crosslink post-film formation when exposed to oxygen, giving films with improved blocking and solvent resistance¹⁴⁰.

Rohm & Haas have many patents relating to such technology specifically for coatings, such as a thermoplastic-elastomeric vinyl core-shell composite, where the term ‘thermoplastic’ specifically refers to an intentionally uncrosslinked polymer as defined in the patent literature¹⁴¹. The T_g of the core polymer was at least 40 °C lower than that of the shell

phase polymer (preferred core T_g values of -30 - -60 °C, preferred shell T_g values of 0 - 60 °C) in order to give a film with low temperature flexibility, high tensile strength and low dirt pickup at high temperatures, the conflicting properties of which would not have been possible from a single phase polymer film. The company also holds several patents relating to polymer compositions that utilise keto-hydrazide chemistry to introduce latent crosslinking, including one for ambient or low-temperature cure coatings from 1980¹⁴². Another patent, granted to the company in 2003, details a vinyl polymer composition to coat substrates including wood, concrete, asphalt, plastics and metal. The formulation contains at least 5 wt% of a monomer containing a carbonyl functional group capable of reacting with a nitrogen moiety, and a crosslinking agent with at least two nitrogen functional groups in a stoichiometric ratio of at least 0.25:1 to the carbonyl functionalities. The compositions were specifically described as 'storable', as after 10 days at 60 °C the latexes had not gelled.

Another invention utilising the keto-hydrazide crosslinking chemistry was published by Solutia in 2003¹⁴³, which describes a method for preparing aqueous self-crosslinking copolymers with a core-shell structure intended for use as binders in coating materials. These copolymers are predominantly composed of (meth)acrylate or vinyl aromatic monomers with a core: shell phase ratio of between 50:50 and 95:5, and contain at least 2 wt% of a monomer containing a carbonyl functional group capable of reacting with a nitrogen moiety. The hydrazide crosslinker component is included at a stoichiometric ratio of approximately 0.5:1 to the carbonyl functionality. Other companies that hold patents relating to this crosslinking chemistry and its application in coating formulations include AkzoNobel^{144, 145}, Sherwin-Williams¹⁴⁶, Cytec¹⁴⁷, Benjamin Moore & Co^{148, 149} and Nuplex Resins BV¹⁵⁰, the latter of which has patented technology based upon the keto-hydrazide crosslinking reaction as recently as 2014.

One approach to varying polymer morphology that has thus far not been discussed in this review is the use of gradient morphology, as was utilised in a patent for a polymer composition by DSM in 2009¹⁵¹. Gradient polymer morphology refers to a continually changing chemical composition of the polymer chains throughout a particle, and can be achieved by combining two separate, different monomer feeds into a single semi-batch emulsion polymerisation process¹⁵². Similar to the principle of core-shell morphology, gradient morphology can be used to incorporate several optimal properties of different polymer compositions into one particle. The patent granted to DSM contains a formulation for a vinyl polymer latex consisting of 70-90 wt% polymer particles with gradient morphology

and 10-30 wt% polymer particles with a non-gradient morphology, targeted specifically for coating applications.

There are also many patents that refer to core-shell nanocomposite particles that contain additives for a specific application. 3M¹⁵³ and Rohm & Haas¹⁴¹ have patented formulations that incorporate UV-absorbing compounds into the core phase of the nanocomposite particles, which is utilised by 3M for coatings specifically for poly(vinyl chloride (PVC) cladding. The incorporation of a protective colloid into the formulation to plasticise the polymer particles and hence lower the MFT was invented by Hercules Inc. in 1999¹⁵⁴, with the view to promoting film formation at lower temperatures without having any detrimental effect on the physical and mechanical performance of the nanocomposite latex.

In summary, the use of core-shell nanocomposite latexes in coating formations is a large field of research, driven by not only environmental concerns and legislation but also a continual need to improve the performance of coating films in order to overcome market competition.

2.6 Summary

This chapter has given an extensive view of not only the scientific principles underpinning such processes as emulsion polymerisation, the formation of core-shell nanocomposites and latex film formation, but also the applications of such materials. As discussed in Section 2.4, the use of core-shell nanocomposites in coatings and adhesives has been widely investigated, with many different branches of both industry and academia conducting their own research in the area.

The soft-soft nanocomposite design strategy had not been related to particles with T_g values closer to room temperature or investigated with a view to being used specifically in coatings prior to this PhD project. The use of such materials could represent a significant advantage to the coatings industry, as when applied to water-borne PSA's the levels of performance observed were found to be similar to that of traditional solvent-borne equivalents⁴⁻⁶. Should this observation also be realised for the use of soft-soft nanocomposites in coating materials, it would facilitate the transfer from solvent-based paints to water-based equivalents.

3 Experimental Methods

3.1 Materials

n-Butyl methacrylate (BMA; Aldrich, >99%), n-butyl acrylate (BA; Aldrich, >99%) and methyl methacrylate (MMA; Aldrich, >99%) were washed twice with 2% aqueous sodium hydroxide solution to remove the phenolic inhibitor, then washed three times with deionised water and dried for at least 4 hours over anhydrous calcium chloride before use. Methacrylic acid (MAA; Aldrich, >99%) was purified immediately before use by standing over silica gel for 30 minutes. Water was deionised using an ElgaStat Option 3 water purifier. Sodium phosphate dibasic (Aldrich, 99%), ammonium persulphate (Aldrich, 98%), diacetone acrylamide (DAAM; Aldrich), adipic acid dihydrazide (ADH; Aldrich), sodium formaldehyde sulphonylate (Bruggolite E.01, Bruggeman, >98%), t-butyl hydroperoxide (Luperox TBH70X, Aldrich, 70% in water), Rhodafac RK 500A (Rhodia, 75% in water) and Lutensol TOx non-ionic surfactants (BASF, all 100%) were all used as received.

3.2 Emulsion polymerisation processes

All emulsion polymerisations were conducted under a flowing nitrogen atmosphere in a 2 litre flanged vessel with an attached condenser, contained in a water bath thermostated at 75 °C and stirred at 160 rpm with an overhead stirrer. Sections 3.2.1 – 3.2.2 describe examples of the different types of preparation carried out in this project. All latex preparations were conducted on a 1600 g scale unless otherwise specified.

3.2.1 Preparation of a standard AkzoNobel latex

Sodium phosphate dibasic (1.78 g) and Rhodafac RK500A (6.72 g) were dissolved in water (695.87 g) in a pre-weighed reaction vessel and stirred for 30 minutes while flushing with nitrogen and heating to reaction temperature (75 °C). A seed-stage mixture of methyl methacrylate (MMA, 19.65 g) and n-butyl acrylate (BA, 9.81 g) was added into the vessel and stirred for 5 minutes to heat to reaction temperature. A solution of ammonium persulphate (2.48 g) in water (20.48 g) was added to initiate the polymerisation. The mixture was stirred for 15 minutes before a monomer mixture consisting of methyl methacrylate (505.14 g), n-butyl acrylate (252.99 g) and methacrylic acid (1.60 g) was fed into the vessel at a controlled rate of 3.30 g min⁻¹ for 180 minutes using a Watson-Marlow Model 505S peristaltic pump. A concurrent surfactant feed of Rhodafac RK500A (15.79 g) in water (47.39 g) was added at a rate of 0.27 g min⁻¹ using a KD Scientific syringe pump. Once the monomer and surfactant feeds were complete, a 4.25 wt% solution of sodium formaldehyde sulphonylate (4.48 g) was added into the reaction vessel and stirred for 10

minutes, before a 5.15 wt% solution of t-butyl hydroperoxide (4.29g) was added and stirring continued for another 10 minutes. A further portion of 4.25 wt% sodium formaldehyde sulfoxylate (4.48 g) was added and the reaction mixture stirred for a further 10 minutes. The latex was then cooled to room temperature whilst being stirred. After cooling, the latex was strained through a 53 μm mesh sieve to separate any coagulum before further characterisation.

3.2.2 Preparation of a core-shell soft-soft nanocomposite latex

Sodium phosphate dibasic (1.78 g) and Rhodafac RK500A (6.72 g) were dissolved in water (695.87 g) in the pre-weighed reaction vessel and stirred for 30 minutes while flushing with nitrogen and heating to reaction temperature (75 °C). A seed-stage mixture consisting of the desired proportions of butyl methacrylate (BMA) and n-butyl acrylate was added into the vessel and stirred for 5 minutes to heat to reaction temperature. A solution of ammonium persulphate (2.48 g) in water (20.48 g) was added to initiate the polymerisation. The mixture was stirred for 15 minutes before a core-stage monomer mixture consisting of varying amounts of butyl methacrylate and n-butyl acrylate was fed into the vessel at a controlled rate of 3.30 g min⁻¹ using a Watson-Marlow Model 505S peristaltic pump. A concurrent surfactant feed of Rhodafac RK500A (11.06 g) and Lutensol TO7 (2.72 g) in water (47.3 g) was added at a rate of 0.27 g min⁻¹ using a kd Scientific syringe pump. Once the core monomer feed had been delivered, the reaction mixture was stirred with no monomer feed for 15 minutes in order to polymerise all unreacted monomer. A shell-stage monomer feed consisting of varying amounts of butyl methacrylate, n-butyl acrylate, methacrylic acid and diacetone acrylamide was fed into the reaction vessel at the same mass flow rate as the core monomer feed. A concurrent shell surfactant feed of Rhodafac RK 500A (4.74 g) and Lutensol TO7 (1.18 g) in water (14.22 g) was also added to the reaction mixture at the same mass flow rate as the core surfactant feed. Once the monomer and surfactant feeds were complete, a 4.25 wt% solution of sodium formaldehyde sulfoxylate (4.48 g) was added into the reaction vessel and stirred for 10 minutes, before a 5.15 wt% solution of t-butyl hydroperoxide was added and stirred for another 10 minutes. A further portion of 4.25 wt% sodium formaldehyde sulfoxylate (4.48 g) was added and the reaction mixture stirring continued for a further 10 minutes. The latex was then cooled to room temperature whilst being stirred. After cooling, the latex was strained through a 53 μm mesh sieve to separate any coagulum before further characterisation.

3.2.3 Determination of coagulum levels

The levels of coagulum formed during the latex preparations was established by pre-weighing the 53 μm mesh sieve used to filter the cooled final latex, then rinsing the sieve with deionised water before drying at 80 $^{\circ}\text{C}$ to constant weight. The mass of latex recovered post-sieving was also recorded, and the level of coagulum was then calculated using Equation 3.1:

$$\text{wt\% coagulum} = \frac{(\text{final sieve mass} - \text{initial sieve mass})}{((\text{final sieve mass} - \text{initial sieve mass}) + \text{mass of latex})} \times 100 \quad (3.1)$$

3.3 Film formation processes

3.3.1 Post-polymerisation addition of ADH

For some latexes containing DAAM in the shell phase copolymer, adipic acid dihydrazide (ADH) was added to impart crosslinking into cast films. ADH was added at a pre-determined molar stoichiometric ratio to DAAM, as a 10 wt% aqueous solution once the pH of the latex had been adjusted to > 8.5 using 2 wt% sodium hydroxide.

3.3.2 Film casting

The films described in this thesis were cast by pouring wet latex into a coated stainless steel tray of dimensions 23 x 23 cm. A layer of a dry lubricant (Electrolube Dry Film Lubricant) was sprayed into the tray before casting in order to facilitate separation of the dried film. Latex was poured in to a depth of approximately 2 mm, then the tray loosely covered with aluminium foil to prevent contamination of the film by dust and other impurities. The film was left to dry at room temperature for 7 days before being gently removed in order to minimise deformation.

3.4 Characterisation methods

3.4.1 Latex characterisation

3.4.1.1 Nuclear magnetic resonance spectroscopy (NMR)

NMR is an extremely powerful characterisation technique that can be used to ascertain information about the chemical structure of molecules. Magnetically active nuclei will absorb radiation at characteristic frequencies when placed in a magnetic field, due to their nuclear spin quantum numbers, I , which dictate how many different characteristic alignments the nucleus can have. The total number of alignment states possible for each nucleus is given by $(2I + 1)$, each of which will have a different characteristic energy. If the

energy difference between two of these states is equal to that of the radiation that is passed through them, resonance will occur which gives rise to an NMR signal. For the most commonly used type of NMR, ^1H NMR, $I = \frac{1}{2}$, so the total number of spin alignment states is only 2. Thus, the energy difference between these two states will depend upon the magnetogyric ratio of the nucleus, γ , and the strength of the externally applied magnetic field, B . The frequency of radiation required to flip between the two energy states, ν , can be expressed as:

$$\nu = \frac{\gamma B}{2\pi} \quad (3.2)$$

Where ν is the frequency of radiation required to flip between energy states, γ is the magnetogyric ratio of nucleus and B is the strength of the applied magnetic field.

Equation 3.2 indicates that for a simple system such as ^1H where only two energy states are accessible, only one radiation frequency would be required to bridge the gap between them. However, within a molecule these active nuclei will be influenced by the electron density of surrounding nuclei, an effect known as 'shielding' which reduces the magnetic field at the active nuclei causing the absorption frequency to change. The resulting change in absorption frequency is known as the 'chemical shift' and is small but measurable, and forms the basis of NMR spectroscopy. The chemical shift is measured relative to a standard, typically tetramethylsilane (TMS), for which the energy of absorption is suitably low to avoid interference with any analyte peaks. The chemical shift of a nucleus, δ , is measured using the mathematical relationship shown in Equation 3.3. In conjunction with signal peak splitting effects from adjacent magnetically-active nuclei, the chemical shifts can be used to determine the structure of the molecule.

$$\delta = \frac{(\nu_{\text{sample}} - \nu_{\text{standard}})}{\nu_{\text{standard}}} \times 10^6 = \frac{(B_{\text{sample}} - B_{\text{standard}})}{B_{\text{standard}}} \times 10^6 \quad (3.3)$$

Where δ is the chemical shift, ν is the frequency of radiation required to flip between energy states and B is the strength of magnetic field.

NMR was only used to confirm the structures of surfactants used in this PhD project. The ^1H NMR spectra were recorded using a Bruker DRX400 NMR spectrometer at 400 MHz using ~ 1 w/v% solutions of the analyte in deuterated solvents, namely D_2O for Rhodafac RK500A and $(\text{CD}_3)_2\text{SO}$ for Lutensol TO7. The pulse interval, pulse duration and number of scans for all spectra reported herein are 1 s, 10 μs and 16, respectively.

3.4.1.2 Photon correlation spectroscopy (PCS)

Photon correlation spectroscopy (PCS) is a light scattering technique, and has arisen from the very earliest 'time-dependent' light scattering methods first developed in the early 1960's¹⁵⁵. PCS has several advantages over other particle sizing methods, including that it is very fast, it can be used to measure particle diameters even in very polydisperse samples and it is an absolute measure of particle diameter so no calibration is required before use¹⁵⁶.

The theory for 'time-dependent', or dynamic, light scattering is based on the Brownian motion of colloidal particles suspended in a liquid, which is caused by the collision of these particles with the molecules of the liquid medium. It is the motion of these particles post-collision that gives rise to the laser light scattering, and the intensity of the scattered light will fluctuate in time thus giving information about the diffusion properties of the colloids. These real-time fluctuations can be accurately detected using very sensitive photomultipliers with small light apertures. A schematic representation of the light intensity fluctuations can be seen in Figure 3.1.

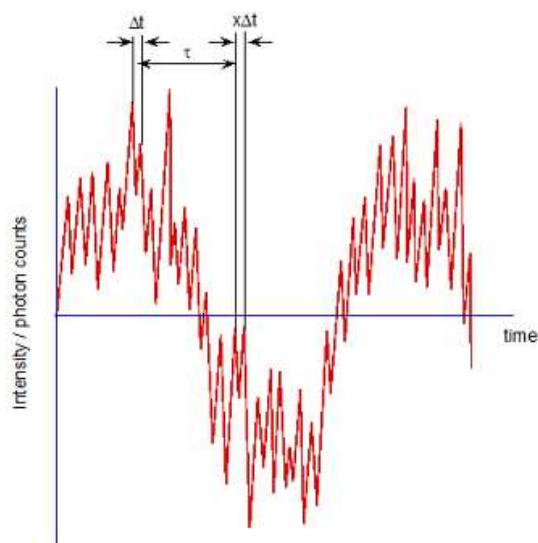


Figure 3.1 Schematic diagram representing the fluctuation of light intensity with time observed in dynamic light scattering measurements, where $x\Delta t$ is the sample time after x measurements and τ is the correlation time¹⁵⁷.

This light intensity fluctuates on extremely fast timescales ($\sim 10^{-6} - 10^{-3}$ s), and undergoes Gaussian random changes. Hence, this leads to the total intensity fluctuating throughout the measurement. The output signal from these measurements is therefore the time average scattered intensity, $\langle I(q) \rangle$, which is a well-defined mean value of the intensities. Equation 3.4 defines $\langle I(q) \rangle$ as a function of the physical parameters of the system:

$$\langle I(q) \rangle = K N M^2 P(\theta) B(c) \quad (3.4)$$

where K = optical constant, N = number of particles in the system, M = the mass of each particle, $P(\theta)$ = the particle form factor and $B(c)$ = concentration factor

The mass of the particles and the particle form factor are especially important in determining the particle size distributions. The magnitude of the scattering vector, q , is defined in Equation 3.5:

$$q = \frac{4\pi n}{\lambda_o} \sin\left(\frac{\theta}{2}\right) \quad (3.5)$$

where n is the the refractive index of the suspending liquid, λ_o is the wavelength of the laser used in vacuo, and θ is the scattering angle.

In order to determine how the time-average scattering intensity $\langle I(q) \rangle$ varies, it is necessary to compute an autocorrelation function, $G^{(2)}(t_d)$, which is shown in Equation 3.6:

$$G^{(2)}(t_d) = \frac{1}{N} \sum_{i=1}^N I(t_i) I(t_i - t_d) = \langle I(t)I(t - t_d) \rangle \quad (3.6)$$

Where N is the number of sampled particles, $I(t)$ is the intensity at time t and t_d is the time delay between samples.

$G^{(2)}(t_d)$ is experimentally determined by recording $I(t)$ at extremely short timescales that are much shorter than a typical intensity fluctuation as a function of the time delay between measurements. Hence, it can also be expressed as shown in Equation 3.7:

$$G^{(2)}(t_d) = B + f e^{-2\Gamma t_d} \quad (3.7)$$

Where B is equal to $\langle I \rangle^2$, or the baseline measurement, f is an instrumental constant and Γ is the reciprocal of the intensity delay time τ .

The reciprocal of the intensity delay time, Γ , can be related to a translational diffusion constant and hence to the actual hydrodynamic diameter of the particles, as can be seen in Equations 3.8 and 3.9, respectively:

$$\Gamma = \frac{1}{\tau} = D_T q^2 \quad (3.8)$$

Where τ is the intensity delay time, D_T is the translational diffusion constant and q is the magnitude of the scattering vector.

$$D_T = \frac{k_B T}{3 \pi \eta(T) d_h} \quad (3.9)$$

Where k_B is the Boltzmann constant, T is the absolute temperature, $\eta(T)$ is the temperature dependent viscosity of the suspending liquid and d_h is the hydrodynamic diameter of the particles.

The hydrodynamic diameter d_h given by PCS is almost always larger than the dry particle diameter due to the electrical double layer that forms on the surface of colloidal particles in dispersion. This electrical double layer stabilises the colloidal particles in suspension, due to the mutual repulsion of like charges on the surface of each particle.

PCS was performed on every sample taken during emulsion polymerisation preparations, using a Brookhaven BI-9000AT correlator with a Brookhaven BI-200SM goniometer set to a scattering angle of 90° and a Spectra Physics 20 mW HeNe laser (632.8nm wavelength). Samples were diluted with filtered (0.2 μm) deionised water to give a count rate of approximately 150 k counts s^{-1} at the detector, and after temperature equilibration at 24.8 $^\circ\text{C}$ were subjected to 10 successive analyses of 1 minute each. The resulting data was analysed using Brookhaven Particle Sizing Software v3.72 to obtain individual values of d_h for each of the 10 measurements, the average of which was used as the reported value of d_h . The standard deviation of d_h is typically about 2 nm.

3.4.1.3 Particle size distribution analysis (PSDA)

Particle size distribution analysis (PSDA) is a type of hydrodynamic chromatography (HDC) technique, which was first experimentally described by Small in 1974¹⁵⁸. HDC is a solution phase separation method, that can be performed in either an open tube (capillary) or in a column, the bed of which is packed with non-porous, inert particles¹⁵⁹.

There are a lot of similarities between HDC and other more established column chromatography methods, such as size exclusion chromatography (SEC), including the same underlying principles of operation, although the separation of the analyte particles in HDC is unusual in that it takes place solely in the interstitial spaces of the column only, due to the column packing material being non-porous.

The separation of analyte colloids in HDC arises from the occurrence of laminar-flow conditions, which give rise to parabolic-like flow conditions. As is shown in Figure 3.2, the fastest flow occurs in the middle of these velocity channels, whereas the slowest is at the 'walls' or packing particle boundaries. The origin of this effect is Poiseuille's Law, which was first reported in 1840 and concerns the flow of Newtonian liquids through narrow tubes¹⁶⁰.

As is shown in Figure 3.3, the larger colloidal analytes cannot approach the 'walls' due to their size, so remain near to the centre of the flow pattern and elute first. Conversely, smaller particles are able to fit close to the edges, and hence travel for part of the elution time in the slower-moving areas of eluent associated with these areas.

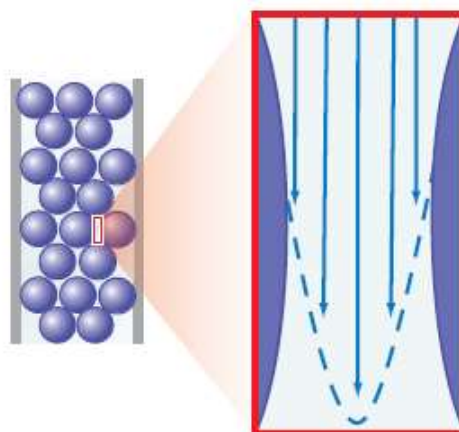


Figure 3.2 Parabolic-type flow velocity conditions in HDC columns¹⁵⁹. The lengths of the arrows indicate relative flow velocities.

The rate at which analyte particles are eluted from the column in HDC is expressed using the term R_f , which is the ratio of the rates of transport of the analyte and the eluent, and is calculated using Equation 3.10:

$$R_f = \frac{R_{analyte}}{R_{eluent}} \quad (3.10)$$

Where $R_{analyte}$ is the rate of transport of analyte and R_{eluent} is the rate of transport of eluent solvent.

The values of R_f for species with known particle diameters are used to create a calibration curve that colloidal species of unknown diameter can be analysed against. To facilitate this, a 'marker' species is used which elutes at a known time and can thus be used to measure the rate of transport of the eluent through the column. Ionic species, such as the dichromate ion $Cr_2O_7^{2-}$ are commonly used for this purpose as they are small species, behave largely like the eluent and due to electrostatic repulsion do not adhere to the anionic column packing material¹⁶¹.

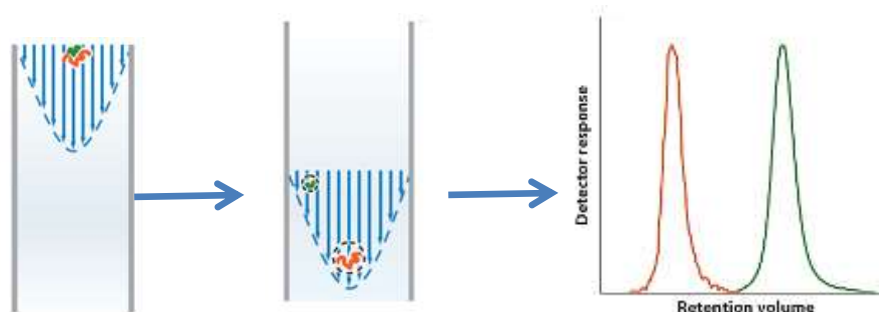


Figure 3.3 Schematic representation of particle size separation in HDC as a consequence of parabolic-type flow velocity conditions. The orange shape represents a large analyte, and the green shape a smaller one.¹⁵⁹

Similar to the effects discussed for PCS in Section 3.4.1.3, the hydrodynamic diameter of the particles is given by HDC due to the electrical double layer effect. As the column packing material is anionic in nature, its interaction with the electrical double layer may cause the analyte particles to be eluted faster, resulting in a larger R_F value.

PSDA was used in this project to analyse latex samples removed from the reaction vessel at the end of the core formation stage and the final particles, to give an indication of whether controlled shell phase growth had occurred. A PL-PSDA (Polymer Laboratories) instrument was used for this analysis, and samples were diluted with pre-filtered PL-PSDA eluent (an aqueous mixture of surfactant and electrolytes) such that the latex formed ~ 0.5 wt% of the analyte mixture, before being passed through a 0.2 μm filter. Each batch of eluent was run against a set of polystyrene latex calibration standards, ranging in size from 50 – 1500 μm and each prepared at individual set concentrations, before use. The data output obtained from the measurement was given in terms of differential volume percentage versus particle number.

3.4.1.4 Gel permeation chromatography (GPC)

Gel permeation chromatography (GPC) is a type of size exclusion column chromatography that was developed as an extension of the size exclusion chromatography (SEC) technique that was first reported in 1956¹⁶². It is an extremely powerful technique for determining the molecular weight distribution (MWD) of a polymer. Contrary to HDC methods, such as PSDA, which was discussed in Section 3.4.1.3, the column packing for GPC is composed of inert but porous beads. As can be seen from the schematic diagram in Figure 3.4 larger polymer chains do not permeate into the column packing and are eluted quickly, whereas smaller chains travel through the porous beads and take longer to be eluted from the column. In order to achieve good resolution, column packing materials with a range of different porosities can be used. This can be done either as a number of columns with different pore sizes connected in series, or by a single column with mixed pore-size packing.

However, it is not the elution time that is used to calculate the molar mass distribution of a polymer sample but the elution volume, V_e , which can be defined as “the volume of solvent required to elute a particular polymer species from the point of injection to the detector”¹⁷. In order to determine the molar mass of a polymer sample from this elution volume, the direct relationship between the two quantities must be established. As the intrinsic viscosity of a polymer in solution can be considered to be directly related to its

hydrodynamic volume, it is possible to use the Marck-Houwink-Sakurada equation shown in Equation 3.11 to relate elution volume and molar mass:

$$\log([\eta]M) = \log K + (1 + a) \log M \quad (3.11)$$

where M is molar mass, $[\eta]$ is intrinsic viscosity and K and a are constants specific to each different polymer species and are determined through a calibration plot.

It is possible to calculate the molar mass of an unknown polymer sample using the relationship shown in Equation 3.11 if, for a given polymer, the relationship between V_e (and hence $[\eta]M$) and M and the constants K and a are known. This is done by constructing a calibration curve, which is a plot of $\log(M)$ against V_e for polymer samples of known molar mass with narrow molar mass distributions. An example of such calibration curves can be seen in Figure 3.5.

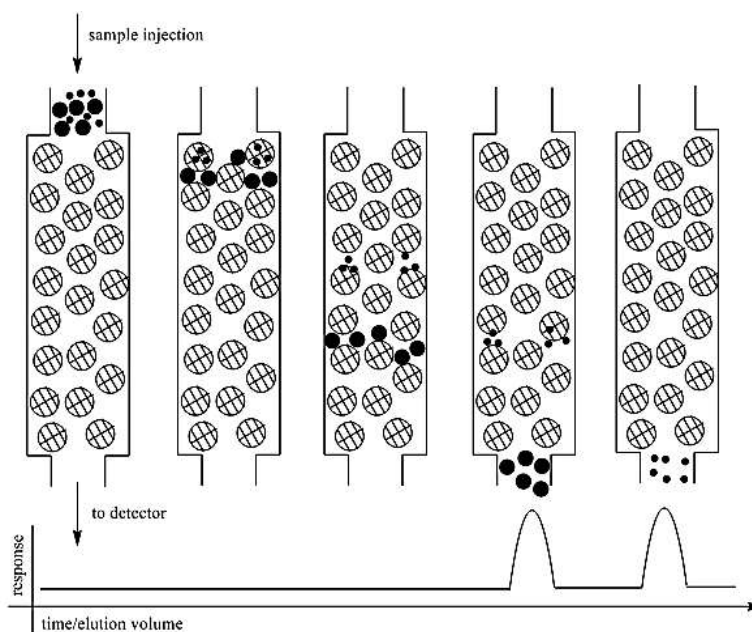


Figure 3.4 Schematic representation of polymer chain separation in GPC¹⁵⁷

After elution, the concentration of the analyte sample with respect to different molar masses must be established to produce a chromatogram. As most polymers will be injected into GPC in very small quantities ($\sim 0.1\text{mg}$), it is necessary for a detector to be highly stable and to be very robust in terms of its detection limits. UV detectors are the most stable for this purpose, but due to only a small amount of polymer species being UV-absorbent they are not particularly versatile. Detectors with IR capability are much more robust, but are very costly. Hence, the most commonly used type of detectors are differential refractometers, which constantly measures the difference in refractive index between the

eluted sample and that of the pure eluent solvent throughout the experiment. The output signal from the refractometer and the area underneath the chromatogram curve can then be combined with data from the calibration curve in order to gain a molar mass distribution.

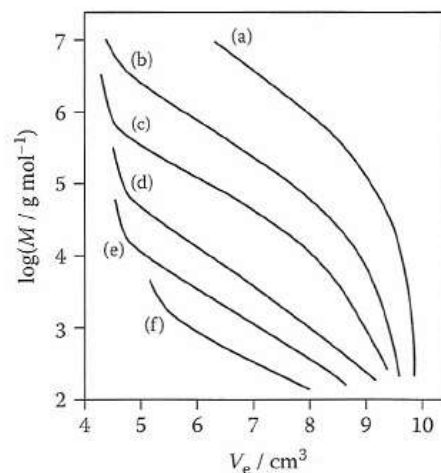


Figure 3.5 Typical GPC calibration curves for polystyrene in THF¹⁷, obtained using six different columns with the following pore sizes: (a) 10^5 nm, (b) 10^4 nm, (c) 10^3 nm, (d) 10^2 nm, (e) 50 nm and (f) 5 nm.

GPC was used to analyse representative latexes of each core:shell ratio to investigate any potential differences in molecular weight. Portions of wet latex were coagulated using a freeze-thaw method, whereby ~ 3 g portions of wet latex were placed into a glass vial then completely frozen in liquid nitrogen before being thawed. This process was repeated until complete coagulation of the latex was observed. The resulting polymer was then rinsed thoroughly in deionised water and dried at 60°C for at least 3 days before use. The dried polymer was then dissolved in distilled and filtered tetrahydrofuran (THF) at a concentration of approximately 0.2 %w/v, and diphenyl ether added as a marker species which had an elution time of approximately 34 minutes. Samples were passed through three Phenomenex Phenogel columns connected in series with pore sizes of 5×10^6 , 5×10^4 and $5 \times 10^2 \text{ \AA}$ at an elution rate of 1 mL min^{-1} and analysed using a Shodex RI-101 refractometer at 35°C . The raw data was then analysed relative to the PMMA calibration standards using PSS WinGPC software.

3.4.1.5 Gas chromatography (GC)

Gas chromatography (GC) is a technique that is widely used to analyse chemical species that can be vaporised at temperatures below 300°C without decomposing. It is especially useful for determining the concentration of specific components in a mixture.

As is common to all forms of chromatography, both a mobile and a stationary phase are employed to separate differing components from a mixture. A detector then analyses the concentration of each species, with the type of detector used depending on the nature of the analyte. The mobile phase in GC is commonly an inert 'carrier' gas such as helium, argon or nitrogen, although for certain detector types a mixture of helium and air can also be used. The relative flow rates of the mobile phase can be controlled electronically and varied to give optimum performance. The stationary phase consists of a polar, non-volatile solution, and it is the adsorption of vaporised analyte molecules onto this stationary phase that causes separation. The rate at which the analyte is eluted will depend on the strength of adsorption between the molecule and the stationary phase, with more strongly adsorbed species being eluted more slowly¹⁶³.

Flame Ionization Detectors (FID) are among the most commonly used detectors due to their versatility and broad sensitivity to a range of different organic species, most notably hydrocarbons¹⁶⁴. FIDs operate using a hydrogen-air fuelled flame to pyrolyse the organic species as they are eluted, which causes them to decompose into charged species which generates a current between a pair of electrodes. The signal from this current is then translated into a peak on a chromatogram. In order to analyse a sample with an unknown concentration, it is necessary to calibrate the GC by using a reference which is eluted at a known time, and the isolated component which is the desired analyte in order to determine its elution time.

GC was used in this project to determine residual monomer levels in polymer latexes, and was conducted using a Perkin Elmer Clarus 500 Gas Chromatograph. Butan-1-ol in methanol at a concentration of $0.123 \text{ mol dm}^{-3}$ was used as an internal standard. Approximately 1 g portions of latex were dissolved in ~4 g of the butan-1-ol/methanol solution, before being sonicated for 20-30 seconds in order to coagulate the polymer. The resulting solution was then filtered through a $0.22 \text{ }\mu\text{m}$ filter into the GC vials. An autosampler injected $1.0 \text{ }\mu\text{L}$ into the GC system which comprised an injection port at $200 \text{ }^\circ\text{C}$, a 10 metre Agilent HP-FFAP column with a bore size of 0.53 mm and a flame ionisation detector held at $250 \text{ }^\circ\text{C}$. A mixture of argon and hydrogen was used as the carrier gas at a flow rate of 45 mL min^{-1} . The temperature programme was for the sample to be held at $35 \text{ }^\circ\text{C}$ for 5 minutes, and then raised to $160 \text{ }^\circ\text{C}$ at a heating rate of $10 \text{ }^\circ\text{C min}^{-1}$ and held there for 25 minutes. Calibration was achieved using solutions with known concentrations of BA

and BMA in the butan-1-ol/methanol solution. Elution times were 1.6 minutes for methanol, 7.0 minutes for butan-1-ol, 7.7 minutes for BA and 8.7 minutes for BMA.

3.4.1.6 Solids content analysis

Solids content analysis was used to gravimetrically deduce the monomer-to-polymer conversion throughout the emulsion polymerisation process. To achieve this, accurately weighed portions (approximately 1.5-2 g) of the latex samples were placed into aluminium foil dishes and dried at 80 °C to constant weight.

The solids contents and hence the polymer content of each latex sample were then deduced using Equation 3.12(a) – (c):

$$\begin{aligned} \text{(a) Solids content (\%)} &= \left(\frac{\text{Dried sample and pan mass} - \text{Empty pan mass}}{\text{Wet sample and pan mass} - \text{Empty pan mass}} \right) \times 100 \\ \text{(b) Weight \% non - polymer solids} &= \left(\frac{\text{Mass of non-polymer solids}}{\text{Total mass of reaction components}} \right) \times 100 \quad \text{(3.12)} \\ \text{(c) Weight \% polymer} &= \text{Solids content (\%)} - \text{Weight \% non - polymer solids} \end{aligned}$$

This polymer content value is then used to calculate both the instantaneous and overall monomer conversions, using the equations given in Equation 3.13(a) and (b), respectively:

$$\begin{aligned} \text{(a) \% Instantaneous monomer conversion at time } t &= \\ &= \left(\frac{\text{Total mass of polymer formed at } t}{\text{Total mass of monomer added upto } t} \right) \times 100 \quad \text{(3.13)} \\ \text{(b) \% Overall monomer conversion} &= \\ &= \left(\frac{\left(\frac{\% \text{ Instantaneous conversion}}{100} \right) \times \text{Mass of monomer added before sample}}{\text{Total mass of monomer in formulation}} \right) \times 100 \end{aligned}$$

3.4.2 Mechanical and morphological characterisation of films

3.4.2.1 Stress-strain tensile testing

Stress-strain tensile testing refers to the deformation of a material in a uniaxial direction at a constant rate, and the measurement of the resulting stress and strain. These values are then plotted against each other and can be used to determine many mechanical properties of a material, for example its modulus, extensibility and failure limits.

Stress refers to the force applied per unit area, with the units of N m⁻² or Pa, and is commonly denoted using the Greek letter σ . Strain can be defined as the ratio of the

uniaxial change of dimension in ratio to its original value, and as such is an inherently dimensionless quantity. The Greek letter used for strain is ϵ ¹⁶⁵.

The simplest method to measure the stress-strain properties of a material is using a simple uniaxial test, whereby a force F is applied to a sample of length l_0 and the resulting change of length in the direction of deformation Δl is measured. The stress required to achieve it can then be calculated using the expressions given in Equation 3.14(a) and (b), respectively. Values of stress and strain calculated using these equations are referred to as ‘engineering’ stress and strain, as opposed to ‘true’ stress and strain which take the constantly changing cross-sectional area of the sample into consideration. All stress and strain values given in this thesis refer to the engineering stresses and strains.

$$\begin{aligned} \text{(a)} \quad \epsilon &= \frac{\Delta l}{l_0} \\ \text{(b)} \quad \sigma &= \frac{F}{A_0} \end{aligned} \tag{3.14}$$

Where A_0 is the original cross-sectional area of the sample.

For small values of strain up to approximately 1%, a simple Hookean linear relationship between stress and strain can be identified, and is shown in Equation 3.15, where E is the Young’s modulus:

$$\sigma = E \epsilon \tag{3.15}$$

The Young’s modulus, E , of a material is a measure of the stiffness of a material, and is defined as being the ratio of stress and strain in the region where the Hookean linear relationship holds⁹⁸. Hence, the value of Young’s modulus is only determined from the very initial section of the stress-strain curve. E is largely dependent upon the composition, crystallographic structure and the nature of the bonding between the elements in the material¹⁶⁶.

Machines to perform stress-strain tensile testing commonly consist of screw-driven beams which can be moved at constant, operator determined speeds. A load cell with a specifically selected range is mounted on the beams, and using a clamp assembly dumbbell-shaped samples of the material to be tested can be fixed between this moving beam and a static base. Figure 3.6 shows the shape of these stress-strain tensile samples, and the section that is used to calculate stress and strain as shown in Equation 3.14.



Figure 3.6 Dumbbell-shaped stress-strain tensile testing samples, with the parallel-sided section of length l_0 indicated.

Stress-strain tensile testing can be used to extract information regarding the arrangement of polymer chains within a sample, as these differing types of polymer will result in characteristic stress-strain curves. Examples of such are shown in Figure 3.7.

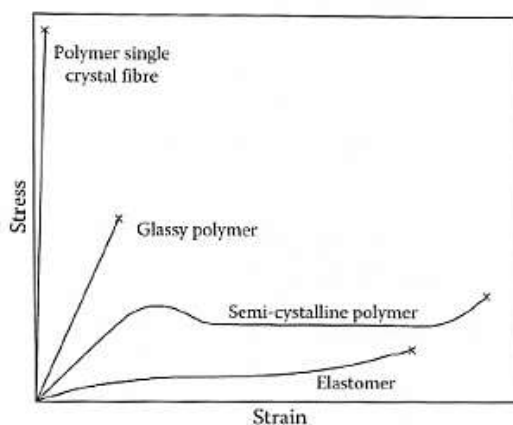


Figure 3.7 Characteristic stress-strain curves for different types of polymers¹⁷

Stress-strain tensile testing of the soft-soft nanocomposite materials discussed in this thesis was performed using an Instron 1122 Series Universal Testing System, fitted with a 500 kN load cell switched to measure within the range 0 – 50 N. Samples were prepared by casting films according to the procedure in Section 3.3.2, then dumbbell-shaped samples with a parallel section of dimensions 30 mm x 4 mm were cut using a mechanical ‘stamp’ cutter. The specimens were conditioned for 24 hours in the testing room which was controlled at 23 (± 1) °C and 50 (± 2) % relative humidity. The samples were then subjected to tensile testing using an extension rate of 25 mm min⁻¹, and measurements performed in quintuplicate to ensure reproducibility and establish the standard deviation.

Young’s modulus was determined by the first (X^1) coefficient of a polynomial fit that had the best correlation with the data points between strain values of 0 and 0.04 (4%). The typical order of the polynomial fits used was between 6 and 8.

3.4.2.2 Stress relaxation testing

Polymers have the inherent ability to behave like both elastic springs and viscous liquids, and as such a mechanical recovery phenomenon known as ‘creep’ can be observed. Provided that the stress does not exceed a value known as the ‘yield stress’, beyond which irreversible plastic deformation occurs, the polymers will creep indefinitely and the viscoelastic component will recover completely upon removal of the load. On a microscopic

scale, creep can be explained by molecular rearrangements of the polymer chains during the extension and relaxation processes. Polymeric creep is significant at all temperatures, compared to metallic creep which only manifests at high temperatures¹⁶⁷.

Due to this duality in mechanical behaviour, it is possible to identify aspects of both viscous flow and elastic strain from graphs of stress or strain against time, an example of which is shown in Figure 3.8. The initial rapid respective rise and decrease of strain upon the application or removal of a load correspond to an instantaneous elastic response, but the eventual slow decrease of the rate of increase or decrease of the strain is due to the viscous flow component of the polymer's behaviour dominating in these domains.

In a viscoelastic polymer, both elastic and viscous components will affect the mechanical behaviour. It is the viscous flow component that is the main contributor to phenomena such as creep and relaxation. Creep and relaxation are both consequences of the same molecular motions, and hence are fairly analogous. However, one key difference between the two phenomena is that relaxation reaches its equilibrium much faster than that of creep¹⁶⁸.

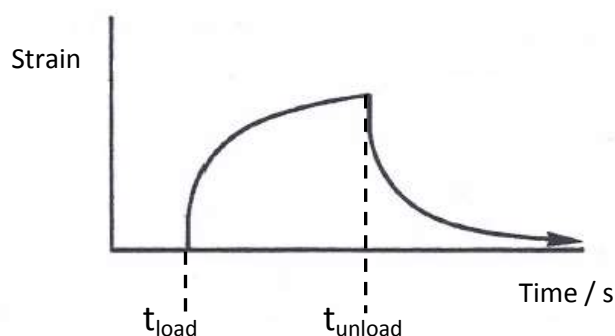


Figure 3.8 Plot of strain versus time demonstrating viscoelastic behaviour during both loading and unloading processes¹⁶⁵

Two main types of viscoelasticity can be identified and rationalised. Non-linear viscoelasticity is the more complex of the two behaviours, and typically occurs during large deformations. In this regime, a linear stress-strain curve will not be produced for any constant extension rate¹⁶⁵. Non-linear viscoelasticity is extremely complex and as such has not been extensively investigated, leading to only a few mathematical models to explain its existence and occurrence. Conversely, many mathematical models exist to explain linear viscoelastic behaviour, whereby linear stress-strain curves are observed at constant extension rates. This linear behaviour occurs at very small strains and at short timescales.

The Maxwell model of viscoelasticity was proposed in the 19th century, and essentially considers the material to consist of a Hookean elastic spring and a Newtonian dashpot,

which resists motion using viscous friction, connected in series. Thus, both elastic and viscous components of the system can be considered. Figure 3.9 shows a schematic representation of this arrangement.



Figure 3.9 Schematic representation of a Maxwell material¹⁶⁸

It is possible to predict the relaxation of a linearly viscoelastic polymer held at constant strain using the Maxwell model¹⁷, which can be written as:

$$\sigma = \sigma_0 \exp\left(\frac{-t}{\tau_0}\right) \quad (3.16)$$

Where σ is the overall stress in the system, σ_0 is the initial stress, t is time and τ_0 is the relaxation time.

The value of τ_0 , which is a characteristic relaxation time, is significant for describing the viscoelastic nature of the system as it relates the viscous and elastic components of the system using the relationship shown in Equation 3.17, where η is the viscosity and E is the elastic modulus.

$$\tau_0 = \frac{\eta}{E} \quad (3.17)$$

Stress relaxation tensile testing was performed using an Instron 5569 Universal Testing System, fitted with a 100 N load cell. Dumbbell-shaped samples were prepared using the standard method described in Section 3.4.2.1 for tensile testing. The samples were uniaxially extended to 100% strain (i.e. 25 mm) at a rate of 25 mm min⁻¹, then held at this fixed extension and the change in stress monitored over a 10 minute period. Measurements were performed in quintuplicate to ensure reproducibility. It should be noted that the environment temperature and humidity were not controlled or monitored during this testing.

3.4.2.3 Mechanical hysteresis testing

'Hysteresis' is defined by Chambers 20th Century Dictionary as "*the retardation or lagging of an effect behind the cause of the effect*". In terms of the mechanical testing of elastomeric polymers, this refers to the recovery of strain when load, and hence stress, is removed from the sample. Figure 3.10 shows a characteristic hysteresis 'loop' for a strain-crystallising elastomer, whereby at high strains the polymer chains become ordered and form crystalline domains in the amorphous polymer matrix.

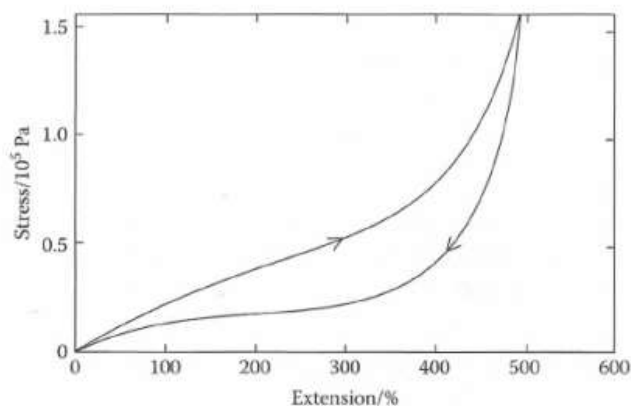


Figure 3.10 Mechanical hysteresis loop showing complete recovery of strain upon the removal of load¹⁷

The area contained within the loading and unloading curves corresponds to the energy dissipated during the relaxation process. Although complete recovery of strain indicates that deformation of the polymer is reversible, if the hysteresis loop is allowed to cycle rapidly the energy released by the processes may result in a build-up of heat that could eventually lead to a decline in mechanical performance of the material.

Hysteresis tensile testing was performed using an Instron 5569 Universal Testing System, fitted with a 100 N load cell. Samples were prepared using the standard method described in Section 3.4.2.1 for tensile testing. The samples were then extended to a nominal strain value at a rate of 25 mm min⁻¹, then retracted to 0% strain at the same rate. The sample was then left to recover for 10 minutes before the extension and retraction was repeated and the difference between the two cycles analysed. The measurements were performed in quintuplicate to ensure reproducibility. It should be noted that the environment temperature and humidity were not controlled or monitored during this testing.

3.4.2.4 Fourier transform infrared spectroscopy (FTIR)

Fourier transform infrared spectroscopy (FTIR) is a type of absorption spectroscopy, whereby the absorption of characteristic infrared wavelengths causes the vibrational excitement of chemical bonds within the analyte molecule. Absorption results from the coupling of the bond vibration with the oscillating electromagnetic IR radiation, and requires the ability for a dipole moment change to be induced¹⁷. This vibrational excitement can be assumed to be a bond 'deformation', for example stretching or bending, and the characteristic wavelength at which the absorption occurs corresponds to the energy difference between the upper and lower vibrational levels of the bond. However,

the reciprocal wavelength or 'wavenumber', with units of cm^{-1} , is more commonly used to express absorption energies. Each absorption of IR radiation can be attributed to a specific bond deformation, for example very strong absorptions between 1640 and 1730 cm^{-1} corresponds to a C=O bond stretching, whereas absorptions in the region of 1670 cm^{-1} can be attributed to C=N bonds in imine functionalities¹⁶⁹. These characteristic absorptions are not vastly affected by the presence of other groups or bonds, and hence FTIR is a very robust method and can be used for all molecules which contain that bond. It can also be performed on analytes in varying physical states, for example polymer latexes and films, both of which are relevant to this project.

The phrase 'Fourier transform' refers to the method by which the sample is irradiated with the entire spectral bandwidth at once. Using a computer algorithm, this data is then transformed to give the absorption wavelengths and intensities. Applying the Fourier transform approach to spectroscopic methods increases the speed of the analysis, and eliminates background noise by a factor of n^2 , where n is the number of runs performed for a single analysis¹⁷⁰.

FTIR was used to complement AFM-IR studies performed, using the methods detailed in Section 3.4.2.5.1. FTIR spectra of polymer films cast according to the method given in Section 3.3.2 were measured in the range of 4000 – 650 cm^{-1} at a rate of 100 $\text{cm}^{-1} \text{min}^{-1}$ using a Thermo Nicolet 5700 FT-IR spectrometer, and analysed using OMNIC software. The absorption spectrum was then produced by subtracting a background spectrum from the measured absorptions.

3.4.2.5 Atomic force microscopy (AFM)

Atomic force microscopy (AFM) is a surface analysis technique that was developed in 1986 by Binnig, Quate and Gerber¹⁷¹ as an extension of scanning tunnelling microscopy (STM), the invention of which was awarded the 1986 Nobel prize in Physics¹⁷². The idea for the AFM arose due to the inability of STM to image insulating materials, as the carrying of a current through the sample formed the basis of that technique. Developed as a joint venture between IBM and Stanford University, the theory behind AFM is that surface topology can be examined on an atomic scale using a tip mounted on a cantilever with an extremely soft spring constant (k), such that the applied force is not strong enough to displace the atoms as they are imaged. Initial calculations by Binnig *et al* suggested that interatomic spring constants are in the range of 10 N m^{-1} , whereas the spring constant of a

cantilever made from household aluminium foil is approximately 1 N m^{-1} . This meant that the fabrication of such a soft cantilever could be very easily achieved.

All force microscopes comprise five essential elements, namely a tip mounted on a soft cantilever, a method of sensing the deflection of the cantilever, a feedback system to monitor and control this deflection, a mechanical scanning system to control the position and movement of the cantilever and a display system to convert these deflections and movements into an image. A schematic representation of the AFM instrumentation is shown in Figure 3.11.

In AFM the feedback, scanning and display systems are very similar to those utilised for STM, thus the method itself is characterised by the cantilevers and detection methods used. The cantilever devised by Binnig in the original prototype consisted of gold foil with a diamond tip, although modern versions are typically comprised of silicon nitride and fabricated using a photolithographic method¹⁷³, and have spring constants in the range of $0.05\text{-}1 \text{ N/m}$. As imaging on an atomic scale is desired, the detection method used needs to be able to operate in the sub-angstrom range. In the original prototype AFM the cantilever deflection was measured using an electron tunnelling current, although due to the extreme sensitivity of this with regards to sample contamination optical detection methods, such as beam deflection, are more usually utilised. In this method, a photodiode-generated laser is reflected off the cantilever into a position-sensitive photodetector unit.

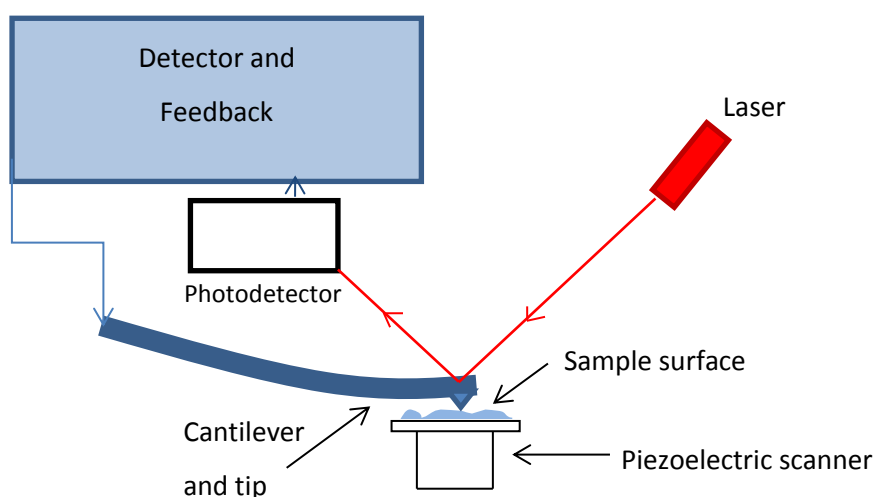


Figure 3.11 Schematic diagram of an atomic force microscope (AFM)

Three modes of AFM are possible, and each are characterised by the type of interaction that the cantilever tip has with the sample surface. Contact mode AFM was among first of these modes to be developed, and refers to the method of 'dragging' the cantilever over the sample surface. The surface topology is then measured by monitoring the deflection motion of the cantilever, which occurs due to repulsive forces between the tip and the sample¹⁷⁴. Conversely, in non-contact mode AFM the probe tip does not make contact with the sample surface, but is instead oscillated above the sample surface. This mode was also one of the earliest to be developed¹⁷¹, and involves the oscillation of the cantilever at just above its resonant frequency. The interaction between this oscillation and long range intermolecular forces such as van der Waals forces from the sample surface that causes the deflection of the cantilever and hence gives rise to an image. Non-contact mode AFM is especially useful for extremely small scale measurements, such as the sub-Angstrom imaging of intramolecular bonds¹⁷⁵. However, due to the small amplitude of oscillation (approximately 5 nm), it is unsuitable for larger scale or liquid applications. The third AFM method, tapping mode, was developed due to the damage to both the probe tip and the sample surface that can occur as a result of contact mode AFM, which due to these consequences is unsuitable for imaging soft materials such as polymer or biological surfaces. In tapping mode, the cantilever is oscillated near to its resonant frequency (~ 300 kHz) which causes the tip to momentarily come into contact with the sample surface before withdrawing. Due to this contact with the surface, relatively stiff cantilevers must be used in order to overcome adhesion to the sample surface, so the careful selection of an appropriate cantilever for the material to be imaged is essential¹⁷⁴.

A great deal of success has been gained from the imaging of soft polymer surfaces using tapping mode AFM, and efforts to reduce the 'noise' produced from excess adhesion to soft surfaces led to the PeakForce Quantitative Nanomechanical Mapping (QNM) method being developed by Bruker in 2011¹⁷⁶. This PeakForce QNM is an extension of the tapping mode method, to combine an increased resolution with a real-time calculation of the Young's modulus of the sample surface at each point of contact. It is claimed by Bruker that PeakForce QNM can be used to accurately measure Young's modulus values between 1 MPa and 2 GPa¹⁷⁷.

In order to calculate the Young's modulus, the Derjaguin-Muller-Toporov (DMT) model of elastic contact between two surfaces is used, which takes into account the adhesion, and hence attractive forces, that occur. Hence, it is ideal to be used for the imaging of soft

polymer surfaces which are inherently 'sticky' if below their T_g at imaging temperature. The equations that are used to calculate this DMT modulus can be summarised as in Equation 3.18:

$$E_r = \frac{3(F_{tip} - F_{adh})}{4(\sqrt{Rd^3})} \quad (3.18)$$

Where E_r is the reduced Young's modulus given by DMT theory, F_{tip} is the force on the AFM probe tip, F_{adh} is the force of adhesion between the sample and the tip, R is the AFM tip radius and d is the deformation depth¹⁷⁸.

This 'reduced Young's modulus', E_r , can be related to the actual Young's modulus of the sample surface by the equation detailed in Equation 3.19:

$$\frac{1}{E_r} = \frac{(1 - \nu_s^2)}{E_s} + \frac{(1 - \nu_i^2)}{E_i} \quad (3.19)$$

Where ν_s and E_s are Poisson's ratio and Young's modulus, respectively, of the sample surface and ν_i and E_i are Poisson's ratio and Young's modulus, respectively, of the 'indenter', which for PeakForce QNM is the AFM probe tip.

As E_i is much larger in magnitude than E_s , the second term of Equation 3.19 becomes negligible, thus the 'reduced' Young's modulus E_r can be considered to be a good measure of the true Young's modulus of a surface.

The measurement of mechanical properties that is enabled by the use of PeakForce QNM is extremely useful for situations where discrimination of discrete phases upon a sample surface would otherwise not be possible. Such is the case for the soft-soft nanocomposites discussed in this thesis, the core and shell phases of which have very similar chemical composition but are able to be mechanically discriminated due to the presence of crosslinking in the shell phase, which increases the modulus of this phase with respect to that of the viscoelastic core.

AFM was performed using a Bruker MultiMode 8 AFM with NanoScope software. The experimental method utilised was PeakForce QNM in air with ScanAsyst enabled to facilitate the user. Bruker SNL-10 cantilever probes were selected according to the general range of Young's modulus of the materials to be imaged, and cantilevers B and C from these probes (spring constants of 0.12 and 0.24 N/m, respectively) used depending on the specific Young's modulus of the sample. Samples to investigate the film surface were prepared for imaging by gluing sections of film as prepared from the procedure given in

Chapter 3.3.2 to 15 mm diameter magnetic AFM stubs using a cyanoacrylate adhesive. Cross-section samples were prepared by thermal fracture, whereby sections of film were frozen in liquid N₂ then mechanically snapped. The exposed cross-section surface was then mounted upright using a Bruker SD-103 clamp-mounted sample holder.

3.4.2.6 Infrared spectromicroscopy (AFM-IR)

The combination of infrared spectroscopy and microscopy has long been of interest for applications such as the imaging of living cells, for which the sample dimensions are similar to the wavelength of infrared radiation (3 – 20 μm). Several methods utilising both synchrotrons and free electron lasers (FELs) were developed, but did not offer good spacial resolution. However in 2005 a novel method utilising an AFM tip as a spacial sensor was reported by Dazzi et al¹⁷⁹, which developed as an extension of the photothermal deflection beam (PTDB) effect. This PTDB phenomenon measures the deflection of a visible laser induced by the irradiation of a sample, which is similar to the laser deflection method used to monitor surface topography by AFM (see Figure 3.11). However, PTDB microscopy has several disadvantages, including the requirement for a reflective surface and a restriction in resolution associated with the laser spot size¹⁸⁰. Use of an AFM tip as a probe for local deformation in conjunction with infrared spectroscopy (referred to as AFM-IR) provides excellent lateral resolution on a sub-wavelength scale, and was successfully used to characterise both commercial resins¹⁷⁹ and biological samples¹⁸¹.

The basis of the AFM-IR technique can be seen from the schematic diagram in Figure 3.12(a) whereby the sample surface is irradiated with an IR laser from beneath, which is the method that was utilised in many of the original AFM-IR systems. However in 2014, the Nano-IR2 system manufactured by Anasys Instruments was introduced, which allows for “top-down IR illumination”, in which the sample is irradiated with IR radiation from the top of the sample surface instead of beneath¹⁸². A schematic representation of this top-down illumination can be seen in Figure 3.12(b).

This development in technology allows the technique to be much more versatile in terms of the samples that can be analysed, as previously deposition of extremely thin sample films onto ZnSe prisms had been necessary. Using the top-down illumination, standard sections of film that are mounted onto conventional AFM stubs can be analysed, including those that can be considered to be “infinitely thick”, i.e. bulk film cross-sections such as were discussed in Section 3.4.2.5.

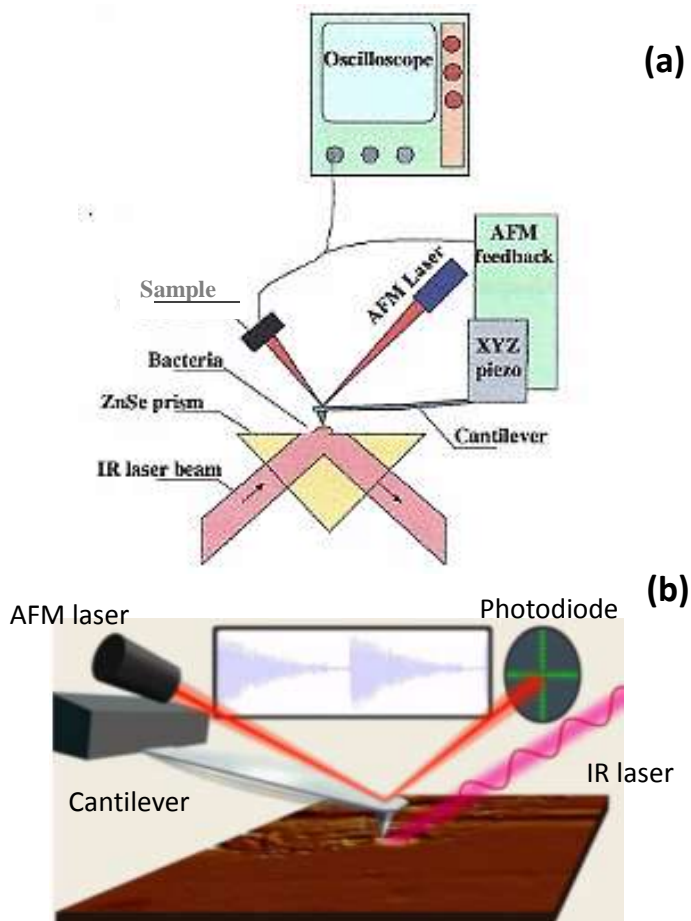


Figure 3.12 Schematic representation of AFM-IR equipment, showing (a) traditional 'bottom-up' IR irradiation¹⁸¹ and (b) novel 'top down' IR irradiation¹⁸²

For both types of IR irradiation, the resulting physical deformation is due to localised heating of the sample which creates a vibration of the cantilever. The magnitude of this vibration corresponds to the sample deformation and by extension the local IR absorption coefficient. Hence, this technique can be used in a number of ways, for example to measure an entire IR spectrum at a specific point on a sample surface or to map the absorption of a specific wavenumber over the entire sample surface. These two possibilities are illustrated in Figure 3.13(a) and (b), respectively.

In this project AFM-IR was used to analyse specifically chosen film cross-sections which were prepared as per the procedure in Section 3.4.2.5, and was performed using a Nano-IR2 manufactured by Anasys Instruments in contact mode, with gold-coated cantilevers. Images and spectra were then manipulated and processed using Analysis Studio v3.8, provided by Anasys Instruments.

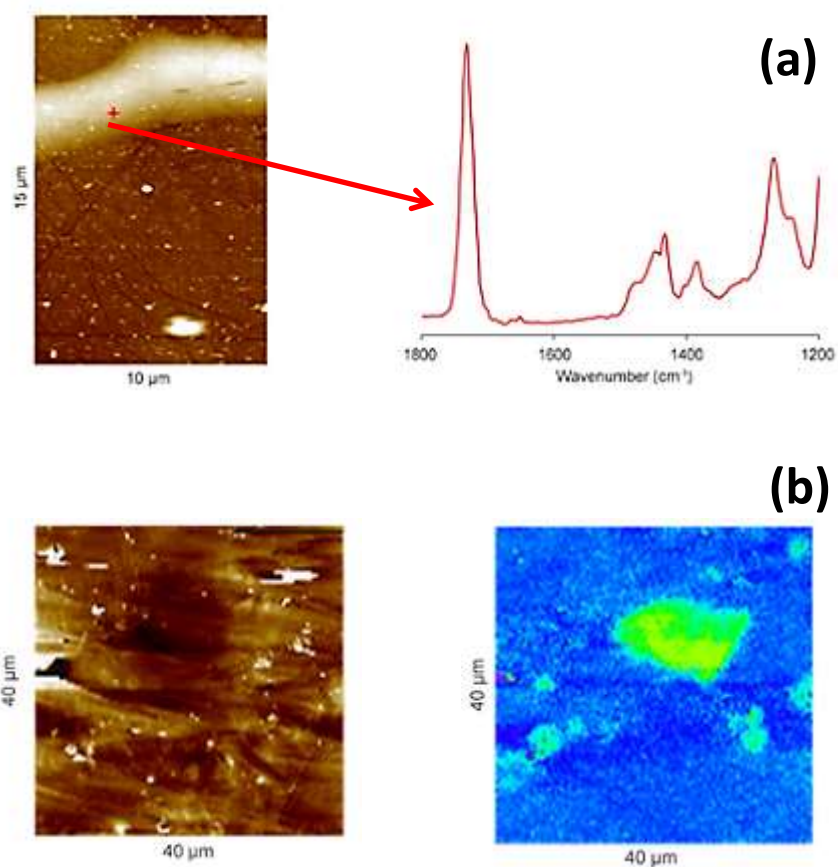


Figure 3.13 Representations of measurements possible using AFM-IR¹⁸². (a) shows point IR spectrum, and (b) shows the surface mapping of a single wavelength

3.4.3 Thermal characterisation of latexes and films

3.4.3.1 Minimum film formation temperature (MFT)

The lowest temperature at which the formation of a fully coherent film may be achieved is known as the minimum film formation temperature (MFT)⁴⁴. It is an extremely important parameter to consider in the formulation of film forming latexes, as below this MFT the particles may not have the required energy for interdiffusion of polymer chains across the particle boundaries to occur, hence resulting in a mechanically weakened film.

The measurement of MFT is a very simple experiment, and is described by several standard test methods^{183, 184}. A film of wet latex is cast onto a metal substrate that is then placed upon a bar with a variable uniform temperature gradient, the range of which is approximately 20 °C and is determined by the desired application properties of the latex.

The latex is then left to dry, and the minimum point at which a film forms deduced manually, using visual judgement of the cloudy-clear boundary.

Minimum film formation temperature (MFT) of wet soft-soft nanocomposite latexes was measured using a Rhopoint WP Unit with various possible temperature ranges, from which two were used in this project, namely -5 to 13 °C and 0 to 18 °C. Films with a wet thickness of 100 µm were drawn down and left to dry for 3 hours before the measurement was taken. Measurements were performed in triplicate and a mean value of MFT reported.

3.4.3.2 Differential scanning calorimetry (DSC)

Differential Scanning Calorimetry (DSC) is a thermo-analytical technique used to investigate the thermal properties of polymers. There are two main classes of DSC, the first of which is 'power-compensation DSC'. In this method, an analyte sample of known mass and an inert reference sample with a well-defined heat capacity are independently heated in an inert atmosphere, usually nitrogen gas¹⁸⁵. The difference in heat flow required to keep the two samples at the same temperature is measured. For the second class of DSC, 'heat flux' DSC, the sample and inert reference are heated simultaneously at the same rate, again in an inert, typically nitrogen gas, atmosphere. The temperature difference between the analyte and the reference is constantly recorded and used as the basis for the measurement. For both types of DSC, the same sample preparation method is used for the analysis of polymers. Small aluminium pans are used to contain an accurately known mass of sample, and are then topped with an aluminium lid. The edges of the join can be sealed hermetically in order to prevent the evaporation of any volatile components from the sample during heating.

The output of each method is a curve on a graphical representation of either differential energy (power-compensation DSC) or differential temperature (heat-flux DSC) versus temperature. A number of different thermal transitions can be measured using both methods, and as only power-compensation DSC was used in this project the characteristic shapes of the transitions as seen from this method can be seen in Figure 3.14.

DSC is commonly used in studies of polymeric systems to determine transition temperatures, such as T_g and T_m , and can also be used for thermodynamic analyses such as gaining the enthalpies of melting and crystallisation, which are determined by analysing the area under the heat flow peak of the transition.

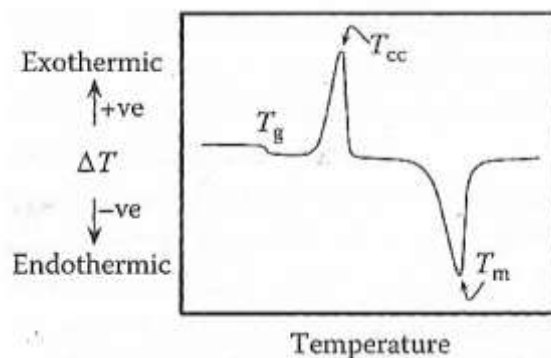


Figure 3.14 Thermal transitions that can be seen from power-compensation DSC, including glass transition (T_g), melting (T_m) and cold crystallisation (T_{cc})¹⁷

DSC was selectively performed on soft-soft nanocomposite materials in order to gain glass transition temperatures, using a TA Instruments Q100 differential scanning calorimeter. Samples were prepared by casting films as per the process described in Section 3.3.2. Sections of the film weighing approximately 10 mg were then encapsulated in hermetically-sealed aluminium pans. The samples were tested against a reference comprising an empty sealed hermetic pan. Four heating-cooling cycles from -50 to 150 °C were performed at a heating rate of 10 °C min^{-1} . Analysis of the data was taken from the 4th of these cycles only, and the T_g determined by the midpoint of the transition as illustrated in Figure 3.15. Three individual DSC measurements were taken for each sample, with the reported value being the average of these.

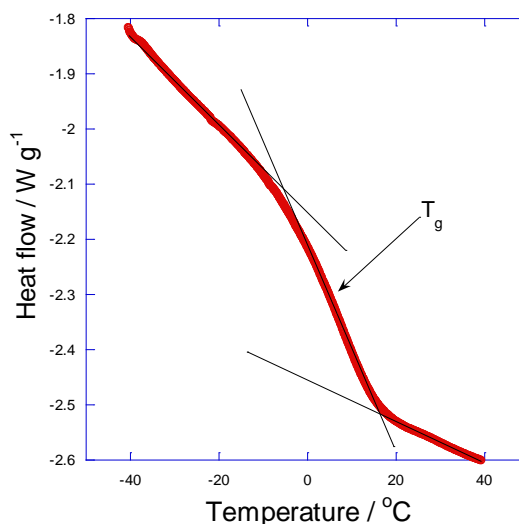


Figure 3.15 Illustration showing how T_g was determined in this PhD project

3.4.3.3 Dynamic mechanical thermal analysis (DMTA)

Dynamic mechanical thermal analysis (DMTA) is a technique that is especially useful for studying the viscoelastic behaviour of polymers. In DMTA, a sinusoidal stress or strain is applied to a sample and the resulting changes in strain or stress, respectively, measured in

order to determine the complex modulus at a range of different temperatures. This complex modulus can be further split into two parts; firstly the elastic storage modulus E' , which represents the energy stored in the sample, and secondly the viscous loss modulus E'' , which measures energy lost by mechanical processes, e.g. heat¹⁶⁶. The respective ratio of these two moduli, $\tan \delta$ relates to δ , which is the phase angle that accounts for the phase lag between the two moduli¹⁶⁶. Peaks in the $\tan \delta$ signal indicate relaxation processes such as glass transition, which can be classified as an ' α -relaxation', and other ' β -relaxations' which occur at low temperatures and are related to the motion of side groups, and in some cases, linking groups in the polymer chain backbones¹⁸⁶. The mathematical relationship of $\tan \delta$ to the storage and loss moduli is shown in Equation 3.20, where E'' is loss modulus and E' is storage modulus.

$$\tan \delta = \frac{E''}{E'} \quad (3.20)$$

A range of different test geometries can be used in DMTA, as can be seen from Figure 3.16, the choice of which is often dictated by the sample properties including stiffness, shape and modulus. The most commonly used of all these geometries is tension, in which the sample undergoes sinusoidal uniaxial stretching during the temperature sweep.

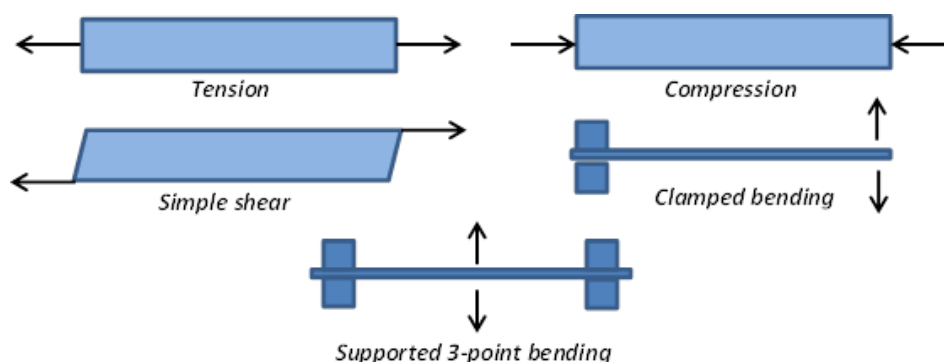


Figure 3.16 Test geometries available in DMTA testing¹⁶⁵

DMTA was performed on soft-soft nanocomposite films using a TA Instruments Q800 DMA with a tensile head fitted. Samples were prepared by casting films according to the procedure discussed in Section 3.3.2. Parallel-sided strips with dimensions of 25 mm (approx.) x 5.35 mm x 0.75 mm (approx.) were then cut from the film and clamped, then tested over a temperature range from -100 to 100 °C at a heating rate of 3 °C min⁻¹ and an oscillating strain of 2% with a frequency of 1 Hz.

3.4.4 Industrial test methods

All of the methods described in this section are from AkzoNobel standard testing procedures, and relate to testing specific to coating applications.

3.4.4.1 Viscosity tests

High-shear viscosity was measured using an ICI cone and plate viscometer at a shear rate of $10,000\text{ s}^{-1}$, with cone angle and diameter of 0.5° and 22 mm, respectively. Low-shear viscosity measurements were performed using a Brookfield DV-E viscometer with spindle 3 attached, at a rate of 10 RPM. These tests represent processes that occur during application, for example applying a paint to a substrate using a brush (high-shear) and drying (low-shear).

3.4.4.2 Erichsen hardness

In the field of coatings technology, 'hardness' is a term used to refer to the scratch resistance of a film, which can provide information about the plastic deformation limits and fracture resistance. The hardness of films cast from soft-soft nanocomposite systems was tested 48 hours and 1 month after film casting using a pendulum method, in which the effect of the film upon dampening the momentum of a pendulum swing is measured. Soft films will dampen the motion of the pendulum more, giving a lower number of swings compared to harder film surfaces.

3.4.4.3 Low temperature film coalescence

Low temperature coalescence was investigated by spreading a $200\text{ }\mu\text{m}$ wet thickness film onto a glass panel in a room at a constant temperature of 7°C . The latex, glass panel and applicator bar had all been conditioned at 7°C for at least 4 hours before application. After 3 days drying in the temperature controlled room, the quality of the film formed was visually inspected, with any cracking or other defects on the film surface being considered a failure.

3.4.4.4 Blocking tests

Blocking tests were performed at constant temperature and humidity of $23 (\pm 2)^\circ\text{C}$ and $50 (\pm 1)\%$, respectively. Latex films with a wet thickness of $200\text{ }\mu\text{m}$ were drawn down onto BYK card and left to dry for 24 hours. Rectangles of dimension $5\text{ cm} \times 4\text{ cm}$ were then cut from the film and arranged in pairs to form an X-shape with the latex film sides in contact with each other. These were then placed under a 1 kg weight for 24 hours before being pulled apart and the force needed to do this, as well as the damage to the two film surfaces, assessed. The films were then given a score from 0 to 5, where 0 indicated a lot of force required/film completely destroyed and 5 indicated no power needed/no damage.

3.4.4.5 Water and solvent resistance

Water and solvent resistance of the films was investigated by placing ~1 mL of either deionised water or methyl ethyl ketone (MEK) onto the film surface for ~1 hour. Evaporation effects were minimised by covering the droplet with a vial. After 1 hour, the droplet was removed using a tissue and the film visually inspected. The scale of grading is given in Table 3.1. The film was also re-inspected ~12 hours after removal of the water to deduce whether any damage to the film surface was permanent.

Table 3.1 Scale of grading for water and solvent resistance tests

Grading	Remarks
1	Excellent - no visible marking or film defects (i.e. blistering)
2	Good - some small signs of film discolouration but no major defects
3	Poor - film discolouration very obvious, major defects also observed
4	Very Poor - film almost completely disintegrated
5	Extremely Poor – film completely destroyed

4 Establishing a framework formulation for the synthesis of soft-soft nanocomposite latexes

4.1 Introduction

In order to investigate the structure-property relationships of soft-soft nanocomposite coatings, a framework formulation was required in order to produce these materials by emulsion polymerisation. It was essential for this framework to be extremely robust, and repeatedly produce structured particle latexes with the predicted physical properties, despite changes in monomer composition and core:shell ratio.

As discussed in Chapter 2, the soft-soft nanocomposite design theory was developed during attempts to produce high performance water-based pressure-sensitive adhesives (PSAs)⁶. Previous attempts to produce such materials using structured particle strategies were based upon latexes with a 'hard' methyl methacrylate (MMA) rich core and a 'soft' 2-ethylhexyl acrylate (2-EHA) rich shell phase^{128, 187}. However, it was found that this structuring of particles did not deliver any additional benefit in performance compared to existing, unstructured water-based PSAs. The principle was built upon by Deplace *et al.* as part of an EC FP6 project, which was conducted in collaboration with a number of different institutes across Europe. This novel 'soft-soft nanocomposite' design theory combines several commonly known properties of polymer colloids to give a route to synthesising high performance water-based systems for applications that require a deformable, soft polymer network such as adhesives, microgels and artificial tissues. The main aspects of this design theory have been discussed in Section 2.4.1.1 of this thesis.

Multi-stage starved-feed semi-batch emulsion polymerisation is most often used to synthesise soft-soft nanocomposite latexes. As was discussed in Section 2.2, semi-batch polymerisation offers several advantages with regards to structured particle formation compared to other methods such as batch polymerisation. These include a very high level of control over the copolymer composition and particle morphology, and an ability to control the rate of polymerisation by controlling the proportion of unreacted monomer-to-polymer ratio present in the reactor²⁴. In studies of soft-soft nanocomposites intended for PSA applications, acrylic monomers such as 2-EHA, n-butyl acrylate (BA) and ethyl acrylate (EA) were used in conjunction with keto-hydrazide crosslinking, which was extensively described in Section 2.5.1.1.

All of the potential applications for polymer systems synthesised using the soft-soft nanocomposite design strategy discussed thus far have been for very low T_g uses, of ~ -40 to -

20 °C for PSAs¹⁸⁸ and ~-70 to -50 °C for the nitrile rubber mimics⁷⁻⁹. Hence, the initial strategy of this project was the synthesis of acrylate- and methacrylate-based nanocomposite core-shell latexes with core- and shell T_g values closer to ambient temperature. Such systems are appropriate for use in paints and coatings, in order to deliver both a coherently formed film and a non-tacky film surface¹⁸⁹. Although extremely successful for very low T_g applications, the soft-soft nanocomposite design theory requires the continuous phase (i.e. the crosslinked shell phase polymer) to be an elastomer⁴. Elastomers are extremely extensible materials, and in order for this behaviour to occur the polymer must be both lightly crosslinked and above its T_g at the application temperature¹⁷. As mentioned previously, the T_g of polymers appropriate for use as binders in paints and coatings is typically between 5 and 30 °C, so due to this small difference between T_g and application temperature it cannot be guaranteed that the elastomeric behaviour will occur in soft-soft nanocomposite coating materials. Hence, this chapter will describe the synthesis of soft-soft nanocomposites with relatively very low T_g values of between -20 and 0 °C, to guarantee the elastomeric nature of films. All T_g values investigated in this PhD project were chosen in order to deliver the optimum balance between coherent film formation, elastomeric behaviour and non-tacky film surfaces at ambient temperature.

Initial soft-soft nanocomposite coating latex formulations were to be based on a poly[(butyl acrylate)-co-(methyl methacrylate)] latex formulation supplied by AkzoNobel, which was adapted to replace methyl methacrylate (MMA) with a more hydrophobic monomer, butyl methacrylate (BMA). Latent crosslinking, and hence potential elastomeric behaviour, was also incorporated with the addition of DAAM to the shell phase polymer backbone with ADH added to the final latex after preparation. This approach of using a pre-existing industrial formulation represents numerous benefits over generating an original recipe, including the potential return to AkzoNobel of a successful soft-soft nanocomposite formulation which could be easily implemented at the end of the project. The original industrial formulation was specifically chosen with regards to the properties of the latex it produced, namely a targeted solids content of 45-50 wt% and particle size of 250 nm, both of which are key parameters derived from the soft-soft nanocomposite design theory. This formulation was supplied by AkzoNobel for evaluation as to its feasibility to be a framework for all future soft-soft nanocomposite coating core-shell latexes, and the results of this are discussed in the following chapter.

4.2 Preliminary investigations

The industrial latex formulation provided by AkzoNobel contained an anionic surfactant, Rhodafac RK-500A, which was previously unknown with regards to research concerning soft-soft nanocomposites. Hence, a preliminary investigation to confirm the chemical structure of this surfactant was carried out using ^1H NMR spectroscopy. This information was not available from supplier's data sheets which only gave the basic chemical structure of the surfactant, see Figure 4.2, but not the degree of polymerisation of the poly(ethylene oxide) chains contained within.

The NMR measurement was conducted in D_2O , and due to the surfactant being 75 wt% solids in water, the sample was spiked with deionised H_2O and re-run to enable easy identification of the water peak, which occurred at a chemical shift of $\delta_{\text{H}} = 4.71$ ppm and has been removed from the spectrum. Figures 4.1 - 4.2 and Table 4.1 summarise the expected chemical structure together with assignments of the ^1H NMR resonances.

The integral values shown in Table 4.1 were calculated by using peak integration to gain the number of protons in each chemical environment, and then peak splitting patterns and characteristic ^1H NMR absorptions to determine the relative molecular structure. The data show that the poly(ethylene oxide) extender chain contains a total of 24 protons. Assuming the molecule is symmetrical, this corresponds to a degree of polymerisation of each chain of 3.

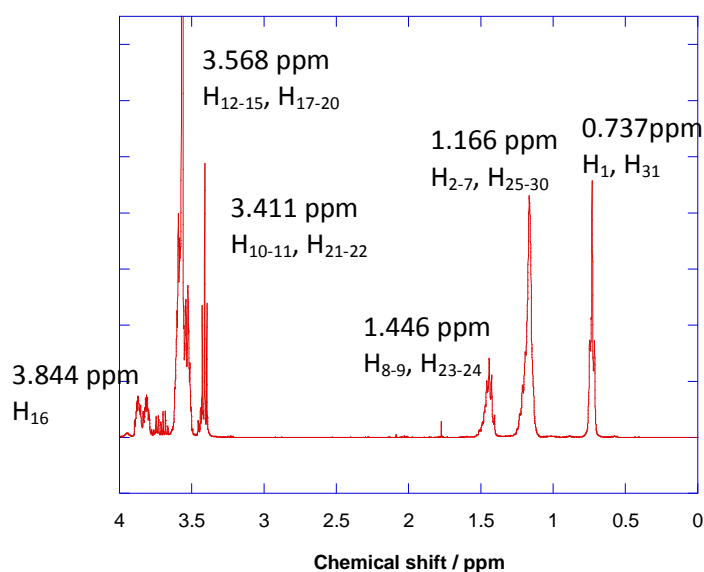


Figure 4.1 ^1H NMR spectrum of Rhodafac RK-500A in D_2O . The peak assignments are given in Table 4.1.

Table 4.1 Summary of the assignments of peaks from the NMR spectrum shown in Figure 4.1 in relation to the structure of the surfactant shown in Figure 4.2.

δ_H (ppm)	No. of protons	Assignment
0.737	6	Terminal methyl group, H ₁ and H ₃₁
1.166	12	Alkyl chain –CH ₂ groups, H ₂₋₇ and H ₂₅₋₃₀
1.446	4	–CH ₂ groups adjacent to alkoxide, H ₈₋₉ and H ₂₃₋₂₄
3.411	4	Alkoxide –CH ₂ groups, H ₁₀₋₁₁ and H ₂₁₋₂₂
3.568	24	Poly(oxy-1,2-ethanediyl) –CH ₂ groups, H ₁₂₋₁₅ and H ₁₇₋₂₀
3.844	4	Ammonium cation, H ₁₆

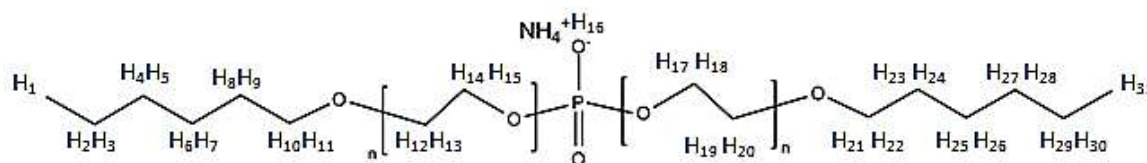


Figure 4.2 Rhodafac RK500A (IUPAC name poly(oxy-1,2-ethanediyl), α,α' -phosphinicobis(ω -(hexyloxy)) ammonium salt) with protons labelled to aid NMR spectrum peak analysis.

4.3 Development of a latex formulation to produce core-shell latexes

4.3.1 Evaluation of original AkzoNobel formulation

The original poly[(MMA)-*co*-(BA)-*co*-(MAA)] formulation provided by AkzoNobel for the purpose of it being used as a framework for soft-soft nanocomposite latexes is given in Table 4.2. The polymerisation of this formulation was performed as described in Chapter 3.2.1, and produced a latex with a low (<0.1 wt%) level of coagulum. Analysis of the reaction kinetics revealed that the reaction progressed in a controlled manner, characteristics of which can be seen from the four plots in Figures 4.3 – 4.6.

Figure 4.3 is a plot of both overall and instantaneous monomer conversion versus time. The overall conversion, when compared to the monomer feed profile, can be roughly used to confirm how controlled the polymerisation has been. The instantaneous conversions gained from this plot can be used to determine how ‘monomer starved’ the semi-batch polymerisation is, as if a very high (> 90%) instantaneous conversion is gained this represents monomer being consumed as soon as it diffuses into the polymer particles. High instantaneous monomer conversion is a key characteristic of semi-batch emulsion polymerisations¹¹. This instantaneous conversion will drop drastically when a system that is extremely monomer starved (e.g. at the end of a seed-growth phase) is flooded with monomer at the beginning of another growth stage. Such an effect can be seen in Figure 4.3 at approximately 15 minutes, when the monomer feed was begun after the seed-growth stage had been completed.

Table 4.2 Original poly[(MMA)-*co*-(BA)-*co*-(MAA)] latex formulation provided by AkzoNobel

Acrylic Copolymer Emulsion			
Aqueous Charge	%	%n.v.	X16 (g)
Demin Water	43.492	0	695.87
Rhodafac RK500A	0.420	75	6.72
Sodium Phosphate Dibasic	0.111	100	1.78
Load aq charge, N₂ blanket, RTT 75 °C			
Seed Monomer			
Methyl Methacrylate	1.228	100	19.65
Butyl Acrylate	0.613	100	9.81
Add seed monomer, hold 10 minutes			
Initiator Charge			
Demin Water	1.280	0	20.48
Ammonium Persulphate	0.155	100	2.48
Add seed initiator, allow to exotherm			
Monomer Feed			
Methyl Methacrylate	31.571	100	505.14
Butyl Acrylate	15.812	100	252.99
Methacrylic Acid	0.100	100	1.60
Surfactant Feed			
Demin Water	2.962	0	47.39
Rhodafac RK500A	0.987	75	15.79
Commence concurrent monomer and surfactant feeds over 3 hours			
Allow temperature to stabilise at 74-75 °C			
Reductant Mop-up			
Demin Water	0.536	0	8.58
Bruggolite E.01 (SFS)	0.024	100	0.38
Add ½ reductant mop-up, hold 10 minutes			
Oxidant Mop-up			
Demin Water	0.268	0	4.29
t-BHP (70%)	0.021	70	0.34
Add oxidant mop-up, hold 10 minutes			
Add remaining reductant mop-up, hold 10 minutes			
RTT 38 °C			
pH Adjustment			
Sodium Hydroxide	0.420	0	6.72
TOTAL	100.000		1600.00

Feed Rates		
Monomer	3.30	g/min
Surfactant	0.27	g/min

Composition	
Seed	
MMA	66.7%
BA	33.3%
Feed	
MMA	66.5%
BA	33.3%
MAA	0.2%
Tg (°C)	
seed	30.1
feed	30.2

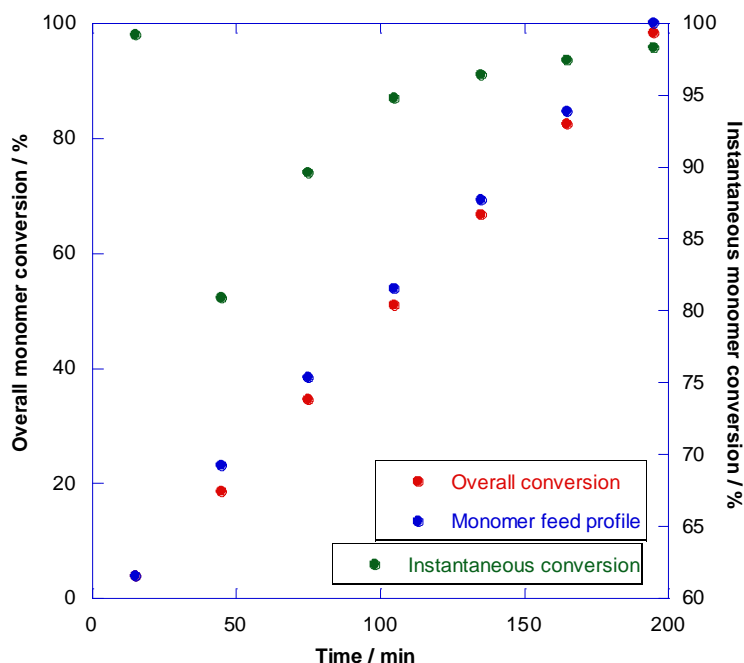


Figure 4.3 Plot of conversion against time for a preparation of the latex formulation given in Table 4.2

The plot shown in Figure 4.4 shows the level of agreement between the theoretically predicted and the experimentally observed z-average particle diameters during the progress of the polymerisation. The theoretical particle diameter is calculated using the expression given in Equation 4.1, and depends upon the final diameter of the seed particles used as a basis for further growth and the instantaneous monomer conversion at the specific point of calculation.

Theoretical particle diameter

(4.1)

$$= (d_z)_{\text{seed}} \times \left(\frac{\text{Mass of monomer added before sample} \times \left(\frac{\% \text{ Instantaneous conversion}}{100} \right)}{\text{Total mass of monomer}} \right)^{\frac{1}{3}}$$

Good agreement between the theoretical and experimentally observed particle diameters indicates that the polymerisation is well controlled and is proceeding as expected.

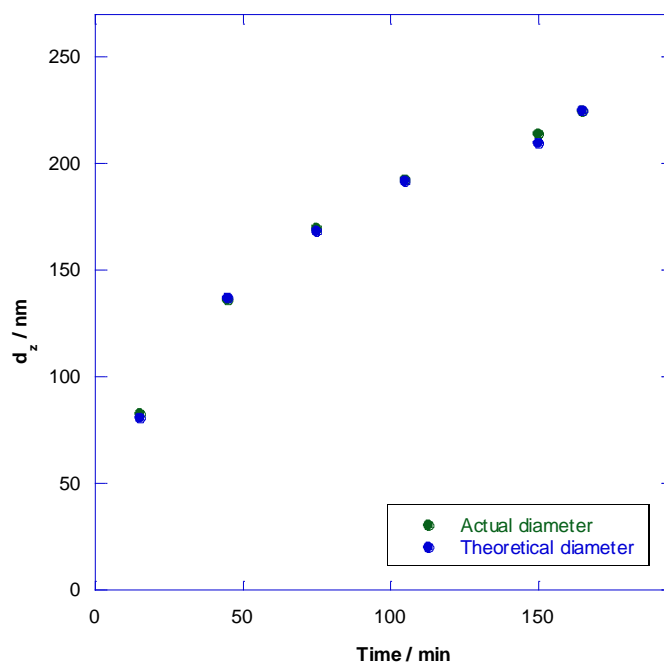


Figure 4.4 Plot of theoretical and actual particle diameter against time for the latex formulation given in Table 4.2

Figure 4.5 shows a plot of the z-average particle diameter³ (d_z^3) and the number of particles present in the reaction vessel against time. A rapid increase in the number of particles is expected during the very initial seed-growth stage of the preparation as initiator radical groups diffuse into monomer-swollen micelles and initiate polymerisation. However, for a controlled preparation after this initial formation of particles their number is expected to stay approximately constant throughout the remainder of the reaction. If an increase in the number of particles present occurs, this is an indication of secondary nucleation of particles by another initiating species. Conversely, if the number of particles in the reaction vessel appears to decrease, this is a sign that the particles are not colloidally stable and that coagulation is occurring, as attractive forces predominate and particles ‘stick’ together.

The average particle diameter³ is an indication of how the particle volume is changing during the course of the preparation. If d_z^3 grows linearly with time, it is showing that the particle volume is growing consistently as the reaction proceeds.

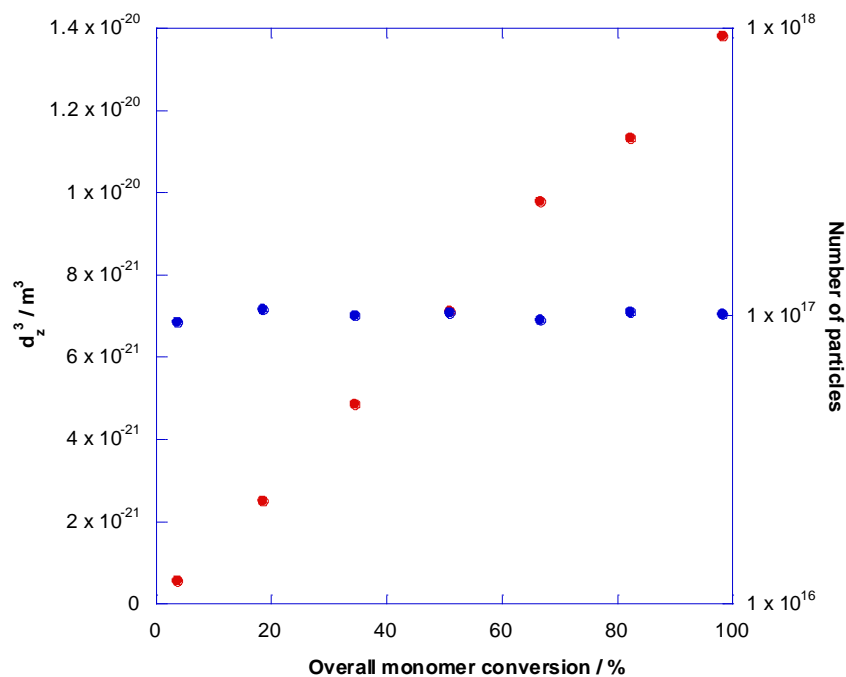


Figure 4.5 Plot of d_z^3 (average particle diameter³, red points) and total number of particles (blue points) against conversion for a preparation of the latex formulation given in Table 4.2

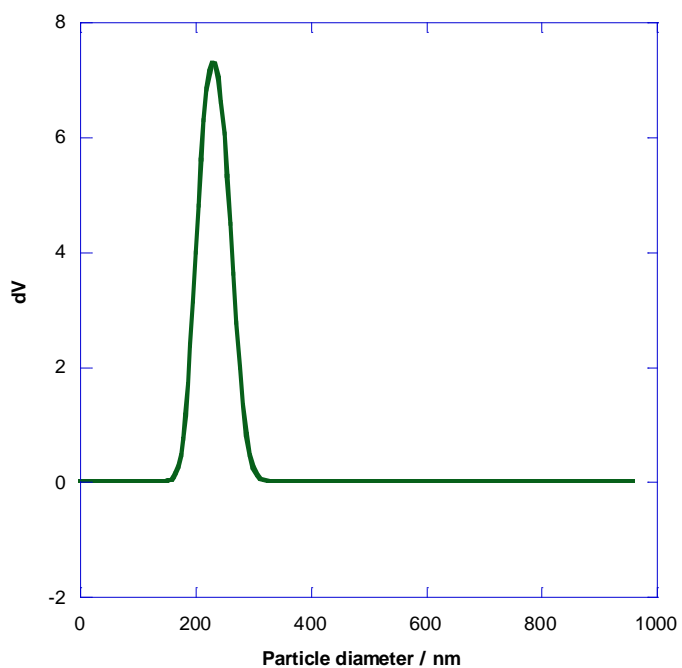


Figure 4.6 Particle size distribution for the latex formulation given in Table 4.2

The final characterisation plot that is commonly used to analyse emulsion preparations is that of particle size distribution, which can be seen in Figure 4.6. This measurement is obtained by PSDA (see Chapter 3.4.1.3), and determines the spread of particle diameters present in a sample taken from a latex preparation. If controlled particle nucleation and

growth is occurring, a narrow, unimodal peak will occur which represents a tight distribution of particle diameters. This parameter is especially useful for monitoring the growth of structured particle phases by sequential semi-batch emulsion polymerisation, as if the phases are growing from existing particles a complete shift of the peak to larger particle diameters will be seen. If secondary nucleation is occurring, causing the new phase to grow as an independent particle, a lower particle diameter peak will occur, causing the particle size distribution of the latex to become bimodal. Similarly, if significant levels of secondary nucleation or coagulation are occurring in an unstructured latex preparation, peaks at lower or higher particle diameter, respectively, will result.

As can be seen from the four plots shown in Figures 4.3 - 4.6 above, the formulation produced a latex with the required particle size and solids content in a controlled manner. Hence, it was deemed to be a good framework for core-shell particle synthesis, and all future latex preparations discussed herein.

4.3.2 Initial changes to formulation to fit the project brief

As discussed in Chapter 4.3.1, the formulation provided by AkzoNobel produced a latex which showed controlled particle growth, no secondary nucleation or coagulation, and high instantaneous monomer conversion.

This section of work investigates the effect of making changes to this formulation to fit the project brief. The most significant change made was to split the monomer feed into two portions, in order to form both core and shell polymer phases. A 15 minute 'mop-up' period with no additional monomer fed into the reaction vessel was left between the two feeds, in order to polymerise all remaining monomer from the core feed before beginning to form the shell phase polymer.

As per the initial research plan, all MMA in the formulation was directly replaced on a weight-for-weight basis by BMA, the homopolymer of which was found in preliminary work to have a T_g of $36 (\pm 2) ^\circ\text{C}$. The polymer used to determine this T_g was synthesised by solution polymerisation in toluene, then isolated by precipitation into methanol, followed by filtration. The resulting rubbery solid polymer was then dried to constant weight at $60 ^\circ\text{C}$ before differential scanning calorimetry (DSC) analysis. Functional monomers such as methacrylic acid, MAA, and/or a crosslinking agent, namely diacetone acrylamide, DAAM, were also incorporated into the monomer feed to form the shell phase of the latex.

Two combinations of core and shell T_g were used in order to deduce the effect of varying the shell phase T_g upon the properties exhibited by the resulting polymer, one with both the core and shell phase $T_g = 0 ^\circ\text{C}$, and another with a core $T_g = 0 ^\circ\text{C}$ and a shell T_g of $-20 ^\circ\text{C}$. The

Fox equation was used to calculate the %wt fractions of each monomer required to form a copolymer with a specific T_g . The project-specific re-modelled equation and a table of monomer compositions to synthesise a copolymer with a specific T_g are shown in Equation 4.2 and Table 4.3, respectively.

$$W_A = \frac{T_{g,\text{copolymer}} - (1 - W_C - W_D)T_{g,B} - W_C T_{g,C} - W_D T_{g,D}}{T_{g,A} - T_{g,B}} \quad (4.2)$$

where W_x = weight fraction of monomer x and $T_{g,x}$ = T_g of homopolymer of monomer x

A = butyl methacrylate (BMA; $T_g = 36$ °C)

B = butyl acrylate (BA; $T_g = -54$ °C)

C = methacrylic acid (MAA; $T_g = 200$ °C)

D = diacetone acrylamide (DAAM; $T_g = 77$ °C)

Table 4.3 Table of monomer feed compositions to form a copolymer with a specified theoretical T_g

Copolymer T_g (°C)	Weight fraction butyl methacrylate	Weight fraction butyl acrylate	Weight fraction methacrylic acid	Weight fraction diacetone acrylamide
0	0.68	0.32	-	-
-20	0.46	0.54	-	-
0	0.64	0.34	0.02	-
-20	0.42	0.56	0.02	-
0	0.62	0.34	0.02	0.02
-20	0.40	0.56	0.02	0.02

As planned, latex preparations with a poly[(BMA)-*co*-(BA)] core phase with $T_g = 0$ °C and shell phases of varying composition were performed. All preparations were conducted according to the procedure described in Chapter 3.2.2, and all showed controlled behaviour similar to that observed for the polymerisation described in Chapter 4.4.1. Characterisation plots for the five latex preparations in this series of work can be found in Appendix (i), and a brief summary of this data is shown in Table 4.4.

Although all five polymerisations carried out in this series of work showed controlled particle growth, high levels of coagulum were produced (between 5-10 wt% when wet), indicating a high level of colloidal instability. This may account for the lower final conversions (ca. 93 %) that were consistently observed, as high monomer conversions of >97 % are a characteristic feature of starved feed semi-batch emulsion polymerisations such as these⁴². Although the particle growth appeared to be controlled from analyses of the preparations, with these high levels of coagulum there is considerable uncertainty about the nature of the particles in the final latex. Hence, the series of work was abandoned before the sixth planned preparation, a latex with a poly[(BMA)-*co*-(BA)] core ($T_g = 0$ °C) and a poly[(BA)-*co*-(BMA)-*co*-(MAA)-*co*-(DAAM)] shell ($T_g = 0$ °C), was conducted in order to address this problem.

Table 4.4 Characterisation data for latexes synthesised to investigate the effect of functional and crosslinking monomers

Shell Composition	Core /Shell T _g / °C	Overall/ Instantaneous conversion ^a / %			Particle diameter ^b /nm			Total particle number ^c / x 10 ¹⁷		
		Seed	Core	Final	Seed	Core	Final	Seed	Core	Final
BA/BMA	0 / -20	3.6/97	67/95	94/94	80	211	239	1.02	1.03	1.00
BA/BMA	0 / 0	3.3/84	67/95	92/92	84	215	240	0.76	0.97	0.90
BA/BMA/ MAA	0 / -20	3.8/97	68/96	93/93	80	210	235	1.04	1.02	1.00
BA/BMA/ MAA	0 / 0	4.0/99	68/96	96/96	85	223	249	0.87	0.85	0.85
BA/BMA/ MAA/DAAM	0 / -20	3.9/96	68/98	96/96	74	195	218	1.28	1.24	1.28

^a Calculated using solids content measurements (see Section 3.4.1.6)

^b z-average particle diameter; obtained using PCS (see Section 3.4.1.2)

^c Calculated using PCS measurements of z-average particle diameter

The route taken to reduce the high levels of coagulum formed during the emulsion preparations was two-fold. Firstly, during the monomer washing process an additional water rinse was added to ensure that no sodium hydroxide remained in the purified monomer. Any sodium hydroxide fed into the emulsion polymerisation as a consequence of the monomer purification process would affect the pH of the system and hence the colloidal stability¹⁹⁰. The second method investigated to reduce the amount of coagulum in the latexes was to introduce an additional non-ionic surfactant to the system.

4.4 Addition of a non-ionic surfactant

Non-ionic surfactants stabilise colloidal particles primarily through steric stabilisation¹⁹¹, and tend not to induce secondary nucleation. They can also be used to control particle morphology, and to impart desirable properties such as mechanical shear resistance and enhanced stability against added electrolytes into the final latex¹¹. The latter effect could be advantageous for these soft-soft nanocomposite systems, as in order for the keto-hydrazide crosslinking mechanism to occur the pH of the latex must be adjusted post-polymerisation to above 8.5.

The non-ionic surfactants used in this section of experimental work were those from the Lutensol TOx series, manufactured by BASF. These were used due to their immediate availability and wide range of poly(ethylene oxide) chain lengths. This family of surfactants are based on an *iso*-C₁₃ alcohol, and have the generic structural formula which is shown in Figure 4.7.

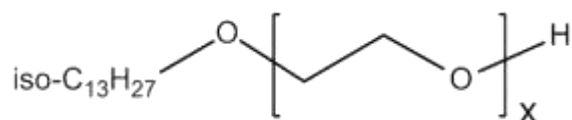


Figure 4.7 Chemical structure of Lutensol TOx non-ionic surfactants, where X indicates the degree of ethoxylation

4.4.1 Effect of surfactant degree of ethoxylation upon coagulum levels

The addition of the non-ionic surfactants was first investigated using Lutensol TOx variants with differering degrees of ethoxylation. The Lutensol TOx was added into the surfactant feeds for the particle growth stages of the polymerisation at 20 wt% relative to the original amount of anionic surfactant (Rhodafac RK-500A). The same amount of anionic surfactant was used as in the standard formulation given in Table 4.2. No non-ionic surfactant was added into the seed stage of the polymerisation, which continued to contain anionic surfactant only, as it was found that coagulum started to form towards the end of the core phase polymerisation and during the formation of the shell phase polymer.

The Lutensol TOx surfactants were evaluated using the emulsion polymerisation formulation designed to give a core-shell latex formed by sequential semi-batch polymerisation, with both core and shell phases consisting of a poly[(BA)-co-(BMA)] copolymer with $T_g = 0^\circ\text{C}$.

The wt% coagulum that resulted from each polymerisation was measured using the process described in Chapter 3.2.3, and the results are shown in Table 4.5. No clear relationship between Lutensol TOx degree of ethoxylation and colloidal stability of the core-shell latex could be identified.

Table 4.5 Coagulum produced by preparations using Lutensol TOx non-ionic surfactants

Non-ionic surfactant	%wt coagulum
Lutensol TO3	2.17
Lutensol TO6	2.26
Lutensol TO7	0.63
Lutensol TO8	2.37
Lutensol TO15	1.25

The data do, however, highlight that Lutensol TO7 gave by far the lowest level of coagulum. Hence, additional work was performed using Lutensol TO7 in order to establish the repeatability of this result and the optimum level of non-ionic surfactant commensurate with low coagulum without having detrimental effects on the film forming properties of the latexes, as non-ionic surfactants are known to plasticise polymer films¹⁹².

4.4.2 Confirmation by ^1H NMR of Lutensol TO7 structure

As for the anionic surfactant present in these emulsion polymerisation formulations, ^1H NMR analysis of Lutensol TO7 was performed to confirm the chemical structure of the surfactant. Using the method described in Chapter 3.4.1.1, a spectrum of Lutensol TO7 in DMSO-d_6 was generated, which can be seen in Figure 4.8. Table 4.6 and Figure 4.9 give the spectral peak assignments and their relation to the structure of the surfactant molecule, respectively. The peak intensities, and hence assignments, were calculated in the same way as for the anionic surfactant shown in Chapter 4.2.

It can be seen from these data that the average degree of ethoxylation from the ^1H NMR analysis of Lutensol TO7 was found to be 8.5, which is much larger than the value of 7 given by the supplier BASF. However, previous analyses of the entire Lutensol TO_x series have found that the degree of ethoxylation quoted by the supplier does not tend to match closely with that found by ^1H NMR¹⁹³.

Although the discrepancy in theoretical and actual structures exists, this is not of crucial importance to this PhD project. Lutensol TO7 has been shown to repeatedly improve colloidal stability and reduce coagulum levels compared to preparations containing no non-ionic surfactant, so it will continue to be used in all formulations discussed in the rest of this thesis.

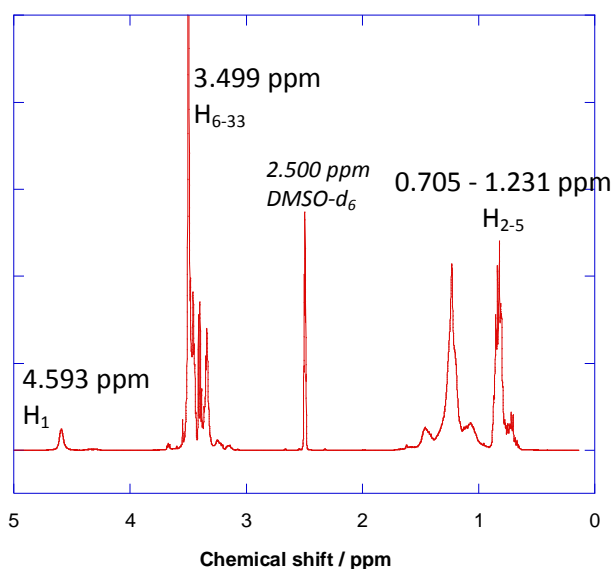


Figure 4.8 ^1H NMR spectrum of Lutensol TO7 in DMSO-d_6 , assignments of the peaks are given in Table 4.6.

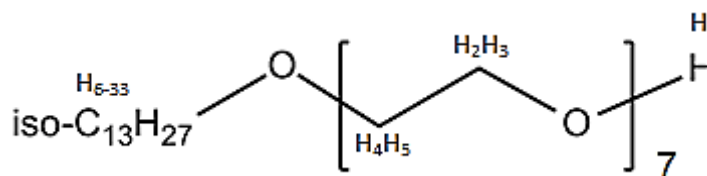


Figure 4.9 Lutensol TO7 (IUPAC name poly(oxy-1,2-ethanediyl) α -isodridecyl- ω -hydroxy ether) with protons labelled to aid NMR spectrum peak analysis

Table 4.6 Summary of the assignments of peaks from the NMR spectrum shown in Figure 4.8 in relation to the structure of the surfactant shown in Figure 4.9

δ_H (ppm)	No. of protons	Assignment
0.705 -1.231	34	H ₂₋₅ – PEG-group
3.499	27	H ₆₋₃₃ – iso-C ₁₃ H ₂₇
4.593	1	H ₁ – ethylene glycol terminal proton

4.4.3 Establishing the optimum level of Lutensol TO7

The polymerisation employing 20 wt% Lutensol TO7 relative to Rhodafac RK-500A in the particle growth stages was repeated, to establish whether the lower level of coagulum shown in Table 4.5 was repeatable. Analysis of the reaction kinetics showed that low levels of coagulum were repeatedly seen; the reaction proceeded in a controlled manner and produced a latex with a narrow, unimodal particle size distribution. Kinetics plots of this data are shown in Figure 4.10.

After repeatable results had been gained when using an additional 20 wt% of Lutensol TO7 relative to Rhodafac RK-500A in the particle growth stages of the polymerisation, a further reaction was performed at 40 wt% Lutensol TO7 relative to Rhodafac RK500A in order to see whether this would result in a further significant reduction in coagulum level.

Using the same formulation except for the higher growth-stage level of Lutensol TO7 it was found that the coagulum level reduced from 0.67 wt% to 0.52 wt% with 40 wt% Lutensol TO7 relative to Rhodafac RK-500A, which was not considered a significant enough reduction to justify the use of the much larger amount of Lutensol TO7, which would be likely to have a detrimental effect upon the properties of films cast from the latexes at a later stage.

Thus, all further work discussed in this thesis was carried out with Lutensol TO7, used at a level of 20 wt% relative to the standard amount of Rhodafac RK-500A.

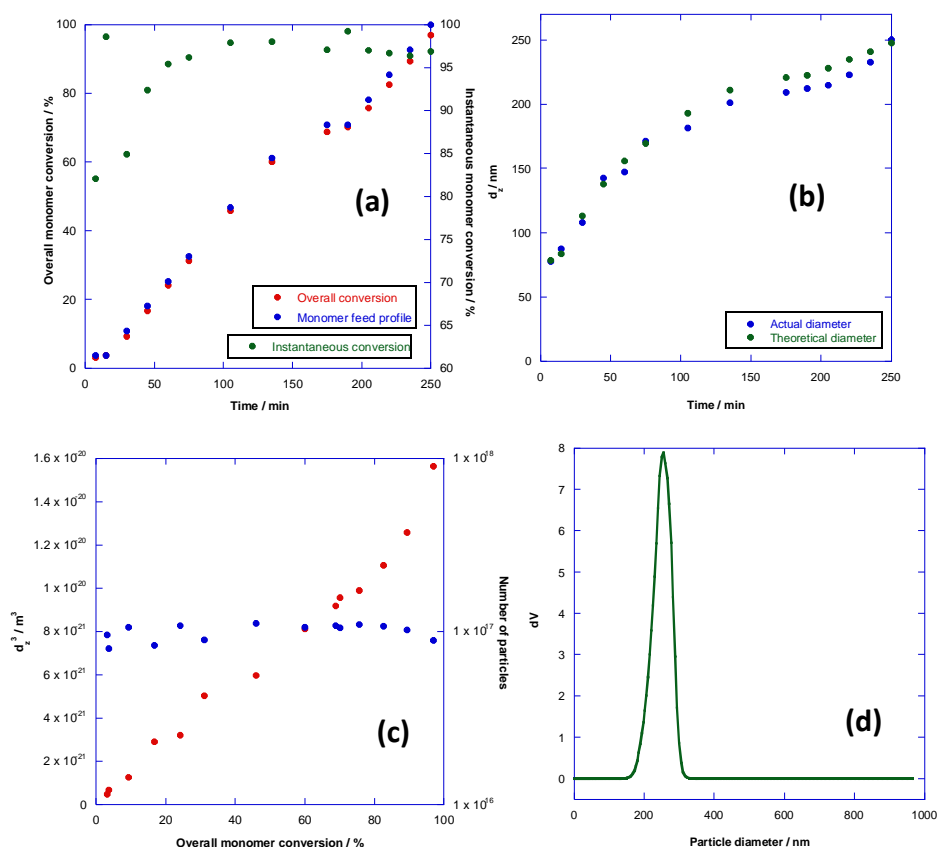


Figure 4.10 Characterisation plots for samples removed from the repeat preparation containing 20 wt% Lutensol TO7 relative to Rhodafac RK-500A – (a) conversion vs time, (b) z-average particle diameter vs time, (c) $(z\text{-average particle diameter})^3$ (red points) and number of particles (blue points) vs conversion and (d) particle size distribution

4.4.4 Establishing the effect of Lutensol TO7 in latexes containing functional monomers

The copolymer compositions used for the work that will be discussed in this section were the same as in Chapter 4.4.2, with the monomer proportions being taken from the Fox equation data in **Error! Reference source not found.** and Table 4.3. However, in order to maximise the efficiency of this section of work only one set of core and shell phase T_g values were used, with both core and shell phase copolymers having $T_g = 0^\circ\text{C}$.

The levels of coagulum for the reactions in this section were significantly lower than for the equivalent reactions without Lutensol TO7, but similar to those for the poly[(BMA)-*co*-(BA)] which contained Lutensol TO7 at the same level, with values of between 0.67 – 0.90 dry wt%. Analysis of the reaction kinetics showed that all reactions proceeded in a controlled manner, as can be seen from the data in Table 4.7. Plots of the data for samples removed during the preparations can be found in Appendix (i).

As the addition of Lutensol TO7 into latex preparations involving these functional monomers did not cause any elevated levels of coagulum or the particle growth to become uncontrolled, the non-ionic surfactant has clearly been shown to be suitable for incorporation into the framework formulation from which all further soft-soft nanocomposite formulations were derived.

Table 4.7 Kinetics data for preparations including Lutensol TO7

Shell Composition	Core /Shell T _g / °C	Coagulum level / wt%	Overall/ Instantaneous conversion ^a / %			Particle diameter ^b / nm			Total particle number ^c / x 10 ¹⁷		
			Seed	Core	Final	Seed	Core	Final	Seed	Core	Final
BA/BMA	0 / 0	0.63	3.7/98	69/97	97/97	87	209	250	0.80	1.05	0.89
BA/BMA/MAA	0 / 0	0.50	4.5/89	69/97	95/95	85	234	263	0.77	0.74	0.73
BA/BMA/MAA/DAAM	0 / 0	0.90	3.2/85	63/89	93/93	87	233	270	0.69	0.72	0.68

^a Calculated using solids content measurements (see Section 3.4.1.6)

^b z-average particle diameter; obtained using PCS (see Section 3.4.1.2)

^c Calculated using PCS measurements of z-average particle diameter

4.5 Adjustments made to formulation to compensate for discrepancies between predicted and observed T_g values

Films of the three latex variants described in Table 4.7 were cast according to the procedure given in Chapter 3.3.2, and analysed by differential scanning calorimetry (DSC) to determine the accuracy of glass transition prediction using the modified Fox equation (see **Error! Reference source not found.** and Table 4.3). As can be seen from the DSC traces in Figure 4.11(a) – (c) and the data in Table 4.8, in all cases the observed T_g was approximately 10 °C below its predicted value.

Table 4.8 DSC data for films from the latex variants discussed in Table 4.7

Core composition	Shell composition	Theoretical core & shell T _g / °C	Average observed T _g / °C
BA/BMA	BA/BMA	0 / 0	-10 (±1)
BA/BMA	BA/BMA/MAA	0 / 0	-11 (±1.5)
BA/BMA	BA/BMA/MAA/DAAM	0 / 0	-11 (± 1)

The discrepancy between theoretical and observed T_g values was approximately 10 °C despite the chemical composition of the shell copolymer. Although the monomer conversions for each polymerisation were found to be relatively high (>98 %), gas chromatography (GC) was used to investigate whether the difference in T_g value was caused by residual unreacted monomer plasticising the film matrix. Two latexes with core and shell phase T_g were synthesised in order to conduct this analysis, and full characterisation plots for both preparations can be found in Appendix (ii). GC was performed on both latexes using the procedure given in Chapter 3.4.1.5, and the results of this testing can be seen in Table 4.9.

As can be seen from the GC data, the levels of residual monomer in the latexes are extremely low. Hence, the lowered T_g values may be due in part to hydroplasticisation of the polymer particles, which is known to have a larger effect for smaller polymer particles such as these¹⁹⁴. Hydroplasticisation is known to be more prevalent in latexes for applications in which the polymers are more likely to be exposed to water for prolonged periods of storage, such as water-borne paints¹⁹⁵. Another possibility is plasticisation by the non-ionic surfactant, Lutensol TO7, that was added into the system to reduce coagulum during particle growth stages of polymerisation because non-ionic surfactants are known to plasticise polymer films⁸³.

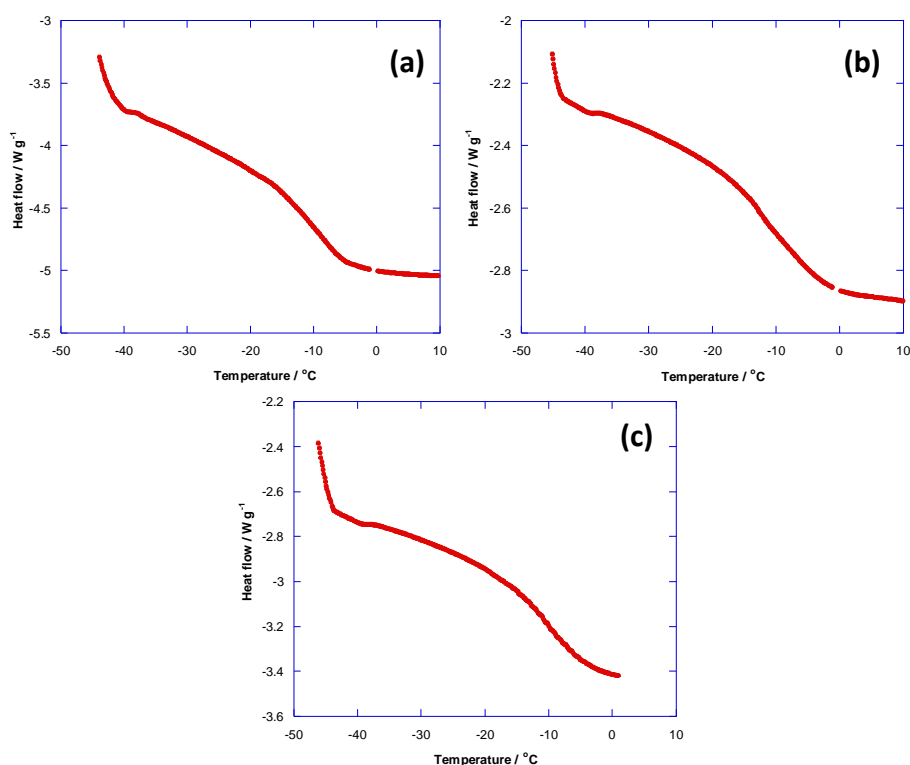


Figure 4.11 DSC traces for (a) poly[(BA)-co-(BMA)] core and shell with theoretical $T_{gS} = 0$ °C, (b) poly[(BA)-co-(BMA)] core and poly[(BA)-co-(BMA)-co-(MAA)] shell with theoretical $T_{gS} = 0$ °C and (c) poly[(BA)-co-(BMA)] core and poly[(BA)-co-(BMA)-co-(MAA)-co-(DAAM)] shell with theoretical $T_{gS} = 0$ °C

Table 4.9 Levels of residual monomer in soft-soft nanocomposite latexes analysed by GC

Core composition	Shell composition	Core/shell T_g / °C	Residual wt% BA	Residual wt% BMA
BA/BMA	BA/BMA	5 / 5	0.013	0.030
BA/BMA	BA/BMA/DAAM	5 / 5	0.035	0.033

As the effects of plasticisation by water or surfactant are not taken into account by the Fox equation (see Equation 4.2), a series of uniform, unstructured poly[(BA)-*co*-(BMA)] latexes with T_g values calculated from Equation 4.2 were synthesised to investigate the effect of the weight fraction of BMA upon the observed T_g values of these simple copolymer latexes. Full characterisation plots for these preparations can be found in Appendix (i). Films were cast from these latexes as per the procedure in Chapter 3.3.2, then analysed by DSC as described in Chapter 3.4.3.2

As can be seen from the data in Table 4.10 and Figure 4.12 a clear trend in this data can be observed. Due to the high R-value (>0.99), the experimentally obtained linear relationship observed presents a means to accurately predict the T_g of these copolymers at any given weight fraction of BMA. Equation 4.3 gives the expression that can be used to calculate the wt% of BMA and BA required to produce a poly[(BA)-*co*-(BMA)] latex with an accurately defined T_g , which was derived from the linear trend shown in Figure 4.12.

Table 4.10 Table showing difference between theoretical and actual T_g values for poly[(BA)-*co*-(BMA)] latexes

Weight fraction of BMA	Theoretical T_g / °C	Average actual T_g from DSC / °C	$\Delta T_{g,(theoretical:actual)}$ / °C
0.87	20	13 (± 1)	-7
0.78	10	6 (± 1.5)	-4
0.95	30	24 (± 1)	-6
1.00	36	31 (± 1.5)	-5

In order to deduce the robustness and accuracy of the relationship detailed above, the copolymer composition for an unstructured poly[(BA)-*co*-(BMA)] latex with a T_g of 0 °C was calculated using Equation 4.3 and the latex synthesised. As per the unstructured poly[(BA)-*co*-(BMA)] latexes discussed in Table 4.10 a film was cast from this latex and analysed by DSC, whereby it was found to have a T_g of -2 °C as can be seen from Figure 4.13.

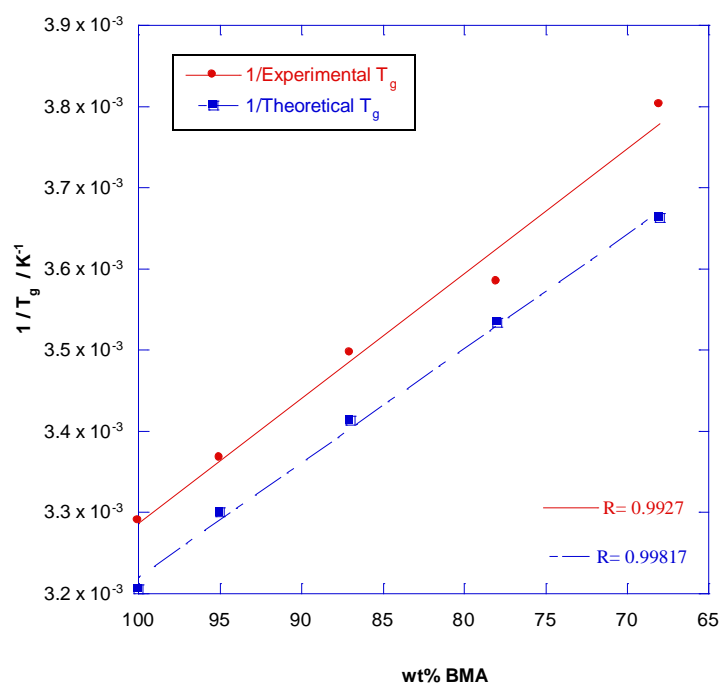


Figure 4.12 Plot showing the linear relationships between theoretical and actual T_g values for unstructured poly[(BA)-co-(BMA)] latexes

$$(a) \text{ wt}\% \text{ BMA} = \frac{\left(\left(\frac{1}{T_g}\right) - 4.8 \times 10^{-3}\right)}{-1.5 \times 10^{-5}} \quad (4.3)$$

$$(b) \text{ wt}\% \text{ BA} = 1 - (\text{wt}\% \text{ BMA})$$

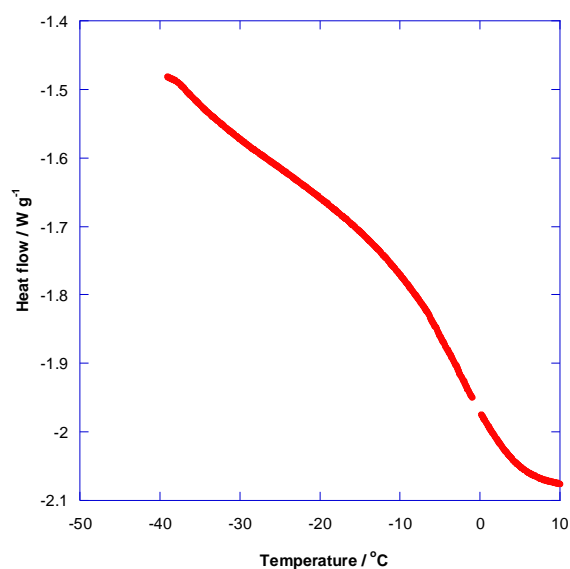


Figure 4.13 DSC trace for poly[(BA)-co-(BMA)] copolymer with theoretical $T_g = 0$ °C as predicted from Error! Reference source not found.

As the discrepancy between theoretical and observed T_g that is observed from Figure 4.13 is within the range of errors typically associated with DSC measurements (± 2 °C) and is a

great improvement upon the discrepancy previously observed when predicting T_g using the Fox equation, the composition of all further poly[(BA)-*co*-(BMA)] copolymers discussed from this point onwards have been predicted using the mathematical equation given in Equation 4.3. This will comprise all soft-soft nanocomposite core phases discussed in all of the remaining chapters of this thesis.

However, the T_g of shell phase copolymers containing additional functional monomers such as DAAM and MAA will continue to be calculated using the Fox equation. This is because of the requirement from the soft-soft nanocomposite design theory for this polymer phase to form a continuous elastomer phase in a film. As elastomeric behaviour only occurs below the polymer T_g , this shell phase polymer will benefit from a lower than predicted T_g due to its proximity to application temperature.

4.6 Conclusions

The results presented in Chapter 4 prove that a robust framework formulation for the synthesis of soft-soft nanocomposite coating materials has been established. The formulation repeatedly gives controlled particle nucleation and growth, high instantaneous conversions and narrow particle size distributions. A formulation for a poly[(MAA)-*co*-(BA)-*co*-(MAA)] latex was provided by AkzoNobel and, upon confirmation of its suitability for purpose, was adapted to form structured core-shell particles. The properties of the particles formed was found to be unaffected by the inclusion of different (meth)acrylate monomers and DAAM.

Initially, problems were encountered with high levels of coagulum, but these were overcome through the addition of a non-ionic surfactant, Lutensol TO7. This additional surfactant was included in the particle growth stages of the polymerisation only, at a level of 20 wt% to the amount of anionic surfactant, Rhodafac RK-500A. Coagulum levels were reduced from ~10 wt% to <1 wt% due to the additional colloidal stability introduced by the non-ionic surfactant.

A secondary problem concerned the lack of accuracy initially encountered with regards to T_g prediction. Analysis of soft-soft nanocomposite films with copolymers of varying monomer compositions found that a discrepancy of ~10 °C was consistently observed compared to the predicted value given by the Fox equation. Plasticisation by unreacted residual monomer was ruled out by GC studies which showed extremely low (< 0.05 wt%) levels of both BA and BMA. Hence, the most likely reason that a discrepancy was observed between predicted and experimentally observed T_g values was thought to be plasticisation

by the non-ionic surfactant added during the preparation of the latexes. A series of preparations to form unstructured poly[(BA)-*co*-(BMA)] latexes with differing theoretical T_g values were carried out, and comparison of the experimentally determined T_g of these systems with the wt% of BMA incorporated into each latex showed a linear trend and hence a method with which to predict the T_g of poly[(BA)-*co*-(BMA)] copolymers. A test conducted to confirm the accuracy of this new T_g prediction equation found that a poly[(BA)-*co*-(BMA)] latex with a predicted T_g of 0 °C had an experimentally determined T_g of -2 °C, which was within the standard error associated with DSC measurements (± 2 °C). Hence, the expression shown in Equation 4.3 will be used to calculate the T_g of all further poly[(BA)-*co*-(BMA)] latexes discussed in further chapters of this thesis.

5 Establishing the effect of keto-hydrazide crosslinking

5.1 Introduction

One of the key principles of the soft-soft nanocomposite design theory is the formation of a lightly crosslinked, elastomeric percolating phase. This requires the polymer to be in the rubbery state with T_g below the application temperature¹⁷. As discussed in Section 2.5.1.1, a number of different crosslinking chemistries have previously been used to achieve this light crosslinking. Soft-soft nanocomposite PSAs⁴⁻⁶ incorporate keto-hydrazide crosslinking, whereas the nitrile rubber-mimics⁷⁻⁹ successfully utilised ionic crosslinking, which will be discussed further in Chapter 8.

Keto-hydrazide crosslinking refers to the chemical reaction of a pendant carbonyl group on a dispersed polymer backbone with a diamine species residing in the aqueous phase⁹⁵, and is commonly used in water-based film-forming latexes to enhance mechanical properties, chemical stability and the solvent resistance of a film^{92, 96}. The crosslinking reaction occurs rapidly after evaporation and particle coalescence during film formation, as it is inhibited by the presence of water. The two moieties also mainly exist in separate domains when in the wet state, with DAAM in the polymer particles and ADH in the aqueous phase. Although some interaction between the two species in the wet state is known to happen due to interfacial interaction and the fact that the keto-hydrazide reaction is an equilibrium process, when the film has coalesced the two moieties are in direct contact, which leads to the acceleration of the crosslinking reaction. The most commonly used species for this crosslinking reaction are diacetone acrylamide (DAAM) repeat units that provide the pendant carbonyl groups, and adipic acid dihydrazide (ADH) as the diamine species. DAAM was first reported as a reactive monomer in 1965, and is very commonly used due to its high thermal stability, long shelf life and high reactivity compared to other n-alkyl acrylamide species¹⁰⁵. ADH is most commonly used as the diamine species for keto-hydrazide crosslinking due to its high water solubility¹⁰⁶ and low toxicity¹⁹⁶. The structures of these two molecules are shown in Figure 5.1.

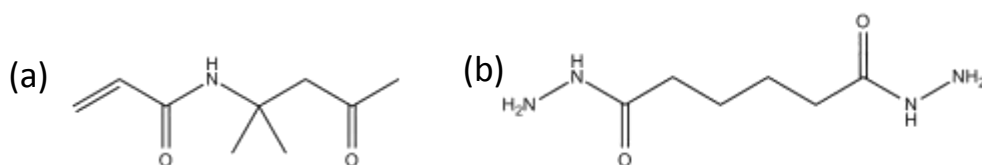


Figure 5.1 Chemical structures of (a) DAAM and (b) ADH

It was a matter of debate for some time whether the product of this crosslinking reaction was an imine or an enamine¹⁰⁷, the structures of both of which are shown in Figure

5.2, but was proved by a thorough study into the mechanism of keto-hydrazone crosslinking conducted by Kessel *et al.* in 2008 to be an imine, through IR absorption studies of a reaction between 2-heptanone and octanoic hydrazide, which represented the carbonyl and hydrazide functionalities, respectively. The FTIR spectra obtained showed the emergence of a characteristic FTIR absorption at $\sim 1670\text{ cm}^{-1}$ as the crosslinking reaction proceeded, which corresponds to a C=N functionality⁹⁵. According to IUPAC classification⁹⁸, the functionality that results from the keto-hydrazone reaction should be classified as a hydrazone, due to the –NHR– substituent adjacent to the C=N imine bond. Hydrazones are much more stable than imines, due to the stabilization of the C=N π -bond by the electronegative secondary amine at the α -position¹¹². However, due to the new bond that is formed by the keto-hydrazone reaction being the C=N functionality, it will be referred to as an imine bond in the rest of this thesis.

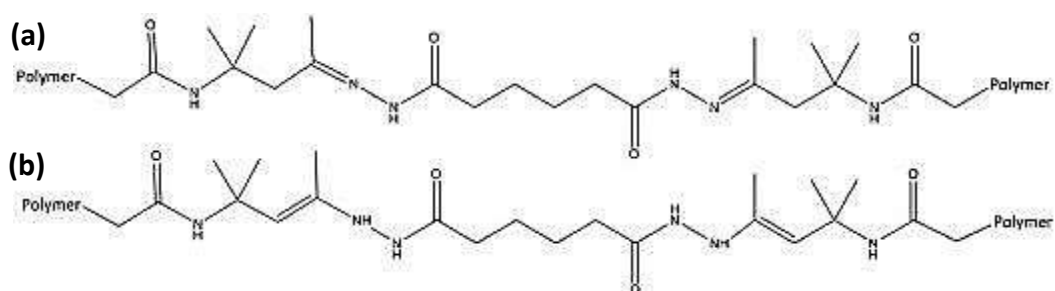


Figure 5.2 Structures of possible (a) imine/hydrazone and (b) enamine products from the DAAM-ADH crosslinking reaction

The mechanism of this DAAM-ADH keto-hydrazone crosslinking reaction was shown in Section 2.4.4.1. The occurrence of this crosslinking after film coalescence has occurred is what makes it attractive as a method of building crosslinking into water-based coating systems, as it will not retard film formation, especially interparticle chain diffusion, leading to coherent, crosslinked films.

The effect of keto-hydrazone crosslinking upon the mechanical properties of latex films was reported by Esser *et al.* in 1999¹⁰⁷. This work was conducted using different carbonyl and diamine moieties than have been discussed thus far in this section, although the reaction mechanism is very similar to that shown in Section 2.4.4.1 and hence the overall principles of the work are still relevant. Acetoacetoxyethyl methacrylate (AAEM) was used as the carbonyl-containing species polymerised into the dispersed polymer backbone, with Jeffamine™ EDR-148, which is a commercially available symmetrical diamine manufactured by Huntsman¹⁹⁷, added into the aqueous phase post-polymerisation. A poly[(MMA)-*co*-(BA)-*co*-(AAEM)-*co*-(MAA)] latex with a Fox equation-predicted T_g of $-13\text{ }^\circ\text{C}$ was synthesised in

order to remove the need for coalescing solvents, with 10 wt% AAEM incorporated into the polymer backbone. For the purpose of tensile testing, hexamethylenediamine (HMDA) was then added at a 2:1 molar stoichiometric ratio to the amount of AAEM in the latex.

It was found that the inclusion of this keto-hydrazide crosslinking into acrylic films led to only a small increase in Young's modulus, but had a dramatic effect upon the high strain properties such as extension to break and the yield stress. The stress-strain plots reported for these systems can be seen in Figure 5.3, and the differences in stress-strain behaviour between the two systems are immediately obvious. The crosslinked film (Figure 5.3(b)) has a much higher yield stress and a far lower extension to break ratio than the uncrosslinked equivalent (Figure 5.3(a)).

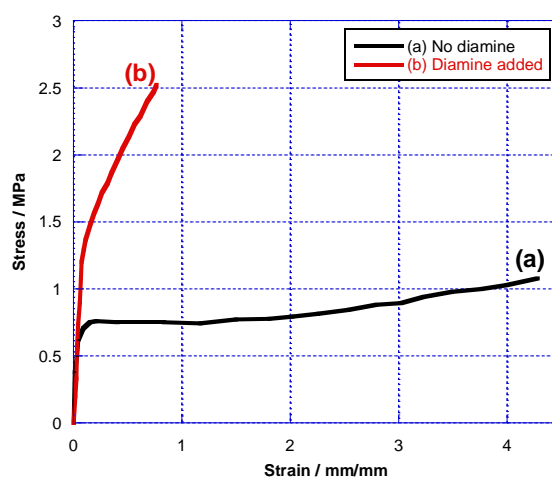


Figure 5.3 Stress-strain profiles for poly[(MMA)-co-(BA)-co-(AAEM)-co-(MAA)] latex films with (a) no diamine and (b) HMDA incorporated at a 2:1 AAEM:HMDA molar stoichiometric ratio ¹⁰⁷

The stress-strain profiles for soft-soft nanocomposite PSAs incorporating keto-hydrazide crosslinking, with conventional DAAM and ADH crosslinking reagents, show a similarly dramatic effect. As can be seen from Figures 5.4 and 5.5, an increasing proportion of crosslinked DAAM units corresponds with an increase in the strain hardening and yield stress and a decrease in extension to break ratio of the films.

This high level of mechanical tuneability that can be accessed very easily by slightly changing the level of crosslinking present in a soft-soft nanocomposite film means that these materials, and the design theory from which they originate, represent a powerful way to access a variety of mechanical behaviour. However, thus far it has only been confirmed that this set of principles holds for systems with T_g values far lower than their intended application temperature, which is essential in order for a lightly crosslinked network to behave as an elastomer. Applying the theory to systems with T_g closer to ambient temperature is a challenge, as this elastomeric behaviour may not be observed.

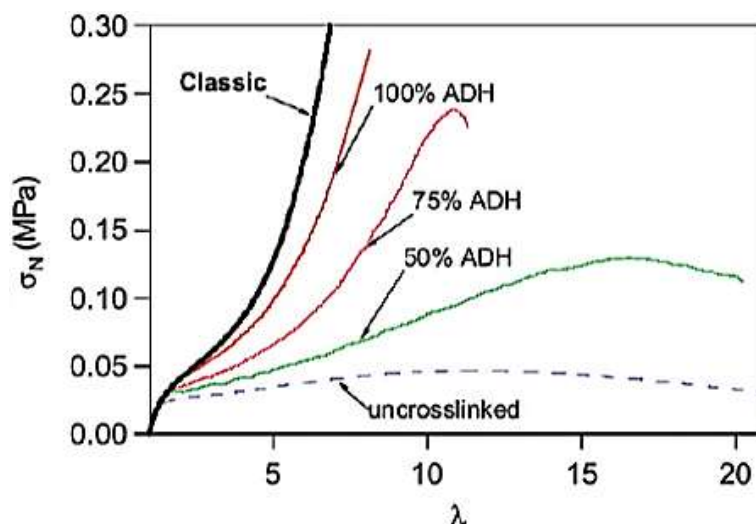


Figure 5.4 Nominal stress (σ_N) vs extension ratio (λ) profiles for soft-soft nanocomposite PSAs with a poly[(2-EHA)-*co*-(EA)-*co*-(BA)-*co*-Sty-*co*-(AA)] core phase and a poly[(2-EHA)-*co*-(EA)-*co*-(BA)-*co*-Sty-*co*-(DAAM)-*co*-(MAA)] shell. The percentage labels for each line identify the stoichiometric percentage of DAAM units that are crosslinked with ADH, and 'Classic' refers to the performance of a commercial water-borne PSA with no internal particle morphology and crosslinking throughout the particle⁵

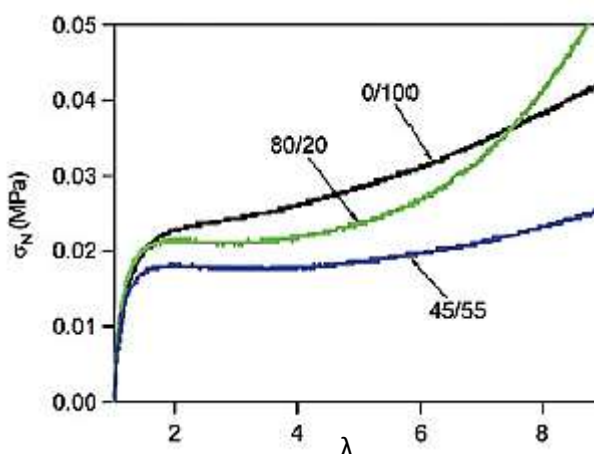


Figure 5.5 Tensile behaviour of soft-soft nanocomposites ($T_g = -38\text{ }^\circ\text{C}$) with varying core-shell ratios and therefore degrees of crosslinking (ratio = non-crosslinked/crosslinked)⁵

The film structure of systems containing keto-hydrazide crosslinking has also been investigated previously using AFM. Kessel *et al.* used the technique to study the film formation of monophasic, unstructured latexes which incorporated DAAM-ADH crosslinking⁹⁵. As can be seen from Figure 5.6, the inclusion of crosslinking into the film matrix retards particle interdiffusion, leading to the retention of morphology and an increased height profile, compared to uncrosslinked films which form a cohesive, homogenous structure. The retention of core-shell morphology in the film is a key part of the soft-soft nanocomposite design theory, so it was hoped that this observation would hold for nanostructured film systems.

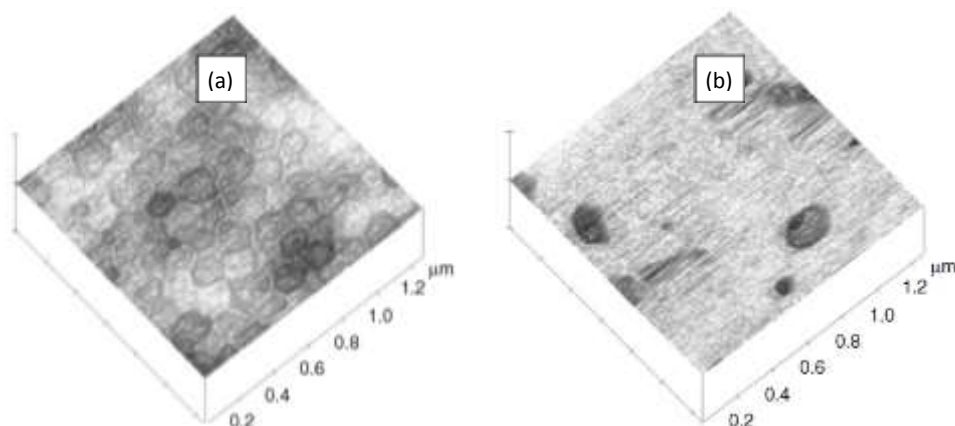


Figure 5.6 AFM height images of low T_g poly[(BA)-*co*-(MAA)-*co*-(MA)-*co*-(DAAM)] copolymers with **(a)** ADH added and **(b)** no ADH⁹⁵

During these film formation AFM studies of keto-hydrazide crosslinked films, a layer of exuded surfactant was found on the surface of uncrosslinked films, but was not present for the crosslinked equivalent. It was deduced from this observation that keto-hydrazide crosslinking prevents the exudation of surfactant from a film. This was thought to be due to particle deformation being restricted due to the crosslinking reaction competing with interparticle chain diffusion, and therefore the surfactant remained ‘trapped’ inside the film matrix. Whether this is observed for soft-soft nanocomposite films will be investigated as they contain only small proportions of crosslinked material, typically less than 30 wt% of the fully-formed film, compared to the uniformly crosslinked particles shown in Figure 5.6.

Previous studies of the effect of keto-hydrazide crosslinking on film properties have proved that it is an effective way to build both mechanical strength¹⁰⁷ and retained morphology⁹⁵ into acrylic films. Hence, it is the chemistry that will be utilised for the application of the soft-soft nanocomposite design theory to systems with T_g closer to ambient temperature.

The work discussed in this chapter will focus upon the effect that incorporating DAAM-ADH crosslinking into soft-soft nanocomposite systems has, more specifically the effect upon film properties. This will be investigated using mechanical tensile testing, AFM and DSC. The chapter will conclude by discussing some application-specific testing that directly relates to the intended use of these systems as binders for decorative coatings.

5.2 Synthesis of soft-soft nanocomposite latexes containing latent crosslinking functionalities

In order to deduce the effect that (i) the addition of DAAM into the shell of a non-crosslinked film and (ii) subsequent keto-hydrazide crosslinking would have on the mechanical properties of a soft-soft nanocomposite film, two latexes with theoretical core and shell T_g values of 5 °C were synthesised. One latex comprised poly[(BA)-*co*-(BMA)] core and shell phases, both with theoretical T_g values of 5 °C which was predicted using the expression given in Equation 4.3. For the other preparation a latent crosslinker, DAAM, was copolymerised into the shell phase polymer, leading to a particle with a poly[(BA)-*co*-(BMA)] core and a poly[(BA)-*co*-(BMA)-*co*-(DAAM)] shell, where the DAAM crosslinking functionality was added at a level of 2 wt% of the shell phase composition. Similarly, both core and shell phase of this second preparation have theoretical T_g s of 5 °C, but whereas the core phase T_g was predicted using Equation 4.3 the shell phase polymer T_g was predicted using the Fox equation shown in Equation 4.2, with the justification for this decision discussed in Section 4.5. The bridging molecule that provides the second component for the post-coalescence crosslinking reaction, adipic acid dihydrazide (ADH), was added to a portion of the second, DAAM-containing latex to give a total of three variants.

As a preliminary investigation into applying this principle to coating materials with T_g closer to ambient temperature, the mass ratio of crosslinkable shell to non-crosslinked core polymer was 30:70. Table 5.1 shows the compositions of the three latex systems tested and discussed in this section, and Table 5.2 gives a summary of the kinetics data for the two polymerisations. Full characterisation plots for the two latex preparations can be found in Appendix (ii).

Table 5.1 Latex compositions and theoretical T_g values discussed in Section 5.2

Core theoretical T_g / °C	Core copolymer composition	Shell theoretical T_g / °C	Shell copolymer composition	ADH post-added
5	80 wt% BMA 20 wt% BA	5	80 wt% BMA 20 wt% BA	No
5	80 wt% BMA 20 wt% BA	5	77 wt% BMA 21 wt% BA 2 wt% DAAM	No Yes

Table 5.2 Kinetics data for the latexes discussed in Section 5.2

Shell copolymer composition	Core & Shell $T_g / ^\circ\text{C}$	Overall/ Instantaneous conversion ^a / %			Particle diameter ^b /nm			Total particle number ^c / $\times 10^{16}$		
		Seed	Core	Final	Seed	Core	Final	Seed	Core	Final
poly[(BA)-co-(BMA)]	5 / 5	2.4/58	69/99	99/99	94	281	321	1.93	4.11	4.00
poly[(BA)-co-(BMA)-co-(DAAM)]	5 / 5	3.7/98	68/97	97/97	98	259	296	5.64	3.22	3.46

^a Calculated using solids content measurements (see Section 3.4.1.6)

^b z-average particle diameter; obtained using PCS (see Section 3.4.1.2)

^c Calculated using PCS measurements of z-average particle diameter

The data in Table 5.2 and the characterisation plots in Appendix (ii) show that both polymerisations were controlled, although for the DAAM-containing latex a slight decrease in particle number can be seen during the core growth phase, indicating a small degree of coagulation which is confirmed in the overall conversion which is slightly lower than expected (97%). However, this is not significant and will not affect the properties of the latex to a great extent. Secondary nucleation is seen to a greater extent during the preparation of the latex with a poly[(BA)-co-(BMA)] shell phase, as the particle number increases during the core growth period. However as the instantaneous conversion was very low at the end of the seed phase (58%), it is possible that particle nucleation continued to occur during the early stages of core phase growth.

ADH was added giving a molar stoichiometric ratio of 1:2 with respect to DAAM as a 10 wt% aqueous solution to 500g of the DAAM-containing latex detailed in Table 5.2. The full procedure for the addition of ADH is given in Section 3.3.1. This stoichiometry was chosen as it represents a theoretical ‘maximum’ number of crosslinks that can be formed with the DAAM units that are present in the latex.

Films of 200 μm wet thickness were drawn down on glass panels and dried at ambient temperature for 24 hours, before portions of the film were cut out and tested using DSC, as detailed in Section 3.4.3.2. Table 5.3 gives the average T_g values observed for each of the three latex systems. These data show that there is no significant difference that can be determined between the three soft-soft nanocomposite variants tested, because the differences there are lie within experimental error. It should also be noticed that the observed T_g values are slightly lower than predicted from the experimental curve that was

discussed in Chapter 4, but are again within the experimental error associated with this method of T_g prediction (± 2 °C).

Table 5.3 Actual T_g values for soft-soft nanocomposites discussed in Section 5.2

Shell copolymer composition	Average T_g^* / °C
poly[(BA)- <i>co</i> -(BMA)]	3 (± 0.5 °C)
poly[(BA)- <i>co</i> -(BMA)- <i>co</i> -(DAAM)]	3 (± 0.5 °C)
Poly[(BA)- <i>co</i> -(BMA)- <i>co</i> -(DAAM)] +ADH	4 (± 1.5 °C)

*Standard deviations are given in the parentheses

5.3 Effect of crosslinking upon mechanical properties

Films of the three soft-soft nanocomposite systems discussed in Section 5.2 were cast according to the procedure given in Section 3.3.2, and tensile tested using the method described in Section 3.4.2.1. Both the stress-strain curves and expansions of the low-strain regions for each of the three soft-soft nanocomposite systems detailed in Table 5.1 can be seen in Figures 5.7 - 5.9. Figure 5.10 shows a comparison of the tensile behaviour for the three systems, and Table 5.4 gives a summary of the mechanical property data, including Young's modulus, for all three variants. Young's modulus, stress at 4% strain and extension to break were all calculated as per the methods given in Section 3.4.2.1.

It should be noted that for all low-strain region expansions that will be presented in this thesis that the initial stress values will often be higher than zero. This is due to inaccuracies that stem from the use of jaw displacement as a measurement of strain rather than a strain gauge, which due to the soft nature of the films it was not possible to use. Although not a commonly used measure of mechanical performance, stress at 4% strain was included in order to provide additional analysis in order to compensate for the inaccuracies due to jaw separation and the use of a polynomial fit, as at these strains the error in jaw separation is much smaller and therefore the value of stress at this strain is a more reliable indication of the low strain mechanical behaviour.

During the latter stages of data analysis for this thesis, it was suggested that in order to compensate for the effects of these inaccuracies whilst calculating the modulus the very initial data points (from strain values of 0 – 0.01) should be disregarded, and a linear fit used for strain values of 0.01-0.04. The results of this are shown in Table 5.4, and are compared to

those Young's modulus values obtained using the polynomial fit method detailed in Section 3.4.2.1.

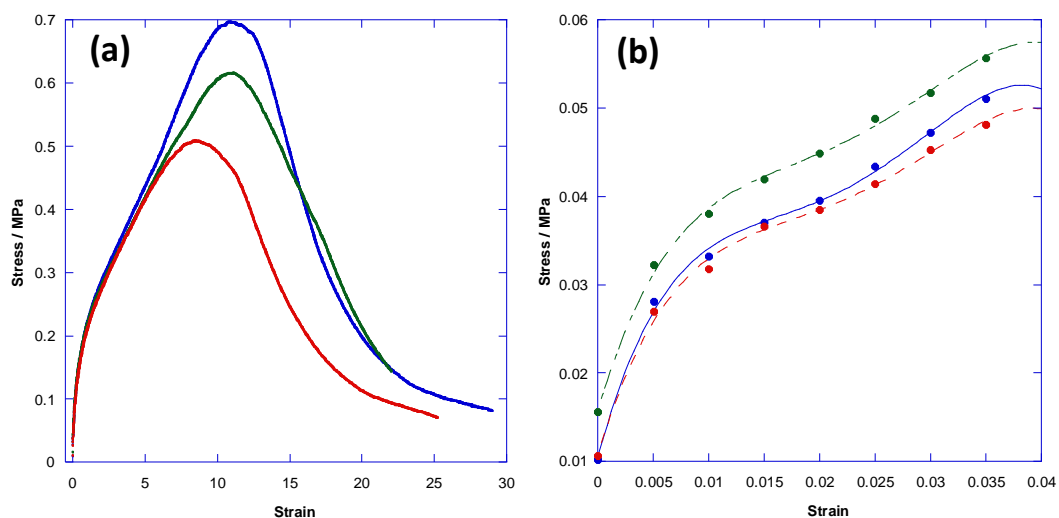


Figure 5.7 (a) Stress-strain curves for film with poly[(BA)-co-(BMA)] core and shell phase copolymer presented in triplicate; (b) Section of stress-strain curves from (a) with strains of 0-4% used to calculate Young's modulus (as the coefficient of first order term in a polynomial fit expression; order of fit = 6)

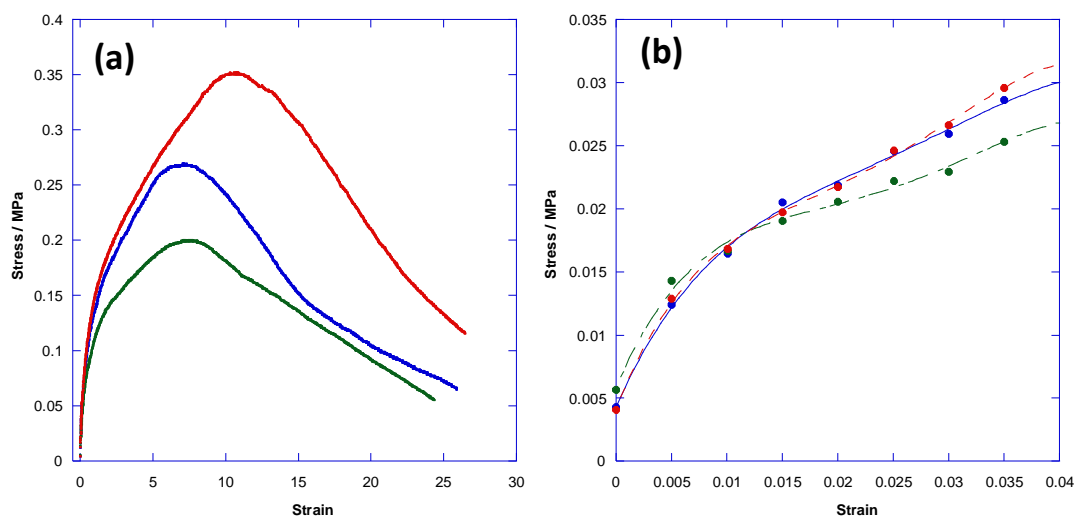


Figure 5.8 (a) Stress-strain curves for film with a poly[(BA)-co-(BMA)] core phase copolymer and poly[(BA)-co-(BMA)-co-(DAAM)] shell phase copolymer presented in triplicate; (b) Section of stress-strain curves from (a) with strains of 0-4% used to calculate Young's modulus (as the coefficient of first order term in a polynomial fit expression; order of fit = 6)

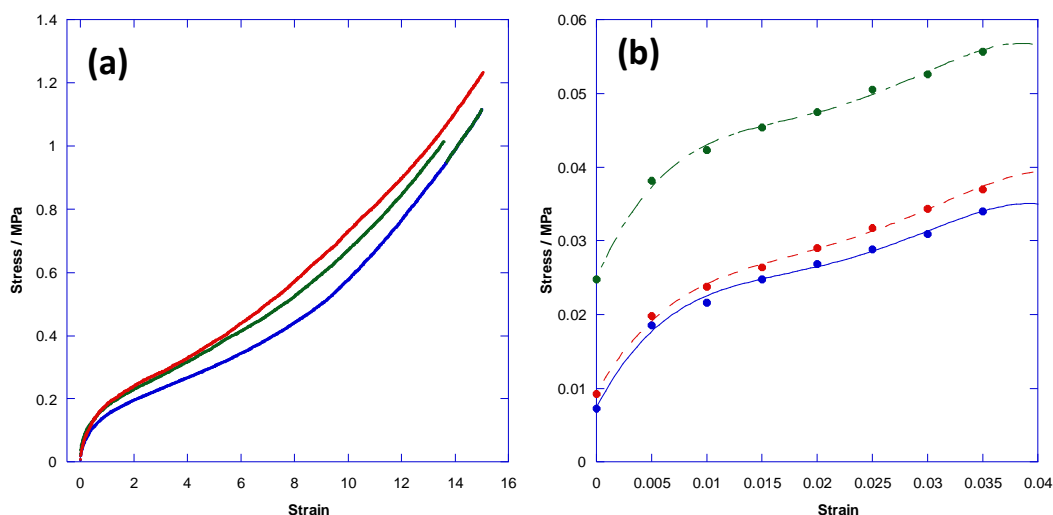


Figure 5.9 (a) Stress-strain curves for film with poly[(BA)-*co*-(BMA)] core phase copolymer and poly[(BA)-*co*-(BMA)-*co*-(DAAM)] shell phase copolymer with ADH added presented in triplicate; (b) Section of stress-strain curves from (a) with strains of 0-4% used to calculate Young's modulus (as the coefficient of first order term in a polynomial fit expression; order of fit = 6)

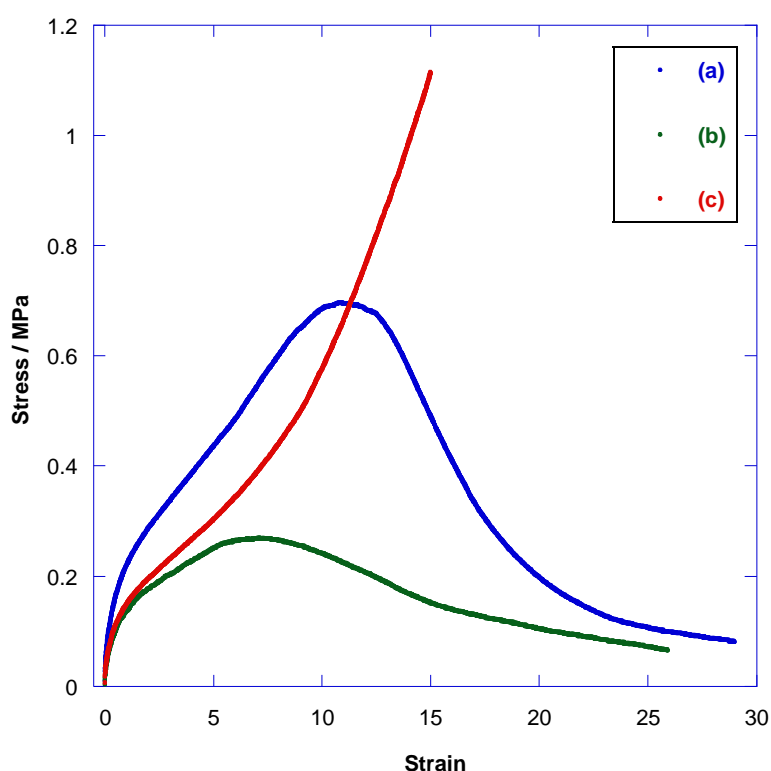


Figure 5.10 Comparison of stress-strain curves for soft-soft nanocomposite systems detailed in Table 5.1, where:

- (a) poly[(BA)-*co*-(BMA)] core and shell phase copolymer
- (b) poly[(BA)-*co*-(BMA)] core phase copolymer and poly[(BA)-*co*-(BMA)-*co*-(DAAM)] shell phase copolymer
- (c) poly[(BA)-*co*-(BMA)] core phase copolymer and poly[(BA)-*co*-(BMA)-*co*-(DAAM)] shell phase copolymer with ADH added

Table 5.4 Mechanical property data for films from the systems defined in Table 5.1

Film composition	Polynomial Young's modulus^a / MPa	Linear Young's modulus^b / MPa	Stress at 4% Strain / MPa	Extension to break / %
poly[(BA)-co-(BMA)] core poly[(BA)-co-(BMA)] shell	4.3 (± 0.2 MPa)	0.64 (± 0.03 MPa)	0.05 (± 0.003)	1900 (± 650%)
poly[(BA)-co-(BMA)] core poly[(BA)-co-(BMA)-co-(DAAM)] shell	2.1 (± 0.1 MPa)	0.57 (± 0.03 MPa)	0.03 (± 0.002)	2290 (± 200%)
poly[(BA)-co-(BMA)] core poly[(BA)-co-(BMA)-co-(DAAM)] shell ADH added	4.9 (± 0.4 MPa)	0.50 (± 0.04 MPa)	0.06 (± 0.006)	1150 (± 30)

^a – Calculated from the first order coefficient of a 6th order polynomial fit from strain values of 0 – 0.04

^b – Calculated from the gradient of a linear fit from strain values of 0.01-0.04

As can be seen from Figures 5.7 and 5.8, films from the non-crosslinked latexes show the same unusual viscoelastic-type behaviour, whereby the films pass through a peak stress before continuing to extend at increasingly lower stress values. However, the addition of ADH, and hence crosslinking, into the DAAM-functionalised latex film causes the tensile behaviour of the films to change completely. Instead of passing through a distinct peak stress and then continuing to soften, the crosslinked film (Figure 5.9) softens initially but then continuously strain hardens before failing at a much higher stress but lower elongation than the non-crosslinked equivalent. This strain hardening at high extension shows that the network formed by the crosslinked shell phase is percolating.

The two sets of Young's modulus values calculated from both polynomial and linear fits shown in Table 5.4 give very different results. Using a polynomial fit from strain values of 0-0.04 gave Young's modulus values approximately an order of magnitude larger than those calculated from a linear fit from strain values of 0.01-0.04. However, it is more difficult to discern a trend from the moduli calculated using a linear fit, as the differences between the three values are extremely small and could be attributed to errors that stem from jaw separation, as was previously discussed. Hence, for the rest of this thesis a polynomial fit from strain values of 0-0.04 will continue to be used (as detailed in Section 3.4.2.1), but future use of the linear fit method will be discussed further in Chapter 11.

A more accurate measure of low strain mechanical behaviour, the stress at 4% strain values in Table 5.4 show how several different parameters affect the tensile behaviour of the soft-soft nanocomposite films. Adding DAAM as a co-monomer into the shell phase of a non-crosslinked film caused a small reduction in both the Young's modulus and stress at 4% strain of the material as well as a large increase in extension to break, implying there is a small

plasticising effect that is not evident from the measurement of T_g . Incorporating crosslinking into the film by adding ADH causes a very slight increase in Young's modulus but a dramatic change in the stress-strain behaviour of the material, with the extension to break being greatly reduced. These findings are in line with those reported by Esser *et al.* in 1999¹⁰⁷. The Young's modulus values recorded for all three variants are all low, which can be attributed to the films being above their T_g at the testing temperature and hence being soft and rubbery in nature.

5.4 Visual differences between crosslinked and non-crosslinked films investigated by AFM

Both the surfaces and cross-sections from films of the three variants defined in Table 5.1 were examined by AFM, using the procedure documented in Section 3.4.2.5. This work was conducted in order to determine the effect that the addition of post-coalescence keto-hydrazide crosslinking would have upon film structure.

AFM was selected as the visualisation technique in preference to other methods, such as scanning electron microscopy (SEM) and transmission electron microscopy (TEM), due to its non-destructive nature, versatility with regards to imaging very soft polymers and ability to provide nanoscale mechanical data using Quantitative Nanomechanical Mapping (QNM)¹⁹⁸. As was discussed in Section 3.4.2.5, QNM represents a unique advantage for imaging nanostructured materials where little definition is likely to be seen between discrete phases. This is the case for soft-soft nanocomposite materials, where the core and shell copolymer phases are very similar with regard to their chemical composition, and are only differentiated by the addition of a latent crosslinking functionality, DAAM, into the shell phase and further by crosslinking with ADH. Hence, the only difference in physical property that is likely to be obvious between core and shell phases of the same T_g is Young's modulus, which is expected to be very slightly higher for the crosslinked shell matrix¹⁰⁷, and is also evident from the mechanical property data presented in Table 5.4.

5.4.1 Investigating film surfaces using AFM

Surface images of all three films revealed some retained particle morphology, with exuded surfactant crystals clearly visible. DMT modulus images for these systems are shown in Figures 5.11 – 5.13

In Figures 5.11 and 5.12 it can be seen that harder areas (the paler areas of the image) are present in the softer film surface, particularly at the interstitial sites between particles in the film for the two uncrosslinked films. However, in Figure 5.13, which is an image of the only sample to incorporate keto-hydrazide crosslinking, the paler areas are larger in size and

appear to sit directly on top of the film. These harder regions are likely to be crystals of either surfactant or unreacted ADH that have migrated to the surface during film formation, the latter suggested due to the significant difference in the appearance of large crystals for the crosslinked film, the only system from the testing series that contains ADH. As was discussed in Section 5.1, previous studies of keto-hydrazone containing film formation by Kessel *et al.* observed a similar residue on the surface of films, which was found by subsequent XPS analysis to be surfactant⁹⁵.

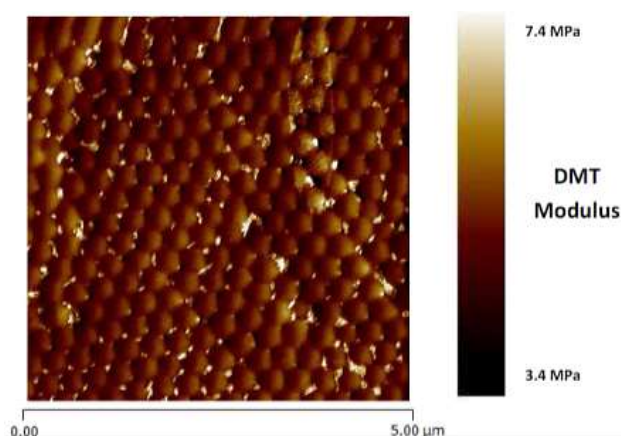


Figure 5.11 DMT Modulus AFM image of a soft-soft nanocomposite film surface with 70:30 core:shell ratio, comprising poly[(BA)-co-(BMA)] core and shell phase copolymers with T_g of $5\text{ }^\circ\text{C}$. Image size = $5\text{ }\mu\text{m}$ square

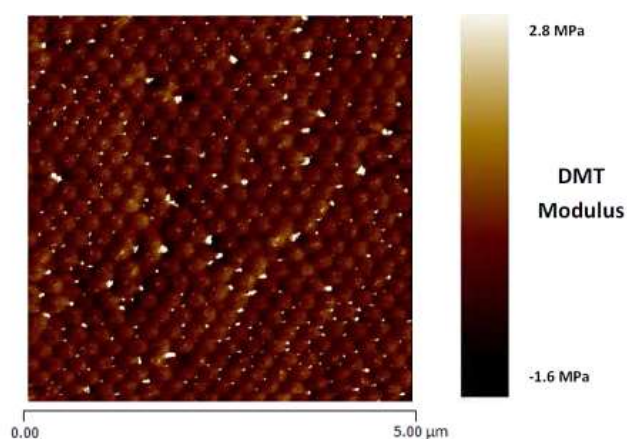


Figure 5.12 DMT Modulus AFM image of a soft-soft nanocomposite film surface with 70:30 core:shell ratio, comprising poly[(BA)-co-(BMA)] core and poly[(BA)-co-(BMA)-co-(DAAM)] shell phase copolymers with T_g of $5\text{ }^\circ\text{C}$. Image size = $5\text{ }\mu\text{m}$ square

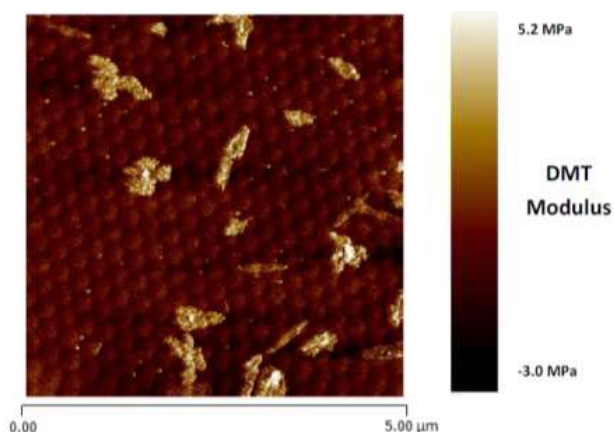


Figure 5.13 DMT Modulus AFM image of a soft-soft nanocomposite film surface with 70:30 core:shell ratio, comprising poly[(BA)-*co*-(BMA)] core and poly[(BA)-*co*-(BMA)-*co*-(DAAM)] shell phase copolymers with T_g s of 5 °C and ADH added. Image size = 5 μm square

The images in Figures 5.14-5.16 show how this difference in behaviour can be observed more clearly on a larger (20 μm) scale:

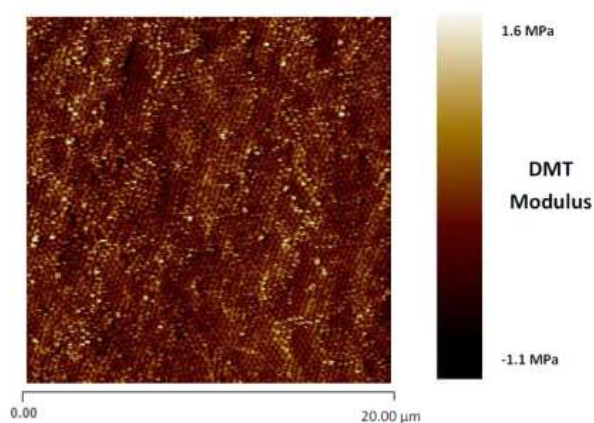


Figure 5.14 DMT Modulus AFM image of a soft-soft nanocomposite film surface with 70:30 core:shell ratio, comprising poly[(BA)-*co*-(BMA)] core and shell phase copolymers with T_g s of 5 °C. Image size = 20 μm square

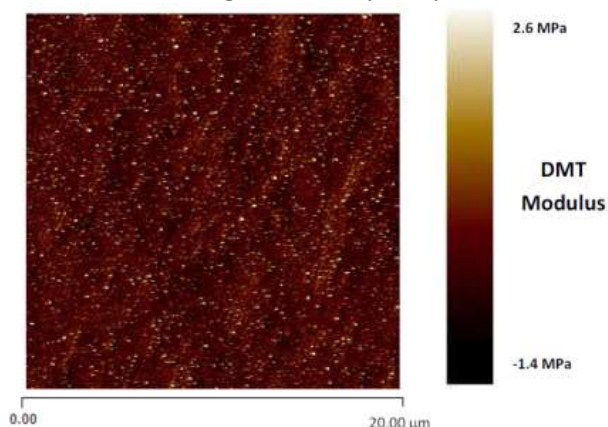


Figure 5.15 DMT Modulus AFM image of a soft-soft nanocomposite film surface with 70:30 core:shell ratio, comprising poly[(BA)-*co*-(BMA)] core and poly[(BA)-*co*-(BMA)-*co*-(DAAM)] shell phase copolymers with T_g s of 5 °C. Image size = 20 μm square

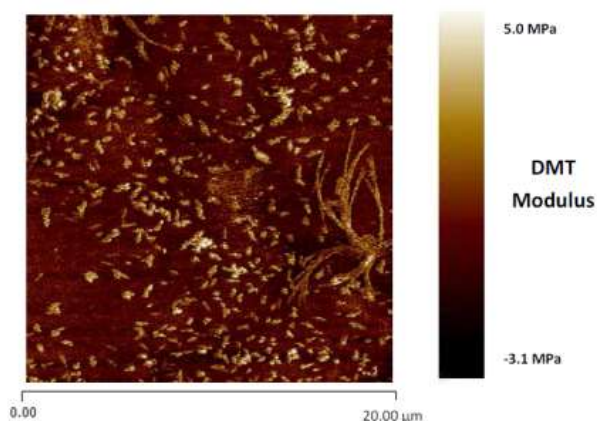


Figure 5.16 DMT Modulus AFM image of a soft-soft nanocomposite film surface with 70:30 core:shell ratio, comprising poly[(BA)-*co*-(BMA)] core and poly[(BA)-*co*-(BMA)-*co*-(DAAM)] shell phase copolymers with T_g s of 5 °C and ADH added. Image size = 20 μm square

The relative proportions of both non-ionic and anionic surfactants and ADH within a 100 g portion of each latex imaged are detailed in Table 5.5, which shows that the amount of anionic surfactant within the latex is greater than that of ADH (where present) by tenfold. As the stress-strain profile for this latex (Figure 5.9) suggests the presence of crosslinking, it is also unlikely that the entire quantity of the ADH lies unreacted within the film matrix. Hence, the crystal structures observed upon the film surface by AFM are more likely to be composed of surfactant. Although the latexes contain both anionic and non-ionic surfactants, these crystals are more likely to be formed of anionic surfactant, which due to its water solubility migrates to the surface during the drying process and is known to retard particle coalescence¹⁹⁹. The non-ionic surfactant, having a greater miscibility with the polymer, stays within the film matrix and is known to have a plasticising effect⁸³.

Table 5.5 Relative mass of surfactant and ADH in 100 g of the latexes discussed in Section 5.3

Component	Mass in 100 g latex / g		
	poly[(BA)- <i>co</i> -(BMA)] core and shell	poly[(BA)- <i>co</i> -(BMA)] core poly[(BA)- <i>co</i> -(BMA)- <i>co</i> -(DAAM)] shell	poly[(BA)- <i>co</i> -(BMA)] core poly[(BA)- <i>co</i> -(BMA)- <i>co</i> -(DAAM)] shell + ADH
Anionic surfactant (<i>Rhodafac RK-500A</i>)	1.41	1.41	1.41
Nonionic surfactant (<i>Lutensol TO7</i>)	0.25	0.25	0.25
ADH	-	-	0.15

The exudation of surfactant during latex film formation has been extensively probed using many methods, including AFM. It is generally accepted that the earliest published example of such a study was in 1936 by Wagner and Fischer, and many authors have expanded upon the subject since. In 2011, Arnold *et al.* reported the exudation of anionic sodium dodecyl sulphate (SDS) surfactant from a poly [(BA)-*co*-(MMA)-*co*-(AA)] film²⁰⁰,

finding that approximately 50% of the total amount of surfactant had migrated to the surface of the film after 10-15 days of drying at ambient temperature and humidity. It has also been extensively reported that the extent to which SDS exudes from the film upon drying is greatly increased by annealing at higher temperatures ($>100\text{ }^{\circ}\text{C}$)^{79, 201}. Aramendia *et al.* suggested that this increased mobility of surfactant may be due to the annealing temperature being above the copolymer T_g , which would aid exudation through the flexibility of polymer chains in the rubbery state²⁰¹.

The immediate difference between the images in Figures 5.11 - 5.17 indicates that the addition of keto-hydrazide crosslinking has had some effect on the film matrix, due to the shape and size of the surfactant crystals that have exuded to the surface of each film. This may be due to several consequences of the crosslinking reaction, including an increased hydrophobicity of the film surface due to the dehydration effect of the keto-hydrazide mechanism and an increased density of the film resulting from the crosslinked units. Both of these effects would cause the anionic surfactant to be exuded from the film matrix, as can be observed for the crosslinked latex in Figure 5.13 compared to the uncrosslinked equivalents in Figures 5.11 and 5.12, where the surfactant crystals can be observed at the interstitial sites of the particles only, indicating that they are still partially embedded within the film.

These observations are contrary to what was observed by Kessel *et al.*, who found that surfactant exudation from low T_g films was inhibited by the presence of DAAM-ADH crosslinking⁹⁵. However, the latexes studied in their 2008 paper were monophasic, unstructured systems with DAAM polymerised radially throughout the particles and hence had a higher level of crosslinking distributed through the entire film matrix. For these structured soft-soft nanocomposite systems, the DAAM-ADH crosslinking is confined to the particle shells and hence the percolating film phases which form the minority (30 wt%) of the overall particle composition. As the majority (70 wt%) of the film comprises uncrosslinked, viscoelastic poly[(BA)-*co*-(BMA)] copolymer, the appearance of surfactant residue on the film surface of a film incorporating keto-hydrazide crosslinking is therefore not unexpected, as surfactant exudation from these uncrosslinked regions is unhindered by network formation.

The 3D height images in Figure 5.17(a)-(c) show that for each of the three systems, memory of the original particle is evident at the surface of the films. Whether this is just a surface effect or prevalent throughout the entire film is unknown, as it is not possible to image cross-section samples of films with the same core and shell T_g due to the lack of mechanical contrast between the two phases.

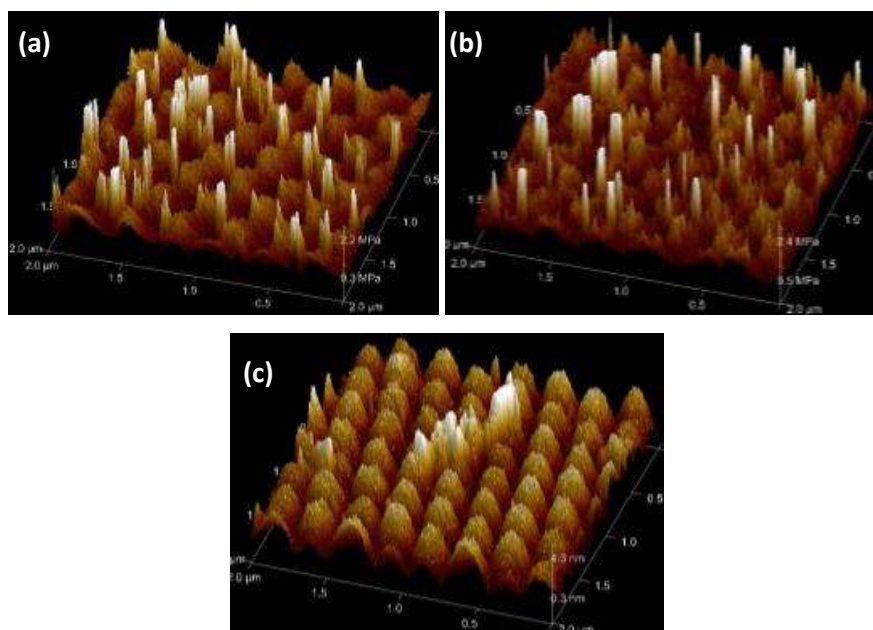


Figure 5.17 3D height images of systems with (a) poly[(BA)-*co*-(BMA)] core and shell, (b) poly[(BA)-*co*-(BMA)] core and poly[(BA)-*co*-(BMA)-*co*-(DAAM)] shell, and (c) poly[(BA)-*co*-(BMA)] core and poly[(BA)-*co*-(BMA)-*co*-(DAAM)] shell with ADH. Image sizes 2 μm square

5.4.2 Investigations of film cross-sections using AFM

An AFM phase image from previous work on soft-soft nanocomposites as pressure sensitive adhesives (PSA), incorporating keto-hydrazide crosslinking, is shown in Figure 5.18. For the surface of the PSA film in Figure 5.18, the continuous percolating shell phase is the harder area of the film, as is indicated by it having a lighter colour than the core phases. The observation of mechanically-defined regions forms one of the key principles of the soft-soft nanocomposite design strategy, and it would typically be expected for the crosslinked shell phase to have a higher modulus than a non-crosslinked core of the same T_g , and hence appear as a lighter area in an AFM phase or DMT modulus image.

The AFM images that are shown and discussed in this section are those of film cross-sections, which were prepared using the procedure given in Section 3.4.2.5. Cross-sections of films were imaged rather than the film surface in order to exclude the effect of surfactant residues, as observed in Section 5.4.1, and any film surface affects that may change the localised T_g and hence the mechanical properties of the film domains¹²⁰.

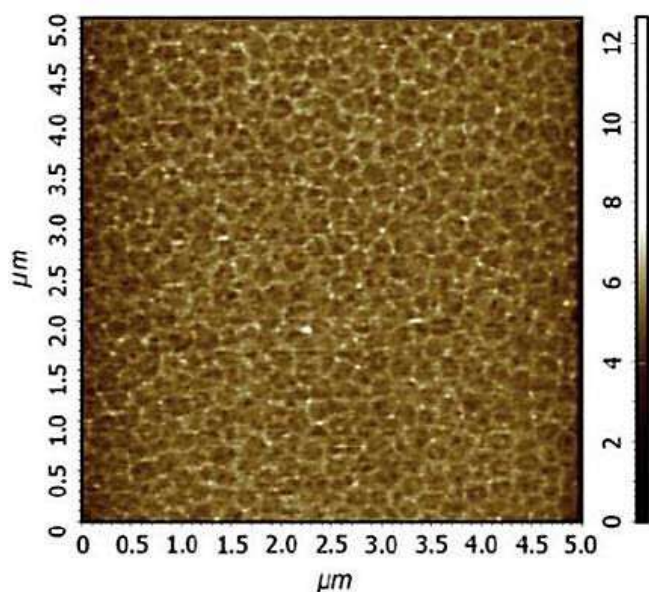


Figure 5.18 AFM phase image of the cross-section of a soft-soft nanocomposite PSA film⁶

Systems with higher core T_g were found to be more suitable for the AFM imaging conducted in this project as the ambient temperature of the testing room was very high, typically above 25 °C. Due to this, films with low (< 15 °C) T_g core (majority) phases were extremely soft at the testing temperature, and good images were not gained due to the resulting adhesive interaction between the cantilever tip and the sample surface in AFM tapping mode. The shell phase copolymer T_g was consistently kept at 5 °C in order to facilitate film formation. Hence, for the DMT modulus AFM images shown from this point onwards, the dispersed higher T_g core phases will be observed as a higher modulus phase, and therefore paler, area than the crosslinked percolating phase.

In order to successfully gain contrast between the core and shell polymer phases, a soft-soft nanocomposite latex comprising 70 wt% of a poly[(BA)-*co*-(BMA)] copolymer core phase with a T_g of 25 °C and 30 wt% of a poly[(BA)-*co*-(BMA)-*co*-(DAAM)] copolymer shell phase with T_g of 5 °C was synthesised. DAAM was incorporated into the shell phase copolymer at a level of 2 wt%. Full characterisation plots for this preparation can be found in Appendix (iv), and a summary of the kinetics data can be found in Section 7.2.1. ADH was then added to a portion of this latex at a 2:1 (DAAM:ADH) molar stoichiometric ratio, and films cast of the latex both with and without ADH according to the procedure given in Section 3.3.2. It should be noted that the units of measurement for all cross-section AFM images are in arbitrary units, compared to the surface AFM images which have units of MPa. This is due to the AFM imaging being done in two different locations, namely AkzoNobel in Slough for the surface images and the University of Manchester for the cross-section images. DMT modulus calibration equipment was available for the AFM in Slough, but not in Manchester. However,

as the scale of both arbitrary and MPa units are the same, this was not seen as a problem. The same model of microscope, a Bruker MultiMode 8, was used for both surface and cross-section images.

Figures 5.19 and 5.20 show DMT modulus images for the uncrosslinked and crosslinked soft-soft nanocomposite films, respectively, and as the images have comparable scales they can be directly compared. It is immediately obvious from Figure 5.20 that the core-shell morphology is very clearly retained for the film that incorporates keto-hydrazide crosslinking into the percolating film matrix. Particle morphology can be seen to be retained in the uncrosslinked system, but the film structure is much more diffuse than in the crosslinked film.

This difference in film structure between the two films suggests that the keto-hydrazide crosslinking in the percolating film phase occurs at a similar rate to interparticle chain diffusion, but at a much faster rate than interphase polymer chain diffusion. This means that the shell phase polymer chains, which are flexible and mobile due to being below their T_g and hence in the rubbery state, can diffuse through particle boundaries to form a coherent film, which simultaneously becomes crosslinked.

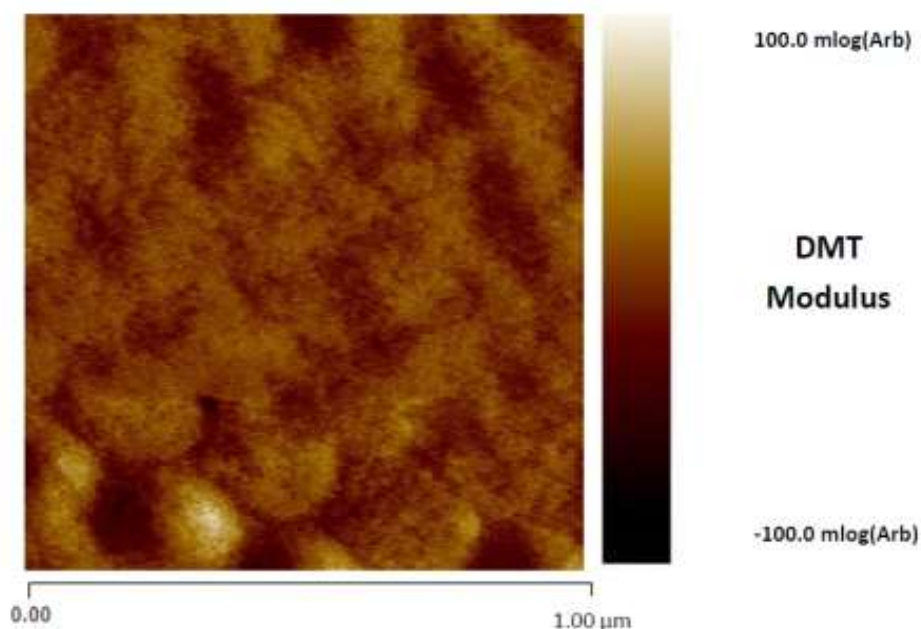


Figure 5.19 DMT Modulus AFM image of an uncrosslinked soft-soft nanocomposite film cross-section with 70:30 core:shell ratio, comprising poly[(BA)-*co*-(BMA)] core and poly[(BA)-*co*-(BMA)-*co*-(DAAM)] shell phase copolymers with T_g s of 25 and 5 °C, respectively. Image size = 1 μm square

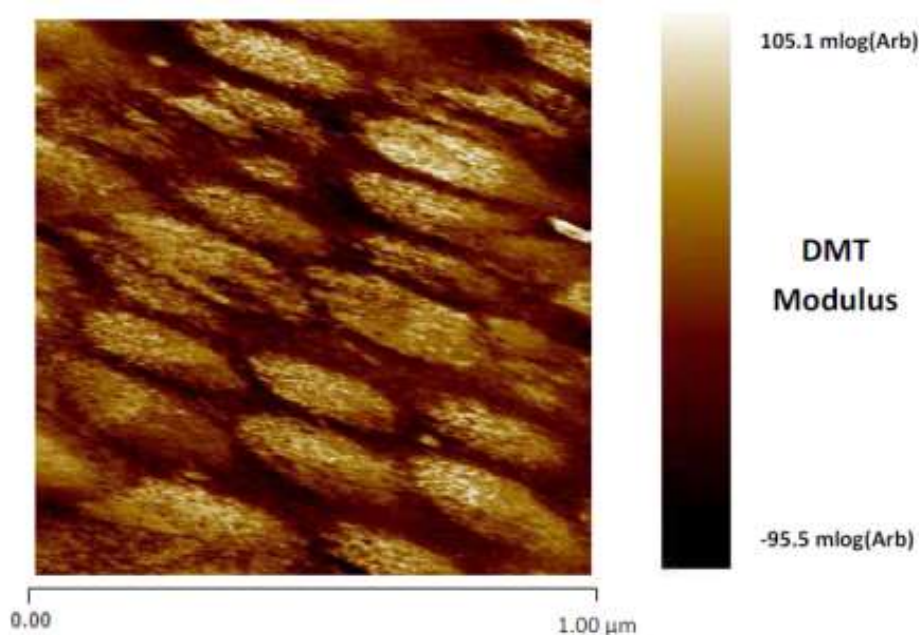


Figure 5.20 DMT Modulus AFM image of a lightly crosslinked soft-soft nanocomposite film cross-section with 70:30 core:shell ratio, comprising poly[(BA)-*co*-(BMA)] core and poly[(BA)-*co*-(BMA)-*co*-(DAAM)] shell phase copolymers with T_g s of 25 and 5 °C, respectively. ADH added at a 2:1 DAAM:ADH molar stoichiometric ratio. Image size = 1 μ m square

These two processes occur at a faster rate than polymer chain diffusion between the core and shell phases, which becomes restricted due to the crosslinked nature of the now coherent shell phase restricting mobility. This leads to the continuous, percolating film matrix formed by the crosslinked shell phase copolymer hence acts as a dispersion media for the viscoelastic uncrosslinked cores. This observation of retained structure in the crosslinked film is consistent with the findings of Kessel *et al.*⁹⁵.

5.4.3 Visualising keto-hydrazone crosslinks using AFM-IR

The novel technique of AFM-IR, which was discussed in detail in Section 3.4.2.6 of this thesis, allows IR spectroscopy to be carried out on the nanoscale. The instrument used for the imaging discussed in this section, the NanoIR2 manufactured by Anasys Instruments, uses top-down IR illumination which enables analysis of samples that can be assumed to be 'infinitely thick' such as those prepared using the procedure given in Section 3.4.2.5.

In order to confirm the presence of keto-hydrazone crosslinks in the percolating phase of soft-soft nanocomposite films, AFM-IR was conducted on the two systems detailed in Section 5.4.2. As can be seen from the reaction schematic in Figure 5.21, new C=N imine bonds are created by the crosslinking process, which are not present in any other component of the film. These imine bonds have a characteristic IR absorption at 1670 - 1690 cm^{-1} ²⁰², and have been previously detected in bulk IR studies of 2-heptanone and octanoic hydrazone, which were used to simulate the carbonyl and hydrazone components involved in keto-hydrazone

crosslinking⁹⁵. However, due to the localised nature and the low levels of the DAAM-ADH crosslinking in soft-soft nanocomposite films, it was not known whether it would be possible to detect the C=N bond by bulk or AFM IR. Another factor that may affect the detection of a small C=N absorption is the presence of many carbonyl ester groups in both the core and shell copolymers and amide groups from unreacted DAAM. These C=O absorptions, which occur in the region of 1730-1750 cm^{-1} for esters and $\sim 1650 \text{ cm}^{-1}$ for amides are very strong¹⁶⁹, so may predominate and overshadow the much weaker C=N transition.

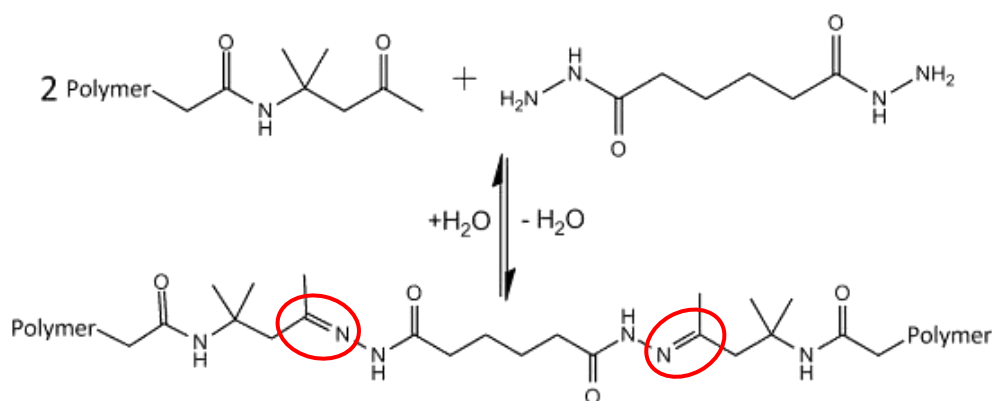


Figure 5.21 Simplified reaction schematic for keto-hydrazide crosslinking, with the imine crosslinks highlighted

Prior to AFM-IR studies, bulk FTIR was performed on films of the chosen soft-soft nanocomposite both with and without ADH in the system using the procedure given in Section 3.4.2.4, in order to ascertain whether a difference in absorption in the target area could be detected. However, as can be seen from Figure 5.22, it was not easy to see any real differences in absorption between 1650 and 1700 cm^{-1} for the two films, most likely due to the overwhelming presence of C=O groups from the acrylic polymer backbone. A clear peak centred around 1730 cm^{-1} can be seen for both the crosslinked and the uncrosslinked films, which corresponds with the huge excess of ester carbonyl functionalities from the (meth)acrylate species that comprise the core and shell copolymers.

Although the C=N stretching absorption could not be detected in the bulk IR spectrum, it was decided to proceed with AFM-IR regardless. This decision was made because of the very low level of DAAM-ADH crosslinking that is actually incorporated into the film (maximum 0.017 mmol g^{-1} of polymer), the localised nature of the C=N functionality which should solely occur in the percolating, continuous shell phase of the film and the superior spatial resolution of the AFM-IR.

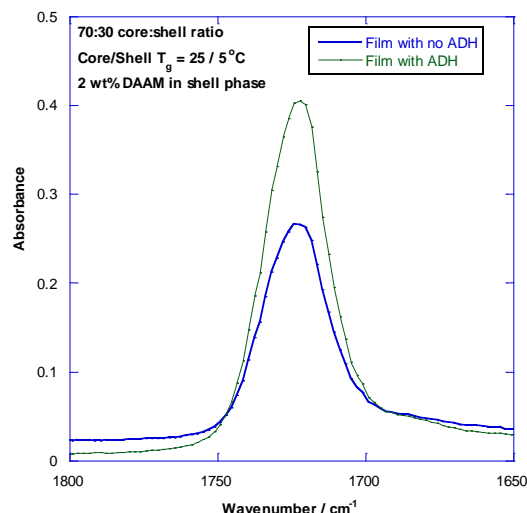


Figure 5.22 Targeted section of the FTIR spectrum of selected soft-soft nanocomposite film with and without ADH added

As previously mentioned and shown in Section 3.4.2.5.1, it is possible to perform multiple types of AFM-IR measurement. The first type that was trialed with a soft-soft nanocomposite film was to measure an array of IR spectra across particle boundaries, the results of which can be seen in Figure 5.23.

As can be seen from the AFM height image in Figure 5.23, the IR array encompasses the core phases, the percolating phase, and the core-percolating phase boundary. Due to the relative dimensions of the phases and the resolution of the instrument, it was only possible to obtain one spectrum solely in the percolating phase. However, as can be seen from Figure 5.24, which contains the relevant zoomed portion of the IR array; a pronounced shoulder at 1684 cm^{-1} can be identified on the side of the strong C=O absorption centred at 1730 cm^{-1} for the spectrum focusing on the percolating shell phase (Spectrum 5; green trace in Figure 5.23 and Figure 5.24). This provides evidence as to the localised existence of the C=N group, as it lies in the region identified for C=N absorptions in the literature^{169, 203}, and is at the same wavenumber as was reported for the C=N absorption resulting from DAAM-ADH crosslinking by BASF (Reck *et al.*) during their investigations of the keto-hydrazide reaction that were presented at the 78th Prague Meeting of Macromolecules in July 2014¹¹¹. A similar wavenumber of 1681 cm^{-1} for the C=N bond from DAAM-ADH crosslinking was also reported by Zhang *et al.* in 2011⁹². This absorption at 1684 cm^{-1} is towards the limits of the C=N stretch absorption range ($1670 - 1690\text{ cm}^{-1}$), which is likely to be due to the adjacent -NHR- group which would be donating electron density to the C=N bond, strengthening it and therefore pushing it to a higher absorption frequency¹⁷⁰.

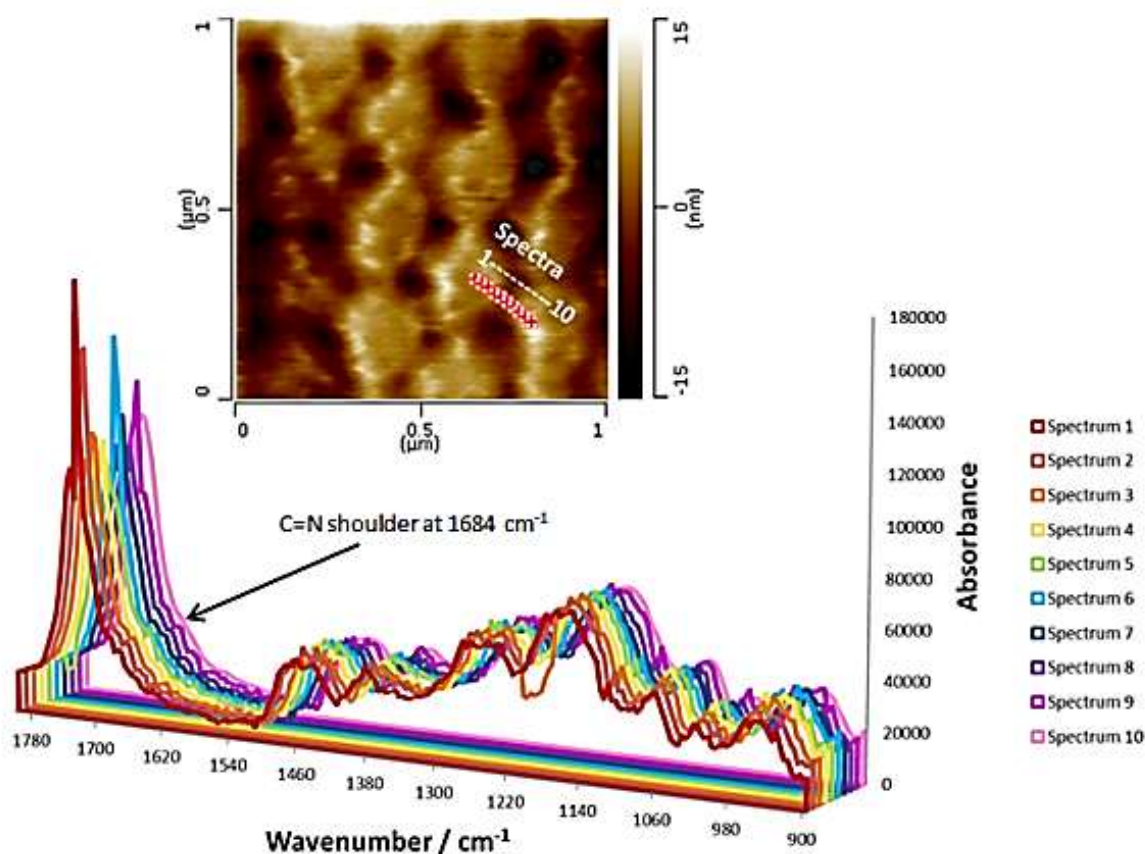


Figure 5.23 AFM-IR array over particle interfaces in a soft-soft nanocomposite film with 70:30 core:shell ratio, comprising poly[(BA)-*co*-(BMA)] core and poly[(BA)-*co*-(BMA)-*co*-(DAAM)] shell phase copolymers with T_g s of 25 and 5 °C and ADH added at a 2:1 DAAM:ADH molar stoichiometric ratio. Spectra 1-4 and 7-10 are of the particle cores, Spectrum 5 is of the percolating phase and Spectrum 6 is of the core-percolating phase boundary.

Due to it being possible to identify an absorption at a wavenumber that is in accordance with an imine C=N stretch in the percolating shell phase, a second type of measurement was performed. This was a ‘mapping’ of the surface’s absorption at one specific wavenumber, namely 1684 cm^{-1} where the absorption that is in agreement with previous reports of a C=N absorption was identified in the arrays shown in Figures 5.23 and 5.24.

Figures 5.25 and 5.26 show both height and absorption of IR radiation at 1684 cm^{-1} images of the same surface for uncrosslinked and crosslinked films, respectively. As can be seen from these images, it is immediately obvious that the retained core-shell ‘honeycomb’ pattern seen for the crosslinked film is mimicked in the IR absorption image, with the strongest absorptions being seen in the percolating phase where the keto-hydrazide crosslinks are localised.

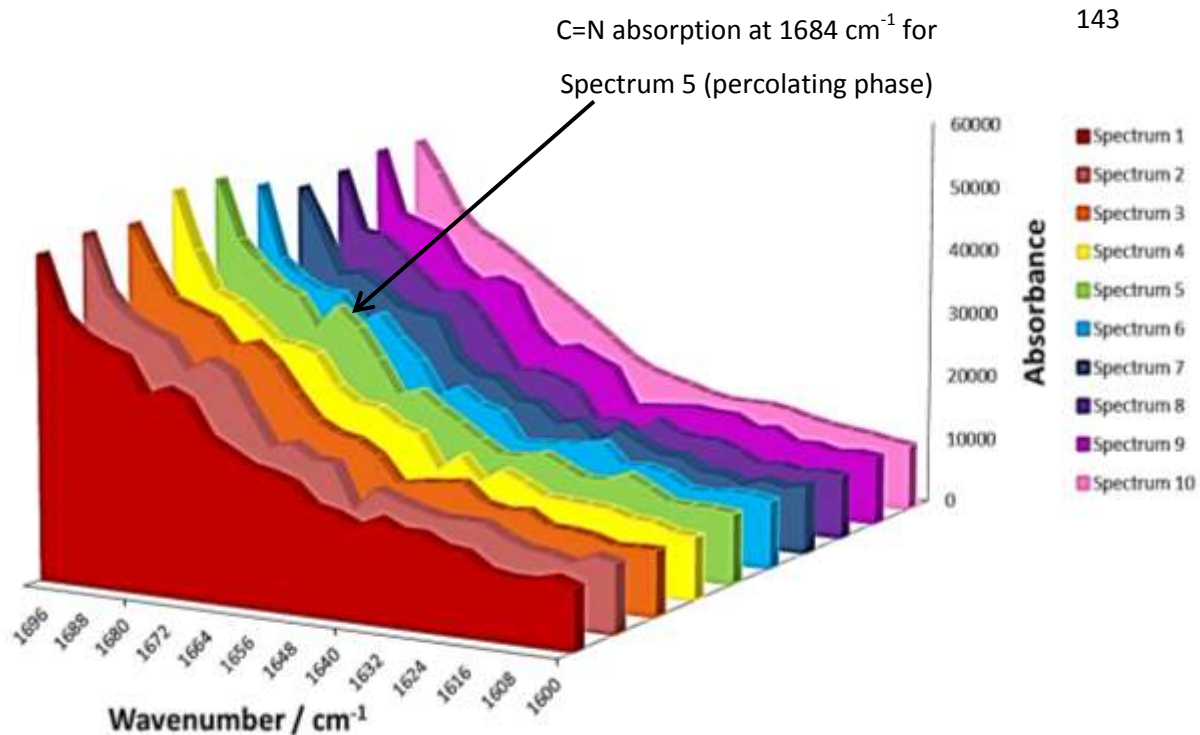


Figure 5.24 Zoomed-in AFM-IR array of a soft-soft nanocomposite film with 70:30 core:shell ratio, comprising poly[(BA)-*co*-(BMA)] core and poly[(BA)-*co*-(BMA)-*co*-(DAAM)] shell phase copolymers with T_g s of 25 and 5 °C, respectively, and ADH added at a 2:1 DAAM:ADH molar stoichiometric ratio, showing specific areas of interest. Spectra 1-4 and 7-10 are of the particle cores, Spectrum 5 is of the percolating phase and Spectrum 6 of the core-percolating phase boundary.

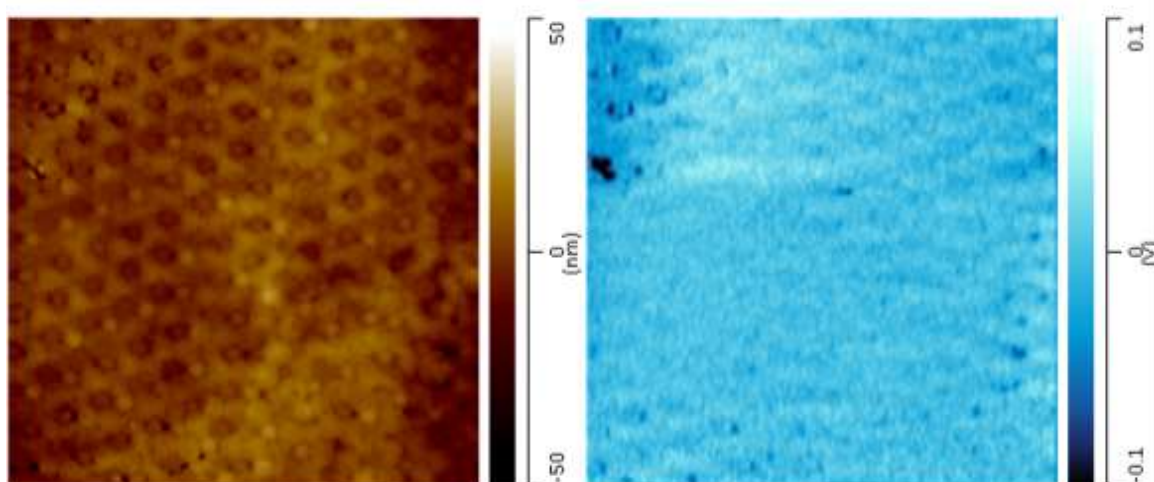


Figure 5.25 AFM-IR height (L) and map of IR absorption at 1684 cm^{-1} (R) images of an uncrosslinked soft-soft nanocomposite film cross-section with 70:30 core:shell ratio, poly[(BA)-*co*-(BMA)] core and poly[(BA)-*co*-(BMA)-*co*-(DAAM)] shell phase copolymers with T_g s of 25 and 5 °C, respectively. Image sizes = 5 μm square

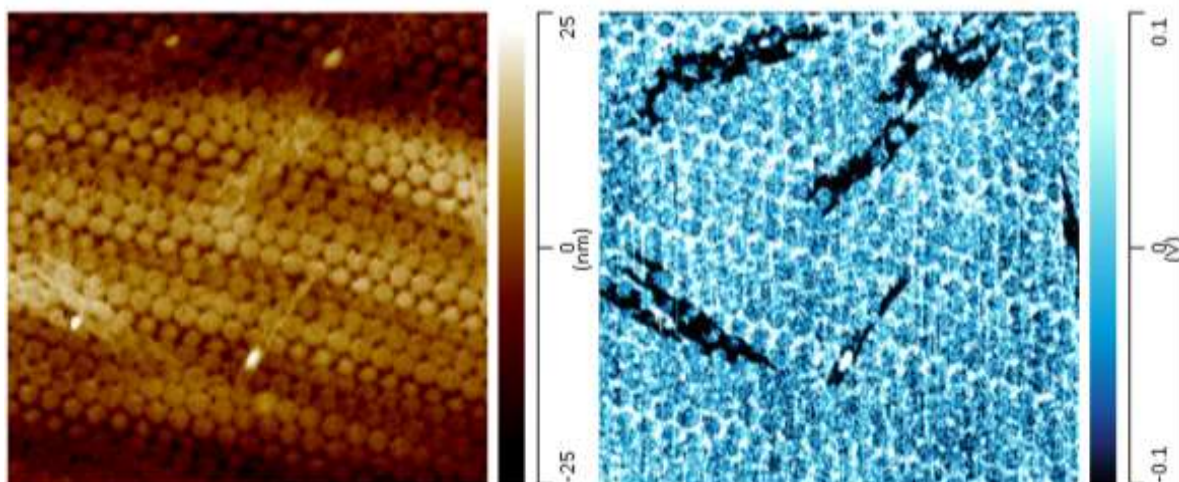


Figure 5.26 AFM-IR height (L) and map of IR absorption at 1684 cm^{-1} (R) images of a lightly crosslinked soft-soft nanocomposite film cross-section with 70:30 core:shell ratio, poly[(BA)-co-(BMA)] core and poly[(BA)-co-(BMA)-co-(DAAM)] shell phase copolymers with T_g s of $5\text{ }^\circ\text{C}$ and ADH added at a 2:1 DAAM:ADH stoichiometric ratio. Image sizes = $5\text{ }\mu\text{m}$ square

The IR absorption image for the uncrosslinked film shown in Figure 5.25 does not show the 'honeycomb' absorption pattern seen for the crosslinked film. There are some slight areas of absorption contrast, but as the scales are the same the images can be assumed to be comparable. The absorptions that can be seen in Figure 5.25 for the uncrosslinked film are significantly darker in colour, and therefore weaker, than the equivalents for the crosslinked film in Figure 5.26. This weaker absorption indicates that there are far less C=N functionalities present in this film, and the absorption pattern may be an artefact of C=O such as a weak amide(I) band, which would be caused by the unreacted DAAM in the uncrosslinked shell phase copolymer, which occurs at approximately 1685 cm^{-1} ²⁰³. The C=N imine absorption at 1684 cm^{-1} is considered to be a much stronger absorption, and as such the 'honeycomb' pattern seen in Figure 5.26 can be considered to be that of the imine bond resulting from the DAAM-ADH crosslinking reaction, and not as a C=O amide(I) band.

The data presented in this section is a brief, initial study into probing keto-hydrazide crosslinking using the novel AFM-IR technique, and has proved that there is significant potential for this to be a powerful tool for the in-depth analysis of film morphology and composition. However, further work will need to be conducted in order to find the limits of the technique and to substantiate the findings described above.

5.5 Effect of crosslinking upon 'paint' film properties

In order to deduce the basic suitability of soft-soft nanocomposite films for their use as binders in decorative paints, a series of standard tests used for industrial paint formulations were conducted. All of the testing conducted in this section was performed on four latex variants and films cast from them, designed to investigate the effects of post-polymerisation addition of ADH and hence keto-hydrazide crosslinking. The compositions of these latexes are detailed in Table 5.6. Five different tests were performed on the chosen systems, and combined investigations of specific wet latex properties, as well as the film formation process and fully dried film properties.

Table 5.6 Composition of latexes discussed in Section 5.5

Core copolymer composition	Shell copolymer composition	Film T_g^a / °C	ADH content / mmol g ⁻¹ latex
80 wt% BMA 20 wt% BA	80 wt% BMA 20 wt% BA	3	0
80 wt% BMA 20 wt% BA	80 wt% BMA 20 wt% BA	3	0.089 ^b
80 wt% BMA 20 wt% BA	77 wt% BMA 21 wt% BA 2 wt% DAAM	3	0
80 wt% BMA 20 wt% BA	77 wt% BMA 21 wt% BA 2 wt% DAAM	4	0.089

^a - Measured by DSC (see Section 5.1)

^b - This latex contained no DAAM, but ADH was added at a theoretical stoichiometric ratio as if 2 wt% DAAM were present.

5.5.1 Minimum film formation temperature (MFT)

The MFT was determined for the four wet latexes, using the procedure given in Section 3.4.3.1. Table 5.7 gives the MFT of each latex, and Figure 5.27 shows the plot of temperature variance along the MFT bar used to gain the measurement.

The results from Table 5.7 show that post-coalescence keto-hydrazide crosslinking in the film matrix does not appear to make a significant difference to the observed MFT, as all latexes failed to form a film below approximately -0.5 °C. An MFT of this magnitude is to be expected given the T_g values of these latexes (3 - 4 °C), as MFT is typically close, but not identical, to T_g^{81} .

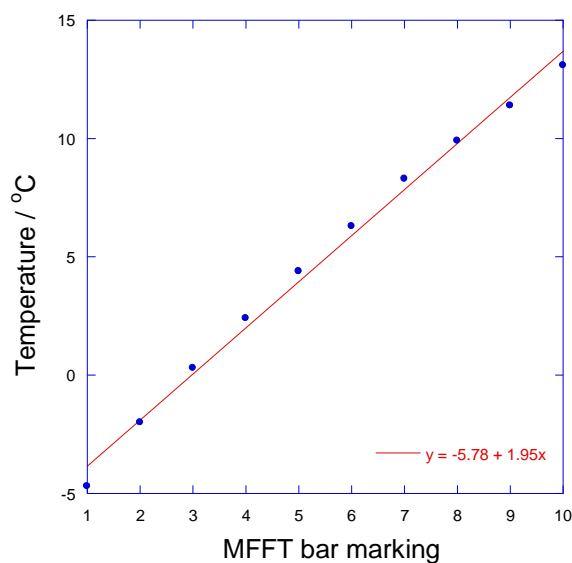


Figure 5.27 Plot of temperature against MFT bar marking

Table 5.7 Results from MFT testing

Shell phase composition	ADH added?	MFT bar marking	MFT of latex / °C
Poly[(BA)- <i>co</i> -(BMA)]	No	2.65	-0.6
Poly[(BA)- <i>co</i> -(BMA)]	Yes	2.70	-0.5
Poly[(BA)- <i>co</i> -(BMA)- <i>co</i> -(DAAM)]	No	2.75	-0.4
Poly[(BA)- <i>co</i> -(BMA)- <i>co</i> -(DAAM)]	Yes	2.75	-0.4

5.5.2 Viscosity testing – high and low shear rheology

Both high- and low-shear viscosity was determined for the latexes detailed in Table 5.6 using cone-and-plate and Brookfield viscometers, respectively, using the procedures given in Section 3.4.4.1. The data obtained from this testing are given in Table 5.8.

The results from the cone-and-plate viscometry show that those latexes that have ADH added have a slightly higher viscosity than those without ADH. This effect may be due to a small amount of keto-hydrazide bonds forming in the wet latex, as the reaction mechanism is known to occur instantaneously and reversibly in the presence of water¹¹¹. As the DAAM-ADH crosslinks form in solution the viscosity-average molar mass, which lies between the number- and weight-average molar masses, \bar{M}_n and \bar{M}_w , respectively, roughly doubles as two polymer chains become linked together and can essentially be considered to be one chain, which will affect the entanglement chain length of the polymer within the latex particles.

The Brookfield viscosity measurements show that neither the inclusion of DAAM repeat units in the particle shell phase nor addition of ADH to the latex affect the low-shear viscosity of the latexes significantly.

Table 5.8 High- and low-shear viscosity testing results

Shell phase composition	ADH added?	Cone-and-plate viscosity /P	Brookfield viscosity /cP
Poly[(BA)- <i>co</i> -(BMA)]	No	1.0	60
Poly[(BA)- <i>co</i> -(BMA)]	Yes	1.3	- ^a
Poly[(BA)- <i>co</i> -(BMA)- <i>co</i> -(DAAM)]	No	1.1	70
Poly[(BA)- <i>co</i> -(BMA)- <i>co</i> -(DAAM)]	Yes	1.3	70

^a - Measurement not possible due to available sample volume being too small

5.6 Conclusions

The work presented in this chapter has shown that one of the fundamental principles that underpins the soft-soft nanocomposite design theory can be successfully applied to polymers with a T_g close to ambient temperature, namely the incorporation of a lightly crosslinked percolating phase into a film in order to introduce elastomeric behaviour.

It was also demonstrated in this chapter that incorporating low levels of crosslinking results in much better mechanical properties at high extensions, whereby the films containing crosslinks strain hardened. AFM imaging showed that the presence of these crosslinks appeared to affect the structure of the film matrix itself, as large, defined surfactant crystals could be seen on the film surface of crosslinked films. Although this was contrary to previous studies of the effect of keto-hydrazide crosslinking on surfactant exudation from unstructured films with an even distribution of DAAM-ADH crosslinks, the majority (> 70 wt%) of the soft-soft nanocomposite films discussed in Section 5.3 comprised uncrosslinked viscoelastic core phase copolymer, which would not inhibit the exudation of surfactant from the film. The observation that larger crystals were seen for the film incorporating DAAM-ADH crosslinks suggested that due to an increased hydrophobicity of areas of the film resulting from the formation of crosslinks, the hydrophilic anionic surfactant was exuded from the film matrix to a larger extent than the completely uncrosslinked equivalents.

Imaging of film cross-sections revealed that for systems incorporating keto-hydrazide crosslinking, core-shell morphology was retained throughout the bulk film structure. Conversely films with no ADH, and therefore no crosslinking, are much more diffuse, which indicates that a higher level of interparticle diffusion has occurred. This is in accordance with theories regarding the rate of keto-hydrazide crosslinking, which suggest that it occurs at a

similar rate to the diffusion of polymer chains across particle boundaries, which is the final stage of coherent film formation, and is fully complete after 7 days^{19, 92, 111}. AFM-IR studies of both crosslinked and uncrosslinked films showed that the nanoscale detection of C=N functionalities was possible, and occurred only for films with both DAAM and ADH. This suggests that the keto-hydrazide crosslinking reaction occurs in accord with the generally accepted mechanism reported by Kessel *et al.*⁹⁵, and forms an imine product not an enamine as had previously been theorised¹⁰⁷.

The practicality and suitability of soft-soft nanocomposites for applications close to polymer T_g is established by the results shown in Section 5.5. Further synthesis parameters were investigated in terms of their individual and combined effects upon film properties. These parameters included the core-to-shell mass ratio, the T_g values of the core and shell polymers and the level of keto-hydrazide crosslinking incorporated into the percolating shell phase of the films.

6 Effect of core:shell ratio and crosslinker content on soft-soft nanocomposite film properties

6.1 Introduction

For all of the work regarding structured particle latexes discussed in Chapter 5, a core:shell ratio of 70:30 was used. This was to ensure that both the core and shell phase polymers were both present in substantial enough proportions to affect film properties, but so that the effect of keto-hydrazide crosslinking, which occurs in the shell phase only, did not predominate over the viscoelastic behaviour of the uncrosslinked core phase. This chapter investigates two different physical parameters, namely the core:shell mass ratio and the crosslinker contents of the particles, and how these affect the mechanical behaviour of soft-soft nanocomposite films.

The effect of structured particle morphology on film formation and subsequent film physical properties has been extensively investigated since the 1980's. Morgan *et al.* first reported the effect of a structured particle upon minimum film formation temperature (MFT) in 1982¹¹⁹, finding that the MFT was heavily dependent upon both the thickness and the T_g of the shell phase copolymer relative to that of the core. These findings were further substantiated by several researchers over the next 30 years^{89, 91, 204}, most recently by Price *et al.*¹²². The effect of core-to-shell mass ratios on film formation was investigated using AFM by Meincken *et al.* in 2002, who found that, unlike particle size or morphology, the core:shell mass ratio had no significant effect upon the kinetics of film formation²⁰⁵. An investigation into the effect of copolymer composition upon the paint application-specific properties of core-shell latexes was described by Khan *et al.*⁵⁷. It found that the best performance for systems with soft poly[Sty-co-(BA)-co-(AA)] copolymer core phases and hard poly[(MMA)-co-(AA)] copolymer shell phases was seen when the hard shell phase comprised 25 – 40 wt% of the total particle, with the optimum system being that with 70:30 core:shell mass ratio.

A body of work relating to the effect of core:shell mass ratios, and hence the effect of changing the crosslinking density, in soft-soft nanocomposite PSA's was reported by Deplace *et al.*⁵ for structured core-shell particles consisting of a 2-EHA-based core phase copolymer and a virtually identical shell phase copolymer with DAAM added at a total level of 0.4 total polymer wt%. It was found that the low-strain mechanical properties were not significantly affected by the core:shell ratio and hence the crosslinking density distribution. However, at high strain the non-linear mechanical properties were strongly affected, proving the existence of a percolating, crosslinked network. Systems with a smaller proportion of

crosslinked shell phase copolymer, most specifically 80:20 core:shell ratio, showed the largest extent of strain hardening as can be seen from Figure 6.1. This is not unexpected due to this thinner shell phase having a higher DAAM-ADH crosslink density than the equivalent with a 45:55 core:shell mass ratio. The emergence of 80:20 as the optimum core:shell mass ratio for soft-soft nanocomposite PSAs was also noted by Foster *et al.*, who found that this core:shell ratio gave the best peel and shear resistance performance⁶.

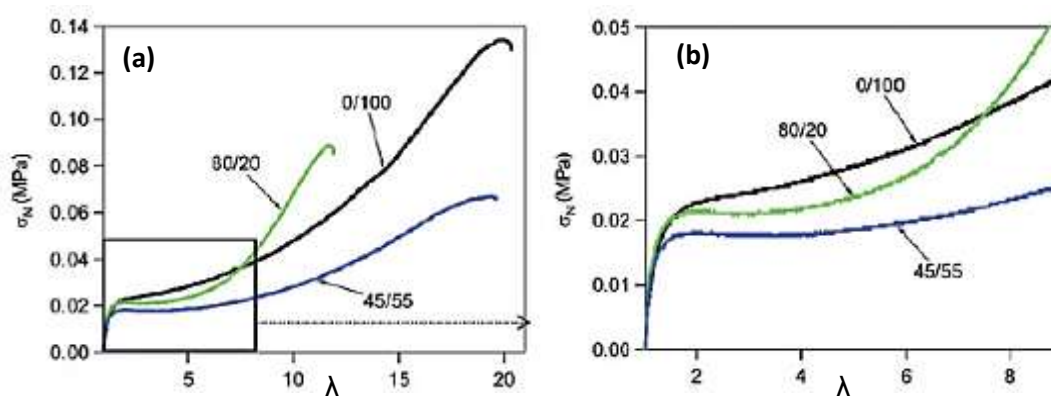


Figure 6.1 Nominal stress (σ_N)-extension ratio (λ) profiles showing (a) the effect of core/shell ratio on soft-soft nanocomposite PSAs with 2-EHA-based core and shell phase copolymers, where DAAM level is 0.4 wt% of the total particle; and (b) close-up of the boxed low-strain area of (a)

The observation that soft-soft nanocomposite films with lower proportions of crosslinked shell phase have optimum mechanical properties was substantiated by Pinprayoon *et al.*, who found that for soft-soft nanocomposite nitrile rubber mimics employing ionic crosslinking, the inclusion of structured particle morphology led to increased mechanical performance relative to equivalent, unstructured nanoparticles. For particles containing a larger proportion of shell, and hence crosslinkable, material a detrimental effect on mechanical properties was observed⁷. In this case the observation was attributed to the ionic crosslinking reaction being suppressed, due to unneutralised MAA-groups being ‘buried’ within the thicker shell phase and hence being unable to react with the Zn^{2+} ions.

The second parameter that will be discussed in this chapter is the effect of the level of DAAM-ADH crosslinking that is incorporated into the shell phase copolymer of soft-soft nanocomposite coating materials. The amount of DAAM that can be incorporated into the shell phase copolymer is limited. The reasoning for this is two-fold; firstly in order to retain the long-term storage stability of the latexes, as although DAAM and ADH reside in different phases of the latex, some reaction at the polymer-aqueous interface is unavoidable and over time can elevate the MFT of the polymer²⁰⁶. Secondly, polymerising large amounts of DAAM

into an emulsion copolymer can cause colloidal instability and particle coagulation. This is because above a certain concentration of DAAM in the monomer feed, approximately 7 wt%, it will polymerise in the aqueous phase to form water-soluble copolymers¹³¹. This relationship can be seen from Figure 6.2, which shows the effect of DAAM level upon both coagulum levels and particle size.

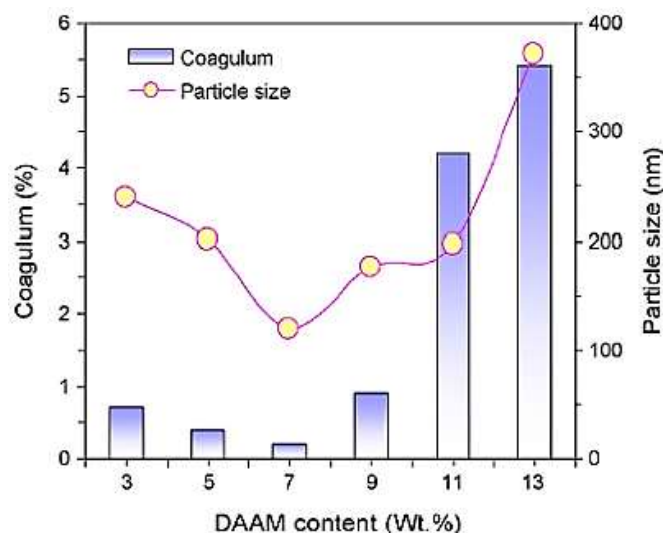


Figure 6.2 Plot showing the effect of DAAM content upon both coagulum levels and particle sizes for a poly[(MMA)-*co*-(BA)-*co*-(AA)-*co*-(HPMA)-*co*-(DAAM)] copolymer¹³¹

A study into the effect of ambient temperature self-crosslinking acrylate emulsions reported by Liu *et al.* found that the particle size and particle size distribution of a latex with a poly[(MMA)-*co*-(BA)-*co*-(AA)] core and a poly[(MMA)-*co*-(BA)-*co*-(AA)-*co*-(DAAM)] shell increased and decreased, respectively, with increasing DAAM content¹¹³. This was attributed to the affinity between hydrophilic DAAM and water and the likely formation of water-soluble DAAM oligomer that adsorbed to the surface of the particles, which is not unexpected at the high (7.0 wt% of shell phase) DAAM content used⁹⁶.

Joshi *et al.* reported on the effect of DAAM level incorporated into unstructured, low T_g poly[(MMA)-*co*-(BA)-*co*-(MAA)-*co*-(DAAM)] copolymers⁹⁶. As can be seen from Figure 6.3 the films, which had T_g values of < 10 °C, clearly show an increase in stress required for deformation and a decrease in extension to break as the DAAM content increases. A corresponding increase in Young's modulus was also reported, from ~20 MPa for a film containing no DAAM to ~40 MPa for that with 5 wt% DAAM. In this research DAAM was polymerised throughout the particle structure, although due to the hydrophilic nature of the DAAM groups it is unlikely that they will be evenly distributed throughout the particle. As previously discussed in this section, migration of DAAM to the particle surface and hence some unintentional structuring of the particle will have occurred.

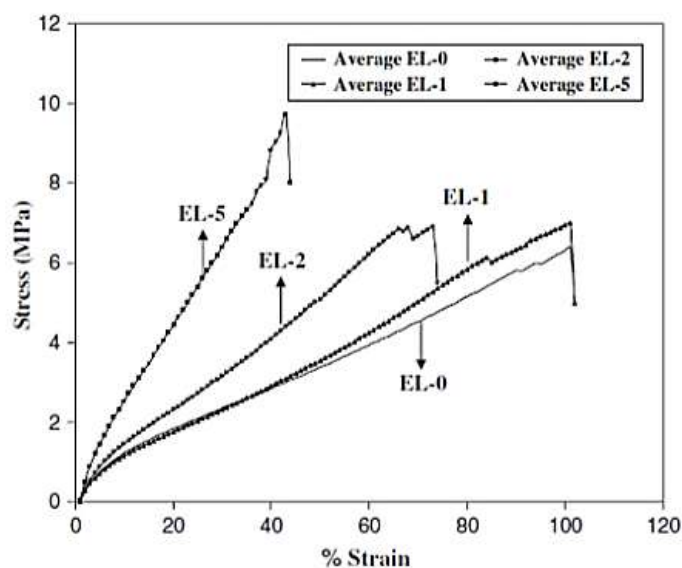


Figure 6.3 Stress-strain profiles showing the effect of DAAM in low T_g poly[(BMA)-*co*-(BA)-*co*-(MAA)-*co*-(DAAM)] films using the notation ‘EL-*x*’, where *x* is the wt% of DAAM incorporated into the copolymer⁹⁶

A similar increase in stress required to deform and decrease in extension to break with increasing DAAM content was observed by Zhang *et al.*²⁰⁷. The systems investigated in this paper were interpenetrating polymer networks (IPN) of poly[Sty-*co*-(2-EHA)-*co*-(1,6-HDDA)] (PS) and poly[(MMA)-*co*-(BA)-*co*-(MAA)-*co*-(DAAM)] (PA) copolymers. Figure 6.4 shows the independent effect of DAAM concentration in systems with a 50:50 ratio of PS:PA copolymers. The effect of DAAM content upon Young’s modulus in these systems was not discussed although from the stress-strain profiles in Figure 6.4 little difference can be seen in the initial slopes of each plot, suggesting that the effect is not as significant at low strain as it is at high strain values. These PS/PA IPN films are an example of a heterogeneous system, which structured core-shell particles such as soft-soft nanocomposites also are. Investigations of the effect of crosslinker content in DAAM-ADH containing soft-soft nanocomposite PSAs mostly concerned the effect of DAAM:ADH stoichiometric ratio rather than the effect of DAAM content⁴⁻⁶.

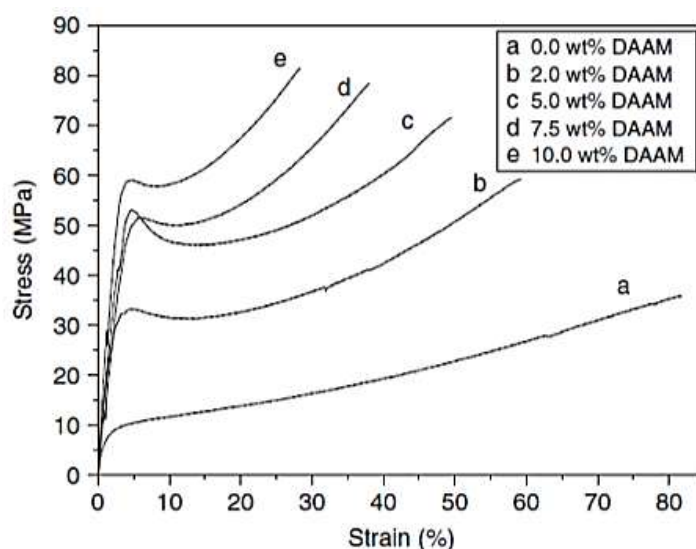


Figure 6.4 Stress-strain profiles showing the independent effect of DAAM content on tensile performance for 50:50 poly[Sty-*co*-(2-EHA)-*co*-(1,6-HDDA)]: poly[(MMA)-*co*-(BA)-*co*-(MAA)-*co*-(DAAM)] interpenetrating polymer networks²⁰⁷

Figure 6.5 shows stress-strain profiles for a soft-soft nanocomposite PSA film with varying levels of ADH added to it, where ‘100% ADH’ represents a 2:1 molar stoichiometric (DAAM:ADH) ratio, whereby in theory 100% of the DAAM pendant groups present react with an ADH functionality. The ‘classic’ system indicated by the bold black line refers to a commercial water-borne PSA consisting of homogenous particles with similar chemical composition to the soft-soft nanocomposite PSAs.

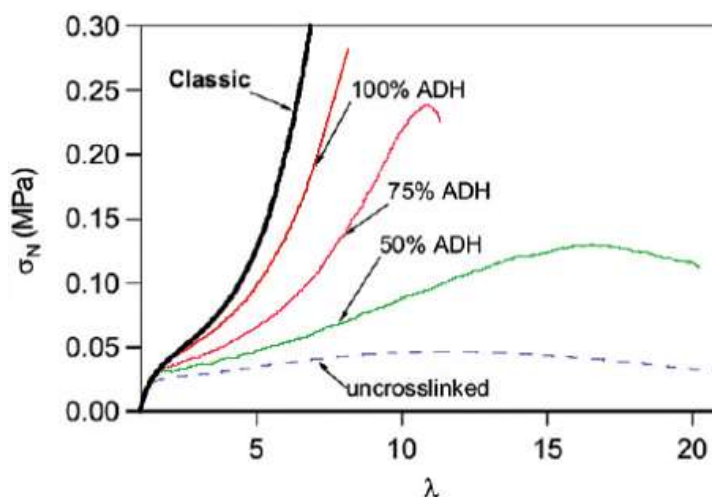


Figure 6.5 Nominal stress (σ_N)-extension ratio (λ) profiles showing the effect of DAAM:ADH stoichiometric ratio in soft-soft nanocomposite PSAs with an 80:20 core:shell ratio, 2-EHA-based core and shell phase copolymers. DAAM level is 0.4 wt% of the total particle, and 100% ADH represents a 2:1 (DAAM:ADH) ratio⁵

The stress-strain curves in Figure 6.5 clearly shows that as the proportion of DAAM units that are crosslinked increases, the films experience an increased degree of strain hardening and reduced extension to break. This observation is in line with those from Figure 6.3 and

Figure 6.4, whereby a similar effect is observed upon an increase in the level of crosslinking present.

As previously stated, Chapter 6 presents two of the key physical parameters involved in the design of lightly crosslinked structured particles. Firstly, an investigation into the effect of core:shell mass ratio will be described. In this section, the synthesis and subsequent mechanical testing of five different systems representing various proportions of both core and shell phase copolymers was performed, and the results discussed. For this work the T_g values of core and shell copolymers were kept constant at 5 °C, and the overall level of DAAM kept constant at 0.4 wt% of the total particle. Core and shell copolymer compositions are poly[(BA)-*co*-(BMA)] and poly[(BA)-*co*-(BMA)-*co*-(DAAM)], respectively. AFM images of soft-soft nanocomposite coating materials with core:shell mass ratios of 70:30, 80:20 and 90:10 will also be shown, in order to ascertain whether the same retained morphology seen in PSA films can be identified. The final two sections of this chapter describe the effect of varying the DAAM content in the shell phase copolymer and the DAAM:ADH stoichiometric ratio, respectively. Again, for all variants discussed in these sections both core and shell copolymer T_g will be constant at 5 °C, with core and shell compositions being poly[(BA)-*co*-(BMA)] and poly[(BA)-*co*-(BMA)-*co*-(DAAM)], respectively.

6.2 Effect of core:shell ratio on soft-soft nanocomposites

In order to establish the effect of core:shell ratio on film properties, a series of latexes with varying core:shell mass ratios were prepared, each with the same mass (and hence a different wt%) of DAAM in the shell phase copolymer, in order to give each variant the same total concentration of DAAM per latex particle. As per the research reported by Deplace *et al.* in 2009⁵, the aim of changing the core:shell ratio was to keep the total DAAM content constant. A consequence of this was a variation in the crosslink concentration in the percolating phase of the film with the shell phase thickness. Each variant incorporating a core-shell structure consisted of a poly[(BA)-*co*-(BMA)] core phase copolymer, and a poly[(BA)-*co*-(BMA)-*co*-(DAAM)] shell phase copolymer. Two ‘unstructured’ variants, which can be assumed to be representative of ‘100% core phase copolymer’ and ‘100% shell phase copolymer’ systems were also included. The T_g of all copolymers discussed in this section is 5 °C. The compositions of these latexes are given in Table 6.1, and a summary of the characterisation data for the preparations shown in Table 6.2. Full characterisation plots for each preparation can be found in Appendix (iii) of this thesis.

Table 6.1 Composition of soft-soft nanocomposite systems with varying core:shell ratios

Core:shell %wt ratio	Core/shell T_g / °C	Core composition	Shell composition	DAAM content / mmol g ⁻¹
0:100	- / 5	-	79.5 wt% BMA 20.1 wt% BA 0.4 wt% DAAM	0.087
70:30	5 / 5	80 wt% BMA 20% BA	77 wt% BMA 21 wt% BA 2 wt% DAAM	0.087
80:20	5 / 5	80 wt% BMA 20% BA	76 wt% BMA 21 wt% BA 3 wt% DAAM	0.087
90:10	5 / 5	80 wt% BMA 20% BA	71.2 wt% BMA 23 wt% BA 5.8 wt% DAAM	0.087
100:0	5 / -	80 wt% BMA 20 wt% BA	-	0.00

Table 6.2 Kinetics data for the soft-soft nanocomposite systems detailed in Table 6.1

Core:shell ratio	Core/Shell T_g / °C	Overall/ Instantaneous conversion ^a / %			Particle diameter ^b / nm			Total particle number ^c / x 10 ¹⁶		
		Seed	Core	Final	Seed	Core	Final	Seed	Core	Final
0:100	N/A / 5	3.2/89	N/A	95/95	94	N/A	275	5.89	N/A	6.86
70:30	5 / 5	3.7/98	68/97	97/97	98	259	296	5.64	3.22	3.46
80:20	5 / 5	3.7/99	77/96	97/97	101	279	305	5.09	5.08	4.86
90:10	5 / 5	3.4/99	81/95	93/93	89	262	272	7.64	7.15	7.40
100:0	5 / N/A	2.4/58	N/A	99/99	94	N/A	321	1.94	N/A	4.00

^a Calculated using solids content measurements (see Section 3.4.1.6)

^b z-average particle diameter; obtained using PCS (see Section 3.4.1.2)

^c Calculated using PCS measurements of z-average particle diameter

The data in Table 6.2 show that for the 90:10 core:shell variant a low final conversion of 93% is gained. As the particle number does not change significantly during the reaction, it can be assumed that this is due to evaporation of monomer and not particle coagulation. This may also explain the smaller particle size that is observed for this variant. A reduction in particle number was seen for the variant with a core:shell ratio of 70:30, which can be attributed to coagulation in conjunction with the slightly lower than expected final conversion of 97%. Secondary nucleation of particles appears to occur in the variant with 100:0 core:shell ratio, although as was previously explained in Section 5.2 this may be due to particle nucleation not being complete at the end of the seed phase, which had a final conversion of only 58%.

The pH of each DAAM-containing system was adjusted to 8.5 - 9 using sodium hydroxide, then an aqueous 10 wt% ADH solution added to give a molar stoichiometric DAAM:ADH ratio of 2:1 (i.e. 100% of DAAM units crosslinked). For the 100:0 core:shell ratio variant (i.e. 100% poly[(BA)-*co*-(BMA)] copolymer), no neutralisation or addition of ADH was done. Tensile testing was then performed on films cast from these latexes using the procedures detailed in Sections 3.3.2 and 3.4.2.1, respectively. As per the low strain expansions of the stress-strain plots given in Chapter 5 it should be noted that some of the initial stresses start above zero, which again can be attributed to inaccuracies encountered from using jaw separation as a measure of strain.

The comparative stress-strain profiles for these variants, which can be seen in Figure 6.6, show that there is no general trend in mechanical properties with core:shell ratio that can be clearly identified between particles incorporating DAAM-ADH crosslinking at different densities. The uncrosslinked 100:0 '100% core' variant showed stress-strain behaviour analogous with uncrosslinked soft-soft nanocomposite PSAs⁵, and passed through a peak stress before softening until failure at almost 2000% of its original length.

All variants incorporating keto-hydrazide crosslinking showed the characteristic increase in stress required for deformation at higher extensions that was seen for crosslinked films in Chapter 5. The data given in Table 6.3 shows that little difference in Young's modulus can be seen between the three variants, and what difference there is well within the limits of experimental error. However, a large difference can be seen in the extension to break values, with the 80:20 film breaking at a significantly lower value than the 70:30 or 90:10 variants. As the shell phase becomes a higher proportion of each particle, the materials appear to show an increasing stress required for deformation up to 100% strain, which is to be expected due to a higher concentration of crosslinked material being present in a thinner shell phase.

Above strains of 600%, the 70:30 variant strain hardens before breaking, whereas the 90:10 film does not. This can be attributed to the very thin shell phase of the 90:10 system, which is only 10 nm in thickness and is therefore unlikely to be a coherent phase, more likely existing as patches of crosslinked material in the film. The likelihood of these thin shell phase copolymers existing as a coherent layer will be discussed further in Section 6.3. Conversely, the shell phase of the 70:30 film is 36 nm thick so will have more of an influence upon the mechanical properties at high strain due to it being likely to exist as a percolating, crosslinked matrix.

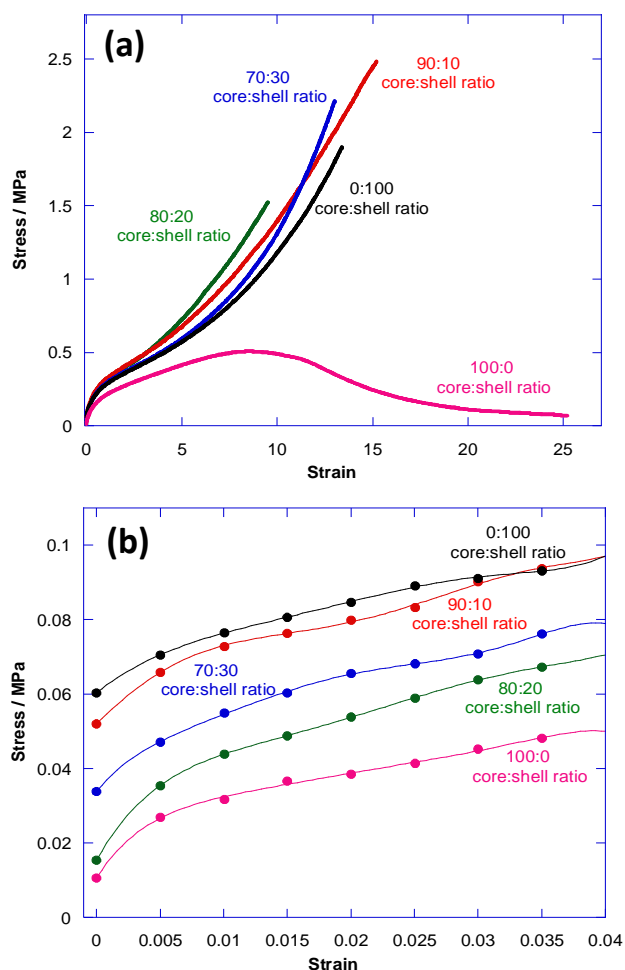


Figure 6.6 (a) Stress-strain curves for films with varying core:shell ratio. Film composition is poly[(BA)-*co*-(BMA)] core phase copolymer and poly[(BA)-*co*-(BMA)-*co*-(DAAM)] shell phase copolymer with ADH added at 2:1 molar stoichiometric ratio; **(b)** Section of stress-strain curves from (a) with strains of 0-4% used to calculate Young's modulus (coefficient of first order term in a polynomial fit expression; order of fit = 6)

Table 6.3 Mechanical property data for variants discussed in Section 6.2

Core:shell ratio	Young's modulus / MPa	Stress at 4% strain / MPa	Extension to break / %
0:100	4.18 (± 1.8 MPa)	0.118 (± 0.006)	1100 ($\pm 45\%$)
70:30	4.9 (± 0.3 MPa)	0.06 (± 0.006)	1300 ($\pm 150\%$)
80:20	11.7 (± 4 MPa)	0.07 (± 0.016)	980 ($\pm 130\%$)
90:10	8.7 (± 1.8 MPa)	0.10 (± 0.011)	1200 ($\pm 60\%$)
100:0	4.3 (± 0.2 MPa)	0.05 (± 0.003)	1900 ($\pm 650\%$)

However, at very high strains (> 200%) it can be clearly seen that the variant with a core:shell mass ratio of 80:20 gives the optimum mechanical behaviour, requiring higher stresses to be axially deformed. There is no explanation that can be easily given for this

observation, however it does substantiate findings by both Foster *et al.*⁶ and Deplace *et al.*⁵, who both reported that optimum mechanical performance of soft-soft nanocomposite PSAs was seen at this core:shell mass ratio. This may be due to the distribution of DAAM groups within the shell phase, as in previous work regarding soft-soft nanocomposite PSAs it has been stated that these are located on the surface of the particles⁶. This assumption stems from studies of the distribution of acid groups on the surface of latex particles that were first reported by Vanderhoff *et al.*²⁰⁸ in 1975, and subsequently expanded on^{209, 210}. The findings in these studies, which relate to weak acid groups, can be applied to the distribution of DAAM groups due to the multiple hydrophilic functionalities present in the molecule. Winnik *et al.* reported that a fraction, specifically 27%²¹¹, of acid groups remained 'buried' in particles with a poly(BMA) core and poly[(BMA)-*co*-(MAA)] shell containing approximately 6 wt% acid in the shell phase²¹² due to the saturation of the particle surface by the MAA side groups.

A far lower concentration of DAAM is present in the shell phase of the latex with an 80:20 core:shell ratio described in Table 6.1, so it can be assumed that for these soft-soft nanocomposite particles the optimum saturation of the particle surface by hydrophilic side-groups such as DAAM occurs at this core:shell ratio, and that no additional DAAM remains buried within the particles. However, due to the nature of these groups it is not possible to confirm this using experimental methods, as the DAAM functionalities are not easily ionised and hence cannot be analysed using the titration methods typically used to analyse the surface concentration of acid groups^{213, 214}.

6.2.1 Hysteresis and stress relaxation mechanical testing of soft-soft nanocomposites with varying core:shell ratio

As was discussed in Sections 3.4.2.3 and 3.4.2.2, respectively, hysteresis and stress relaxation mechanical testing both investigate the viscoelastic properties of polymer films. It is important to establish this for coatings intended for use on dimensionally unstable substrates, such as wood which fluctuates in size depending on environmental conditions such as temperature and humidity. A coating for such substrates must be able to recover fully after deformation, in order to remain coherent and mechanically strong.

Hysteresis and stress relaxation testing was performed on selected soft-soft nanocomposites, with the main variable being the core:shell mass ratio. Table 6.4 shows a summary of the films used for the testing discussed in this section. The composition of all films was poly[(BA)-*co*-(BMA)] core phase and poly[(BA)-*co*-(BMA)-*co*-(DAAM)] shell phase copolymers, with DAAM at a fixed level of 2 wt% in the shell phase copolymer throughout the testing.

Table 6.4 Films used for hysteresis and stress relaxation testing discussed in Section 6.2.1

Core:shell ratio	Core/Shell T_g / °C	DAAM content / shell wt%	Young's modulus / MPa
0:100	N/A / 5	2.00	9.5 (± 0.5 MPa)
70:30	5 / 5	2.00	4.9 (± 0.4 MPa)
80:20*	5/5	2.00	11.6 (± 3.3 MPa)
90:10	5 / 5	2.00	6.5 (± 1.1 MPa)

Hysteresis testing was performed according to the method described in Section 3.4.2.3, whereby the films were extended to 12.5% strain before being retracted back to 0% strain and rested for 10 minutes. The extension and retraction processes were then repeated.

The resulting mechanical profiles from this testing are shown in Figure 6.7. It can be seen that after 10 minutes rest all strain is recovered from the films at every core:shell ratio tested, with the second extension cycles starting from zero stress, indicating that complete mechanical recovery had occurred. Other observations that can be made from these hysteresis curves are that higher stresses are needed to extend the sample for the second cycle than for the initial extension, and that there is a dissipation of energy observed between the extension and relaxation phases of all films, which is to be expected for the mechanical hysteresis of elastomers¹⁷.

Some negative stress values can be seen in Figure 6.7(a) and (c) for the unloading section of the curves. This is an artefact from the testing equipment, whereby zero stress is taken when the sample has been clamped and therefore may be under very small nominal stresses that are not present when the sample becomes totally unloaded.

These observations regarding strain recovery and mechanical hysteresis provide further proof that these soft-soft nanocomposite-type materials are suitable for use as coatings, as they can fluctuate in dimension without any loss of elasticity. Higher stresses were required for subsequent extension processes, which may be due to the chains being extended into the non-Gaussian region²¹⁵. This indicates that over time the coating may harden further and ultimately fail. However it should be considered that, realistically, a dimensionally unstable substrate will not expand and contract to the extent that the films in Figure 6.7 have.

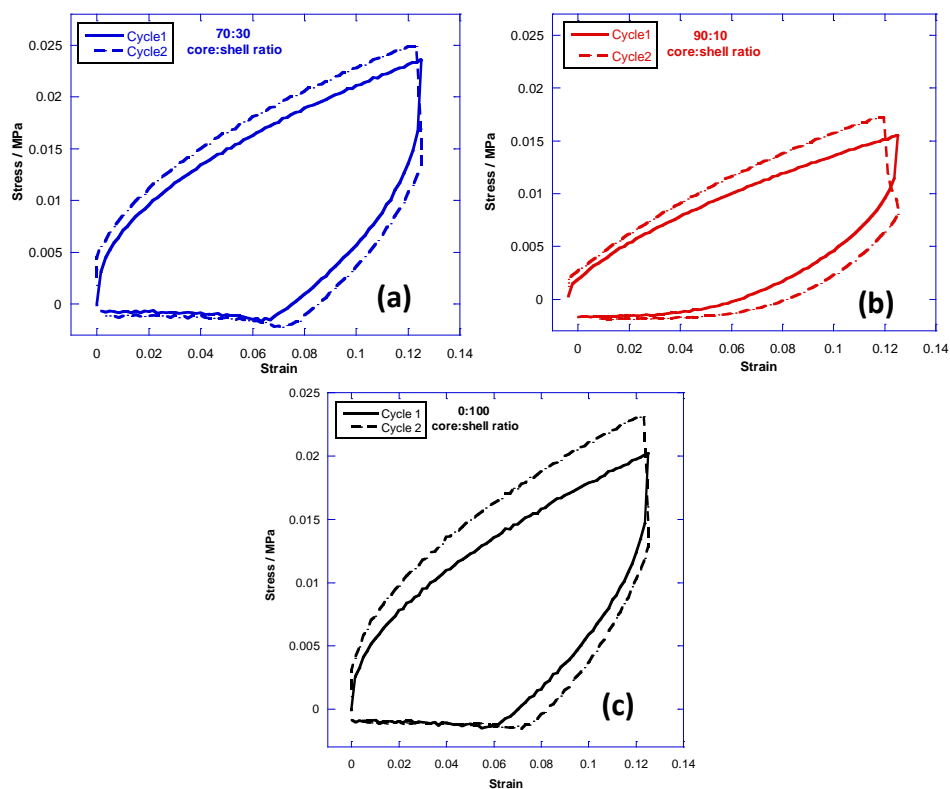


Figure 6.7 Mechanical hysteresis profiles for soft-soft nanocomposites with 2 wt% DAAM in the shell phase copolymer and **(a)** 70:30; **(b)** 90:10 and **(c)** 0:100 core:shell mass ratios. Samples extended to 12.5% strain before retraction to 0% strain, 10 minutes left between cycles 1 and 2

Stress relaxation testing was conducted on the films detailed in Table 6.4, in order to investigate the time-dependent mechanical relaxation behaviour. The procedure discussed in Section 3.4.2.2 was used, whereby the films were extended to 100% strain then held, and the stress monitored over a 10 minute period.

The resulting stress-time profiles are shown in Figure 6.8, and it can be immediately seen that two regimes of relaxation occur. The first occurs on a very short (< 10 second) timescale, and the second over a much longer period (> 400 seconds). The characteristic relaxation times, τ_0 , for both of these regimes are given in Table 6.5, and were calculated using the Maxwell equation (see Section 3.4.2.2).

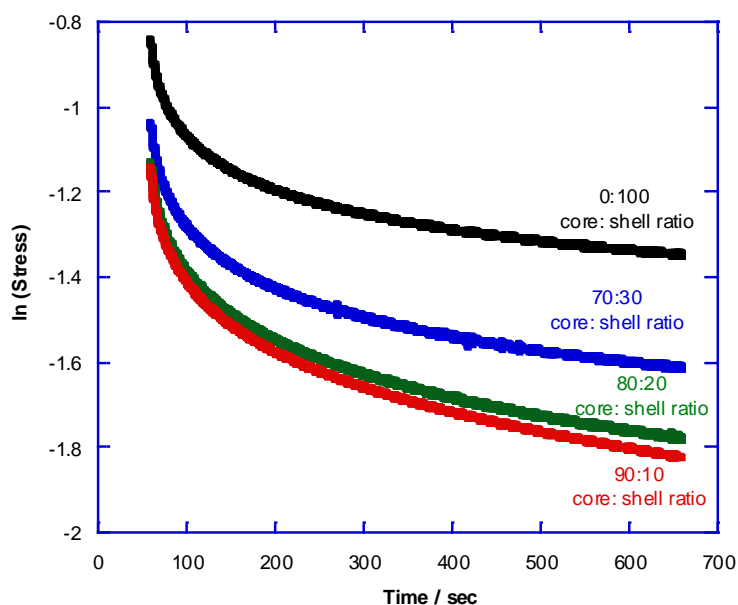


Figure 6.8 Stress relaxation profiles for soft-soft nanocomposites of varying core:shell ratio. All variants contain 2 wt% DAAM in the shell phase copolymer

Table 6.5 Stress relaxation property data for the films detailed in Table 6.4

Core:shell ratio	Relaxation time τ_0 / s (Short times; $t = 0-10$ s)	Relaxation time τ_0 / s (Long times; $t > 400$ s)
0:100	92.2	4310
70:30	89.2	3500
80:20	86.8	2730
90:10	83.2	2450

The plot in Figure 6.8 and the data in Table 6.5 show that all systems tested exhibited very similar stress relaxation profiles, shifted from each other by the relative Young's modulus values for each film (see Table 6.4). As previously discussed, two very different regimes of stress relaxation behaviour are observed - an initial period of rapid relaxation (from approximately 0 – 10 seconds) is associated with short relaxation times. This can be attributed to the relaxation of uncrosslinked polymer chains, such as are present in the core phase of the particles. Although little difference can be discerned between each system, the value of τ_0 decreases slightly as the proportion of core phase polymer increases. A curved transition region then leads into a secondary regime (above ~ 400 seconds) in which the relaxation stress behaviour becomes linear and more differentiation can be made between each system. This regime represents the comparatively more hindered relaxation of the crosslinked shell phase polymer chains, and it can be seen from Table 6.5 that longer relaxation times are found for films with a higher proportion of shell phase copolymer, which

may be a consequence of the increased proportion of crosslinked shell material within each film.

The data presented in this section shows that these soft-soft nanocomposite materials exhibit viscoelastic mechanical behaviour. Mechanical hysteresis testing showed that the relaxation of the films was accompanied by a very small dissipation of energy relative to the extension, and that after 10 minutes rest between cycles the film had almost completely recovered. Stress relaxation tests showed that the overall behaviour of each system was very similar, with two regimes of behaviour observed that could be analysed using the linear Maxwell model. The initial regime lasted for up to 10 seconds from the start of relaxation, and relaxation time τ_0 showed little difference between the core:shell ratios tested. The secondary regime onset at ~ 400 seconds and lasted until the end of the test (600 seconds), and a more significant difference in relaxation time could be seen between each core:shell ratio for this region of the relaxation process.

6.2.2 Effect of core:shell ratio on copolymer molar mass

In order to deduce whether core:shell mass ratio affects the molar mass of the copolymers produced during the emulsion polymerisation process, gel permeation chromatography (GPC) was used to analyse selected soft-soft nanocomposite systems. The variants used for this testing all consisted of a poly[(BA)-*co*-(BMA)] core phase copolymer and a poly[(BA)-*co*-(BMA)-*co*-(DAAM)] shell phase copolymer, both with T_g of 5 °C. It should be noted that no ADH was added into any of the systems tested, so these can be considered to be completely uncrosslinked. Table 6.6 shows the systems used for the testing discussed in this section.

Table 6.6 Soft-soft nanocomposite latexes used for GPC analysis

Core:shell ratio	DAAM content /wt% in shell	Core/shell T_g /°C	Particle size /nm	Solids content / wt%
0:100	2.0	- / 5	275	51.6
70:30	2.0	5 / 5	326	51.8
80:20	2.0	5 / 5	306	52.4
90:10	2.0	5 / 5	273	53.3
100:0	-	5 / -	321	52.4

Samples were prepared for analysis by firstly coagulating the polymer using a freeze-thaw method, then washing and drying the coagulated latex at 60 °C for at least 3 days. The polymer was then dissolved in distilled and filtered THF at a concentration of 0.2 wt%, and run through the GPC column. A full description of the method used can be found in Section 3.4.1.4. Table 6.7 and Figure 6.9 show the GPC data and the molar mass distribution curves, respectively, for the variants discussed in Table 6.6.

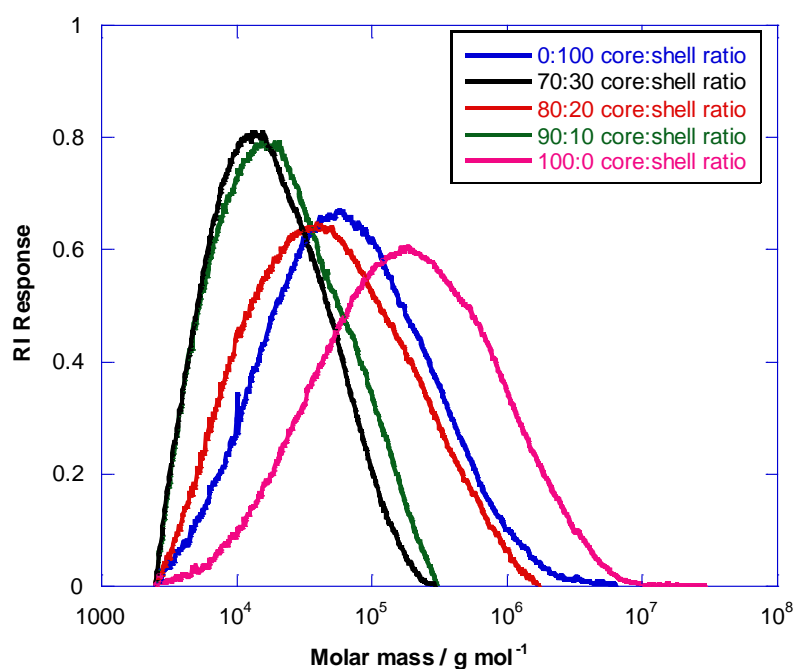


Figure 6.9 GPC traces for soft-soft nanocomposite systems

Table 6.7 GPC analysis data for soft-soft nanocomposite polymers with varying core:shell ratios

Core:shell ratio	DAAM content / wt% in shell	\overline{M}_n / g mol ⁻¹	\overline{M}_w / g mol ⁻¹	$\frac{\overline{M}_w}{\overline{M}_n}$
0:100	2.0	63,900	340,000	5.32
70:30	2.0	103,400 (± 42,800)	359,000 (± 61,600)	3.94 (± 1.26)
80:20	2.0	106,400 (± 19,000)	430,000 (± 40,300)	4.12 (± 0.51)
90:10	2.0	90,300 (± 12,200)	305,000 (± 48,600)	3.41 (± 0.61)
100:0	-	68,300	474,000	6.94

As can be seen from these data, no correlation between core:shell mass ratio and molar mass can be identified, although in all cases the \overline{M}_n of the polymer was $\sim 100,000$ g mol⁻¹ and the $\overline{M}_w \sim 350,000$ g mol⁻¹. The dispersities ($\frac{\overline{M}_w}{\overline{M}_n}$) were large (~ 4 -7) observed for all core:shell ratios, which was not unexpected as large dispersities are not uncommon for polymer

latexes. This is potentially due to chain transfer to polymer occurring²¹⁶, which creates non-linear structures that are known to have large molar mass distributions and dispersities²¹⁷.

6.2.3 Visualisation of soft-soft nanocomposite films with varying core:shell ratio

An important principle of the soft-soft nanocomposite design strategy is the retention of core-shell morphology in the fully-formed film. In order to see whether this has been achieved, cross-sections of soft-soft nanocomposite coating films were imaged using AFM. As the core and shell phases are very similar in chemical composition and T_g , Quantitative Nanomechanical Mapping (QNM) was used to look at the relative moduli of the phases. Due to the presence of keto-hydrazide crosslinking in the shell phase only, this part of the film will have a higher Young's modulus than the uncrosslinked, viscoelastic core polymer when the two phases are composed of virtually identical copolymers. It is a matter of debate whether it is possible to visualise a defined core-shell morphology, because the shell phases of the particles are very thin (theoretical thickness < 15 nm for 90:10 core:shell mass ratio based on a 250 nm particle size) and may not exist as a coherent layer but instead as 'patches' on the surface of the shell phase copolymer particles⁶².

To facilitate the successful discrimination of the two phases, films with core phase T_g above 20 °C and shell phase T_g of 5 °C were imaged, as this would provide the optimum mechanical differentiation at the testing temperature of approximately 18 °C. Figures 6.10 – 6.14 show DMT modulus AFM images for films with 70:30, 80:20 and 90:10 core:shell ratios. The retention of core-shell morphology is immediately obvious for the 70:30 core:shell ratio films (Figures 6.10 and 6.11). The core phase polymer, which is in the closer to the glass transition at the testing temperature and therefore slightly harder than the rubbery shell phase, can be seen as isolated, deformed particles distributed in a percolating, continuous shell polymer matrix.

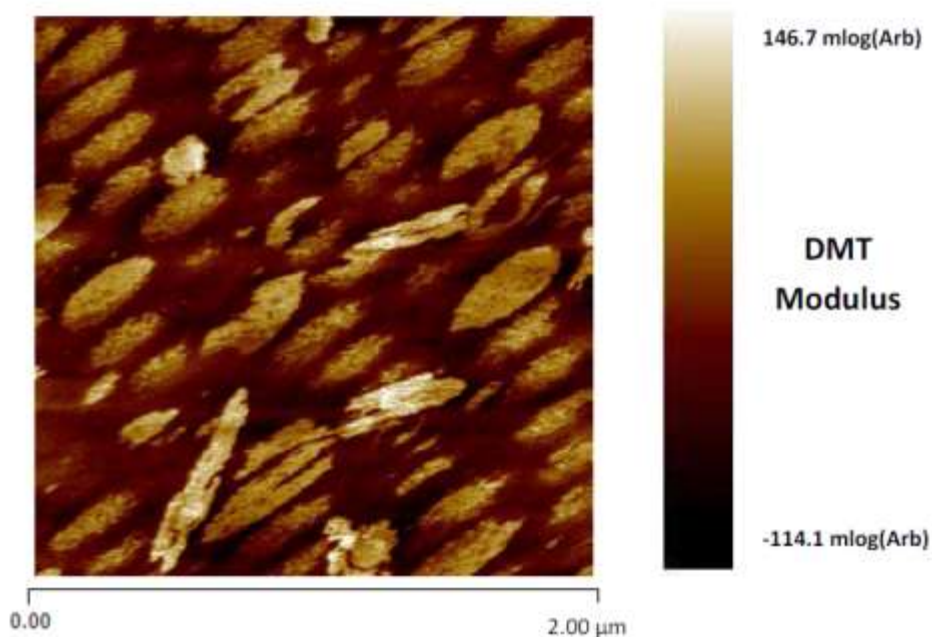


Figure 6.10 DMT Modulus AFM image of a lightly crosslinked soft-soft nanocomposite film cross-section with 70:30 core:shell ratio, comprising poly[(BA)-*co*-(BMA)] core and poly[(BA)-*co*-(BMA)-*co*-(DAAM)] shell phase copolymers with T_g s of 25 and 5 °C, respectively. ADH added at a 2:1 DAAM:ADH molar stoichiometric ratio. Image size = 2 μm square

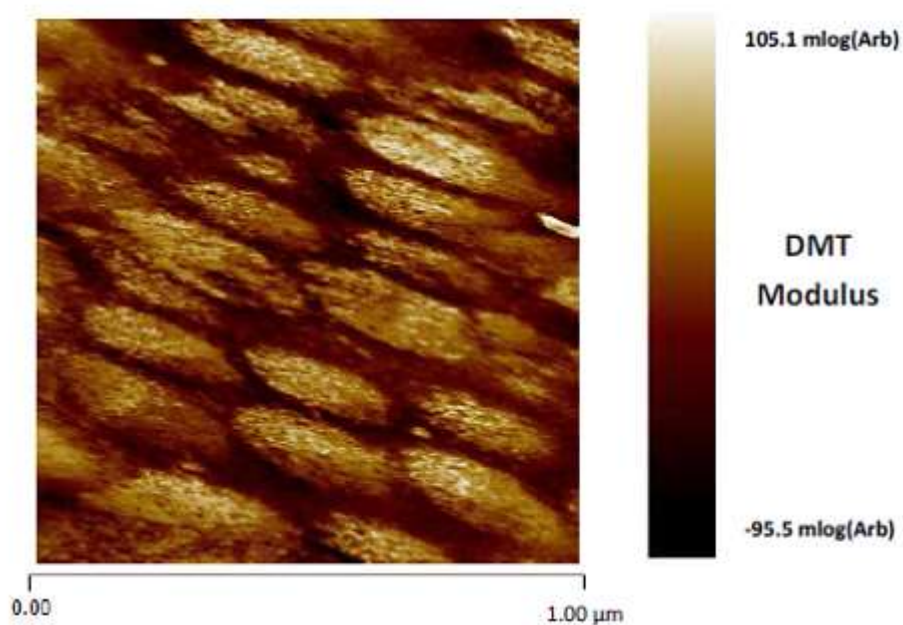


Figure 6.11 DMT Modulus AFM image of a lightly crosslinked soft-soft nanocomposite film cross-section with 70:30 core:shell ratio, comprising poly[(BA)-*co*-(BMA)] core and poly[(BA)-*co*-(BMA)-*co*-(DAAM)] shell phase copolymers with T_g s of 25 and 5 °C, respectively. ADH added at a 2:1 DAAM:ADH molar stoichiometric ratio. Image size = 1 μm square

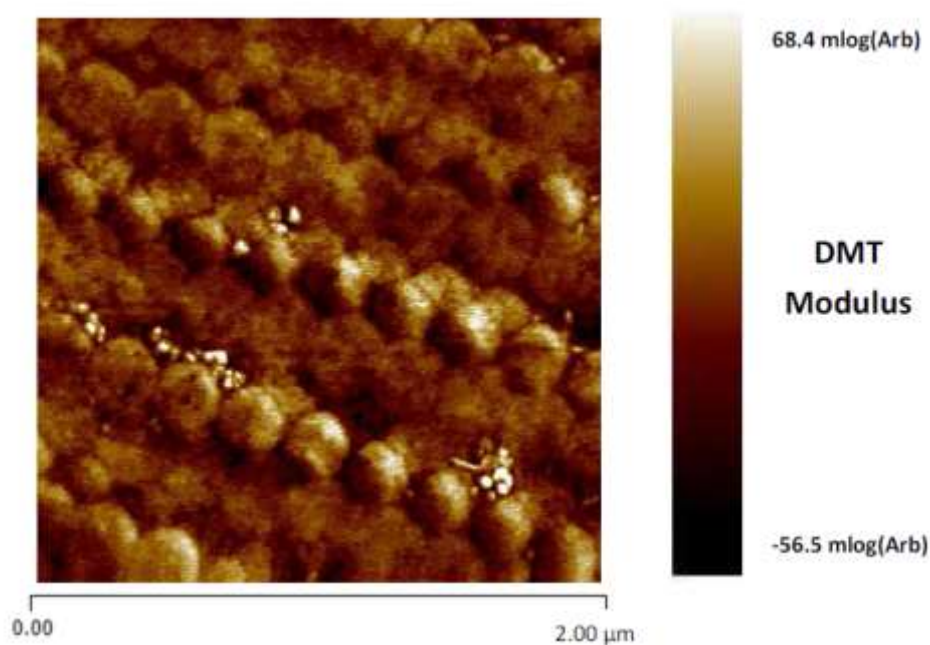


Figure 6.12 DMT Modulus AFM image of a lightly crosslinked soft-soft nanocomposite film cross-section with 80:20 core:shell ratio, comprising poly[(BA)-*co*-(BMA)] core and poly[(BA)-*co*-(BMA)-*co*-(DAAM)] shell phase copolymers with T_g s of 25 and 5 °C, respectively. ADH added at a 2:1 DAAM:ADH molar stoichiometric ratio. Image size = 2 μm square

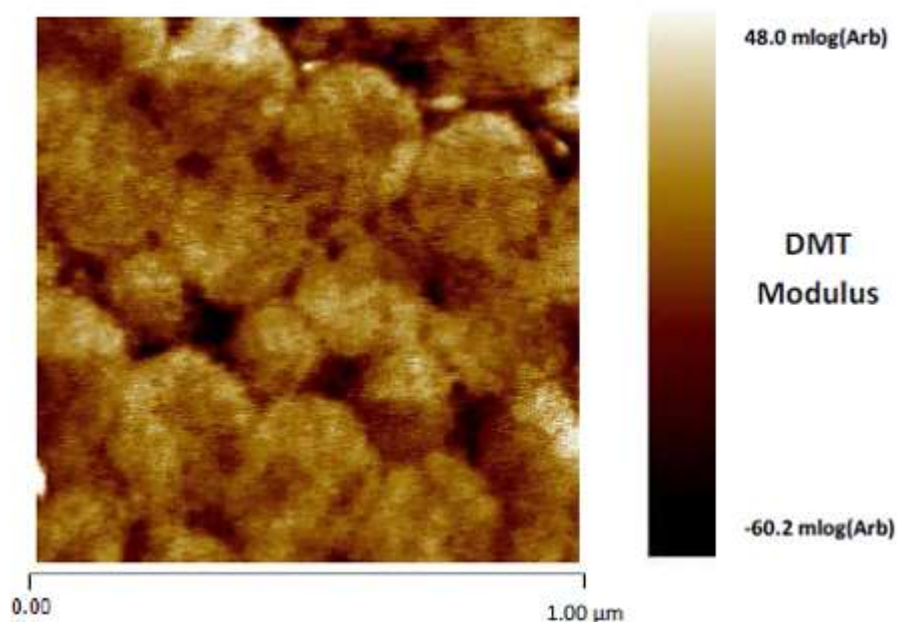


Figure 6.13 DMT Modulus AFM image of a lightly crosslinked soft-soft nanocomposite film cross-section with 80:20 core:shell ratio, comprising poly[(BA)-*co*-(BMA)] core and poly[(BA)-*co*-(BMA)-*co*-(DAAM)] shell phase copolymers with T_g s of 25 and 5 °C, respectively. ADH added at a 2:1 DAAM:ADH molar stoichiometric ratio. Image size = 1 μm square

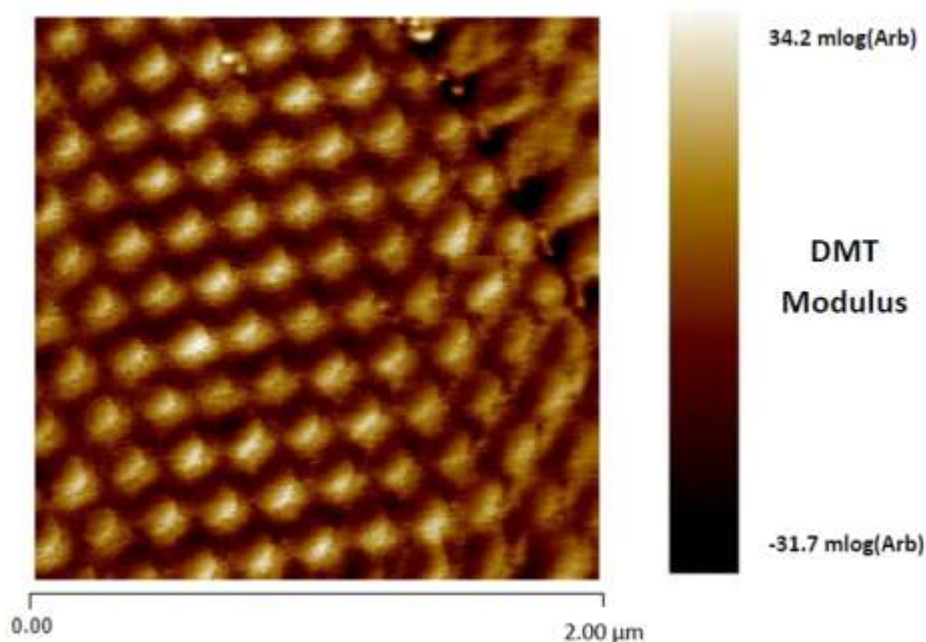


Figure 6.14 DMT Modulus AFM image of a lightly crosslinked soft-soft nanocomposite film cross-section with 90:10 core:shell ratio, comprising poly[(BA)-*co*-(BMA)] core and poly[(BA)-*co*-(BMA)-*co*-(DAAM)] shell phase copolymers with T_g s of 20 and 5 °C, respectively. ADH added at a 2:1 DAAM:ADH molar stoichiometric ratio. Image size = 2 μ m square

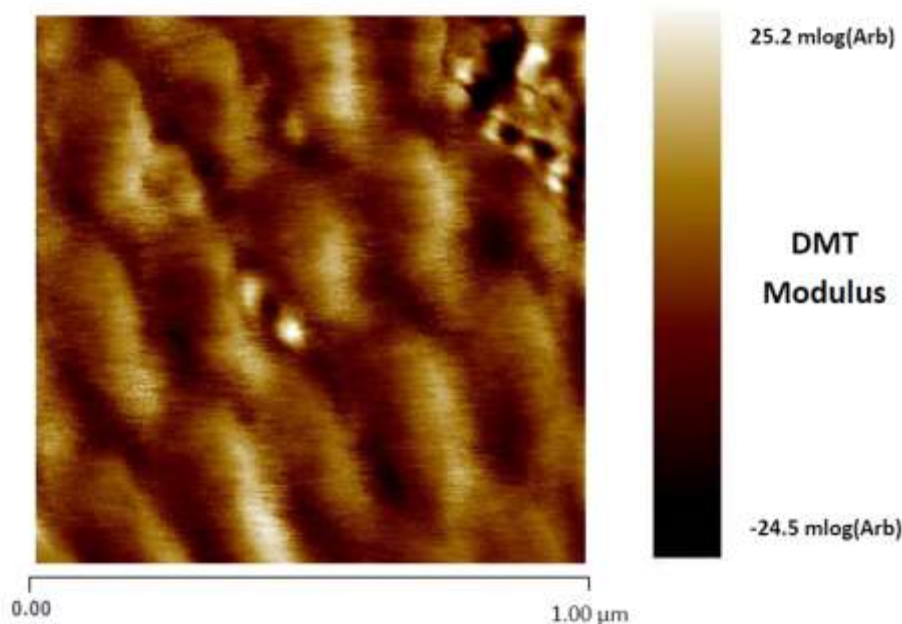


Figure 6.15 DMT Modulus AFM image of a lightly crosslinked soft-soft nanocomposite film cross-section with 90:10 core:shell ratio, comprising poly[(BA)-*co*-(BMA)] core and poly[(BA)-*co*-(BMA)-*co*-(DAAM)] shell phase copolymers with T_g s of 20 and 5 °C, respectively. ADH added at a 2:1 DAAM:ADH molar stoichiometric ratio. Image size = 1 μ m square

The apparent orientation of the particles in Figures 6.10 and 6.11 is due to the orientation of the sample relative to the AFM cantilever, and not an inherent property of the

film. This image was captured in early experiments with the equipment and in all subsequent imaging the orientation of the sample was carefully aligned perpendicular to the cantilever in order to eliminate these effects.

Figures 6.12 and 6.13, which are of the 80:20 core:shell ratio film, show that individual particle artefacts of approximately 270 nm in diameter can be discerned within the film structure. However, an extremely well defined core-shell structure, as in for the 70:30 core:shell film images, cannot be seen for this system. In the 1 μm square image (Figure 6.13), it is possible to see darker areas around the particle boundaries and also in interstitial areas between the particle cores. This suggests retention of the morphology in the fully formed film, although due to the relative proportions of core and shell phase polymer it is naturally less well defined.

The images of a 90:10 core:shell ratio shown in Figures 6.14 and 6.15 show that a core-shell type morphology is clearly observable. Despite the very small thickness of the shell phase in this system, it can be seen from the 1 μm image in Figure 6.15 that darker areas, which correspond to the lower T_g crosslinked shell phase copolymer, can be seen dispersed around the lighter, and therefore harder, higher T_g core phases. The distribution of the darker coloured percolating matrix is not particularly even which may indicate that, although the shell phase forms a more complete layer around the core particle than expected, it is not entirely coherent and some 'patches' remain uncovered on the particle surfaces.

The AFM images shown in this section confirm that the retention of core-shell morphology in the fully-formed film occurs for soft-soft nanocomposite coating materials, even at core:shell mass ratios where the shell phase is too thin to be expected to form a coherent layer. This is further proof that it is possible to successfully apply the soft-soft nanocomposite design theory to systems with T_g very close to application temperature, as the images shown in Figure 6.10 -Figure 6.15 show that another of its key principles holds.

6.3 Effect of crosslinker content on film properties

The inclusion of a latent crosslinking system, for example keto-hydrazide crosslinking, is another of the fundamental principles of the soft-soft nanocomposite design theory. Preliminary studies, reported in Chapter 5, show significant effects upon the mechanical properties of films with T_g close to ambient temperature. The effects of varying both the diacetone acrylamide content of the latex particles and the DAAM:ADH stoichiometric ratio are described in this section.

6.3.1 Unstructured particles of uniform composition

In order to provide a 'control' for the core-shell systems, two latexes consisting of unstructured particles with uniform radial composition were synthesised and tested. To be consistent with the nomenclature of previously discussed soft-soft nanocomposite systems, these will be described as '0:100 core:shell latexes'. One 0:100 core:shell system contained a standard 2 wt% of DAAM, and the other a much lower amount that corresponded to the same overall concentration of DAAM per particle as for the structured systems investigated in Chapter 5. Table 6.8 provides a summary of the kinetics data for these preparations, and detailed characterisation plots can be found in Appendix (iii).

Table 6.8 Latex characterisation data for the synthesis of 0:100 core:shell latexes

DAAM content / wt% in shell phase copolymer	Overall/ Instantaneous conversion ^a		Particle diameter ^b / nm		Total particle number ^c / x 10 ¹⁶	
	Seed	Final	Seed	Final	Seed	Final
0.4	3.1/87	96/96	100	297	4.68	5.49
2.0	3.2/89	95/95	93	275	5.89	6.86

^a Calculated using solids content measurements (see Section 3.4.1.6)

^b z-average particle diameter; obtained using PCS (see Section 3.4.1.2)

^c Calculated using PCS measurements of z-average particle diameter

For both sets of data in Table 6.8, a slight increase in particle number occurs during the polymerisation process. However, as can be seen from the characterisation plots in Appendix (iii), these changes are not significant enough to affect the properties of the latex. Lower than expected conversions are also seen, which can be attributed to the evaporation of monomer rather than coagulation when examined in tandem with the particle number data.

ADH was added to these latexes at a 2:1 DAAM:ADH stoichiometric ratio, which would theoretically mean that the maximum possible extent of crosslinking will occur (i.e. every single DAAM present molecule forms a crosslink), assuming 100% efficiency of the crosslinking reaction. Films were then cast from these latexes and tensile tested according to the procedures given in Sections 3.3.2 and 3.4.2.1, respectively, and the resulting stress-strain profiles are shown in Figure 6.16. Table 6.9 gives the resulting mechanical property data.

It is immediately obvious from the stress-strain profiles in Figure 6.16 that an increased level of crosslinking leads to a more significant degree of hardening at high (> 50%) strains and a reduced extension to break. However, this difference is not reflected in the low strain behaviour, as the Young's modulus and stress at 4% values for the two systems are quite

similar. This observation is consistent with that made in Chapter 5, whereby the addition of low levels of keto-hydrazone crosslinking appeared to only significantly affect the high strain tensile behaviour of the film.

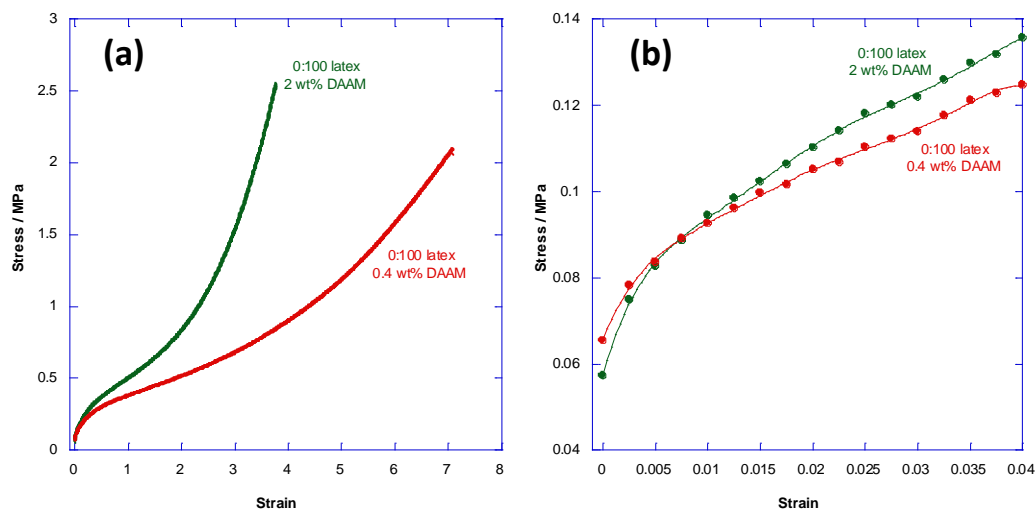


Figure 6.16 (a) Stress-strain curves for 0:100 core:shell ratio films with varying DAAM contents. Film composition is poly[(BA)-*co*-(BMA)] core phase copolymer and poly[(BA)-*co*-(BMA)-*co*-(DAAM)] shell phase copolymer with ADH added at 2:1 molar stoichiometric ratio; **(b)** Section of stress-strain curves from **(a)** with strains of 0-4% used to calculate Young's modulus (coefficient of first order term in a polynomial fit expression; order of fit = 6)

Table 6.9 Mechanical property data for 0:100 core:shell latexes with varying levels of DAAM

DAAM content / shell phase wt%	Young's Modulus/ MPa	Stress @ 4% Strain/ MPa	Extension to break /%
0.4	4.18 (± 1.8 MPa)	0.118 (± 0.006)	1100 ($\pm 45\%$)
2.0	9.48 (± 0.5 MPa)	0.136 (± 0.008)	630 ($\pm 70\%$)

6.3.2 Structured core-shell particle latexes

6.3.2.1 70:30 core:shell ratio

Four latexes were prepared and tested for this work, up to a maximum DAAM content of 6 shell phase wt%. Attempts to prepare latexes with higher DAAM contents of 7.5 and 10 wt% gave high levels of coagulum (~2-3 wt% when dried), so these variants were not included in the testing schedule. This is a well-known effect, and arises due to DAAM polymerising in the aqueous phase to form a water-soluble copolymer¹³¹. The latex characterisation data given in Table 6.10 shows the controlled nature of each synthesis, as high instantaneous conversion and consistent particle numbers are seen for all variants. Detailed plots of the data given in Appendix (iii).

Table 6.10 Latex characterisation data for the synthesis of 70:30 core:shell latexes with varying levels of DAAM

DAAM content / shell wt%	Overall / Instantaneous conversion ^a			Particle diameter ^b / nm			Total particle number ^c / x 10 ¹⁶		
	Seed	Core	Final	Seed	Core	Final	Seed	Core	Final
2.0	3.7/98	68/97	97/97	98	263	296	5.64	3.09	3.46
3.0	3.7/99	69/98	97/97	91	242	277	7.05	7.00	6.55
5.0	3.5/94	69/98	98/98	96	270	296	5.62	5.53	5.36
6.0	3.5/94	70/98	98/98	90	237	270	6.95	7.52	7.04

^a Calculated using solids content measurements (see Section 3.4.1.6)

^b z-average particle diameter; obtained using PCS (see Section 3.4.1.2)

^c Calculated using PCS measurements of z-average particle diameter

For all four of the prepared latexes a good level of control was gained, with approximately constant particle numbers. As can be seen from Table 6.10 the seed, core and final particle diameters are all fairly similar and grow in accordance with each other, although slightly lower than expected conversion of 97% were gained for the latexes with 2 and 3 wt% DAAM. This can be attributed to a small degree of coagulation for the latex with 2 wt% DAAM, as a corresponding decrease in particle number is seen, however it is more likely to be due to monomer evaporation for the latex with 3 wt% DAAM as no significant change in particle number is seen.

Figure 6.17 and Table 6.11 detail the stress-strain properties of the four variants, which show that as the DAAM content, and hence the amount of crosslinkable material present, increases the strain hardening of the films becomes evident to an increasing extent earlier in the stress-strain curve. Another trend that can be identified from the data is the reduction in extension to break ratio as the crosslinker content increases. However, this difference in mechanical behaviour is not realised at low (<20%) strains as can be seen from the Young's modulus values which do not show any clear pattern of variation, although a very slight increase is seen in the value of stress at 4% strain as the DAAM content increases. This observation is consistent with that made in Section 6.4.1, which looked at varying the crosslinker content of unstructured particles of uniform composition, whereby varying the DAAM content in the particle only significantly affected the high strain tensile behaviour of the films.

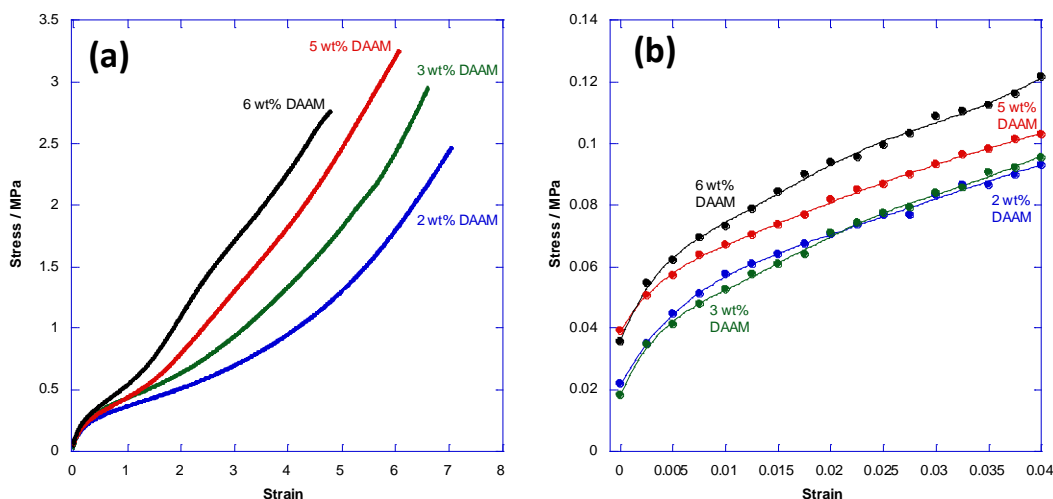


Figure 6.17 (a) Stress-strain curves for 70:30 core:shell ratio films with varying DAAM contents. Film composition is poly[(BA)-*co*-(BMA)] core phase copolymer and poly[(BA)-*co*-(BMA)-*co*-(DAAM)] shell phase copolymer with ADH added at 2:1 molar stoichiometric ratio; (b) Section of stress-strain curves from (a) with strains of 0-4% used to calculate Young's modulus (coefficient of first order term in a polynomial fit expression; order of fit = 6)

Table 6.11 Mechanical property data for 70:30 core:shell latexes with varying levels of DAAM in the shell phase

DAAM content / shell phase wt%	Young's Modulus /MPa	Stress @ 4% Strain /MPa	Extension to break /%
2.0	5 (± 0.4 MPa)	0.093 (± 0.006)	1150 ($\pm 30\%$)
3.0	7 (± 1.0 MPa)	0.096 (± 0.004)	970 ($\pm 90\%$)
5.0	6 (± 0.5 MPa)	0.103 (± 0.003)	850 ($\pm 120\%$)
6.0	9 (± 2.0 MPa)	0.121 (± 0.006)	775 ($\pm 50\%$)

6.3.2.2 80:20 core:shell ratio

Four variants were synthesised with an 80:20 core:shell ratio, all incorporating a different shell phase wt% of DAAM. However, for this core:shell ratio it was possible to synthesise a variant with 7.5 wt% DAAM, as the overall amount of DAAM was lower due to the higher core:shell wt% ratio. An attempt was made to incorporate 10 wt% into the shell phase of an 80:20 core:shell latex, but this failed due to high levels of coagulum forming during synthesis. Table 6.12 shows data that proves each preparation produced particles in a controlled manner; complete characterisation plots for the syntheses can be found in Appendix (iii).

Again, good control was gained of all polymerisations. Large seed particles for the variants with 2 and 3 wt% DAAM led to larger final diameters, and a slightly low seed monomer conversion (94%) may explain the small size of the 7.5 wt% seed, and subsequent

core and final particles. Approximately constant particle numbers were obtained for all latexes, which shows that no significant coagulation or secondary nucleation occurred.

Table 6.12 Latex characterisation data for the synthesis of 80:20 core:shell latexes with varying levels of DAAM

DAAM content / shell wt%	Overall / Instantaneous conversion ^a			Particle diameter ^b / nm			Total particle number ^c / $\times 10^{16}$		
	Seed	Core	Final	Seed	Core	Final	Seed	Core	Final
2.0	3.7/99	78/97	97/97	103	283	306	4.77	4.98	4.87
3.0	3.8/99	78/97	97/97	101	287	305	5.09	4.73	4.86
5.0	3.7/98	79/98	96/96	96	255	274	6.79	6.77	6.71
7.5	3.6/94	80/97	98/98	84	253	266	8.64	6.89	7.32

^a Calculated using solids content measurements (see Section 3.4.1.6)

^b z-average particle diameter; obtained using PCS (see Section 3.4.1.2)

^c Calculated using PCS measurements of z-average particle diameter

Figure 6.18 and Table 6.13 show that similar trends in the stress-strain properties are observed for 80:20 latexes as for the 70:30 variants discussed in Section 6.4.2.1. No clear trend in Young's Modulus can be deduced, and differences in the stress-strain profiles are only realised at higher strains. However, it is very obvious from Figure 6.18 that as the DAAM content in the shell phase increases, the material undergoes an increasing degree of strain hardening, similar to the trend observed for the 70:30 core:shell latexes.

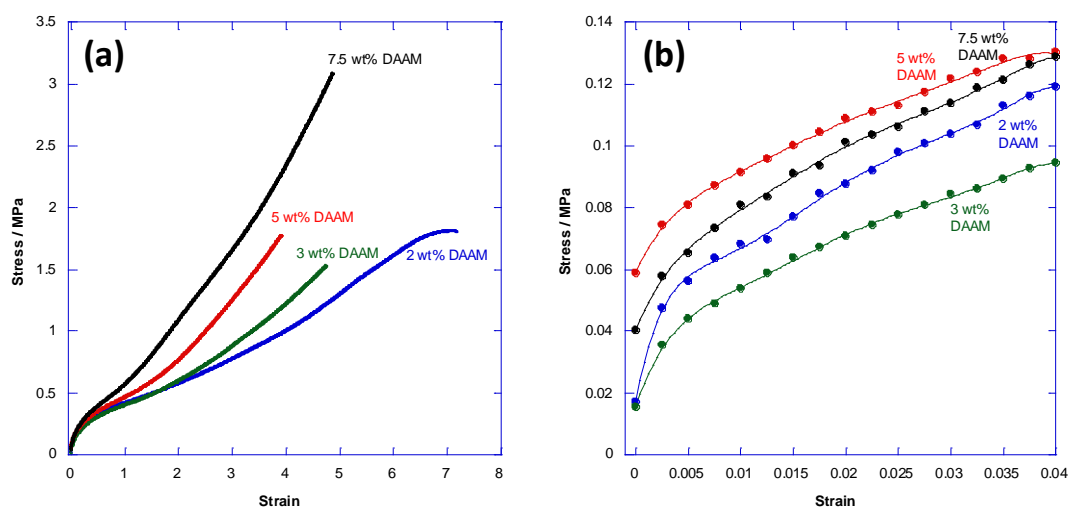


Figure 6.18 (a) Stress-strain curves for 80:20 core:shell ratio films with varying DAAM contents. Film composition is poly[(BA)-*co*-(BMA)] core phase copolymer and poly[(BA)-*co*-(BMA)-*co*-(DAAM)] shell phase copolymer with ADH added at 2:1 molar stoichiometric ratio; (b) Section of stress-strain curves from (a) with strains of 0-4% used to calculate Young's modulus (coefficient of first order term in a polynomial fit expression; order of fit = 6)

Table 6.13 Mechanical property data for 80:20 core:shell latexes with varying levels of DAAM in the shell phase

DAAM content / shell phase wt%	Young's Modulus / MPa	Stress @ 4% Strain / MPa	Extension to break / %
2.0	12 (± 3.3 MPa)	0.119 (± 0.016)	1200 ($\pm 80\%$)
3.0	12 (± 4.0 MPa)	0.095 (± 0.016)	980 ($\pm 130\%$)
5.0	8 (± 0.2 MPa)	0.131 (± 0.015)	675 ($\pm 15\%$)
7.5	8 (± 0.3 MPa)	0.128 (± 0.02)	754 ($\pm 80\%$)

Another trend that is consistent with previous observations is that as the crosslinker content increases, the extension to break of the films reduces significantly. The variant containing the very highest level of DAAM appears to be an anomaly in this regard, although there is a high error associated with this measurement.

6.3.2.3 90:10 core:shell ratio

Four latexes were originally included in this series of testing, incorporating levels of DAAM from 2.0 – 7.5 shell phase wt%. It was attempted to synthesise a latex with 10 wt% DAAM in the shell phase, but as was previously found for the 70:30 and 80:20 core:shell mass ratio systems, large amounts of coagulum were encountered during the shell phase polymerisation. A fifth variant, with 4.5 shell phase wt% DAAM was later included in the testing schedule after a large difference in the stress-strain profiles of 90:10 core:shell latexes with 5.8 and 3 wt% DAAM was observed. Table 6.14 shows characterisation data that confirms that each latex was prepared in a controlled manner; detailed characterisation plots for these preparations can be found in Appendix (iii).

Table 6.14 Latex characterisation data for the synthesis of 90:10 core:shell latexes with varying levels of DAAM

DAAM content / shell wt%	Overall / Instantaneous conversion ^a			Particle diameter ^b / nm			Total particle number ^c / $\times 10^{16}$		
	Seed	Core	Final	Seed	Core	Final	Seed	Core	Final
2.0	3.6/98	87/97	95/95	89	260	273	7.59	7.25	6.82
3.0	3.3/94	85/94	93/93	85	251	257	8.27	8.06	8.15
4.5	3.3/93	84/93	93/93	81	242	258	9.24	8.80	8.08
5.8	3.4/99	85/94	93/93	89	263	272	7.64	7.49	7.40
7.5	3.2/90	86/94	93/93	84	253	266	8.23	7.86	7.41

^a Calculated using solids content measurements (see Section 3.4.1.6)

^b z-average particle diameter; obtained using PCS (see Section 3.4.1.2)

^c Calculated using PCS measurements of z-average particle diameter

These data show that a good level of repeatable control was gained over the latex preparations, as the particle diameters increase in accord with each other and the particle numbers stay approximately constant for each latex. However, lower than expected conversions were seen of ca. 93%, which was not expected and is probably due to monomer evaporation rather than a significant occurrence of coagulum.

Films were cast and tensile tested according to the protocols given in Sections 3.3.2 and 3.4.2.1, respectively; the results are shown in Figure 6.19 and Table 6.15. As was observed for both the 70:30 and 80:20 core:shell latexes, as the crosslinker content increases the material undergoes an increasing degree of strain hardening, but there are no major differences in the Young's modulus value, which is measured at very low strains (<4%).

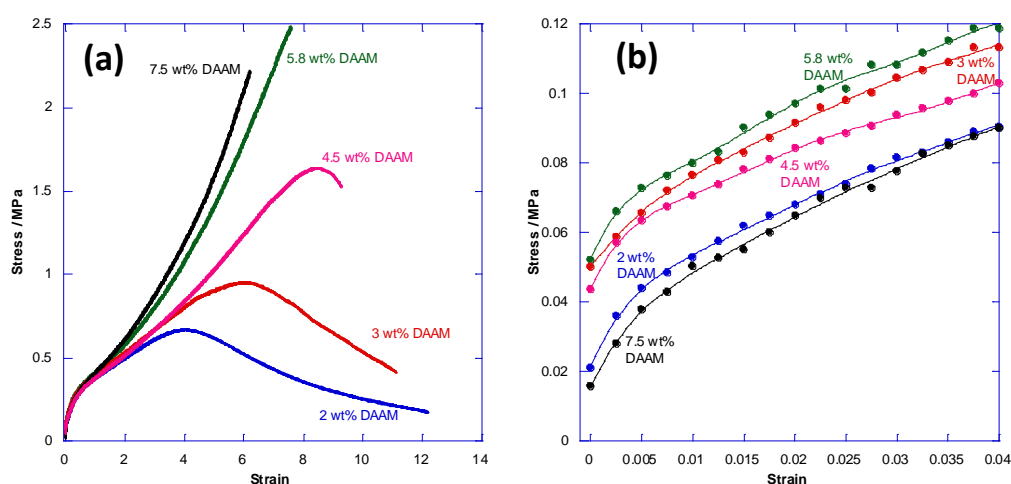


Figure 6.19 (a) Stress-strain curves for 90:10 core:shell ratio films with varying DAAM contents. Film composition is poly[(BA)-*co*-(BMA)] core phase copolymer and poly[(BA)-*co*-(BMA)-*co*-(DAAM)] shell phase copolymer with ADH added at 2:1 molar stoichiometric ratio; (b) Section of stress-strain curves from (a) with strains of 0-4% used to calculate Young's modulus (coefficient of first order term in a polynomial fit expression; order of fit = 6)

Table 6.15 Mechanical property data for 90:10 core:shell latexes with varying levels of DAAM in the shell phase

DAAM content / shell phase wt%	Young's Modulus / MPa	Stress @ 4% Strain / MPa	Extension to break / %
2.0	7 (± 1.1 MPa)	0.091 (± 0.011)	1800 (± 430%)
3.0	3 (± 0.2 MPa)	0.113 (± 0.01)	1700 (± 260%)
4.5	6 (± 0.8 MPa)	0.103 (± 0.009)	1500 (± 60%)
5.8	9 (± 1.8 MPa)	0.119 (± 0.011)	1200 (± 60%)
7.5	5 (± 0.2 MPa)	0.090 (± 0.016)	1100 (± 45%)

It can be clearly seen from Figure 6.19 that there is a significant difference in the stress-strain profiles of the latexes with 2 wt%, 3 wt% and 5.8 wt% DAAM, with the lower levels exhibiting behaviour previously observed for soft-soft nanocomposite coatings with no keto-hydrazide crosslinking incorporated into the matrix (see Chapter 5) whereby the films pass through a peak stress before softening until failure. This is most likely to be due to the low concentration of DAAM (~ 0.10 wt% of total latex for 2 wt% DAAM in the shell phase) in the 90:10 core:shell materials compared to that in the other levels tested in this series (~ 0.20 and ~ 0.30 wt% of total latex for 2 shell phase wt% 80:20 and 70:30 core:shell latexes, respectively). Above 4.5 wt% DAAM (~ 0.23 wt% of total latex), this is overcome and the materials behave as per other crosslinked soft-soft nanocomposites. Again, no significant differences can be identified in either the Young's modulus or stress at 4% strain values, which is in accord with the observations made for the other core:shell ratios examined in this section.

6.4 Effect of DAAM-ADH stoichiometric ratio

In order to investigate the effect that the level of ADH added into a latex post-polymerisation, and hence the theoretical number of crosslinks that occur during film formation, would have on the mechanical properties of a film a number of variants were made, each with a varying molar stoichiometric DAAM: ADH level which are shown in Table 6.16.

Table 6.16 Variants tested to deduce the effect of DAAM:ADH molar stoichiometry

Molar stoichiometric DAAM:ADH ratio	% of DAAM units crosslinked*	ADH content / $\mu\text{mol g}^{-1}$
10:1	20%	1.72
5:1	40%	3.44
10:3	60%	5.16
5:2	80%	6.88
2:1	100%	8.60
7:4	125%	9.75
3:2	150%	10.32
5:4	175%	13.76
1:1	200%	17.20

* = Assuming 100% crosslinking efficiency

The variants shown in Table 6.16 were made by adding different amounts of an aqueous 10 wt% ADH solution to portions of a latex with a 70:30 core:shell ratio, poly[(BA)-*co*-(BMA)] core copolymer and poly[(BA)-*co*-(BMA)-*co*-(DAAM)] shell phase copolymer, both phases with a T_g of 5 °C, and 2 wt% DAAM in the shell phase polymer. Films were then cast from these latexes and tensile tested according to the procedure given in Sections 3.3.2 and 3.4.2.1, respectively. The results of this testing can be seen in Figure 6.20 and Table 6.17.

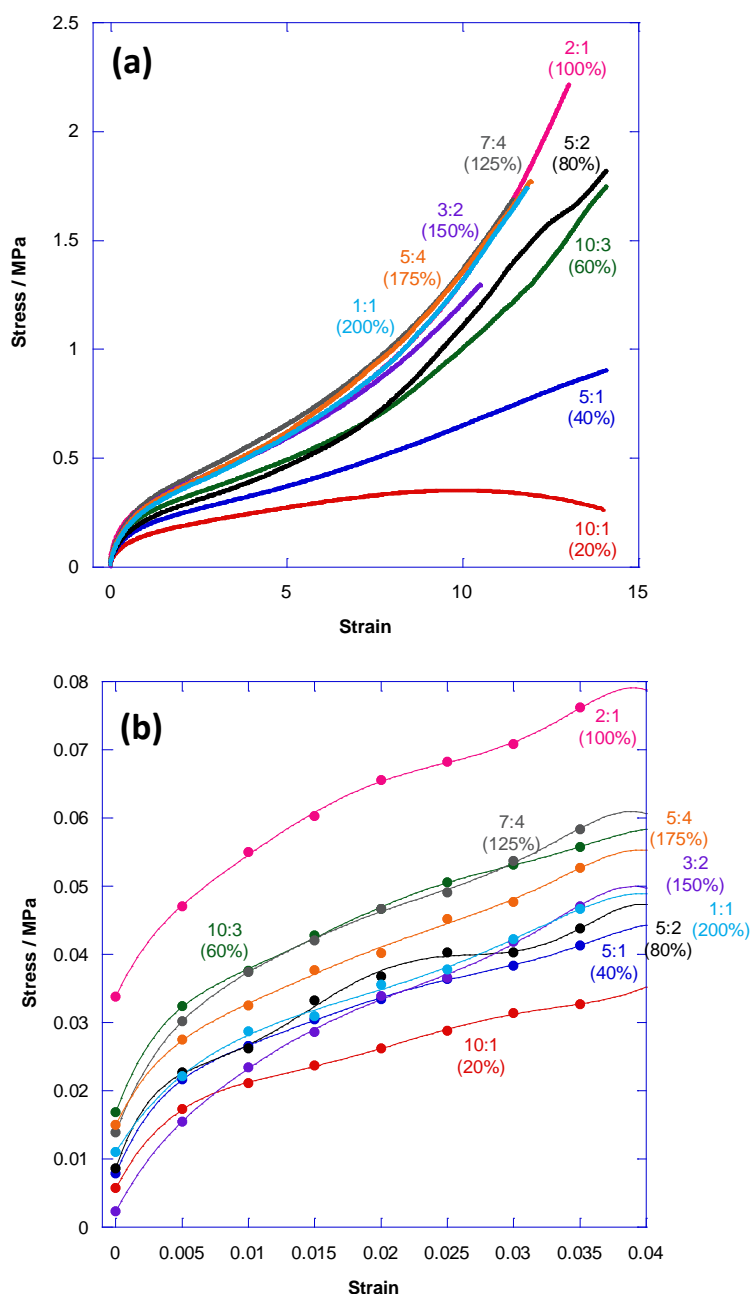


Figure 6.20 (a) Stress-strain curve for 70:30 core:shell ratio films with poly[(BA)-*co*-(BMA)] core phase copolymer and poly[(BA)-*co*-(BMA)-*co*-(DAAM)] shell phase copolymer with 2 wt% of DAAM. ADH added at various stoichiometric ratios, as can be seen in the legend; **(b)** Section of stress-strain curve from (a) with strains of 0-4% used to calculate Young's modulus (coefficient of first order term in a polynomial fit expression; order of fit = 6)

Table 6.17 Mechanical property data for systems discussed in Section 3.2.5

Molar stoichiometric DAAM:ADH ratio	% of DAAM units crosslinked*	Young's modulus / MPa	Stress at 4% strain / MPa	Extension to break / %
10:1	20%	4 (± 0.4 MPa)	0.05 (± 0.005)	1400 ($\pm 200\%$)
5:1	40%	5 (± 0.2 MPa)	0.04 (± 0.002)	1550 ($\pm 350\%$)
10:3	60%	4 (± 1.2 MPa)	0.06 (± 0.007)	1350 ($\pm 180\%$)
5:2	80%	6 (± 0.3 MPa)	0.05 (± 0.003)	1150 ($\pm 300\%$)
2:1	100%	5 (± 0.4 MPa)	0.093 (± 0.006)	1150 ($\pm 30\%$)
7:4	125%	5 (± 0.4 MPa)	0.062 (± 0.003)	990 ($\pm 60\%$)
3:2	150%	5 (± 1.1 MPa)	0.053 (± 0.002)	880 ($\pm 60\%$)
5:4	175%	4 (± 0.9 MPa)	0.061 (± 0.002)	990 ($\pm 40\%$)
1:1	200%	4 (± 0.7 MPa)	0.054 (± 0.004)	990 ($\pm 70\%$)

* = Assuming 100% crosslinking efficiency

The data from Table 6.17 shows that there is no correlation between the theoretical degree of crosslinking and the Young's modulus of the material or the value of stress at 4% strain. Although a slight increase in Young's modulus would be expected with an increased amount of crosslinking, this may be due the small amount of crosslinking present that all materials behave very similarly at low strain, as the differences in stress-strain behaviour only become apparent at above 100% strain. No significant difference can be seen between the extension to break values for any of the films, as large errors are associated with this measurement. Figure 6.20 shows that the molar stoichiometric DAAM: ADH ratio does affect the tensile behaviour of the films. As the molar stoichiometric DAAM:ADH ratio and hence the theoretical degree of crosslinking within the sample increases, the material becomes increasingly stiffer at higher strains which is due to the increased number of keto-hydrazide crosslinks within the sample.

No additional benefit in stress-strain properties results from adding excess amounts of ADH. Very little difference can be seen between the stress-strain curves for the variants with DAAM:ADH ratios delivering $\geq 100\%$ theoretical DAAM crosslinking, which is contrary to the

trend observed when lower amounts of ADH are present. This suggests that the DAAM-ADH crosslinking reaction is very efficient, and reaches a 'saturation level' at a 2:1 (DAAM:ADH) ratio, when 100% of DAAM units present in the sample will be crosslinked. The findings that have been discussed in this section substantiate observations made by Deplace *et al.*⁵, who found that for soft-soft nanocomposite PSAs the level of ADH incorporated had a significant effect upon the high shear properties of the films. Similar to the PSAs, film softening was observed at low levels of ADH, whereby the ADH level was too low to provide enough crosslinking to induce elastomeric behaviour, and the onset of strain hardening at increasingly lower strains as the DAAM:ADH ratio increased up to a maximum of 2:1 (i.e. 100% theoretical crosslinks formed).

6.5 Conclusions

The work presented in Chapter 6 has shown that two of the main soft-soft nanocomposite design parameters, namely the core:shell ratio of the structured particles and the crosslinker content, both affect the high strain mechanical properties of films, but have very little effect upon mechanical behaviour below $\sim 50\%$ strain. All of the findings discussed substantiate previous trends observed for soft-soft nanocomposite PSAs reported by Deplace *et al.*^{4, 5} and Foster *et al.*⁶ in 2009. This can be attributed to these parameters changing the nature of the shell phase of the particles, which in the film forms the crosslinked continuous phase. It is this phase which determines the stress-strain behaviour of the films at higher strains due to chain extensions that are restricted by the presence of the crosslinks, which form an interpenetrating, percolating matrix. However, these crosslinking interactions will have little or no influence upon the low strain mechanical behaviour of the films, as the deformations in this region are sufficiently small to be accommodated by the flexibility of the crosslinked, networked chains. Hence, all of the systems that were discussed in this chapter were very soft and flexible films, with low (< 20 MPa) Young's modulus and high ($> 600\%$) extension to break ratios. This is due to these systems being of low core and shell T_g , which at 5°C meant that the polymer T_g was always in the rubbery state at testing temperatures. Despite their excellent film forming credentials, these films would not be ideal for use as binders in paints due to their propensity for dirt pickup and blocking, which are detrimental to the overall properties of a coating.

It can also be seen from both the kinetics data and the stress-strain profiles that the particle size has little effect upon the tensile properties of a film, as no anomalous results are seen for latexes with an especially big or small particle size. This can therefore be considered

to be a negligible effect, provided that the particle diameter is within the original specification for soft-soft nanocomposites of 250-350 nm, and not be a concern in any further work regarding the mechanical properties of these systems.

7 Effect of core and shell phase polymer T_g on film properties

7.1 Introduction

The work presented in Chapter 6 showed that both the core:shell ratio and the crosslinker content of soft-soft nanocomposite films affected only the high-strain tensile behaviour of these materials, with little or no significant effect upon Young's modulus, which was typically below 15 MPa. However, as discussed in Section 6.4, these observations are not unexpected as mechanical deformation in the low strain region, from which the Young's modulus is derived, do not affect the crosslinked shell phase polymer chains.

A very simple way to affect the low strain mechanical properties of a polymer is to exploit the large changes in modulus close to the glass transition temperature (T_g). Glass transition is a reversible transition that occurs in amorphous materials, whereby the properties of the material change from being soft and rubbery to hard and brittle¹⁷. Above its T_g , a polymer can be considered to be a rubbery solid or an extremely viscous liquid²¹⁸. The phenomenon of the glass transition is due to chain mobility effects, as below T_g the chains are 'frozen' and therefore unable to move. However, when the temperature is raised above T_g , the chains gain enough energy to be able to move in free space, and hence cause the polymer itself to become rubbery and flexible. The most important factor that affects the onset of the glass transition is the chemical structure of the polymer chains, both the nature of the chain backbone itself and any side groups. As bulky substituents, such as aromatic groups, are added as side groups the T_g of the polymer will increase. This is due to the rigidity of such functionalities restricting the ease with which a polymer can become rubbery and soft, which increases the energy barrier for such a process and therefore raises the temperature at which the transition can occur¹⁰.

The glass transition is known to have a very significant effect upon the thermomechanical and rheological properties of a film, and as such is an important parameter to consider when designing a copolymer system for a specific application²¹⁹. As can be seen in Figure 7.1, the modulus of a polymer rapidly changes over a very small temperature range as the glass transition is crossed. The figure also shows that this occurs at different temperatures for different polymers. The dashed-line curve representing polystyrene has a glass transition at much higher temperature than that of polyisobutylene, which can be attributed to the difference in the properties of the side groups, shown in Figure 7.2. The aromatic side groups of the polystyrene chain impart more rigidity than the

methyl substituents of the polyisobutylene, and therefore more energy is required for the chain to become flexible.

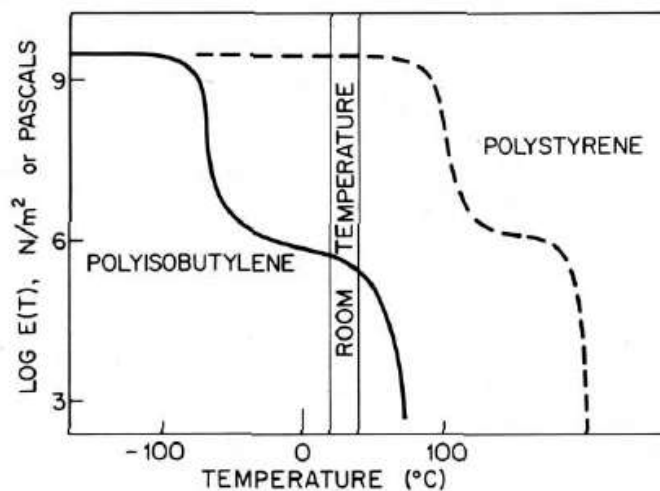


Figure 7.1 Plot of $\log(\text{modulus})$ versus temperature for polystyrene and polyisobutylene.²²⁰ The rapid change in gradient, and hence the modulus of a polymer film, represents the glass transition.

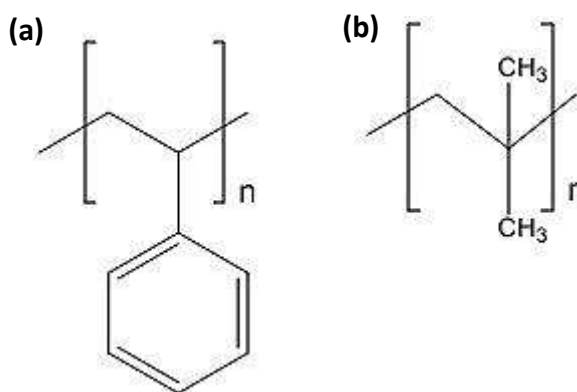


Figure 7.2 Structure of (a) polystyrene repeat unit and (b) polyisobutylene repeat unit

Low T_g film surfaces are likely to be tacky at ambient temperature²²¹, and thus are more suited to applications such as adhesives⁴. Latex films that are intended for use as paints or coatings, such as the soft-soft nanocomposite latexes discussed in this thesis, require a T_g much closer to ambient temperature in order to gain harder films with higher resistance to dirt pickup. However, such properties are associated with higher T_g systems, and can lead to poor film formation properties. In order to counteract this, hard core, soft shell latexes have been used in order to maximise the film forming properties by minimising MFT as a consequence of the low T_g shell phase, whilst retaining optimal application properties that result from the high T_g core phase^{50, 55, 222}.

Shell phase polymer T_g was found by Hasanzadeh *et al.* to be an important parameter affecting the MFT of latexes with poly[(MMA)-*co*-(BA)] core and poly[(MMA)-*co*-(BA)-*co*-

(DMAEMA)-*co*-(AA)] shell phases with a bimodal particle size distribution, where DMAEMA is N,N'-dimethylaminoethyl methacrylate²²³. Reducing the shell phase T_g from 30 °C to -56 °C had a marked effect upon the modulus of the films, which reduced by ca. 300 MPa.

The influence of seed stage T_g upon the formation of core-shell particle morphology was established by Sundberg *et al.*⁶³ and Karlsson *et al.*²²⁴. As discussed in Section 2.3.3.2, the penetration of shell phase polymer chain radicals into the particle core phases was facilitated by the T_g of the core phase polymer being below the reaction temperature, and resulted in a better defined core-shell morphology. However, as the T_g of the seed, core and shell phase copolymers in the soft-soft nanocomposites discussed in this thesis are well below reaction temperature, the effect of varying the T_g of the core and shell phases on the particle morphology is not a concern as at all stages during the polymerisation process these polymers will be well above their T_g and therefore in the rubbery state.

As the soft-soft nanocomposite materials discussed in Chapters 5 and 6 of this thesis have both core and shell copolymer T_g s of 5 °C, all the systems tested thus far have been completely in the rubbery state and therefore the low Young's modulus values seen were not unexpected. The T_g of the homopolymer of BMA is 36 °C (see Section 4.3.2), so at the mechanical testing temperature (23 °C) the poly[(BA)-*co*-(BMA)] and poly[(BA)-*co*-(BMA)-*co*-(DAAM)] copolymers will be within the region where modulus changes rapidly with temperature. This is likely to have a dramatic effect upon the low strain mechanical properties of the films cast from these soft-soft nanocomposite latexes a large range of modulus values will be easily accessible just by changing the chemical composition of the core and shell copolymers.

Hence, a series of preparations were undertaken in order to deduce the effect of changing both the T_g of the core and shell phase copolymers in soft-soft nanocomposite films. The core polymer is the predominant phase in terms of mass ratio in the particles, and in order to retain the elastomeric properties of the shell phase the shell phase copolymer T_g was varied over a much smaller temperature range than that of the core phase T_g .

7.2 Investigating the effect of core T_g upon film properties

Three core:shell ratios have been examined, namely 70:30, 80:20 and 90:10, of which five variants were synthesised, incorporating a poly[(BA)-*co*-(BMA)] core phase copolymer with T_g values of 25, 20, 15, 10 and 5 °C. The chemical composition of the poly[(BA)-*co*-(BMA)-*co*-(DAAM)] shell phase copolymer, the shell phase T_g , and the DAAM content and

hence crosslinking density, were all kept constant as detailed in Table 7.1. Copolymer chemical compositions for a given T_g were predicted using the modified Fox equation that was derived in Section 4.5 of this thesis to compensate for plasticisation effects likely caused by non-ionic surfactant and water.

Table 7.1 List of parameters kept constant for work detailed in Section 7.2

Parameter	Value for each latex discussed in Section 7.2
Shell T_g	5 °C
Shell phase chemical composition	Poly[(BA)-co-(BMA)-co-(DAAM)]
DAAM level	2 wt% of shell phase copolymer
DAAM:ADH ratio	2:1

7.2.1 70:30 core:shell ratio

Each of the five variants synthesised showed controlled particle nucleation and growth, as can be seen from Table 7.2. Detailed kinetics plots for each latex can be found in Appendix (iv) of this thesis. All syntheses showed high instantaneous conversion indicating a starved-feed polymerisation, the particle number remaining approximately constant throughout the reaction and the particle diameter growing in accordance with the predicted value. Hence, all five preparations were deemed to be suitable for further testing.

Table 7.2 Kinetics characterisation data for the synthesis of 70:30 core:shell latexes with varying core phase T_g values

Core T_g / °C	Overall / Instantaneous conversion ^a / %			Particle diameter ^b / nm			Total particle number ^c / $\times 10^{16}$		
	Seed	Core	Final	Seed	Core	Final	Seed	Core	Final
5	3.7/98	68/97	97/97	98	263	296	5.64	3.09	3.46
10	3.6/96	69/98	96/96	91	246	286	4.30	6.60	5.91
15	3.6/95	69/97	97/97	96	254	290	5.86	6.02	5.70
20	3.5/94	68/97	97/97	94	259	296	6.05	5.63	5.35
25	3.6/97	68/97	97/97	112	300	341	3.74	3.65	3.54

^a Calculated using solids content measurements (see Section 3.4.1.6)

^b z-average particle diameter; obtained using PCS (see Section 3.4.1.2)

^c Calculated using PCS measurements of z-average particle diameter

The data in Table 7.2 show that a good level of control was gained over each polymerisation. A large particle diameter for the latex with a core T_g of 25 °C can be

attributed to a larger seed particle, but as has been the case in previous chapters particle diameter does not affect the mechanical properties of these soft-soft nanocomposite materials. Slightly low final conversions of ca. 97% were seen which, in conjunction with a very slight decrease in particle number over the course of the preparations, is likely to be due to small amounts of coagulum being formed during the polymerisation.

The pH of each latex was adjusted to ~ 8.5 and ADH added to each preparation at a molar stoichiometric ratio of 2:1 DAAM:ADH, as described in Section 3.3.1. Films from all five variants were then cast and analysed by DSC using the procedure given in Section 3.4.3.2 to determine their T_g (see Table 7.3).

Table 7.3 DSC data for 70:30 core:shell ratio films with variable core phase copolymer T_g

Core T_g^a / °C	Shell T_g^b / °C	Theoretical average T_g^c / °C	Observed T_g / °C
5	5	5	4 (± 1.5 °C)
10	5	8.5	6 (± 0.6 °C)
15	5	12	8 (± 1 °C)
20	5	15.5	8 (± 0.5 °C)
25	5	19	15 (± 0.8 °C)

^a Calculated using the modified Fox equation derived in Section 4.5

^b Calculated using the fox equation (see Equation 4.2)

^c Calculated by (core T_g x core proportion)+(shell T_g x shell proportion)

In each case, the observed T_g is significantly lower than its theoretical value. This is because a single T_g is observed for the overall particle, which is an average T_g from both the core and shell phases. It is due to the proximity of the two T_g s that they are not individually resolved, and as can be seen in Figure 7.3(b), these merged transitions are broader than those of unstructured particles with a single associated T_g (Figure 7.3(a)). The influence of the much lower T_g shell phase results in the observed T_g values seen in Table 7.3 being lower than the theoretical core phase T_g . Further plasticisation by water and surfactant, as were previously discussed in Section 4.5, may also contribute to these lower than expected values, although the extent of this discrepancy between the predicted and observed values was unexpected. This effect will be further discussed and explained in Section 7.4.

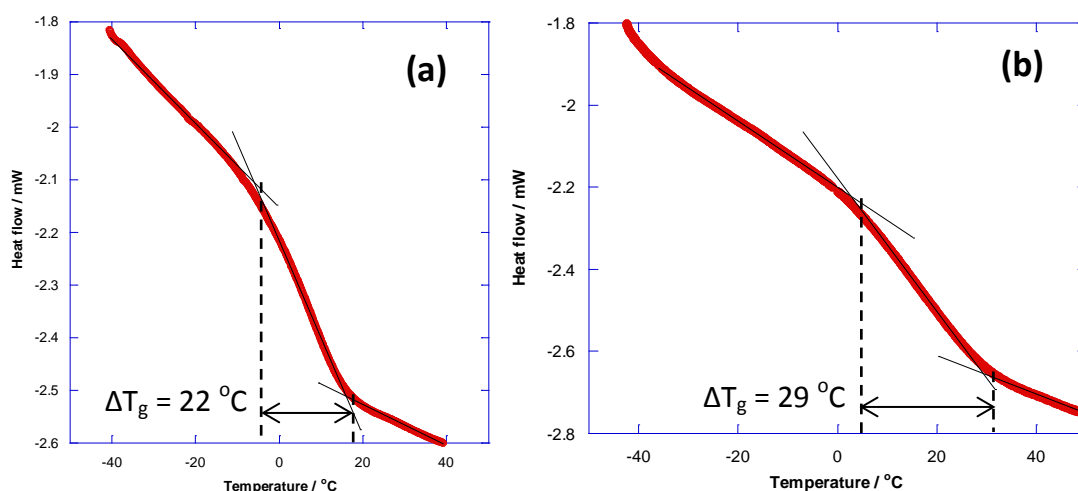


Figure 7.3 DSC traces for (a) unstructured poly[(BA)-*co*-(BMA)] particle and (b) structured particle with poly[(BA)-*co*-(BMA)] core and poly[(BA)-*co*-(BMA)-*co*-(DAAM)] shell phase copolymers and a core:shell ratio of 70:30. ΔT_g is the glass transition temperature width.

The films were also characterised by tensile testing according to procedures given in Sections 3.3.2 and 3.4.2.1, respectively. The tensile stress-strain curves of the films and Young's modulus, extension to break and stress at 4% strain data are given in Figure 7.4 and Table 7.4, respectively.

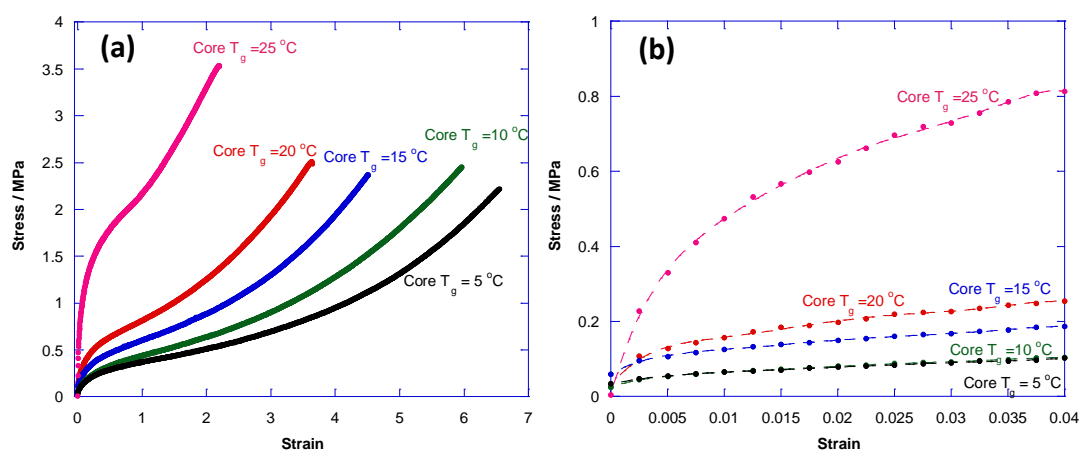


Figure 7.4(a) Stress-strain curves for 70:30 core:shell ratio films with varying core phase T_g . Film composition is poly[(BA)-*co*-(BMA)] core phase copolymer and poly[(BA)-*co*-(BMA)-*co*-(DAAM)] shell phase copolymer with ADH added at 2:1 molar stoichiometric ratio; **(b)** Section of stress-strain curves from (a) with strains of 0-4% used to calculate Young's modulus (coefficient of first order term in a polynomial fit expression; order of fit = 6)

It can be clearly seen from these data that, as expected due to the proximity of the testing temperature to T_g , the core phase polymer T_g increases, the Young's modulus of the film rises, an effect that is especially noticeable for the film with a core T_g of 25 °C, whereby the core phase is likely to be in a 'leathery' at the tensile testing temperature of 23 °C (see Section 7.1). This trend is further substantiated by the values of stress at 4% strain, which

show an identical pattern in a region where inaccuracies due to jaw separation are not as prevalent. This indicates that for the variant with core copolymer T_g of 25 °C the core phase, which comprises the majority (70 wt%) of the film, predominates the mechanical behaviour of the soft-soft nanocomposite film. A corresponding decrease in extension to break is also seen with increasing core phase T_g which also adds weight to this hypothesis of stiffer films at higher core T_g .

Table 7.4 Mechanical property data for 70:30 core:shell latexes with varying core phase T_g

Core T_g / °C	Young's modulus / MPa	Stress @ 4% strain / MPa	Extension to break / %
5	5 (± 0.4 MPa)	0.10 (± 0.006)	1150 (± 30%)
10	7 (± 2.5 MPa)	0.11 (± 0.014)	900 (± 70%)
15	18 (± 2.7 MPa)	0.18 (± 0.009)	780 (± 90%)
20	51 (± 3.8 MPa)	0.25 (± 0.016)	630 (± 20%)
25	138 (± 24 MPa)	0.81 (± 0.07)	320 (± 50%)

7.2.2 80:20 core:shell ratio

As for the systems discussed in the previous section, all five 80:20 core:shell ratio latexes synthesised in this section of work showed controlled particle nucleation and growth with high instantaneous conversion, approximately constant particle number and diameter growth in accordance with theoretical values. Table 7.5 shows the characterisation data for each variant, and detailed kinetics plots for each preparation are given in Appendix (iv).

Table 7.5 Latex characterisation data for the synthesis of 80:20 core:shell latexes with varying core phase T_g values

Core T_g / °C	Overall / Instantaneous conversion ^a / %			Particle diameter ^b / nm			Total particle number ^c / x 10 ¹⁶		
	Seed	Core	Final	Seed	Core	Final	Seed	Core	Final
5	3.7/99	78/97	97/97	103	283	306	4.77	4.98	4.87
10	3.7/98	78/96	97/97	95	260	293	6.20	6.32	5.48
15	3.6/96	79/98	97/97	92	265	295	6.70	6.10	5.43
20	3.5/92	78/97	96/96	90	254	285	6.79	6.80	5.93
25	3.7/96	78/95	97/97	108	304	331	4.09	3.91	3.83

^a Calculated using solids content measurements (see Section 3.4.1.6)

^b z-average particle diameter; obtained using PCS (see Section 3.4.1.2)

^c Calculated using PCS measurements of z-average particle diameter

Similar to the data given in Section 7.2.1, all polymerisations can be considered to be controlled, with particle diameter growth in accordance with the seed particle diameters and a small decrease in the particle number over the course of the reaction resulting in low levels of coagulum, which is supported by slightly lower overall monomer conversion values.

Once it had been established that all five latexes had been prepared in a controlled manner, films were cast according to the procedure given in Section 3.3.2. These films were then characterised by tensile testing as described in Section 3.4.2.1, the results of which are given in Figure 7.5 and Table 7.6

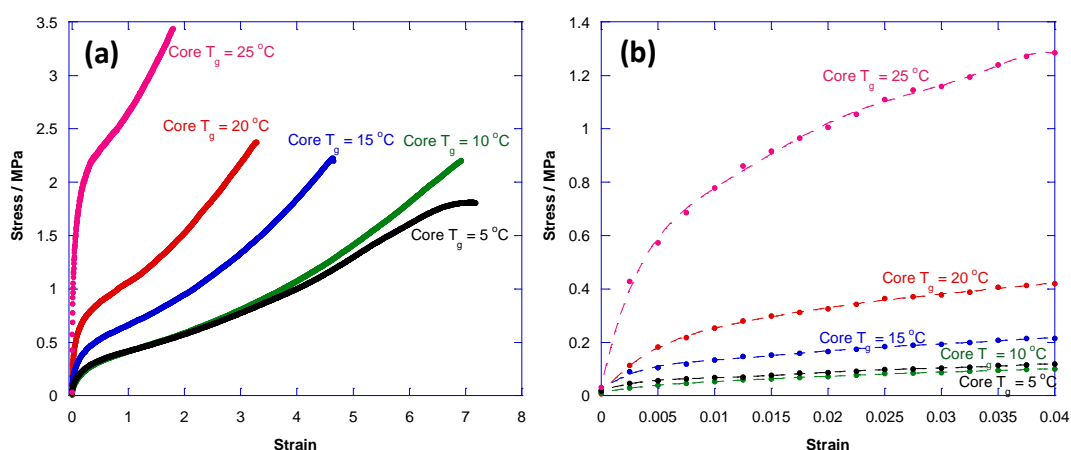


Figure 7.5(a) Stress-strain curves for 80:20 core:shell ratio films with varying core phase T_g . Film composition is poly[(BA)-*co*-(BMA)] core phase copolymer and poly[(BA)-*co*-(BMA)-*co*-(DAAM)] shell phase copolymer with ADH added at 2:1 molar stoichiometric ratio; **(b)** Section of stress-strain curves from (a) with strains of 0-4% used to calculate Young's modulus (coefficient of first order term in a polynomial fit expression; order of fit = 6)

Table 7.6 Mechanical property data for 80:20 core:shell latexes with varying core phase T_g

Core T_g / °C	Young's modulus / MPa	Stress @ 4% strain / MPa	Extension to break / %
5	11 (± 3.3 MPa)	0.10 (± 0.016)	1200 (± 80%)
10	12 (± 2.4 MPa)	0.12 (± 0.006)	1150 (± 40%)
15	40 (± 7.4 MPa)	0.20 (± 0.013)	780 (± 40%)
20	75 (± 19 MPa)	0.42 (± 0.005)	490 (± 40%)
25	182 (± 133 MPa)	1.36 (± 0.124)	260 (± 30%)

As was observed for the 70:30 core:shell latexes, the data show that a clear trend exists between Young's modulus and core polymer T_g . A corresponding increase and decrease in stress at 4% strain and extension to break, respectively, with core T_g also is observed, which is again consistent with the results given in Section 7.2.1.

It should be noted that the Young's modulus of the variant with a core phase copolymer T_g of 25 °C is the highest obtained thus far in the project. Although a very large error is associated with this measurement, which can be attributed to jaw separation being used to measure very low strains (see Section 5.3), a corresponding trend is seen in the value of stress at 4% strain which is a much more reliable measurement with a far smaller error. This observation further substantiates previous observations made in Chapter 6, and by Foster *et al.*⁶ and Deplace *et al.*⁵, that the optimum mechanical behaviour of soft-soft nanocomposite systems is seen at this core:shell mass ratio.

As for the 70:30 core:shell systems, the five films discussed in this section were analysed by DSC according to the procedure given in Section 3.4.3.2 to determine their T_g s (see Table 7.7) Again, it can be seen from these data that for each system, an average T_g is seen and is lower than the theoretical core T_g value, although not as significantly as for the data given in Table 7.3. This may be because for these 80:20 core:shell systems, the shell phase polymer forms a lower proportion of the overall particle and therefore has less influence upon overall film T_g . However, the measured T_g values for this core:shell ratio are much more in agreement with theoretical average values than for the 70:30 films.

Table 7.7 DSC data for 80:20 core:shell ratio films with variable core phase copolymer T_g

Core T_g^a / °C	Shell T_g^b / °C	Theoretical average T_g^c / °C	Observed T_g / °C
5	5	5	4 (± 0.8 °C)
10	5	9	5 (± 0.3 °C)
15	5	13	11 (± 0.7 °C)
20	5	17	14 (± 1.3 °C)
25	5	21	22 (± 1.5 °C)

^a Calculated using the modified Fox equation derived in Section 4.5

^b Calculated using the fox equation (see Equation 4.2)

^c Calculated by (core T_g x core proportion) + (shell T_g x shell proportion)

7.2.3 90:10 core:shell ratio

The final core:shell ratio investigated was 90:10, again with five variants having core copolymer T_g values of 5 - 25 °C being synthesised and analysed. As for the other two core:shell ratios, all showed high instantaneous conversion, an approximately constant particle number and particle diameter growth in line with predicted values. The kinetics characterisation data for these latexes can be seen in Table 7.8 , and detailed kinetics plots can be found in Appendix (iv).

Table 7.8 Latex characterisation data for the synthesis of 90:10 core:shell latexes with varying core phase T_g values

Core T_g / °C	Overall / Instantaneous conversion ^a / %			Particle diameter ^b / nm			Total particle number ^c / $\times 10^{16}$		
	Seed	Core	Final	Seed	Core	Final	Seed	Core	Final
5	3.7/98	87/97	95/95	89	260	273	7.59	7.25	6.82
10	3.6/100	87/96	98/98	100	294	308	5.46	5.07	5.01
15	3.6/99	87/97	98/98	96	312	337	5.98	4.28	3.81
20	3.6/99	87/98	98/98	89	263	279	7.63	7.28	6.76
25	3.6/99	89/98	98/98	101	301	314	5.20	4.88	4.74

^a Calculated using solids content measurements (see Section 3.4.1.6)

^b z-average particle diameter; obtained using PCS (see Section 3.4.1.2)

^c Calculated using PCS measurements of z-average particle diameter

ADH was added to each latex, and films were cast according to the procedures in Section 3.3.1 and Section 3.3.2, respectively, all of which formed coherent films at ambient temperature with the exception of the latex with a core T_g of 25 °C. Attempts to form a film with a wet thickness of approximately 800 μm , which is the minimum film thickness in order to gain a soft-soft nanocomposite film with the required robustness to avoid inadvertent deformation before stress-strain testing, failed in environments with an ambient temperature of both 15 and 21 °C. This will be investigated further in Section 7.2.4 which will discuss the minimum film formation temperature of these latexes. Hence, only four films from this series underwent analysis by tensile testing using the method given in Section 3.4.2.1, the results of which are shown in Figure 7.6 and Table 7.9.

As for the other two core:shell ratios, clear trends between Young's modulus, stress at 4% strain and extension to break with increasing core polymer T_g can be seen from these data. Behaviour previously seen for uncrosslinked soft-soft nanocomposite films (see Section 5.3) and other 90:10 core:shell latexes with low levels of crosslinking (see Section 6.4.2.3) was also observed for the variants with core copolymer T_g below 20 °C, i.e. when in the rubbery state at testing temperature. This unusual viscoelastic-type behaviour, whereby the films pass through a peak stress before softening to failure at very high extension values, is likely to be due to the DAAM-containing shell phase forming a very small (10wt%) proportion of the overall film and therefore not forming a coherent, percolating crosslinked phase as is necessary for the elastomeric strain hardening behaviour to be observed. The observation of a severely reduced extension to break for the film with core phase copolymer T_g of 20 °C is

likely to be due to the leathery nature of the polymer at this proximity to glass transition at the testing temperature (23 °C).

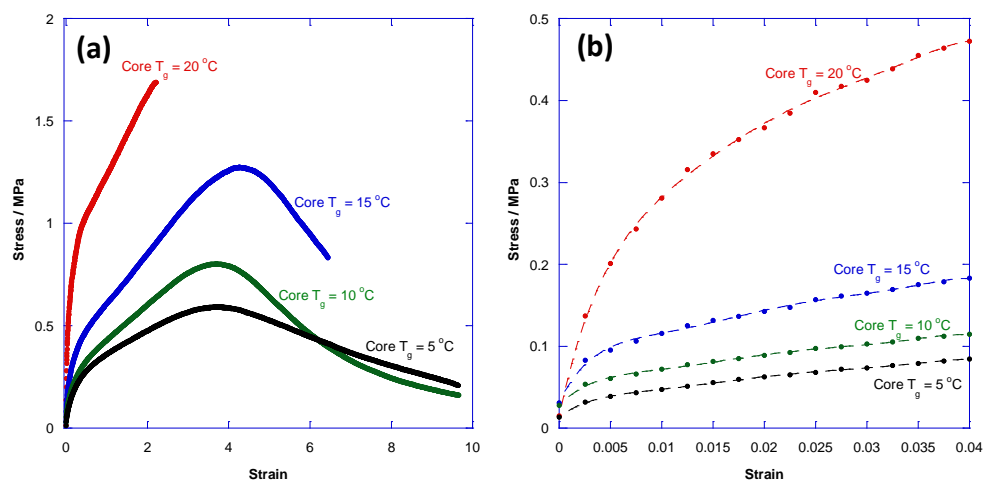


Figure 7.6(a) Stress-strain curves for 80:20 core:shell ratio films with varying core phase T_g . Film composition is poly[(BA)-*co*-(BMA)] core phase copolymer and poly[(BA)-*co*-(BMA)-*co*-(DAAM)] shell phase copolymer with ADH added at 2:1 molar stoichiometric ratio; **(b)** Section of stress-strain curves from (a) with strains of 0-4% used to calculate Young's modulus (coefficient of first order term in a polynomial fit expression; order of fit = 6)

Table 7.9 Mechanical property data for 80:20 core:shell latexes with varying core phase T_g

Core T_g / °C	Young's modulus / MPa	Stress @ 4% strain / MPa	Extension to break / %
5	7 (± 1.1 MPa)	0.09 (± 0.011)	1800 (± 430%)
10	16 (± 0.9 MPa)	0.12 (± 0.01)	2100 (± 50%)
15	40 (± 5.5 MPa)	0.19 (± 0.013)	1120 (± 80%)
20	45 (± 3.4 MPa)	0.47 (± 0.03)	370 (± 70%)
25*	-	-	-

* Did not film form at ambient temperature

DSC analysis of the five films discussed in this section used the procedure given in Section 3.4.3.2, and the data is given in Table 7.10. In each case, the observed average T_g is lower than the theoretical core T_g value, although not as significantly as for the other two ratios as the low T_g shell phase polymer forms much smaller proportion of the overall particle, and therefore affects the overall film T_g to a much lesser extent.

Table 7.10 DSC data for 90:10 core:shell ratio films with variable core phase T_g

Core T_g^a / °C	Shell T_g^b / °C	Theoretical average T_g^c / °C	Observed T_g / °C
5	5	5	4 (± 0.9 °C)
10	5	9.5	6 (± 0.3 °C)
15	5	14	9 (± 0.5 °C)
20	5	18.5	16 (± 0.1 °C)
25	5	23	24 (± 0.7 °C)

^a Calculated using the modified Fox equation derived in Section 4.5

^b Calculated using the fox equation (see Equation 4.2)

^c Calculated by (core T_g x core proportion)+(shell T_g x shell proportion)

7.2.4 Effect of core phase copolymer T_g on minimum film formation temperature (MFT)

The importance of minimum film formation temperature (MFT) during the film formation process was discussed in Section 2.4.1.2, and MFT testing was conducted according to the procedure given in Section 3.4.3.1. Latexes were chosen from those described in Section 7.2, with one high core copolymer T_g and one low core copolymer T_g example chosen for each core:shell mass ratio examined. The one variant from the testing series that did not form a coherent film at ambient temperature, namely the 90:10 core:shell latex with a core phase copolymer of 25 °C (see Section 7.2.3) was specifically included in the MFT testing in order to ascertain whether a high MFT was the cause of its failure to film form. The results of this testing can be seen in Table 7.11.

Table 7.11 MFT analysis of soft-soft nanocomposite latexes described in Section 7.2

Core:shell ratio	Core T_g / °C	Shell T_g / °C	MFT / °C	T_g^{**} / °C
70:30	10	5	< 0	6
70:30	25	5	12-13	15
80:20	10	5	< 0	5
80:20	25	5	15-16	22
90:10	10	5	< 0	6
90:10	25*	5	16-18	24

* - Did not film form at room temperature

** - Measured by DSC

It can be seen from these results that in all cases, the observed MFT is lower than the T_g as measured by DSC. For those latexes with higher core T_g values, the MFT also increases

with the core:shell volume ratio, which can be attributed to the greater influence of the core copolymer over the lower T_g shell phase upon the film forming properties of the system when present in a greater proportion and is in accordance with findings reported by Morgan *et al.*¹¹⁹.

However, these results do not fully explain the failure of the 90:10 core:shell latex with a core copolymer T_g of 25 °C to film form, as its MFT (16-18 °C) is below one of the temperatures at which film formation was attempted. This therefore suggests that the successful film formation of these soft-soft nanocomposite latexes is strongly dependent on wet film thickness, with thinner films such as those used to measure MFT (100 μm wet thickness) forming films at lower temperatures than thicker examples as are required for mechanical testing. Initial wet thickness of films is known to affect the onset of the drying process^{77, 225}. As the film dries from the surface down, water will become trapped in a thicker film and induce stresses as particle deformation occurs, retracting the dimensions of the film. If the polymer is not sufficiently flexible, as this variant with high core T_g close to its MFT and T_g will not be, this leads to a 'mud cracking' effect and failure to form a coherent film²²⁶.

7.3 Effect of crosslinker content at higher core T_g

The results presented in Section 7.2, showed that changing the core phase T_g of a soft-soft nanocomposite system affects the low strain mechanical behaviour of the films, whereas changing the crosslinker level affects the high strain mechanical behaviour (see Section 6.4). Hence, a natural area of interest was to investigate the effect that combining these two parameters would have upon film properties. An 80:20 core:shell ratio has shown to be the optimum with regard to mechanical properties (see Section 7.2.2), so this is the only ratio will be discussed in this work. It also was shown, both in this project (see Section 6.3.2.2) and in the literature¹³¹, that the maximum amount of DAAM that can be incorporated into a latex is 7.5 wt%, as above this level large amounts of coagulum are produced (see Section 6.1). Hence, DAAM contents between 2 and 7.5 wt% shell phase have been investigated.

In all cases, the core and shell phases comprised poly[(BA)-*co*-(BMA)] and poly[(BA)-*co*-(BMA)-*co*-(DAAM)] copolymers, respectively. Table 7.12 shows the details of the latexes synthesised, and Table 7.13 shows the characterisation data for these syntheses. Full kinetics plots can be found in Appendix (iv).

Table 7.12 Synthesis matrix to investigate the effect of crosslinker content at higher poly[(BA)-co-(BMA)] core phase T_g

Core:shell ratio	Core T_g / °C	Shell T_g / °C	DAAM content / wt% in shell	DAAM:ADH ratio
80:20	25	5	2	2:1
80:20	25	5	3	2:1
80:20	25	5	5	2:1
80:20	25	5	7.5	2:1
80:20	20	5	2	2:1
80:20	20	5	3	2:1
80:20	20	5	5	2:1
80:20	20	5	7.5	2:1

Table 7.13 Characterisation data for syntheses detailed in Table 7.12

Core T_g / °C	DAAM content / shell wt%	Overall / Instantaneous conversion ^a / %			Particle diameter ^b / nm			Total particle number ^c / x 10 ¹⁶		
		Seed	Core	Final	Seed	Core	Final	Seed	Core	Final
20	2	4/92	78/97	96/96	90	254	285	6.79	6.80	5.93
20	3	4/93	76/95	97/97	101	290	318	4.90	4.52	4.37
20	5	4/95	74/96	97/97	98	275	306	5.48	5.34	4.41
20	7.5	4/96	82/95	99/99	99	296	321	5.33	4.26	4.01
25	2	4/96	76/95	97/97	108	304	331	4.09	3.91	3.83
25	3	3/78	80/92	99/99	91	266	293	5.66	5.68	5.32
25	5	4/95	79/91	99/99	105	290	323	4.36	4.32	3.91
25	7.5	3/75	83/95	99/99	99	292	313	4.21	4.44	4.28

^a Calculated using solids content measurements (see Section 3.4.1.6)

^b z-average particle diameter; obtained using PCS (see Section 3.4.1.2)

^c Calculated using PCS measurements of z-average particle diameter

As can be seen from the data in Table 7.13, all latexes were synthesised in a controlled manner, with high instantaneous and overall monomer conversion, constant particle number and increasing diameter throughout the reaction. Similar to observations made in Chapter 6 and Section 7.2 larger seed particles resulted in larger final particle diameters, which do not affect the mechanical properties of films. Lower monomer conversions of approximately 98% were seen for some latexes, although in these cases an accompanying decrease in particle number was seen indicating small amounts of coagulum formation. ADH was added to each latex as described in Section 3.3.1, at a DAAM:ADH molar stoichiometry of 2:1.

Films were cast from all of the latexes detailed in Table 7.12 using the procedure given in Section 3.3.2, and it was found that all eight variants formed cohesive films at ambient temperature. The thermal properties of each film were investigated using DSC as per the method in Section 3.4.3.2, the results of which are shown in Table 7.14. As can be seen from these data, there appears to be a general trend that as the DAAM content increases, the T_g of the film increases. However, there are a few anomalous results shown, especially at the very highest DAAM levels for the films with core T_g of 25 °C, with these observations being consistent upon repetition of the measurement.

Table 7.14 DSC data for films with high core phase T_g and crosslinker content

Core T_g^a / °C	DAAM content / shell wt%	Theoretical average T_g^b / °C	Observed T_g / °C
20	2	17	14 (± 1.3 °C)
20	3	17	15 (± 1 °C)
20	5	17	15 (± 1 °C)
20	7.5	17	16 (± 0.5 °C)
25	2	21	22 (± 1.5 °C)
25	3	21	22 (± 1 °C)
25	5	21	28 (± 1 °C)
25	7.5	21	23 (± 0.3 °C)

^a Calculated using the modified Fox equation derived in Section 4.5

^b Calculated by (core T_g x core proportion) + (shell T_g x shell proportion)

The stress-strain curves for each film are shown in Figure 7.7, and were obtained using the procedure for tensile testing given in Section 3.4.2.1. The derived Young's modulus, extension to break and stress at 4% strain values are given in Table 7.15 beneath. The films with higher core T_g are generally stiffer, which substantiates previous trends observed. However, there seems to be no identifiable trend in either Young's modulus or extension to break with increasing DAAM content, the former of which is not unexpected due to previous observations that the crosslinker content affects only high strain behaviour and is further substantiated by the values of stress at 4% strain, which show little variation between films with the same theoretical core phase T_g . An anomalous stress at 4% strain value is seen for the film with core T_g of 25 °C and 5 wt% DAAM in the shell phase, although a relatively large error is associated with this measurement so this may be due to experimental error.

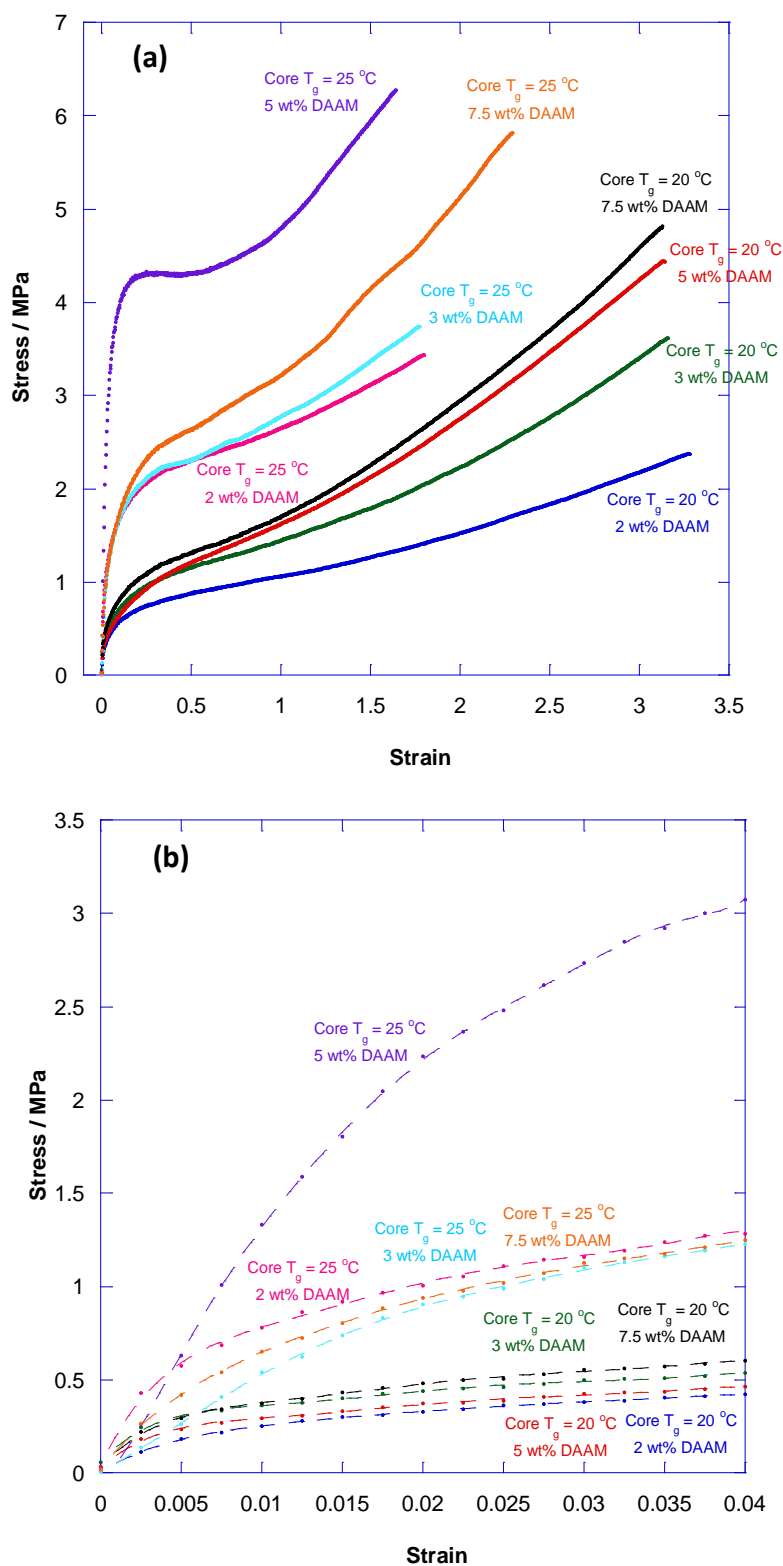


Figure 7.7(a) Stress-strain curves for 80:20 core:shell ratio films with varying core phase T_g and DAAM content. Film composition is poly[(BA)-*co*-(BMA)] core phase copolymer and poly[(BA)-*co*-(BMA)-*co*-(DAAM)] shell phase copolymer with ADH added at 2:1 molar stoichiometric ratio; **(b)** Section of stress-strain curves from (a) with strains of 0-4% used to calculate Young's modulus (coefficient of first order term in a polynomial fit expression; order of fit = 6)

Table 7.15 Mechanical property data for soft-soft nanocomposite films with 80:20 core:shell ratio, fixed shell T_g of 5 °C, high core copolymer T_g and variable DAAM content

Core T_g /°C	DAAM content / shell phase wt%	Young's modulus /MPa	Stress @ 4% strain / MPa	Extension to Break / %
20	2	75 (± 19 MPa)	0.43 (± 0.005)	500 (± 40%)
20	3	90 (± 15 MPa)	0.46 (±0.014)	530 (± 20%)
20	5	68 (± 8 MPa)	0.48 (± 0.036)	520 (± 30%)
20	7.5	99 (± 8 MPa)	0.48 (± 0.016)	540 (± 10 %)
25	2	182 (± 130 MPa)	1.08 (± 0.124)	270 (± 30 %)
25	3	87 (± 27 MPa)	0.99 (± 0.012)	320 (± 20%)
25	5	80 (± 68 MPa)	1.93 (± 0.260)	225 (± 35%)
25	7.5	98 (± 90 MPa)	1.07 (± 0.062)	375 (± 10%)

There is a slightly anomalous trend in peak stress and extension to break for the series with a core copolymer T_g of 25 °C, where the variant with 5 wt% DAAM in the shell appears to outperform the equivalent with 7.5 wt% DAAM. This trend was still evident after re-testing of both variants approximately one month after initial film formation. This was investigated further by AFM of film cross sections to deduce whether it was an effect of particle morphology retention in the film. Figure 7.8 shows optical images of the two film cross-section surfaces. Figures 7.9 and 7.10 show AFM images for the variant with core copolymer T_g of 25 °C and 5 wt% DAAM, and Figures 7.11 and 7.12 show images of the variant with the same core phase copolymer T_g but 7.5 wt% DAAM in the shell.

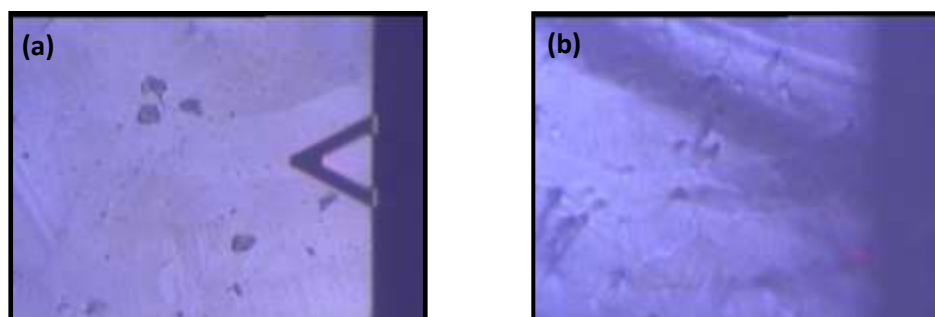


Figure 7.8 Optical images of film cross-sections for **(a)** Core copolymer $T_g = 25$ °C; 5 wt% DAAM in shell and **(b)** Core copolymer $T_g = 25$ °C; 7.5 wt% DAAM in shell

Figure 7.8 shows that there is very little difference optically in the film cross-sections, and what small differences are visible can be attributed to the sample preparation method (see Section 3.4.2.5). However, it is very obvious, especially from the larger images in Figures 7.10 and 7.12 that although the particle morphology looks to have been retained in a very similar way for both variants, the larger scale arrangements of the particles is very different on a scale of 1-2 μm . The implication of the AFM height image shown in Figure 7.13(b) for the 7.5 wt% DAAM film is that there are relatively deep 'valleys' in the fracture surface, compared to the much smoother surface for the 5 wt% DAAM film shown in Figure 7.13(a).

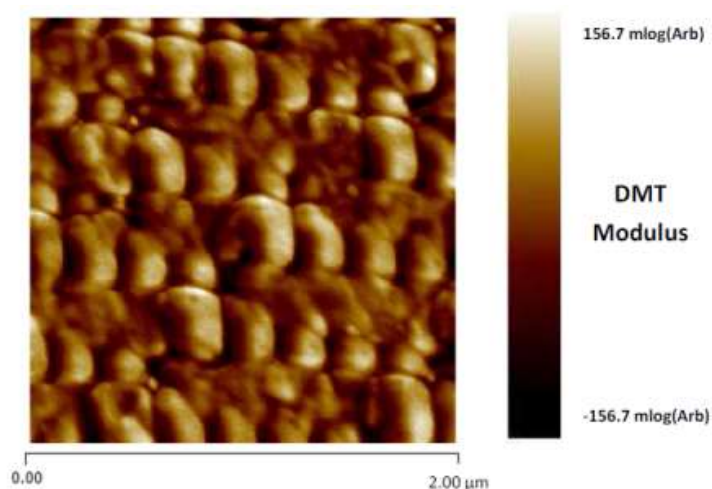


Figure 7.9 DMT Modulus AFM image of a lightly crosslinked soft-soft nanocomposite film cross-section with 80:20 core:shell ratio, comprising poly[(BA)-*co*-(BMA)] core and poly[(BA)-*co*-(BMA)-*co*-(DAAM)] shell phase copolymers with T_g s of 25 and 5 $^{\circ}\text{C}$, respectively and 5 wt% DAAM in the shell phase. ADH added at a 2:1 DAAM:ADH molar stoichiometric ratio. Image size = 2 μm square

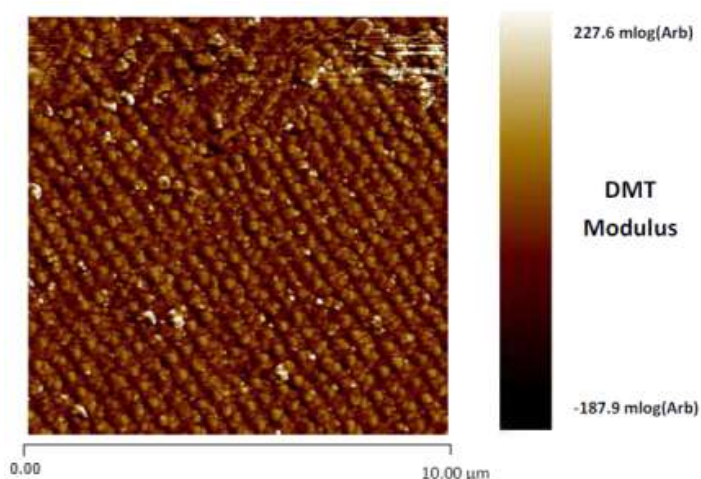


Figure 7.10 DMT Modulus AFM image of a lightly crosslinked soft-soft nanocomposite film cross-section with 80:20 core:shell ratio, comprising poly[(BA)-*co*-(BMA)] core and poly[(BA)-*co*-(BMA)-*co*-(DAAM)] shell phase copolymers with T_g s of 25 and 5 $^{\circ}\text{C}$, respectively and 5 wt% DAAM in the shell phase. ADH added at a 2:1 DAAM:ADH molar stoichiometric ratio. Image size = 10 μm square

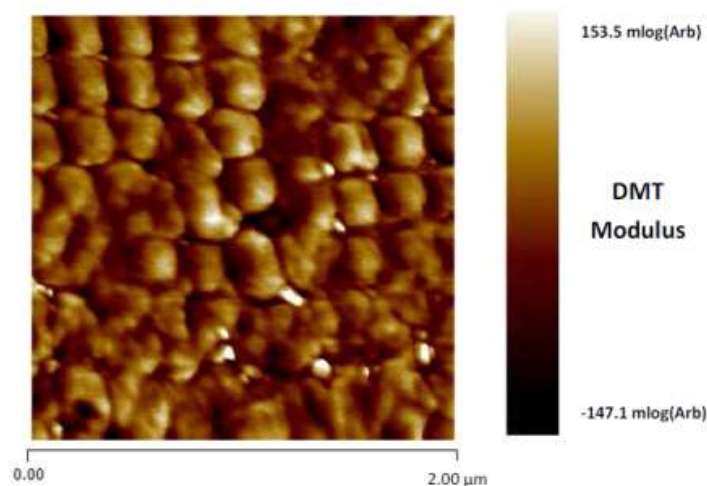


Figure 7.11 DMT Modulus AFM image of a lightly crosslinked soft-soft nanocomposite film cross-section with 80:20 core:shell ratio, comprising poly[(BA)-*co*-(BMA)] core and poly[(BA)-*co*-(BMA)-*co*-(DAAM)] shell phase copolymers with T_g s of 25 and 5 °C, respectively and 7.5 wt% DAAM in the shell phase. ADH added at a 2:1 DAAM:ADH molar stoichiometric ratio. Image size = 2 μ m square

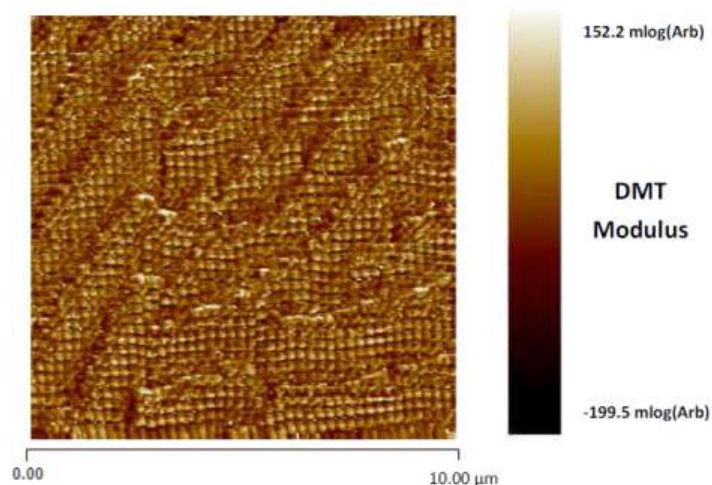


Figure 7.12 DMT Modulus AFM image of a lightly crosslinked soft-soft nanocomposite film cross-section with 80:20 core:shell ratio, comprising poly[(BA)-*co*-(BMA)] core and poly[(BA)-*co*-(BMA)-*co*-(DAAM)] shell phase copolymers with T_g s of 25 and 5 °C, respectively and 7.5 wt% DAAM in the shell phase. ADH added at a 2:1 DAAM:ADH molar stoichiometric ratio. Image size = 10 μ m square

In the system with the highest DAAM content, which would have been expected to outperform the film with a lower crosslinker level in terms of stress at failure, it can be seen that there is a secondary structure within the film, which is clearly visible in images larger than 5 μ m. Figure 7.13 shows the 10 μ m image size height images for these two films, from which this difference in film structure is immediately obvious. The height profiles of a section from these AFM images, shown in Figure 7.14, also show that a greater variation in height is seen across the film cross-section.

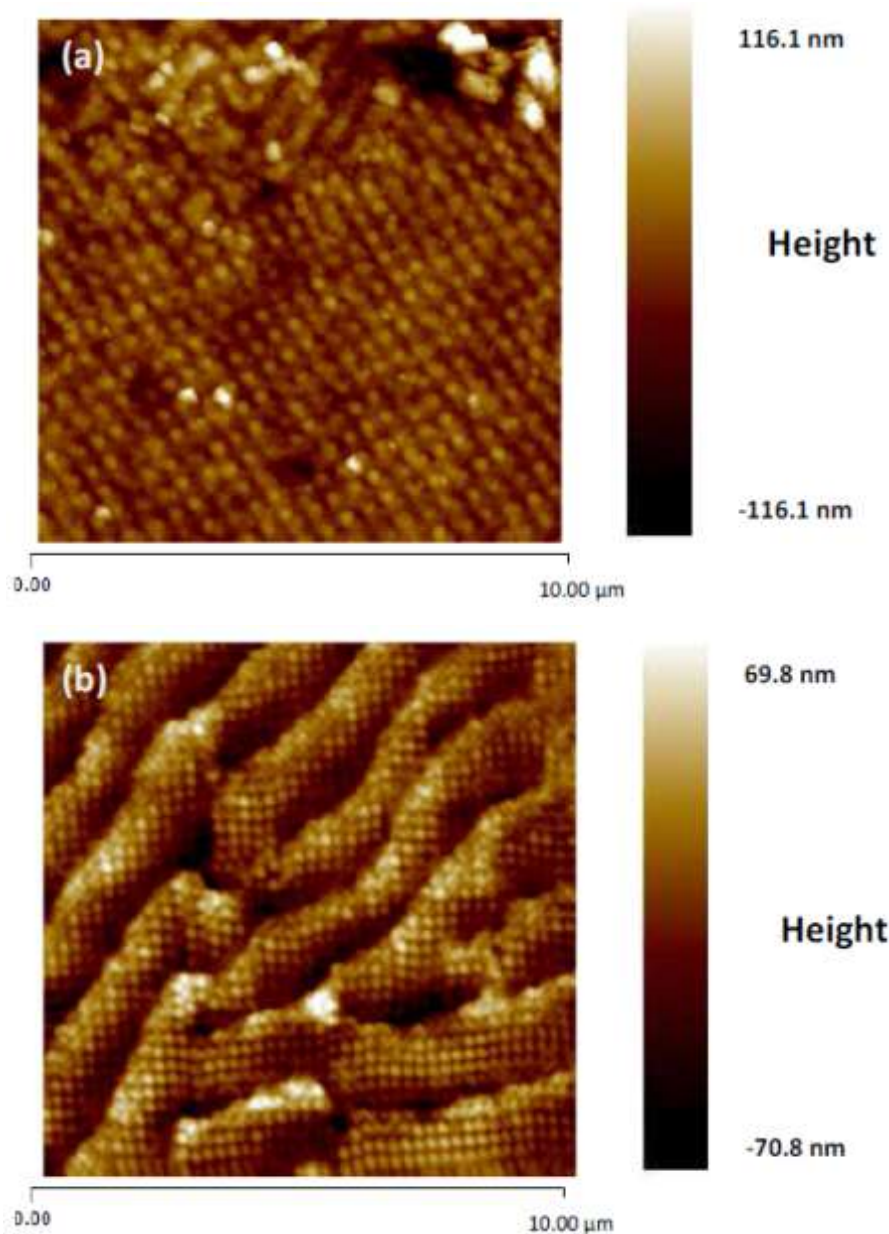


Figure 7.13 Height AFM images of a lightly crosslinked soft-soft nanocomposite film cross-section with 80:20 core:shell ratio, comprising poly[(BA)-*co*-(BMA)] core and poly[(BA)-*co*-(BMA)-*co*-(DAAM)] shell phase copolymers with **(a)** T_g s of 25 and 5 °C, respectively, and 5 wt% DAAM in the shell phase and **(b)** T_g s of 25 and 5 °C, respectively, and 7.5 wt% DAAM in the shell phase . ADH added at a 2:1 DAAM:ADH molar stoichiometric ratio. Image sizes = 10 μm square

These AFM images parallels the appearance of the two modulus images shown in Figures 7.10 and 7.12 and, when considered together with the height profile shown in Figure 7.14 and the stress-strain curves, suggest that the rate of keto-hydrazide crosslinking may be similar to or in excess of the rate of chain interdiffusion between particles in the case of the film with 7.5 wt% DAAM, leading to a lack of molecular mobility and therefore a lack of cohesion, causing mechanical weaknesses within the film^{227, 228}.

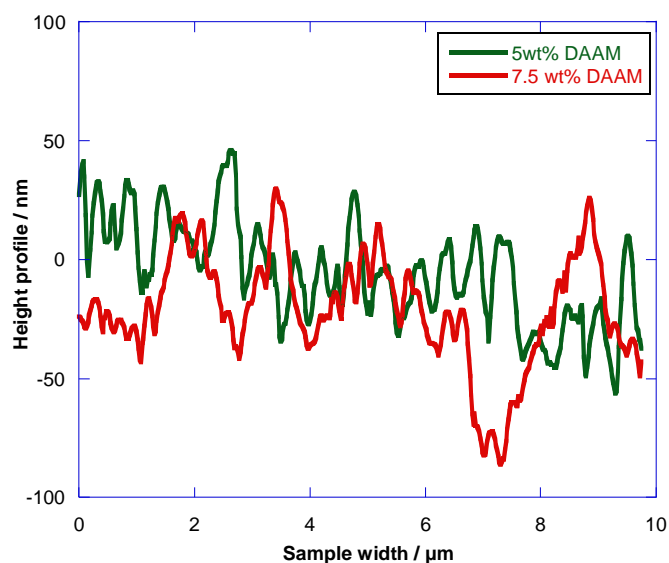


Figure 7.14 Height profiles for a lightly crosslinked soft-soft nanocomposite film cross-sections with 80:20 core:shell ratio, comprising poly[(BA)-*co*-(BMA)] core and poly[(BA)-*co*-(BMA)-*co*-(DAAM)] shell phase copolymers with T_g s of 25 and 5 °C, respectively, and 5 wt% and 7.5 wt% DAAM in the shell phase.

Despite this anomalous result, a general trend was observed which supports the findings from Section 7.2 and Chapter 6, whereby the elevated core copolymer T_g affected the low strain mechanical performance of the films, and an elevated level of crosslinking led to increased strain hardening at high strains.

7.4 Investigating the effect of shell T_g upon film properties

The effect of shell phase T_g is investigated in this section at three different core:shell ratios, with the core phase T_g , shell DAAM content and DAAM:ADH ratio kept constant. Table 7.16 details the parameters that were kept constant.

Table 7.16 Parameters kept constant throughout Section 7.4

Parameter	Value for each latex discussed in Section 7.4
Core T_g	10 °C
Core phase chemical composition	Poly[(BA)- <i>co</i> -(BMA)]
Shell phase chemical composition	Poly[(BA)- <i>co</i> -(BMA)- <i>co</i> -(DAAM)]
DAAM level	2 wt% of shell phase copolymer
DAAM:ADH ratio	2:1

Based on the MFT results in Section 7.2.4, the highest shell T_g investigated in this section was 15 °C, in order to retain the film forming properties. Latexes with core:shell ratios of 70:30, 80:20 and 90:10 were synthesised with core phase comprising a poly[(BA)-*co*-(BMA)] copolymer of constant $T_g = 10$ °C and poly[(BA)-*co*-(BMA)-*co*-(DAAM)] shell phase copolymers

with T_g of 5, 10 and 15 °C. As discussed in Section 4.5, the T_g of the shell phase copolymer was predicted using the Fox equation, which is given in Equation 4.2.

A summary of characterisation data is given in Table 7.17, which shows that all polymerisations were found to proceed in a controlled manner, with constant particle numbers, high instantaneous and overall monomer conversion and steadily increasing diameter throughout the reaction. Full kinetics characterisation plots for each preparation can be found in Appendix (iv).

Table 7.17 Synthesis characterisation data for preparations detailed in Table 7.16

Core:shell ratio	Shell T_g / °C	Overall/ Instantaneous conversion ^a / %			Particle diameter ^b /nm			Total particle number ^c / x 10 ¹⁶		
		Seed	Core	Final	Seed	Core	Final	Seed	Core	Final
70:30	5	3.6/96	69/98	96/96	91	246	286	4.30	6.60	5.91
70:30	10	4.0/97	67/99	97/97	96	237	277	5.95	6.54	6.00
70:30	15	4.0/98	65/98	99/99	93	237	273	6.59	5.87	6.48
80:20	5	3.7/98	78/96	97/97	95	260	293	6.20	6.32	5.48
80:20	10	3.5/95	76/95	96/96	96	258	279	5.86	6.40	6.45
80:20	15	3.9/96	77/96	98/98	92	248	277	6.71	7.28	6.21
90:10	5	3.6/100	87/96	98/98	100	294	308	5.46	5.07	5.01
90:10	10	3.0/99	82/95	91/91	93	254	273	6.70	7.83	7.92
90:10	15	3.0/99	81/93	92/92	74	205	215	13.5	14.7	16.3

^a Calculated using solids content measurements (see Section 3.4.1.6)

^b z-average particle diameter; obtained using PCS (see Section 3.4.1.2)

^c Calculated using PCS measurements of z-average particle diameter

These data show that for all latexes detailed in Table 7.17, control of the polymerisation was gained. Similar to previous observations, the size of the seed particle determined the final particle diameters. A very small particle diameter was gained for the latex with a core:shell ratio of 90:10 and a shell T_g of 15 °C, which can be explained by a large particle number almost three times in excess of the other latexes prepared. However as it has been shown that the particle size does not affect the mechanical properties of the films, this latex will be used as planned. Very low conversions of 91 and 92%, respectively, were gained for the 90:10 latexes with shell T_g s of 10 and 15 °C. As no decrease is seen in particle number, it can be assumed that this is due to monomer evaporation.

ADH was added to the latexes at a 2:1 DAAM:ADH ratio, as described in Section 3.3.1. Films were cast from each latex in accord with Section 3.3.2; coherent films were formed at ambient temperature for all systems. Films were analysed by DSC and tensile testing, the

methods for which are given in Section 3.4.3.2 and Section 3.4.2.1, respectively. The results are summarised in Table 7.18 and Figures 7.15 – 7.17 and Table 7.19.

Table 7.18 DSC data for films with varying shell phase T_g

Core:shell ratio	Theoretical core $T_g^a / ^\circ\text{C}$	Theoretical shell $T_g^b / ^\circ\text{C}$	Theoretical average $T_g^c / ^\circ\text{C}$	Observed $T_g / ^\circ\text{C}$
70:30	10	5	8.5	6 (± 0.5)
70:30	10	10	10	7 (± 1)
70:30	10	15	11.5	5 (± 1)
80:20	10	5	9	5 (± 0.3)
80:20	10	10	10	5 (± 1)
80:20	10	15	11	8 (± 0.2)
90:10	10	5	9.5	6 (± 0.3)
90:10	10	10	10	4 (± 0.2)
90:10	10	15	10.5	5 (± 1)

^a Calculated using the modified Fox equation derived in Section 4.5

^b Calculated using the fox equation (see Equation 4.2)

^c Calculated by (core T_g x core proportion)+(shell T_g x shell proportion)

Little difference between variants was seen in the experimentally determined T_g values, as seen in Table 7.18, which again can be attributed to the low level of shell copolymer present not significantly affecting the film properties. However as has been previously seen throughout this chapter, and especially in Section 7.2.1 for films with a 70:30 core:shell ratio, the observed T_g s are much lower than their theoretically predicted values. A contributing factor to this consistent observation may be the slightly lower overall monomer conversions of ca. 96-97% that are seen in the kinetics data. As discussed in Section 4.5, unreacted residual monomer is known to plasticise and lower the polymer T_g , although GC analysis of a latex with an overall monomer conversion of 97% showed extremely low levels of residual BA and BMA, with both present at concentration of approximately 0.003 wt%. Hence, it is not possible to definitively identify the cause of these depressed T_g values, with plasticisation by water and surfactant remaining in the film matrix the best explanation.

The stress-strain curves in Figures 7.15-7.17 show that for all core:shell ratios, increasingly higher stresses are needed to axially deform films with higher shell phase T_g , although the Young's modulus and extension to break values for each are not dramatically different. This can be attributed to the shell phase copolymer forming the minority (< 30 wt%) of each film, and hence not being the predominant factor in determining the mechanical behaviour.

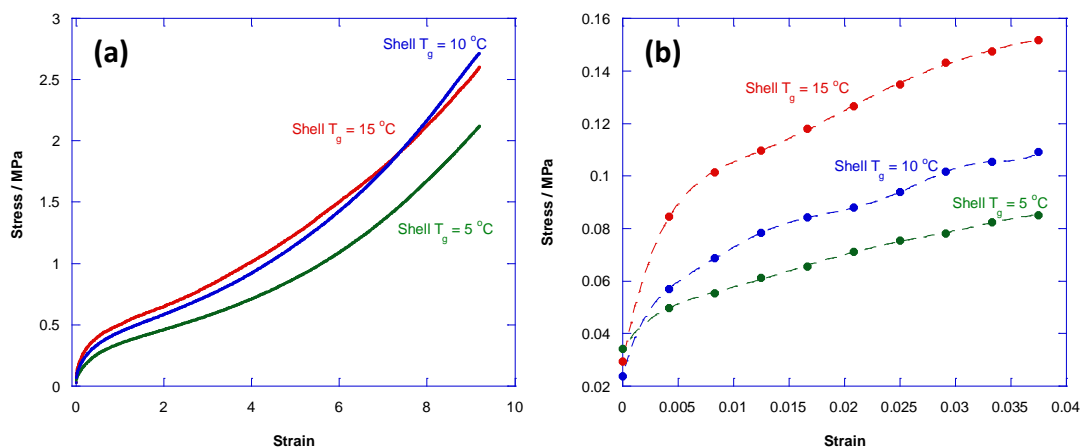


Figure 7.15 (a) Stress-strain curves for 70:30 core:shell ratio films with varying shell phase T_g . Film composition is poly[(BA)-*co*-(BMA)] core phase copolymer with $T_g = 10\text{ }^\circ\text{C}$ and poly[(BA)-*co*-(BMA)-*co*-(DAAM)] shell phase copolymer with ADH added at 2:1 molar stoichiometric ratio; **(b)** Section of stress-strain curves from (a) with strains of 0-4% used to calculate Young's modulus (coefficient of first order term in a polynomial fit expression; order of fit = 6)

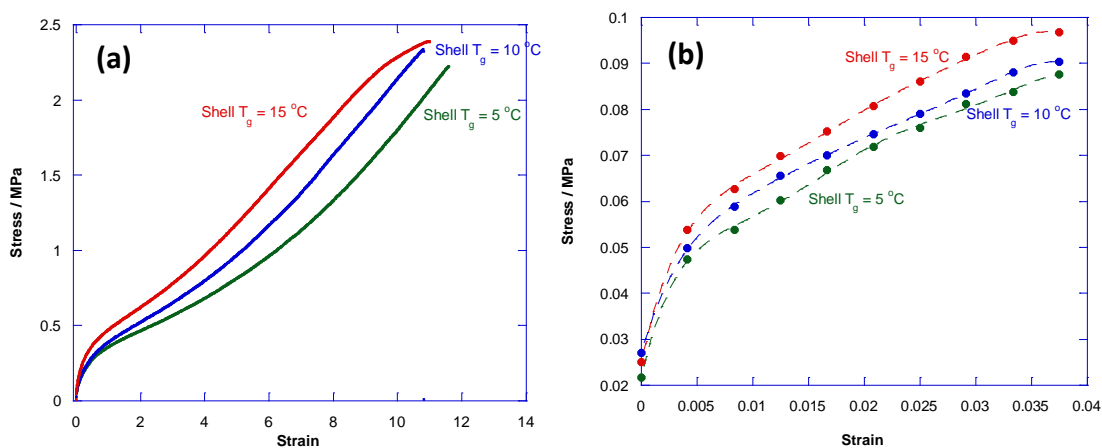


Figure 7.16(a) Stress-strain curves for 80:20 core:shell ratio films with varying shell phase T_g . Film composition is poly[(BA)-*co*-(BMA)] core phase copolymer with $T_g = 10\text{ }^\circ\text{C}$ and poly[(BA)-*co*-(BMA)-*co*-(DAAM)] shell phase copolymer with ADH added at 2:1 molar stoichiometric ratio; **(b)** Section of stress-strain curves from (a) with strains of 0-4% used to calculate Young's modulus (coefficient of first order term in a polynomial fit expression; order of fit = 6)

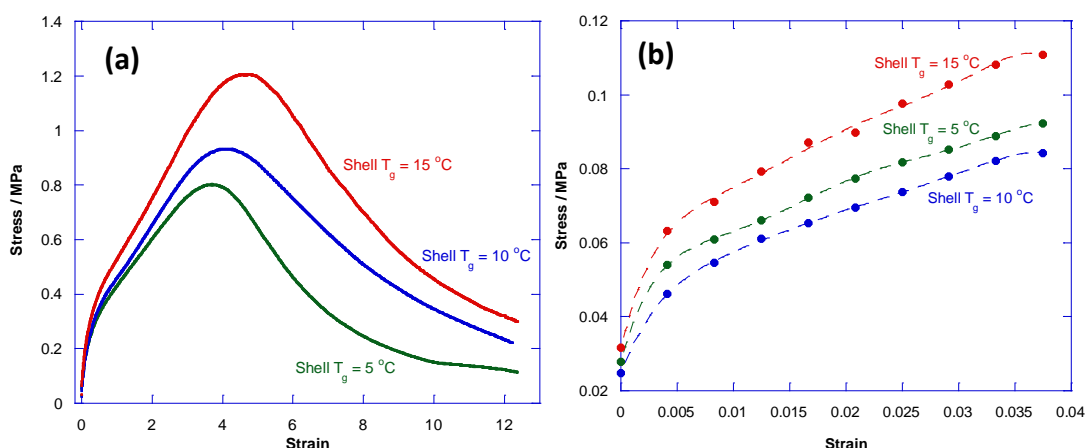


Figure 7.17(a) Stress-strain curves for 90:10 core:shell ratio films with varying shell phase T_g . Film composition is poly[(BA)-*co*-(BMA)] core phase copolymer with $T_g = 10\text{ }^\circ\text{C}$ and poly[(BA)-*co*-(BMA)-*co*-(DAAM)] shell phase copolymer with ADH added at 2:1 molar stoichiometric ratio; **(b)** Section of stress-strain curves from (a) with strains of 0-4% used to calculate Young's modulus (coefficient of first order term in a polynomial fit expression; order of fit = 6)

Table 7.19 Mechanical property data for films with fixed core T_g of $10\text{ }^\circ\text{C}$ and varying shell phase T_g

Core:shell ratio	Shell T_g / $^\circ\text{C}$	Young's modulus /MPa	Stress @ 4% strain /MPa	Extension to break /%
70:30	5	7 (± 2.5 MPa)	0.11 (± 0.014)	900 ($\pm 75\%$)
70:30	10	17 (± 1 MPa)	0.12 (± 0.017)	800 ($\pm 100\%$)
70:30	15	16 (± 4 MPa)	0.13 (± 0.014)	1010 ($\pm 30\%$)
<hr/>				
80:20	5	12 (± 5.5 MPa)	0.12 (± 0.06)	1170 ($\pm 40\%$)
80:20	10	10 (± 0.5 MPa)	0.10 (± 0.003)	1470 ($\pm 40\%$)
80:20	15	11 (± 1 MPa)	0.09 (± 0.005)	1000 ($\pm 75\%$)
<hr/>				
90:10	5	16 (± 1 MPa)	0.12 (± 0.01)	1990 ($\pm 50\%$)
90:10	10	12 (± 2.5 MPa)	0.10 (± 0.009)	1930 ($\pm 140\%$)
90:10	15	13 (± 2.5 MPa)	0.10 (± 0.010)	2220 ($\pm 170\%$)

From the results that have been discussed in this section, it has been established that the shell phase copolymer T_g does not significantly alter the high- or low-strain mechanical behaviour, unlike for crosslinker content and core phase T_g . Little significant difference between Young's modulus or extension to break can be seen at any of the core:shell ratios

studied in this section. This is not an unexpected observation, as in all cases the shell phase forms the lesser proportion (< 30wt%) of the particles, so will have less influence upon the mechanical properties of the film than the predominant core phase copolymer even though it is the percolating phase and would be expected to significantly affect high strain properties. As this is the case, it will be advantageous in future studies to keep the shell phase copolymer T_g as low as possible in order to retain optimum film formation properties.

7.5 Effect of the average T_g upon Young's modulus

The work that has been discussed in this chapter shows that there is a strong relationship between core phase copolymer T_g and the Young's modulus of the resulting soft-soft nanocomposite film, a trend which is evident for all three core:shell ratios that have been tested. For all systems discussed herein, the shell phase comprises a poly[(BA)-co-(BMA)-co-(DAAM)] copolymer with $T_g = 5\text{ }^\circ\text{C}$.

It can be seen from the plot in Figure 7.18 that there is a general trend for Young's modulus to increase with the observed film T_g , independent of core:shell ratio. However, the correlation is much better defined when Young's modulus is plotted against the theoretical core copolymer T_g values, as can be seen in Figure 7.19, and it becomes evident that predicting the Young's modulus of a film using core copolymer T_g may be possible.

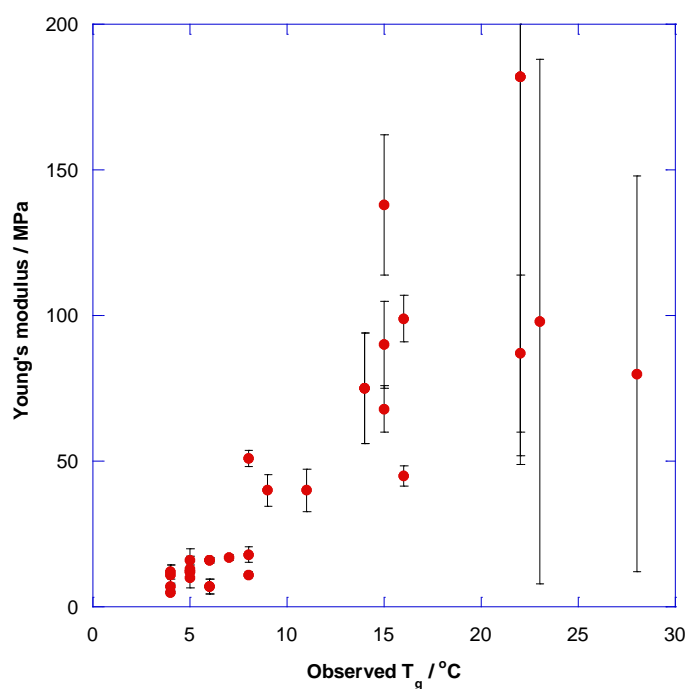


Figure 7.18 Variation of Young's modulus with observed T_g for soft-soft nanocomposite films with a poly[(BA)-co-(BMA)] core phase copolymer and a poly[(BA)-co-(BMA)-co-(DAAM)] shell phase copolymer with fixed $T_g = 5\text{ }^\circ\text{C}$. ADH was added to each film at a 2:1 DAAM:ADH molar stoichiometry

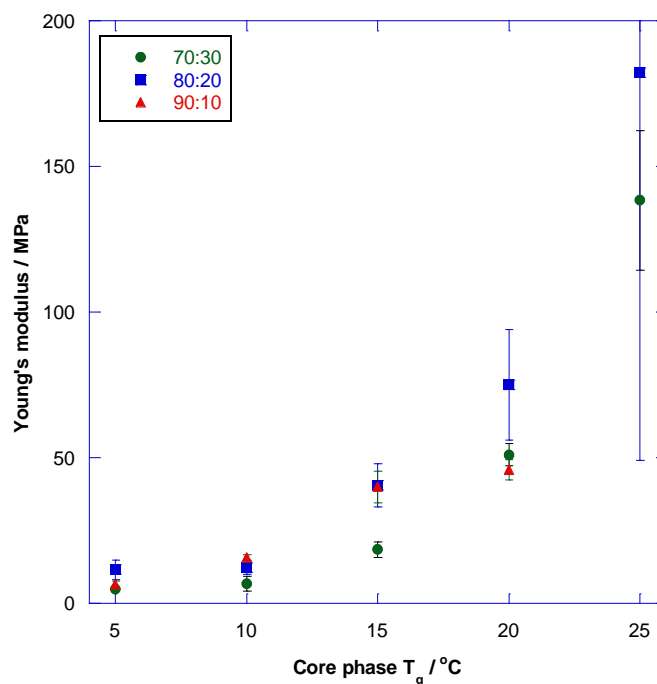


Figure 7.19 Variation of Young's modulus values with core phase T_g for soft-soft nanocomposite films with a poly[(BA)-*co*-(BMA)] core phase copolymer and a poly[(BA)-*co*-(BMA)-*co*-(DAAM)] shell phase copolymer with fixed $T_g = 5$ °C. ADH was added to each film at a 2:1 DAAM:ADH molar stoichiometry

The effect of core phase T_g is likely to be a consequence of the film T_g values being in the region where modulus changes rapidly with temperature, so that much higher Young's modulus is seen for films with higher core T_g . Figure 7.20 shows DMTA profiles for soft-soft nanocomposite films with both low (5 °C) and high (25 °C) core T_g . It is immediately obvious that the observed T_g s of the films, as given by the peak in $\tan \delta$ ¹⁶⁵, are much higher than those given by DSC. DSC is much more controlled with regard to recording the exact temperature of the sample during measurements due to a much smaller sample being used that is in very good thermal contact with the thermocouple, and DMTA measures the changes in modulus with temperature, which is changed at a much slower rate than in DSC. Hence, the modulus values have been shifted to lower temperatures by the average difference in T_g between DMTA and DSC, which was 22 °C. The plot of storage modulus versus adjusted temperature shown in Figure 7.21 shows why the variance in modulus of lower T_g films is so low, as at ambient temperatures (10-25 °C) the modulus is approximately constant. However, it can clearly be seen that a much larger variation in modulus can be accessed in this temperature range for the film with a higher core T_g , which explains the much larger range of moduli seen for higher core T_g systems in Figure 7.19.

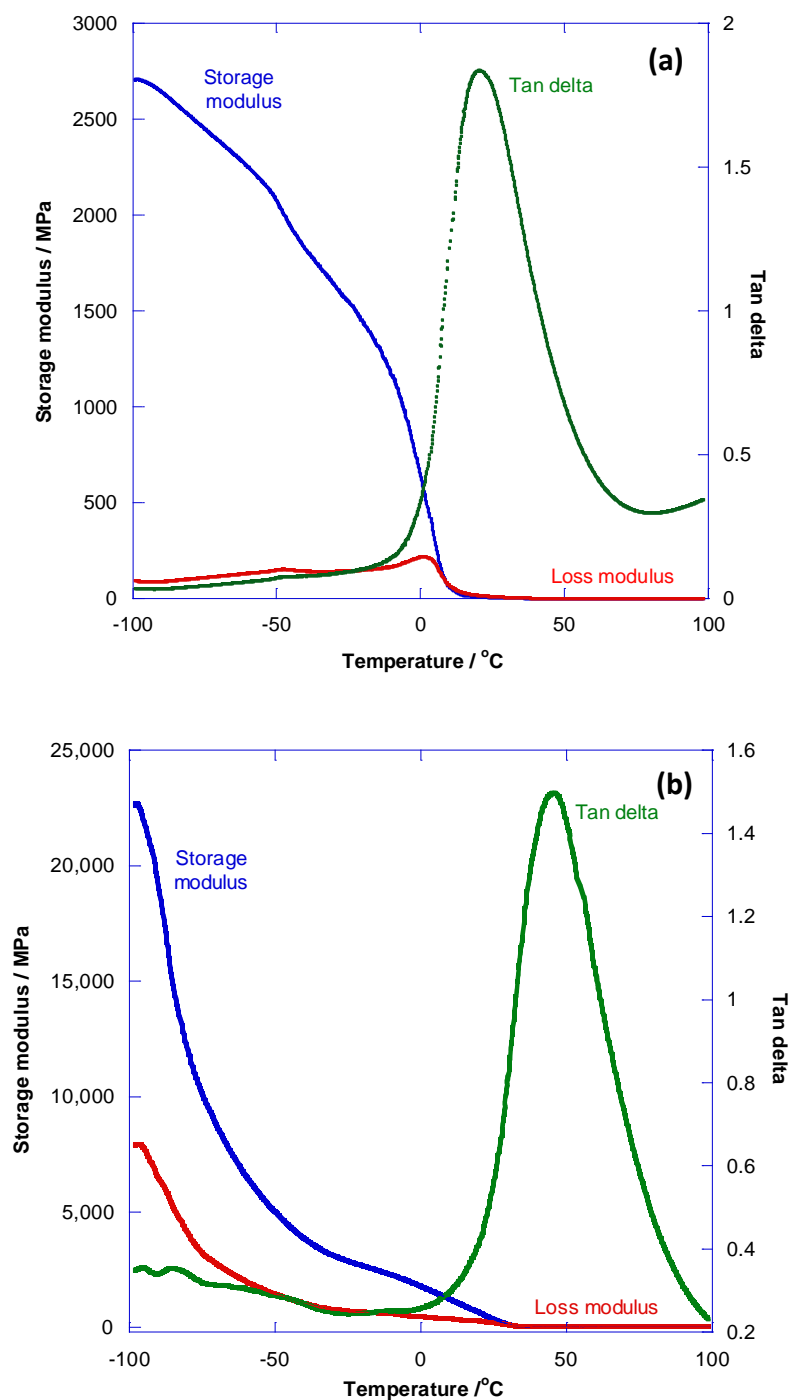


Figure 7.20 DMTA profiles for soft-soft nanocomposite films with a poly[(BA)-*co*-(BMA)] core phase copolymer and a poly[(BA)-*co*-(BMA)-*co*-(DAAM)] shell phase copolymer with (a) fixed core and shell $T_g = 5\text{ }^\circ\text{C}$ and (b) core $T_g = 25\text{ }^\circ\text{C}$ and shell $T_g = 5\text{ }^\circ\text{C}$. ADH was added to the films at a 2:1 DAAM:ADH molar stoichiometry.

NB: The comparison between high and low core T_g systems can only be considered approximate as the high core T_g system, which has a large difference between core and shell T_g , can be considered to be truly 'core-shell', but the low T_g system, for which the core and shell phases have identical T_g and very similar chemical compositions, cannot.

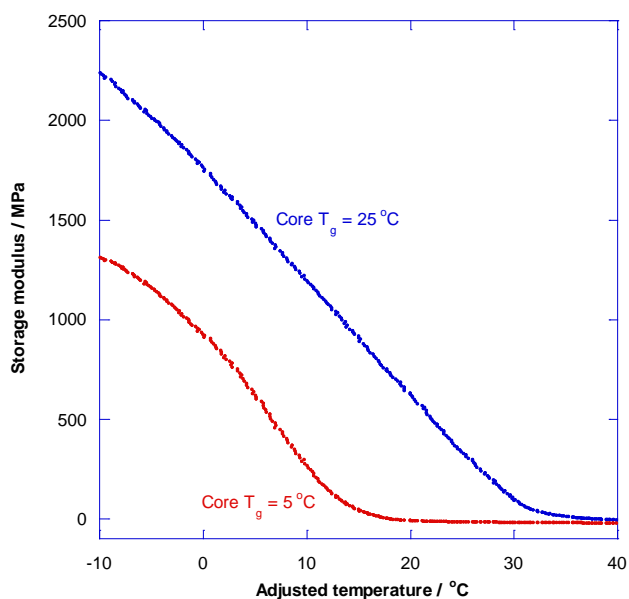


Figure 7.21 Zoomed portion of Storage modulus vs. adjusted temperature plot for soft-soft nanocomposite films with a poly[(BA)-*co*-(BMA)] core phase copolymer and a poly[(BA)-*co*-(BMA)-*co*-(DAAM)] shell phase copolymer with fixed core and shell $T_g = 5\text{ }^\circ\text{C}$ and core $T_g = 25\text{ }^\circ\text{C}$ and shell $T_g = 5\text{ }^\circ\text{C}$. ADH was added to the films at a 2:1 DAAM:ADH molar stoichiometry

Given that the core T_g appears to be dominant, a plot of Young's modulus against $V_c \cdot T_g$, where V_c is the volume fraction of the core phase and T_g is the theoretical core phase T_g , was considered appropriate and is shown in Figure 7.22. The correlation is significantly improved with the data collapsing to a single line, showing that there is definite scope for predicting the Young's modulus of soft-soft nanocomposite materials.

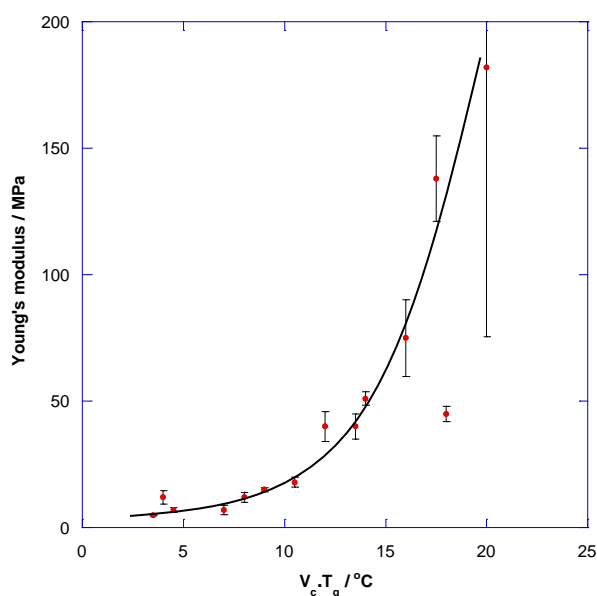


Figure 7.22 Variation of Young's modulus with $V_c \cdot T_g$, where V_c is the core phase volume fraction, for soft-soft nanocomposite films with a poly[(BA)-*co*-(BMA)] core phase copolymer and a poly[(BA)-*co*-(BMA)-*co*-(DAAM)] shell phase copolymer with fixed $T_g = 5\text{ }^\circ\text{C}$. ADH was added to each film at a 2:1 DAAM:ADH molar stoichiometry

7.6 Conclusions

The work discussed in this chapter has shown that it is possible to control the Young's modulus, and low strain mechanical behaviour of soft-soft nanocomposite films by changing the core phase polymer T_g . This was found to be especially noticeable when the core copolymer T_g was in excess of ambient temperature ($> 20\text{ }^\circ\text{C}$), and is not unexpected due to the nature of glass transition which causes polymer chains to become rigid and glassy at temperatures below T_g . As the core phase copolymer comprises a large ($> 70\text{ wt}\%$) proportion of all the films tested, the rigidity of the phase at higher copolymer T_g led to a significant increase in Young's modulus of the films tested, with the highest value, 180 MPa, being gained for a film with an 80:20 core:shell ratio and a core copolymer T_g of $25\text{ }^\circ\text{C}$. A corresponding decrease in extensibility was also seen for these films, which was also expected due to the more rigid nature of the film at high T_g .

Incorporating both high core copolymer T_g and high crosslinker contents into soft-soft nanocomposite resulted in mechanical behaviour in accordance with the trends shown for the two individual parameters. All films had high Young's modulus, resulting from the high core phase T_g , and films with higher DAAM content typically had lower extension to break ratios and showed an increased degree of strain hardening. Based on AFM images, an anomalous result whereby the variant with core copolymer $T_g = 25\text{ }^\circ\text{C}$ and 5 wt% DAAM mechanically outperformed the equivalent system with 7.5 wt% DAAM was attributed to the rate of crosslinking in the percolating shell phase copolymer for the latter being similar to, or exceeding, the rate of inter-particle chain diffusion, which resulted in inherent mechanical weaknesses in the films.

Changing the shell phase copolymer T_g did not significantly affect either the high or low strain behaviour, but did affect the amount of energy required to continually deform the film until failure. This shows that varying the T_g to just below ambient temperature (maximum of $15\text{ }^\circ\text{C}$) does not affect the elastomeric properties of the percolating, crosslinked shell phase, and hence indicates that the key principles of the soft-soft nanocomposite theory still hold at T_g very close to application temperature.

8 Effect of methacrylic acid on film properties

8.1 Introduction

A 'functional monomer' is the description given to a monomer that has a secondary function and does not simply just become a structural part of the polymer backbone. Examples of this functionality may be crosslinking ability, particle stabilization effects or antimicrobial activity. Diacetone acrylamide (DAAM), has already been extensively discussed in this thesis as it is used to impart crosslinking into the percolating shell phase of a film formed from a soft-soft nanocomposite latex. Carboxylic acid co-monomers, such as acrylic acid (AA) and methacrylic acid (MAA), the structures of which are shown in Figure 8.1, are commonly used in emulsion polymerisation processes to provide additional colloidal stability²²⁹ and to alter the surface characteristics of the particles in order to promote the desired application properties of the latex¹¹. When ionised, these side groups give rise to enhanced colloidal stability through electrosteric stabilisation, whereby electrostatic and steric stabilisation effects combine^{230, 231}.

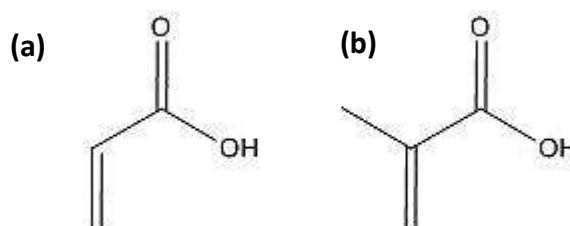


Figure 8.1 Structures of (a) acrylic acid (AA) and (b) methacrylic acid (MAA)

Dobler *et al.* reported that carboxylic acid functionalities incorporated into poly[Sty-*co*-(BA)] and poly[Sty-*co*-Bd] copolymers resided largely at the particle surfaces, which was established by acid titration of the latexes²³². This provides both steric stabilisation, from the pendant, hydrophilic MAA groups, and electrostatic stabilisation as the carboxylate anions on the surface repel each other and thus preventing particles from aggregating.

The addition of acrylic carboxylate monomers to film-forming latexes has been extensively reported in the literature, and is found to increase the rigidity and hardness of films. This is partly due to ionic crosslinking reactions that are facilitated by the presence of additional carboxylate groups²³³, and also the high T_g of the acid monomer homopolymers (106 °C for poly(AA) and 220 °C for poly(MAA))⁵⁶.

Guo *et al.* reported in 2007 that the addition of AA to a poly[(MMA)-*co*-(BA)-*co*-(DAAM)] copolymer enhanced the DAAM-ADH crosslinking reaction (used in this thesis), leading to

improved tensile strength and solvent resistance²³⁴. An optimum level of 1.5 wt% AA gave the best tensile strength and failure stress, with higher levels of AA delivering no additional benefits. Hence, it was established that a relatively low level of acid monomer can deliver big improvements in film properties, with higher levels being detrimental due to an increased hydrophilicity of the film. Improvement in film and latex properties when (meth)acrylic acid functionality is present has also been reported for PSAs^{229, 235}, inks²³⁶ and coatings²³⁷⁻²³⁹.

The use of MAA as a crosslinking monomer with regards to the soft-soft nanocomposite design theory has been reported by both Pinprayoon *et al.*⁷ and Tungchaiwattana *et al.*^{8, 9}. In their work, ionomerically crosslinked nitrile rubber mimics, the pH of the latex was adjusted to 8.0 after the addition of a ZnO particle dispersion, which causes the carboxylate groups to become 'bridged' by the Zn²⁺ cations and hence form a crosslinked network. A schematic representation of this process is shown in Figure 8.2.

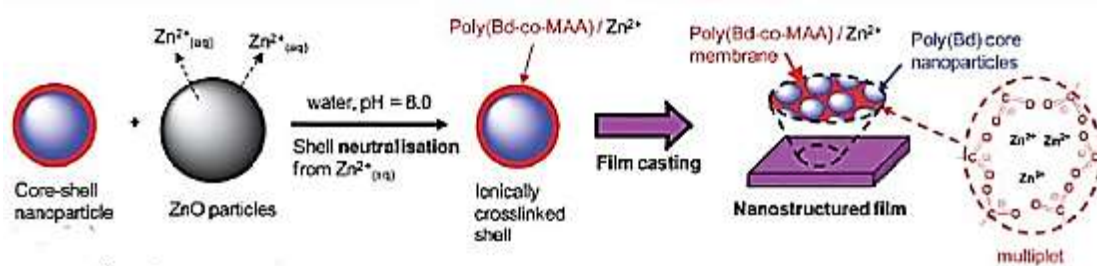


Figure 8.2 Schematic diagram showing the incorporation of ionic crosslinking into soft-soft nanocomposite nitrile rubber films using MAA and Zn species⁹

Large changes in the mechanical properties of these soft-soft nanocomposite nitrile films was observed when only small changes in the MAA content were made (between 1-2 mol% of the shell phase copolymer), which enabled a high level of tuneability with regard to the film properties⁹. The effect of MAA-ZnO ionomeric crosslinking level upon film properties was also investigated by Bas *et al.* in poly[(MAA)-*co*-(BA)-*co*-(HEMA)-*co*-(MAA)] latexes in 2013²⁴⁰. It was found that latexes incorporating this crosslinking chemistry had very high Young's modulus but poor toughness compared to equivalent copolymers crosslinked using a melamine-formaldehyde resin.

The effect of adding methacrylic acid into the shell phase copolymer upon film properties is reported in this chapter. In addition to possible enhancements in film properties from ionomeric crosslinking, it was also hoped that the addition of acid functionalities would impart additional colloidal stability to the latex, as problems with coagulum levels have been previously encountered (see Section 4.3), although these were countered by the addition of a non-ionic surfactant (see Section 4.4). MAA was chosen as the carboxylic acid co-monomer

over AA due to its greater hydrophobicity²⁴¹, which helps to retain the water resistance of the films.

8.2 Effect of adding methacrylic acid to the shell phase copolymer of soft-soft nanocomposites

The composition of seven latexes prepared to investigate the effect of including MAA in the shell phase are given in Table 8.1, and encompasses two different core and shell T_g combinations to deduce whether this affects the film performance. The core:shell ratio, shell phase copolymer T_g , DAAM content and DAAM:ADH ratio were all kept constant. The core phase copolymer composition was poly[(BA)-*co*-(BMA)], and the shell phase copolymer was poly[(BA)-*co*-(BMA)-*co*-(MAA)-*co*-(DAAM)]. Core copolymer T_g was calculated using the modified Fox equation derived in Section 4.5 and shell copolymer T_g using the Fox equation (see Equation 4.1).

After evaluation of the first six of these systems, the seventh variant (with 3.5 wt% MAA) was added to the high core copolymer T_g set to broaden the investigation after slightly anomalous results were gained at 2 and 5 wt% MAA.

Table 8.1 Synthesis matrix of variants to evaluate the effect of adding MAA

Core:shell ratio	DAAM content / shell phase wt%	MAA content / shell phase wt%	Core T_g / °C	Shell T_g / °C	DAAM:ADH ratio
80:20	2	0	10	5	2:1
80:20	2	2	10	5	2:1
80:20	2	5	10	5	2:1
80:20	2	0	25	5	2:1
80:20	2	2	25	5	2:1
80:20	2	3.5	25	5	2:1
80:20	2	5	25	5	2:1

A summary of the characterisation data for each of the seven polymerisations are given in Table 8.2, and detailed kinetics plots for each preparation can be found in Appendix (v). All polymerisations were found to be controlled, with high instantaneous conversion, constant particle number and particle growth in alignment with theoretical values. However, low overall monomer conversions were seen for the series of latexes with a core phase T_g of 25 °C, which can be explained as evaporation of monomer from the reaction vessel as the number of particles for each preparation remains approximately constant, ruling out any significant occurrence of coagulum. As per all other latexes in this work the seed particle diameter dictated the final particle diameter, and all latexes had a final diameter within the specification as described in the soft-soft nanocomposite design theory (250-350 nm).

Table 8.2 Synthesis characterisation data for preparations described in Table 8.1

Core T _g / °C	MAA content /Shell wt%	Overall/ Instantaneous conversion ^a / %			Particle diameter ^b /nm			Total particle number ^c / x 10 ¹⁶		
		Seed	Core	Final	Seed	Core	Final	Seed	Core	Final
10	0	3.7/98	78/96	97/97	95	260	293	6.20	6.32	5.48
10	2	3.7/94	80/95	99/99	106	274	295	4.19	5.34	5.26
10	5	3.8/95	80/96	99/99	99	269	294	5.24	5.73	5.24
25	0	3.7/96	78/95	97/97	108	304	331	4.09	3.91	3.83
25	2	3.5/89	82/95	98/98	112	304	331	3.40	3.89	3.63
25	3.5	3.4/92	76/94	97/97	101	282	305	4.75	4.84	4.88
25	5	3.9/95	82/93	99/99	116	311	340	3.24	3.56	3.31

^a Calculated using solids content measurements (see Section 3.4.1.6)

^b z-average particle diameter; obtained using PCS (see Section 3.4.1.2)

^c Calculated using PCS measurements of z-average particle diameter

ADH was added to all seven latexes at a 2:1 molar stoichiometric DAAM:ADH ratio, as described in Section 3.3.1. Films were then cast from these latexes and analysed using DSC and tensile testing according to the descriptions in Sections 3.4.3.2 and 3.3.2, respectively.

8.2.1 Systems with lower core T_g

The stress-strain curves for the soft-soft nanocomposite films with a core phase copolymer T_g of 10 °C can be seen in Figure 8.3, and Table 8.3 gives the resulting Young's modulus, extension to break and stress at 4% strain data. Thermal analysis data are given in Table 8.4.

It was found that as the shell phase copolymer MAA content increased in lower core T_g systems, no significant differences could be found in either the high or low strain mechanical behaviour, as the Young's modulus and extension to break values for all three films are very similar. A small degree of strain hardening was observed as the MAA content increased. In addition, a very slight increase in the observed film T_g was found, although this is within the limits of experimental error.

Table 8.3 Mechanical property data for the lower core T_g systems with varying amounts of MAA in the shell phase

Core T _g / °C	MAA content /Shell phase wt%	Young's modulus /MPa	Stress @ 4% Strain /MPa	Extension to Break /%
10	0	12 (± 2.4 MPa)	0.08 (± 0.006)	1150 (± 40%)
10	2	12 (± 1.2 MPa)	0.11 (± 0.007)	1050 (± 60%)
10	5	14 (± 2.3 MPa)	0.11 (± 0.006)	1000 (± 40%)

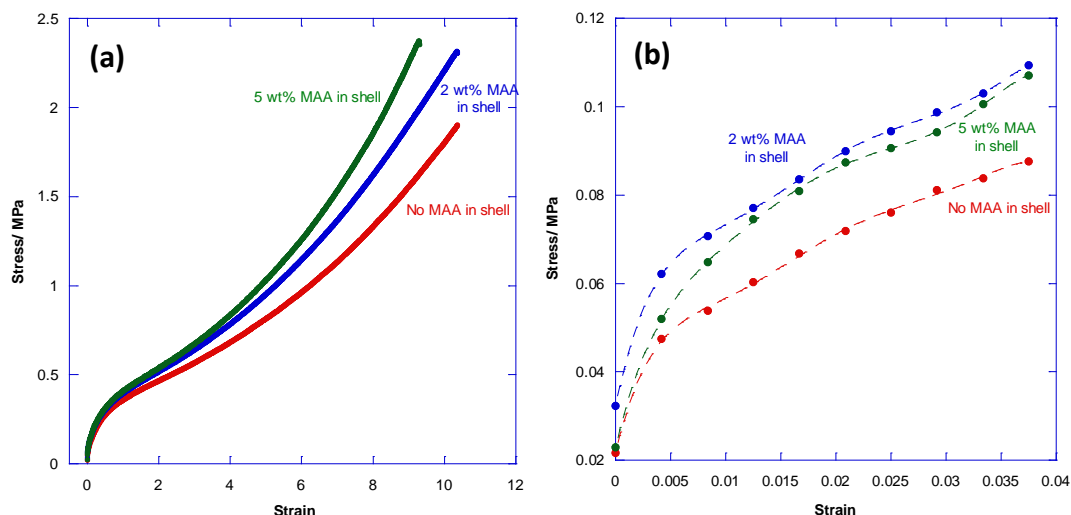


Figure 8.3 (a) Stress-strain curves for 80:20 core:shell ratio films with core copolymer $T_g = 10$ °C and varying levels of MAA in the shell phase copolymer. Film composition is poly[(BA)-*co*-(BMA)] core phase copolymer and poly[(BA)-*co*-(BMA)-*co*-(DAAM)-*co*-(MAA)] shell phase copolymer with ADH added at 2:1 molar stoichiometric ratio; **(b)** Section of stress-strain curves from (a) with strains of 0-4% used to calculate Young's modulus (coefficient of first order term in a polynomial fit expression; order of fit = 6)

Table 8.4 DSC data for low core T_g systems with varying amounts of MAA in the shell phase

Core T_g / °C	MAA content /Shell phase wt%	Observed T_g / °C
10	0	5 (± 0.3 °C)
10	2	6 (± 1.6 °C)
10	5	7 (± 1 °C)

8.2.2 Systems with higher core T_g

Figure 8.4 and Table 8.5 show the stress-strain profiles and mechanical data, respectively, for systems with core copolymer T_g of 25 °C, and the results of DSC analysis are shown in Table 8.6. The stress-strain curves in Figure 8.4 reveal an anomalous result for the variant with 5 wt% MAA in the shell, which has inferior mechanical properties to those with 2 and 3.5 wt%. It is clear that the addition of MAA into the shell phase copolymer of these soft-soft nanocomposite films with higher core copolymer T_g has a significant effect upon the mechanical properties of the materials.

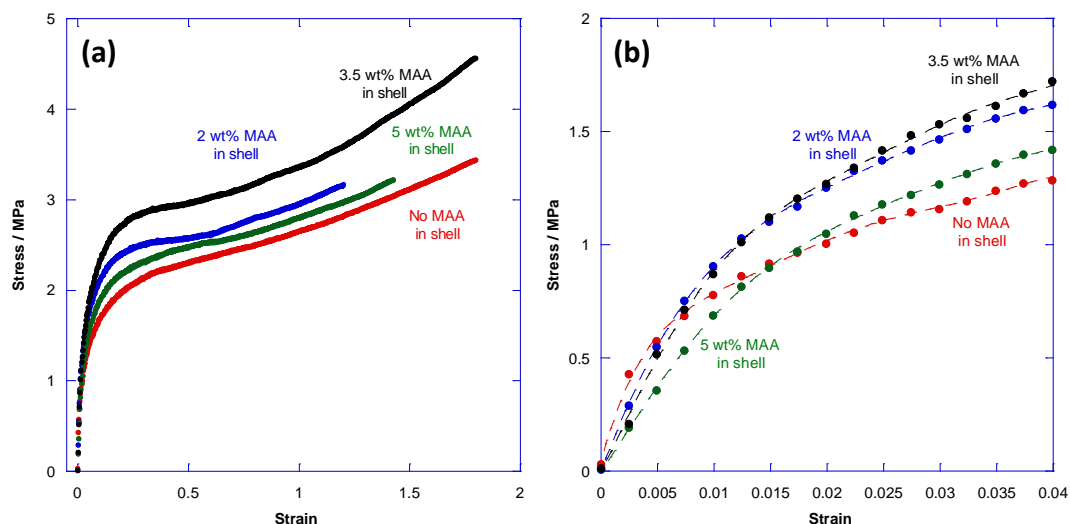


Figure 8.4 (a) Stress-strain curves for 80:20 core:shell ratio films with core copolymer $T_g = 25$ °C and varying levels of MAA in the shell phase copolymer. Film composition is poly[(BA)-*co*-(BMA)] core phase copolymer and poly[(BA)-*co*-(BMA)-*co*-(DAAM)-*co*-(MAA)] shell phase copolymer with ADH added at 2:1 molar stoichiometric ratio; **(b)** Section of stress-strain curves from (a) with strains of 0-4% used to calculate Young's modulus (coefficient of first order term in a polynomial fit expression; order of fit = 6)

Table 8.5 Mechanical property data for high core T_g systems with varying amounts of MAA in the shell phase

Core T_g / °C	MAA content /Shell phase wt%	Young's modulus /MPa	Stress @ 4% strain /MPa	Extension to Break /%
25	0	182 (± 133 MPa)	1.36 (± 0.124)	260 (± 30%)
25	2	426 (± 155 MPa)	1.62 (± 0.040)	240 (± 30%)
25	3.5	150 (± 70 MPa)	1.45 (± 0.080)	340 (± 30%)
25	5	51 (± 27 MPa)	1.43 (± 0.031)	210 (± 40%)

Table 8.6 DSC data for high core T_g systems with varying amounts of MAA in the shell phase

Core T_g / °C	MAA content /Shell phase wt%	Observed T_g / °C
25	0	22 (± 1.3 °C)
25	2	24 (± 1.4 °C)
25	3.5	23 (± 0.4 °C)
25	5	24 (± 1.5 °C)

In order to explain these anomalous stress-strain profiles, the behaviour of the acid groups in the film environment must be taken into account. For the homopolymer poly(MAA) the pK_a of the acid groups is approximately 5²⁴², meaning that at a pH of 8.5 these groups

would be expected to be fully dissociated. However, Saunders *et al.* reported that a poly[(EA)-*co*-(MAA)-*co*-(BDDA)] microgel, where BDDA is 1,4-butanediol diacrylate, with a low MAA content of 5.6 wt% had a pKa of 8.2²⁴³. This apparent increase in pKa was attributed to the hydrophobic environment provided by EA, which composed 93% of the microgel, and has a low dielectric constant that would restrict the dissociation of the acid groups. Similar effects whereby an increase in pKa with a decrease in acid content have also been reported by Saunders *et al.*²⁴⁴ and Khokhlov *et al.*²⁴⁵. As both butyl acrylate and butyl methacrylate are hydrophobic monomers, the pKa of the MAA repeat units, which are present at low levels of below 5 wt%, can be assumed to be similar to the value of 8.2 as reported by Saunders *et al.*. Hence, the -CO₂H groups will be, at least, partly ionised in the film as the latex is adjusted to pH 8.5 prior to ADH addition and film formation. This will introduce a small degree of ionomer behaviour, which would be expected to increase crosslinking in the percolating phase.

No significant differences are seen in the observed T_g values for the films, which is not unexpected as all have the same core and shell T_g , and low levels of crosslinking. Although the highest Young's modulus value observed thus far (426 MPa) was observed during this work for a film with 2 wt% MAA, very large error was associated with it as jaw separation was used to measure the strain. This represents huge inaccuracies at the very small strain values, which are used to calculate Young's modulus, as have been previously discussed in Chapters 5-7. However, this variant with 2 wt% MAA also has the highest value of stress at 4% strain, which is a more reliable measurement of low strain mechanical performance and thus supports the high Young's modulus.

An apparent optimum level of MAA can be identified depending on which region of stress-strain behaviour is being targeted. A system with 2 wt% MAA appears optimum for Young's modulus, but the system that gives optimum extensibility has 3.5 wt% MAA in the shell phase copolymer, which is somewhat unexpected. The system with 5wt% MAA shows inferior mechanical properties to all the other systems tested, including that with no MAA incorporated. This suggests that there is a deteriorious effect of adding the higher levels of methacrylic acid. According to Saunders *et al.*, as the concentration of acid groups increases the pKa of the polymer will decrease. At a constant pH, this means that more acid groups will become dissociated into carboxylate anions, and results in a greater degree of ionomer formation. These ionomer clusters would be expected to form quickly, and at higher levels may restrict molecular processes such as chain interdiffusion and DAAM-ADH crosslinking which occur during the film formation process.

This effect was reported by Winnik *et al.* in 1994²⁴⁶, who investigated the rate of chain diffusion in systems with poly(BMA) core and poly[(BMA)-*co*-(MAA)] shell copolymers, with levels of MAA that varied from 1.25% to 5.78 wt% of the shell phase. It was found from direct non-radiative energy transfer measurements using fluorescence spectroscopy that increasing the concentration of MAA in the shell phase copolymer does not prevent interparticle chain diffusion, but causes it to occur at a much slower rate. This was attributed to the effect of molecular weight dispersity upon diffusion coefficients of the polymer chains, and the effect of MAA upon shell copolymer T_g .

It is theorised that the formation of a 'membrane' consisting of acid end-groups around the particle surfaces may occur when higher levels of acid groups are present, which restrict interparticle chain diffusion during the final stage of film formation²⁴⁷⁻²⁵⁰. The hypotheses state that this membrane remains intact in the dry film, until elevation of the temperature above film T_g , after which it is dispelled into the film matrix and does not continue to retard the film formation processes. This explains why little difference is observed with varying MAA content in the films with low core copolymer T_g , which are above T_g at the mechanical testing temperature of 23 °C (see Table 8.4), but such significant differences in mechanical behaviour are seen for the films which have higher T_g values that are above this (see Table 8.6).

8.2.3 AFM imaging of MAA-containing films

The effect of ionomeric crosslinking and the possible formation of an ionic membrane in the soft-soft nanocomposite films with higher core phase copolymer T_g clearly has a significant effect upon the film properties. Hence, AFM imaging was used to investigate whether any differences in film structure and retained morphology exist. AFM imaging was performed using the methodology described in Section 3.4.2.5.

As was previously observed (see Section 7.3), larger scale images that show more of the film surface are more useful. Figure 8.5 and Figure 8.6 show 5 μm square images of soft-soft nanocomposite films containing 2 and 5 wt% MAA, respectively.

A significant difference in film structure can be seen from the images in Figures 8.5 and 8.6, with a more cohesive film being formed for the film with 2 wt% MAA. Although defined lines along particle boundaries can be seen in both images, these are sharper and more definitive in Figure 8.6 for the film with 5 wt% MAA, and may indicate that interparticle diffusion has been restricted which would lead to a decrease in the cohesiveness of the film. This observation potentially supports the hypothesis that was previously suggested by

Winnik *et al.* that the increased concentration of MAA groups restricts intermolecular diffusion, and hence leads to inherent mechanical weaknesses in the films²¹².

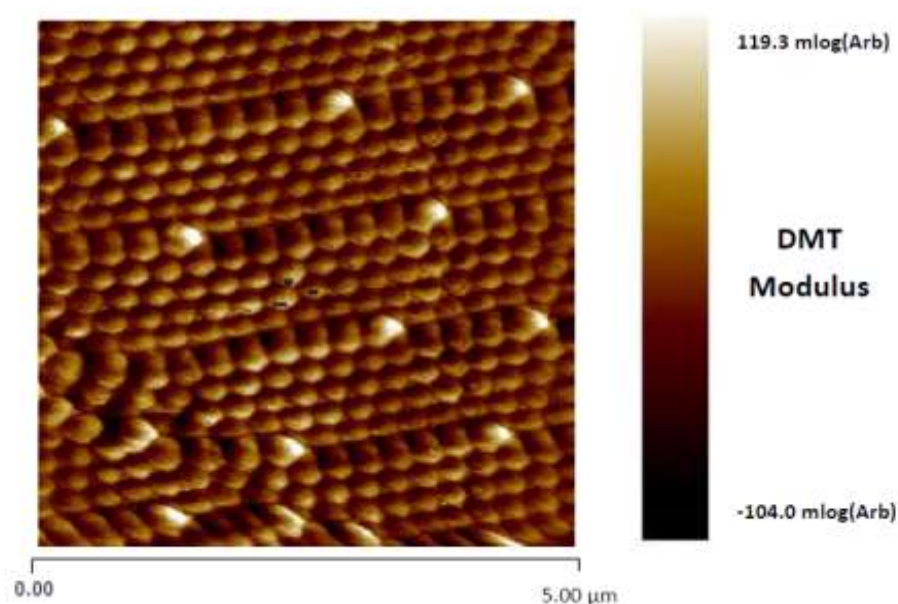


Figure 8.5 DMT Modulus AFM image of a lightly-crosslinked soft-soft nanocomposite film cross-section with 80:20 core:shell ratio, comprising poly[(BA)-*co*-(BMA)] core and poly[(BA)-*co*-(BMA)-*co*-(DAAM)-*co*-(MAA)] shell phase copolymers with T_g s of 25 and 5 °C, respectively, with 2 wt% MAA present in the shell phase only. ADH was added at a 2:1 DAAM:ADH molar stoichiometric ratio. Image size = 5 μm square

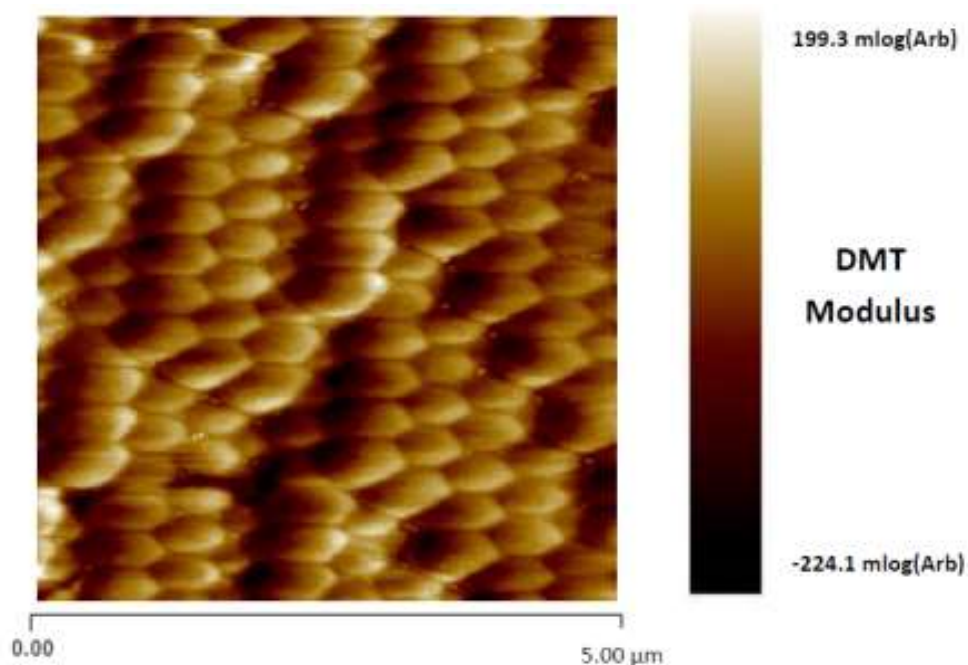


Figure 8.6 DMT Modulus AFM image of a lightly-crosslinked soft-soft nanocomposite film cross-section with 80:20 core:shell ratio, comprising poly[(BA)-*co*-(BMA)] core and poly[(BA)-*co*-(BMA)-*co*-(DAAM)-*co*-(MAA)] shell phase copolymers with T_g s of 25 and 5 °C, respectively, with 5 wt% MAA present in the shell phase. ADH was added at a 2:1 DAAM:ADH molar stoichiometric ratio. Image size = 5 μm square

However, it can be clearly seen in these images that there is a significant difference in particle size between the films shown in Figures 8.5 and 8.6, which may make visually discerning the particle boundaries more challenging.

In 2014, Adelnia *et al.* reported that higher levels of carboxylate monomers in a poly[(MMA)-*co*-(BA)-*co*-(AA)] film led to a higher degree of ordering in the film matrix²⁵¹, which can be observed by AFM. Such a trend is not seen in the films imaged in Figure 8.5 and Figure 8.6, which may be due to the surface of the film being imaged rather than the bulk cross-section, as is the case for the images presented in Section 8.2.3.

8.3 Effect of type of neutralisation on the film properties of MAA-containing soft-soft nanocomposites

During discussions about the film properties reported in Section 8.2, the possibility was raised that type of neutralisation may affect the behaviour. In all work presented thus far, sodium hydroxide (NaOH) has been used to adjust the pH of the latexes to ~ 8.5 . This type of neutralisation is permanent, as NaOH is non-volatile. Use of ammonia (NH₃) to neutralise the latexes may result in only 'temporary' neutralisation occurring, as due to its volatility NH₃ can evaporate out of the film matrix during the first stage of film formation. This would lead to the ionomeric clusters that arise from neutralisation not being retained in the final film (or at least not to the same extent) and hence not delivering the additional benefits to mechanical performance that were discussed in Section 8.2.

The effect of the type of neutralisation upon the migration of surfactant and the level of interparticle diffusion in poly[(MMA)-*co*-(BA)-*co*-(MAA)] latex films, as measured by force modulation AFM, was reported by Hellgren in 1998²⁵². An ionic membrane surrounding the particle surface which restricted both surfactant migration and interparticle chain diffusion was observed for those samples which had been neutralised with NaOH, but no such effect was seen for those with NH₃ neutralisation. This was attributed to the evaporation of the volatile NH₃ base resulting in the carboxylic acid side groups being neutralised and therefore not forming an ionic membrane. This was further investigated by Backfolk *et al.* in 2008 who found that a higher T_g 'salt shell' was present around the surface of poly[Sty-*co*-(BA)-*co*-(MAA)] copolymer particles, which was found by AFM to have a thickness of approximately 10 nm²⁵³. It was also reported that neutralisation of a carboxylated film, and hence the formation of an ionic shell, with NH₃ and NaOH led to interparticle chain diffusion being 6- and 10-fold slower, respectively, than in an unneutralised carboxylated film with no such ionic membrane surrounding the particle surface.

Winnik *et al.* reported in 1994 that Na^+ ions retarded interparticle diffusion to a much greater extent than NH_4^+ ions, although both were less effective at this retardation than Ba^{2+} ions²¹². However, in order to avoid the bridging of carboxylate groups by the divalent cation, and hence deliberately forming additional ionic crosslinks, Ba^{2+} species were not included in the work discussed in this section.

Only one latex was used to investigate the effect of the type of neutralisation upon MAA-containing soft-soft nanocomposite latexes, which is the system containing 2 wt% MAA that had the highest Young's modulus of 425 MPa. Full details of this system are given in Table 8.7.

Table 8.7 Details of latex used for the investigation discussed in Section 8.3.

Parameter	Value
Core:shell mass ratio	80:20
Core/shell copolymer T_g	25 / 5 °C
Core copolymer composition	Poly[(BA)- <i>co</i> -(BMA)]
Shell copolymer composition	Poly[(BA)- <i>co</i> -(BMA)- <i>co</i> -(DAAM)- <i>co</i> -(MAA)]
DAAM content	2 wt% in shell phase
MAA content	2 wt% in shell phase
DAAM:ADH stoichiometric ratio	2:1 (neutralised latexes only)

N.B. Kinetics data for the preparation of this latex can be found in Appendix (v)

Portions of the latex were then prepared in three different ways – (i) ‘permanent’ neutralisation using NaOH followed by addition of ADH, (ii) ‘temporary’ neutralisation using NH_3 then addition of ADH and (iii) no neutralisation or ADH. Films were cast according to the protocol in Section 3.3.2, and then tensile tested as described in Section 3.4.3.2. Figure 8.7 and Table 8.8 show the results.

The results presented in Figure 8.5 and Table 8.8 show that the type of neutralisation has an effect upon the Young's modulus and the higher strain mechanical properties of these MAA-containing films. ‘Temporary’ neutralisation with NH_3 resulted in a film with a much lower Young's modulus, but a higher peak stress than that ‘permanently’ neutralised with NaOH. The uncrosslinked, unneutralised film included in the study had a high Young's modulus and a lower extension to break ratio than the other two neutralised films. However, a strong trend is observed in the stress at 4% strain values, whereby $\text{NaOH} > \text{NH}_3 > \text{unneutralised}$. Due to large errors associated with the Young's modulus, this is a better

indication of the low strain mechanical properties of these systems, and shows that neutralising these MAA-containing latexes is beneficial to the film.

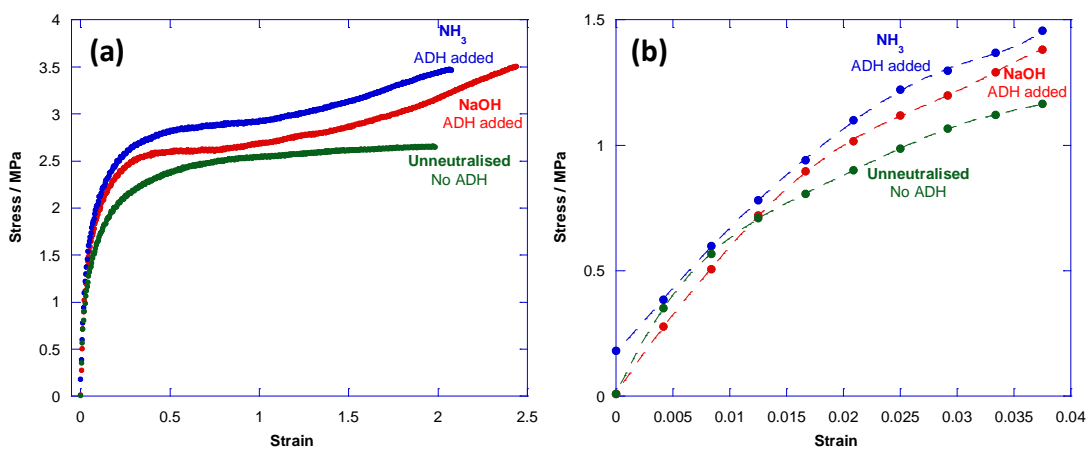


Figure 8.7 Stress-strain curves for 80:20 core:shell ratio films with core copolymer $T_g = 25^\circ\text{C}$ and 2 wt% MAA in the shell phase copolymer. Film composition is poly[(BA)-*co*-(BMA)] core phase copolymer and poly[(BA)-*co*-(BMA)-*co*-(DAAM)-*co*-(MAA)] shell phase copolymer with ADH added at 2:1 molar stoichiometric ratio; **(b)** Section of stress-strain curves from (a) with strains of 0-4% used to calculate Young's modulus (coefficient of first order term in a polynomial fit expression; order of fit = 6)

Table 8.8 Mechanical property data for MAA-containing latex with varying methods of neutralisation

ADH added?	Type of neutralisation	Young's modulus /MPa	Stress @ 4% strain /MPa	Extension to Break /%
Yes	NaOH (Permanent)	426 (± 155 MPa)	1.62 (± 0.040)	240 ($\pm 30\%$)
Yes	NH ₃ (Temporary)	46 (± 9 MPa)	1.41 (± 0.080)	230 ($\pm 10\%$)
No	None	125 (± 30 MPa)	1.28 (± 0.020)	164 ($\pm 30\%$)

Due to these differences in mechanical behaviour, the film structure and morphology of each of these systems was investigated by AFM, using the methodology given in Section 3.4.2.5. Figures 8.8 – 8.10 show 5 μm square DMT modulus images for NaOH, NH₃ and unneutralised films, respectively.

These images reveal a large difference in film structure between the neutralised films and the unneutralised, uncrosslinked film. The latter film has much higher degree of coalescence and less retained particle memory, indicating that a higher level of interparticle chain diffusion has occurred, which is in line with the effect reported by Backfolk *et al.* regarding the relative rates of particle diffusion in neutralised and unneutralised systems. However, it should be noted that these effects are due to a combination of the lack of both

neutralisation and ADH, and it cannot be easily established which of these had the greater impact upon the film structure.

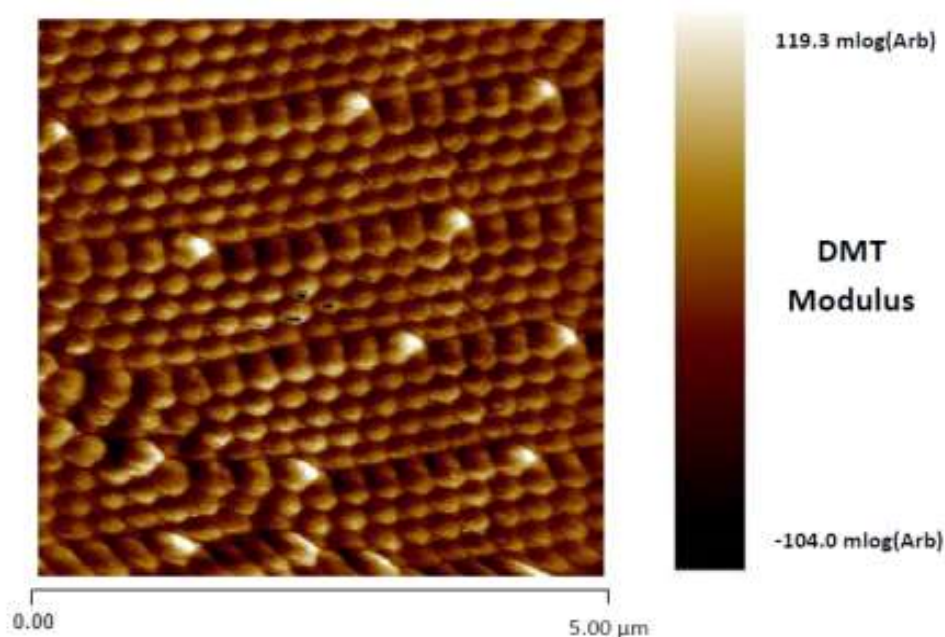


Figure 8.8 DMT Modulus AFM image of a lightly crosslinked soft-soft nanocomposite film cross-section with 80:20 core:shell ratio, comprising poly[(BA)-*co*-(BMA)] core and poly[(BA)-*co*-(BMA)-*co*-(DAAM)-*co*-(MAA)] shell phase copolymers with T_g s of 25 and 5 °C, respectively, with 2 wt% MAA present in the shell phase and latex neutralised with NaOH. ADH was added at a 2:1 DAAM:ADH molar stoichiometric ratio. Image size = 5 μm square

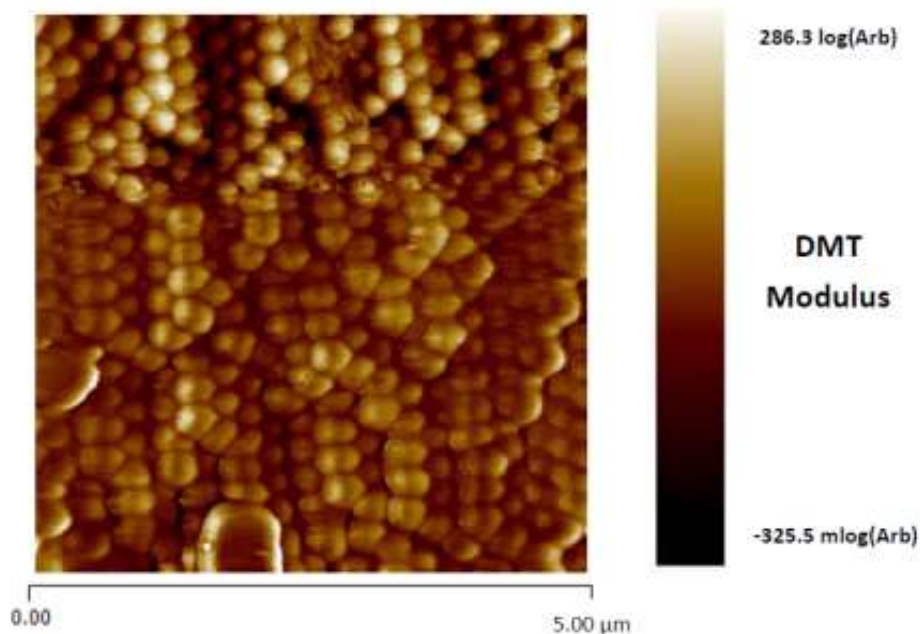


Figure 8.9 DMT Modulus AFM image of a lightly crosslinked soft-soft nanocomposite film cross-section with 80:20 core:shell ratio, comprising poly[(BA)-*co*-(BMA)] core and poly[(BA)-*co*-(BMA)-*co*-(DAAM)-*co*-(MAA)] shell phase copolymers with T_g s of 25 and 5 °C, respectively, with 2 wt% MAA present in the shell phase and latex neutralised with NH_3 . ADH added at a 2:1 DAAM:ADH molar stoichiometric ratio. Image size = 5 μm square

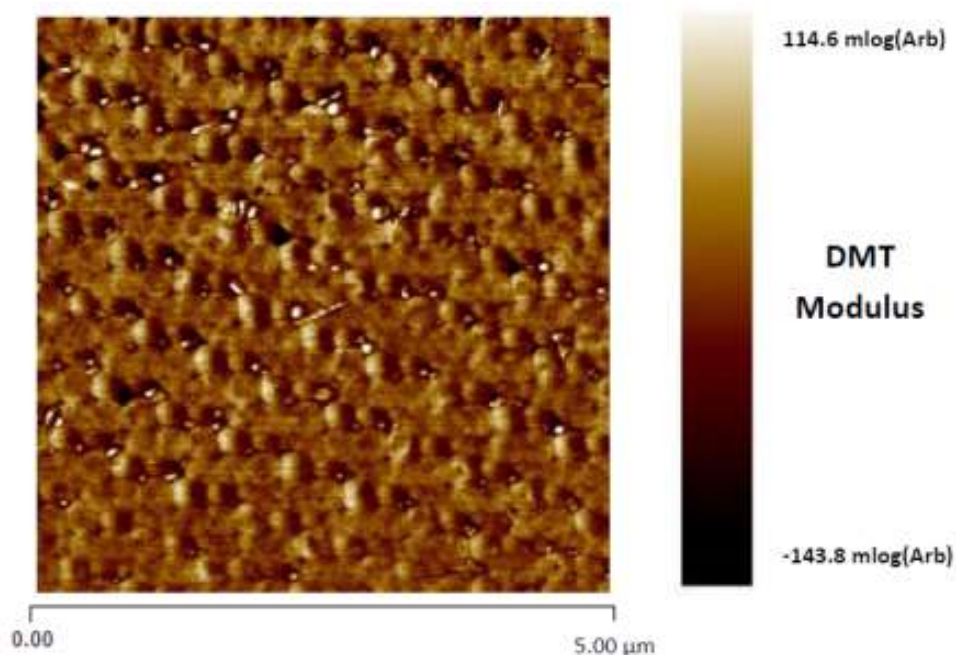


Figure 8.10 DMT Modulus AFM image of a lightly crosslinked soft-soft nanocomposite film cross-section with 80:20 core:shell ratio, comprising poly[(BA)-*co*-(BMA)] core and poly[(BA)-*co*-(BMA)-*co*-(DAAM)-*co*-(MAA)] shell phase copolymers with T_g s of 25 and 5 °C, respectively, with 2 wt% MAA present in the shell phase and latex unneutralised. No ADH was added.

Image size = 5 μ m square

There are areas of hardness \sim 250-300 nm in diameter that form a regular array that can be observed on the sample surface in Figure 8.10. This is likely to be an artefact of the AFM imaging process, and can be attributed to either damage or contamination to the probe tip or the scanning rate used to gain these images²⁵⁴. The differences between the films ‘permanently’ and ‘temporarily’ neutralised are much more subtle, and could be interpreted as an artefact of sample preparation. They do not fully explain the differences in film properties seen from tensile testing, but a more ordered structure is seen for the ‘permanently’ NaOH neutralised film, which could explain the difference in Young’s modulus between the two films.

It can be seen from both the mechanical testing and AFM performed that the type of neutralisation used for MAA-containing soft-soft nanocomposite latexes does affect the film properties, which is in accord with previous studies by Hellgren²⁵² and by Backfolk *et al.*²⁵³.

8.4 Conclusions

The results presented in this chapter show that in lower core copolymer T_g systems, the addition of methacrylic acid to the shell phase of the soft-soft nanocomposite particles had

only a small effect upon film mechanical performance. However, at higher core copolymer T_g , a large variance in mechanical behaviour was seen, most likely due to ionomer behaviour resulting from the at least partly neutralised acid groups. This could potentially be due to the absence of an 'ionic membrane', as has been theorised to surround the surface of acid-containing latex particles^{212, 246}, around the lower T_g particles which film form at above their T_g and dispels the theoretically interparticle diffusion-restricting membrane. However, it is hypothetically likely that this shell still exists around the higher T_g particles with a greater concentration of MAA, as they are mechanically tested at or above their T_g . This would restrict chain diffusion, and lead to deterioration of mechanical properties and the lack of cohesion that is seen from AFM images of the bulk film.

The variant with 2 wt% MAA in the shell phase copolymer gave the highest Young's modulus observed in this project, and although a large error was associated with this measurement due to the method used to measure low strains this superior low strain mechanical performance was in accord with the stress at 4% strain values. The variant with 3.5 wt% MAA showed the highest peak stress and extension to break for any variant discussed in the high core copolymer T_g data set.

An investigation into the effect of the type of neutralisation on film properties was conducted. In work previously discussed in this thesis, only NaOH was used, so both neutralisation with NH_3 , which would evaporate during the coalescence phase of film formation, and unneutralised latex films were formed. Comparison of the film and mechanical properties showed that much lower Young's modulus values were observed for both temporarily (NH_3) and un-neutralised systems compared to the permanently (NaOH) neutralised equivalent. AFM imaging of the three films showed little difference in film structure between the NH_3 and NaOH neutralised systems, but a large difference in the unneutralised film in which the particles had fully coalesced and the structured particle morphology had not been retained. This is in agreement trends published in the literature which suggests that neutralisation, and hence the formation of an ionic salt shell, retards interparticle diffusion by at least 6-fold.

9 Comparing soft-soft nanocomposite systems with commercial water-based paint binders

9.1 Introduction

In order to establish the viability of the soft-soft nanocomposite latexes and films for their intended use as binders for paints and coatings, samples of five different binder systems currently used in AkzoNobel products were investigated. These were then completely characterised as for the soft-soft nanocomposite latexes synthesised in this project. Table 9.1 shows the technical information that was supplied for each of these latex systems, and the physical properties of the soft-soft nanocomposite latex that was chosen for comparison due to its superior mechanical performance as observed from the work discussed in Chapter 7. Due to commercial secrecy, the exact chemical and morphological compositions of the five systems to be compared to the selected soft-soft nanocomposite latex were not provided. Basic information regarding the particle structures of the AkzoNobel in-house binders was supplied. Scant information regarding the other two commercially-available latexes was found from literature searches.

Table 9.1 Technical information for systems discussed in Chapter 9

System name	Technical information
NeoCryl XK-98	Manufactured by DSM NeoResins. Core-shell all acrylic, ambient temperature crosslinking.
Primal AC-337	Manufactured by Dow. Acrylic system, morphology unknown.
PU-acrylic hybrid	In-house manufactured by AkzoNobel. Acrylic core, polyurethane (PU) shell.
Linear acrylic 1	In-house manufactured by AkzoNobel. Linear, soft acrylic.
Linear acrylic 2	In-house manufactured by AkzoNobel. Linear, soft acrylic with large particle size.
Soft-soft nanocomposite	80:20 core:shell ratio. poly[(BA)- <i>co</i> -(BMA)] core and poly[(BA)- <i>co</i> -(BMA)- <i>co</i> -(DAAM)] shell phase copolymers with $T_g = 25$ and 5 °C, respectively, with 2 wt% DAAM in shell phase & 2:1 DAAM:ADH ratio.

Primal AC-337, which was originally formulated by Rohm and Haas but is now manufactured by Dow, is an alkylphenol ethoxylate (APEO)-free hydrophobic acrylic polymer, with an MFT of 14 °C and very good compatibility with other components of a paint formulation²⁵⁵. It is typically utilised in high-end applications, such as high performance exterior wood varnishes, and it has been claimed to have been designed specifically for such a purpose¹³⁸.

NeoCryl XK-98, designed and manufactured by DSM NeoResins B.V., is another water-borne binder latex that was specifically formulated for use in wood coatings. Comparative tests performed in 2001 found that compared to traditional acrylic binder latexes made for the same purpose, NeoCryl XK-98 gives improved solvent and blocking resistance²⁵⁶, both of which are important considerations in the formulation of high performance wood varnishes. Some literature exists that may describe the chemistry of NeoCryl XK-98. Papers presented by DSM technical staff at international conferences in 2001 and 2002, which was around the time that NeoCryl XK-98 was first introduced onto the coatings market, describe core-shell particles that comprise a hydrophobic low T_g acrylic core of high molecular weight, surrounded by a high T_g shell phase polymer that contains a low molecular weight “self-crosslinking polymeric dispersant”^{257, 258}. The combination of these two phases gave a film-forming binder with low MFT and exceptional blocking and solvent resistance, and good compatibility with pigments and other paint formulation components²⁵⁹. The novelty of this binder chemistry is the “self-crosslinking polymeric dispersant”. It is not discussed in detail in any of the available literature, but is thought to be due to alkali-soluble resin (ASR) stabilisers²⁵⁸. The hydrophilic acid groups will stabilise a hydrophobic particle by forming a ‘shell’ phase around it, and can also form ionic crosslinks upon a change in pH of the system. The low molecular weight of these ASR chains aids their diffusion across particle boundaries, hence increasing the level of cohesion that occurs in the film²⁴⁶.

Hence, a range of differing latex technologies are included in this comparison study, including simple linear acrylic random copolymers and more sophisticated systems, such as a PU-acrylic core-shell composite latex. Binders specifically designed for use in high-performance exterior wood coatings, namely NeoCryl XK-98 and Primal AC-337, present an interesting benchmark with regard to the levels of performance desired for such an application.

9.2 Wet latex characterisation

The latexes were analysed in their wet states, as received, using the techniques detailed in Section 3.4.1. Table 9.2 shows the particle size and solids content data as analysed by PCS and gravimetric methods, respectively, with particle size distribution data for each system shown in Figure 9.1.

Table 9.2 Characterisation data for the binder systems in the wet state

System name	Particle diameter ^a / nm	Solids content ^b / %
NeoCryl XK-98	69	43.8
Primal AC-337	131	45.4
PU/acrylic hybrid	61	38.6
Linear acrylic 1	433	52.1
Linear acrylic 2	508	37.4
Soft-soft nanocomposite	330	51.8

^a z-average particle diameter, obtained by PCS

^b Gravimetrically determined

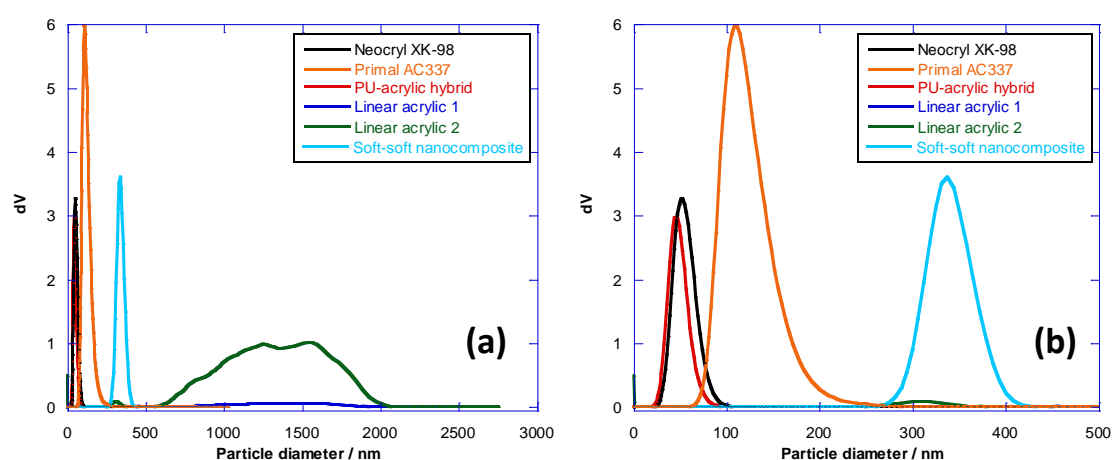


Figure 9.1 (a) Comparative particle size distribution curves for the latexes described in Table 9.1; **(b)** zoomed section of (a) from 0-500 nm

The data in Table 9.2 show that all the latexes have a relatively high solids content and small (≤ 500 nm) particle size. Due to the vastly differing scales of each particle size distribution, it is not possible to easily compare them on the same set of axes. However, it can be seen from Figure 9.1 that the latexes known to definitely have well-defined particle morphology (NeoCryl XK-98, the PU/acrylic hybrid and the soft-soft nanocomposite) have unimodal, narrow particle size distributions, whereas their linear, non-structured counterparts (Linear acrylic 1 and 2) have extremely broad, unsymmetrical particle size distributions. This observation is not unexpected due to the tight control of particle size distribution required to achieve a tightly controlled structured morphology. Although the morphology of Primal AC-337 is unknown from the data given by its manufacturer, it has a narrow, unimodal particle size distribution, so may also have some defined particle morphology.

9.3 Thermal and mechanical characterisation

9.3.1 Thermal properties

Films were cast from each latex using the method given in Section 3.3.2 and analysed by DSC, using the protocol detailed in Section 3.4.3.2. A summary of the data is provided in Table 9.3, and selected DSC traces are shown in Figure 9.2.

Table 9.3 Summary of DSC data for latexes described in Table 9.1

System	Observed T_g / °C
NeoCryl XK-98	-3 / 122 (± 1.8 / 0.8 °C)
Primal AC-337	22 (± 1.3 °C)
PU/acrylic hybrid	18 (± 4.5 °C)
Linear acrylic 1	7 (± 0.2 °C)
Linear acrylic 2	2 (± 0.5 °C)
Soft-soft nanocomposite	21 (± 0.5 °C)

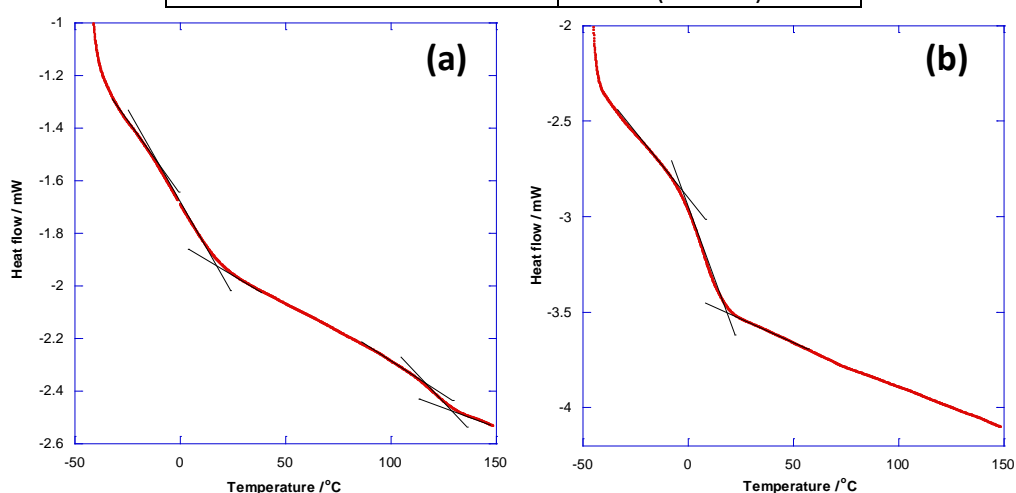


Figure 9.2 DSC traces for (a) NeoCryl XK-98 and (b) Linear acrylic 1

It can be seen from the data in Table 9.3 that only one system, NeoCryl XK-98, exhibits more than one glass transition. This is shown in Figure 9.2(a), and is most likely due to vastly differing compositions of the core and shell phases, as was assumed from the literature discussed in Section 9.1. It is also an explanation for the failure of this system to initially film form at ambient temperature when a thicker (~ 1800 μm wet thickness) film was cast. The other four films analysed all showed one clearly defined glass transition in the ambient temperature region in the range 2–22 °C, as can be seen from Figure 9.2(b).

9.3.2 Mechanical (tensile) properties

NeoCryl XK-98 did not initially film form at room temperature, but after subsequent casting of a thinner film (~400 μm dry thickness) it was possible to gain a coherent film sample which was used for mechanical testing. Tensile testing was performed on these films according to the procedure described in Section 3.4.2.1. Figure 9.3 shows comparative stress-strain curves for the six systems, and the respective Young's modulus, extension to break and stress at 4% strain values for each film are given in Table 9.4.

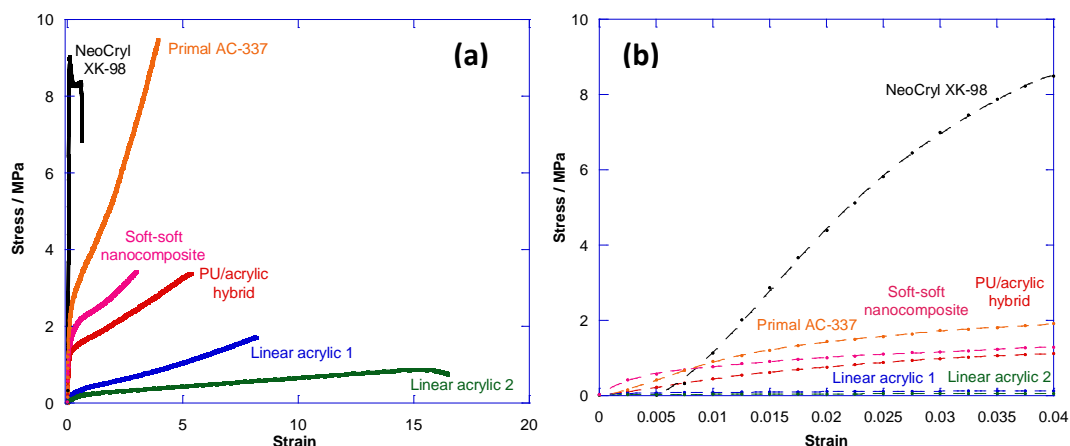


Figure 9.3 (a) Stress-strain curves for films from selected water-borne binder latexes described in Table 9.1; (b) Section of stress-strain curves from (a) with strains of 0-4% used to calculate Young's modulus (coefficient of first order term in a polynomial fit expression; order of fit = 6)

Table 9.4 Mechanical property data for AkzoNobel comparison binder systems

System	Young's modulus /MPa	Stress at 4% strain /MPa	Extension to break /%
NeoCryl XK-98	1980 (± 1100 MPa)	8.53 (± 0.27)	61 ($\pm 7\%$)
Primal AC-337	68 (± 28 MPa)	1.55 (± 0.078)	392 ($\pm 22\%$)
PU/acrylic hybrid	58 (± 5 MPa)	1.16 (± 0.03)	491 ($\pm 62\%$)
Linear acrylic 1	26 (± 1 MPa)	0.14 (± 0.02)	762 ($\pm 35\%$)
Linear acrylic 2	8 (± 0.5 MPa)	0.08 (± 0.04)	1610 ($\pm 180\%$)
Soft-soft nanocomposite	182 (± 130 MPa)	1.08 (± 0.124)	271 ($\pm 34\%$)

These data show that the soft-soft nanocomposite film outperforms films from the three in-house AkzoNobel binder latexes. This soft-soft nanocomposite film exhibited a higher Young's modulus, representing a higher degree of stiffness. However, it can be clearly seen from Figure 3.5.2 that the soft-soft nanocomposite film has a lower extension-to-break

than the other systems, indicating lower flexibility at high strains. However, although dimensional instability is a key consideration for substrates such as wood (see Section 6.2.1), it is unlikely that such a large deformation will occur during service as a wood coating.

9.4 Mechanical property comparisons to a wider range of AkzoNobel binder systems

The promising property results that were seen in Section 9.3 regarding the potential of the soft-soft nanocomposite system led to an expansion of the comparison study. Four soft-soft nanocomposites of specific interest were identified, and the compositions and stress-strain curves of these can be seen in Table 9.5 and Figure 9.4, respectively. These systems were chosen as they represent the range of properties that can be achieved using the soft-soft nanocomposite design theory.

Table 9.5 Soft-soft nanocomposite systems of interest discussed in Section 9.4

System name	Core:shell ratio	Core and shell copolymer composition	Core/Shell $T_g / ^\circ\text{C}$	MAA level /wt% in shell	DAAM level /wt% in shell
SSNC1	80:20	Poly[(BA)- <i>co</i> -(BMA)] Poly[(BA)- <i>co</i> -(BMA)- <i>co</i> -(DAAM)]	25 / 5	0	2
SSNC2	80:20	Poly[(BA)- <i>co</i> -(BMA)] Poly[(BA)- <i>co</i> -(BMA)- <i>co</i> -(DAAM)]	20 / 5	0	5
SSNC3	80:20	Poly[(BA)- <i>co</i> -(BMA)] Poly[(BA)- <i>co</i> -(BMA)- <i>co</i> -(DAAM)]	5 / 5	0	7.5
SSNC4	80:20	Poly[(BA)- <i>co</i> -(BMA)] Poly[(BA)- <i>co</i> -(BMA)- <i>co</i> -(DAAM)- <i>co</i> -(MAA)]	25 / 5	2	2

SSNC1, which was the soft-soft nanocomposite included in the testing discussed in Section 9.3, gave the highest Young's modulus from the core copolymer T_g study reported in Section 7.2. This was also the case for SSNC4, which had the very highest Young's modulus (425 MPa) that was seen during the work reported in this thesis (see Section 8.2.2).

SSNC2 and SSNC3, which both had higher levels of DAAM-ADH crosslinking incorporated into the shell phase copolymer (see Section 7.3 and 6.4.2.2, respectively), showed the highest extent of strain hardening whilst retaining high extensibility, so were included on this basis. SSNC2 also had a relatively high Young's modulus (68 MPa), so combines both mechanical failure properties and flexibility.

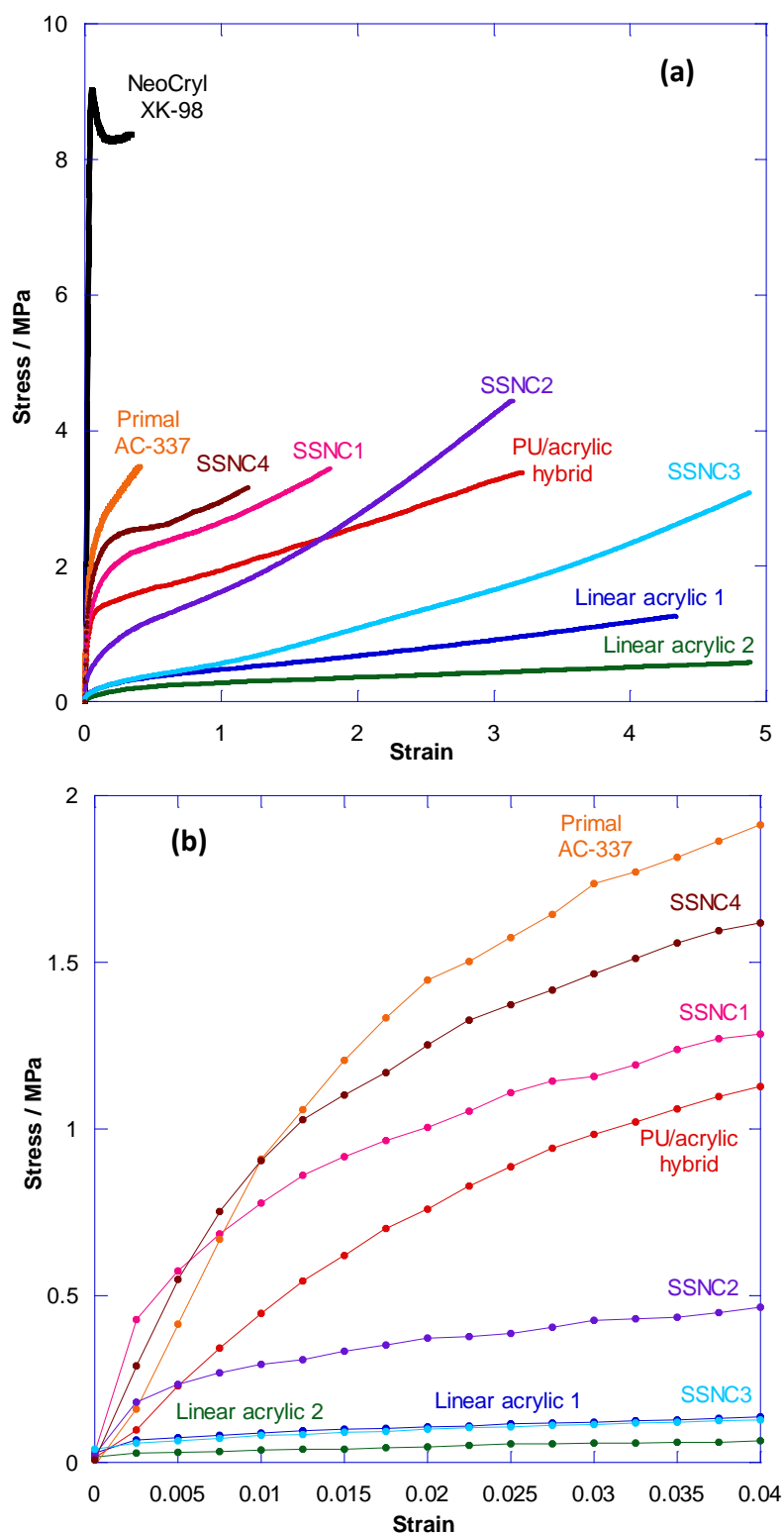


Figure 9.4 (a) Stress-strain curves for films from selected water-borne binder latexes described in Table 9.1 compared to soft-soft nanocomposites; **(b)** Section of stress-strain curves from (a) (minus NeoCryl XK-98) with strains of 0-4% used to calculate Young's modulus (coefficient of first order term in a polynomial fit expression; order of fit = 6)

The Young's modulus and extension to break values for the four systems specified in Table 9.5 were then plotted together with a large range of AkzoNobel binder systems, in order to compare the nature of their mechanical behaviour (see Figure 9.5). The original plot

was provided by AkzoNobel Decorative Coatings, and the soft-soft nanocomposite data subsequently added. The chemical and morphological nature of the latexes from the original data (red points) are unknown due to commercial secrecy.

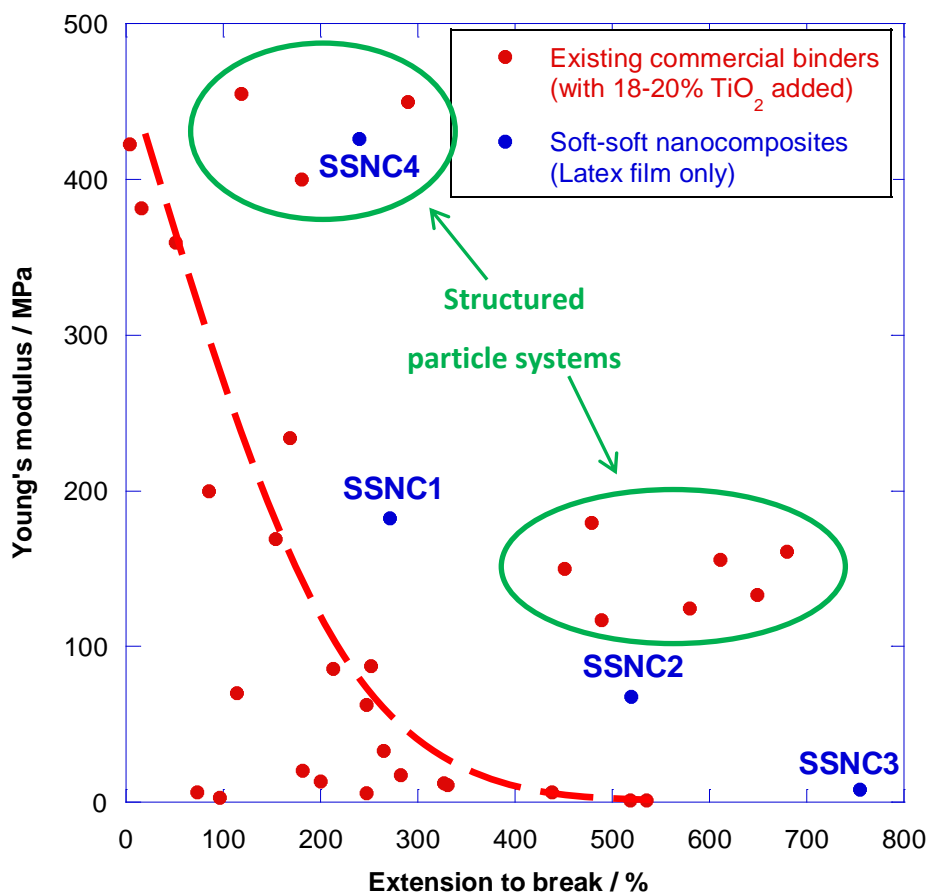


Figure 9.5 Plot of Young's modulus vs extension to break for a range of AkzoNobel binders and four soft-soft nanocomposite variants.

N.B. The dashed line indicates a typical binder composition-mechanical performance balance as identified by AkzoNobel.

It can be seen from Figure 9.5 that the four soft-soft nanocomposite systems showed different mechanical behaviour. SSNC2 and SSNC4 showed behaviour more commonly associated with PU/acrylic structured particle systems. SSNC1 and SSNC3 were more in line with a conventional acrylic film composition-performance balance, as represented by the dashed line in Figure 9.5.

9.5 Conclusions

The data presented in this chapter show clearly that the soft-soft nanocomposite systems produced in this project can compete with existing water-borne binders currently utilised in commercial products, showing comparable mechanical, thermal and wet latex

properties. The mechanical property data shown in Section 9.4 also revealed that soft-soft nanocomposite films are capable of extremely versatile behaviour and, depending on their design, can exhibit a large range of different mechanical behaviours.

The huge degree of versatility that can be gained from materials synthesised using the soft-soft nanocomposite design theory can be accessed very easily. By simply changing one or more synthesis parameter, such as core phase copolymer T_g or crosslinker content, it is possible to tailor the mechanical properties of the resulting film for a desired application. Although the exploration of this set of design principles with regards to ambient T_g coating applications is still in the very early stages, the results shown in this chapter demonstrate its potential importance with regard to many different applications within the field of water-borne binders for paints and coatings.

10 Conclusions

The principal conclusions that can be drawn from the work discussed in this thesis are summarised below.

Chapter 4 discussed the establishing of a framework formulation for the synthesis of soft-soft nanocomposite latexes, by adaptation of an existing AkzoNobel latex formulation that had the desired particle size and solids content. This formulation was rigorously tested to prove its adaptability, with specific focus on how altering the monomer composition of the shell phase copolymer, the core to shell phase copolymer mass ratio and the DAAM content affected the properties of the particles. Initially, large amounts of coagulum were formed during the polymerisation which indicated inherent colloidal instability. In order to address this problem, a range of non-ionic surfactants were evaluated with regard to their effect on coagulum level and it was found that Lutensol TO7 repeatedly gave the best results, reducing coagulum from approximately 8% to 0.3% of the latex mass. This additional surfactant was added to the formulation during particle growth stages at a level of 20 wt% relative to the original anionic surfactant, as no additional reduction in coagulum was seen at higher levels. Secondary problems with a lower film T_g predicted using the Fox equation were overcome by using an experimentally-determined modification of the equation. This enabled more accurate prediction of the T_g of simple poly[(BA)-*co*-(BMA)] copolymers. After these problems were addressed, it was found that a high level of control was gained over the polymerisations, with high monomer conversion and approximately constant particle number regardless of core:shell ratio, crosslinker content or core and shell T_g . AFM imaging of film cross-sections showed that for all morphologies investigated, namely 70:30, 80:20 and 90:10 core-shell ratios, it was possible to see the core-shell morphology retained in the fully formed films with a dispersed phase from particle cores and a percolating phase from the particle shells. Varying the core:shell ratio also did not have a significant effect on the copolymer molar masses, with \overline{M}_n and \overline{M}_w values of $\sim 100,000$ and $\sim 350,000$ kg mol⁻¹, respectively, and large dispersities of >3 being observed for all variants tested.

The addition of ADH to introduce keto-hydrazone crosslinking of the DAAM groups, described in Chapter 5, proved to have a large impact upon the properties of the soft-soft nanocomposite films. The crosslinked films became stiffer at higher strains, instead of passing through a maximum stress then softening as for their non-crosslinked counterparts, although no significant differences in the low strain mechanical properties were seen, with low Young's moduli of approximately 5 MPa for both crosslinked and uncrosslinked films. It

was also seen from AFM images that the exuded surfactant resided in larger areas on the surface of the crosslinked films, instead of in the interstitial gaps between particles, indicating a high degree of cohesiveness. AFM-IR imaging confirmed the presence of C=N imine linkages formed by keto-hydrazide crosslinking, and showed that these groups were located solely in the percolating phase. The results discussed in this chapter also showed that one of the fundamental principles that underpins the soft-soft nanocomposite design theory can be successfully applied to polymers with a T_g close to ambient temperature, namely the incorporation of a lightly crosslinked percolating phase into a film in order to introduce elastomeric behaviour.

As was shown in Chapter 6, varying the core:shell ratio of soft-soft nanocomposites led to slight differences in the high strain tensile behaviour of films, but otherwise had little significant effect on the Young's modulus or stress at 4% strain, which were approximately constant at < 10 MPa and ~0.01 MPa respectively. The optimum core:shell ratio that emerged from this testing, and all other testing performed throughout the project, was 80:20 core:shell which had previously been shown to give the optimum mechanical performance for soft-soft nanocomposite PSAs⁴⁻⁶. Chapter 6 also showed that it was possible to synthesise poly[(BA)-*co*-(BMA)-*co*-(DAAM)] copolymers containing a maximum of 7.5 wt% DAAM without encountering excessive amounts of coagulum. Increasing the crosslink content in the percolating phase derived from the shell phase copolymer, by changing both DAAM and ADH levels, affected the high strain mechanical behaviour of the films, increasing the stresses required to deform the film and also causing mechanical failure at lower extensions. However, little difference was seen in the Young's modulus or stress at 4% strain of these variants, which again had consistent values of ~10 and 0.01 MPa, respectively, suggesting that crosslinker concentration does not significantly affect the low strain behaviour of soft-soft nanocomposite films at these levels of incorporation.

Increasing the core phase polymer T_g from 5 °C up to 25 °C increases the Young's modulus and stress at 4% strain of a soft-soft nanocomposite film, a trend which was evident for each core:shell ratio tested and discussed in Chapter 7. Young's modulus values of up to 180 MPa were gained for films with a core phase T_g of 25 °C and, although large errors were associated with these values, the trend was substantiated by stress at 4% strain values which also were markedly higher for higher core T_g systems. Core T_g also affected the high strain behaviour, with much lower extension to break values being observed for systems with higher core T_g .

Systems combining high crosslinker content (up to 7.5 wt% of the shell phase) and high core copolymer T_g s of 20 and 25 °C showed behaviour in accordance with the trends shown for the two individual parameters, with high Young's modulus and stress at 4% strain values. Films with higher DAAM content had lower extension to break, higher failure stresses and showed an increased degree of strain hardening. Based on AFM images an anomalous result, where the variant with a core phase copolymer T_g of 25 °C and 5 wt% DAAM in the shell phase outperformed the equivalent system with 7.5 wt% DAAM, has been explained as being due to the rate of crosslinking being similar to, or exceeding, the rate of interparticle chain diffusion, which resulted in a lack of cohesion and inherent mechanical weaknesses within the films.

The final parameter discussed in Chapter 7 was the effect of shell phase copolymer T_g upon the mechanical properties of soft-soft nanocomposite films. Unlike core copolymer T_g , increasing the shell phase copolymer T_g from 5 °C up to 15 °C had only a small effect upon either the high or low strain mechanical properties. This is unexpected as the shell phase forms the percolating phase of the film, but is most likely due to the shell phase forming the minority (<30 wt%) of all of the films and hence not predominating the low- or high-strain mechanical behaviour of the system.

Chapter 8 discussed the effect of incorporating MAA into the shell phase of soft-soft nanocomposite films, which was found to have a small effect upon the stress-strain profiles of lower core phase copolymer T_g systems, but for systems with high core T_g (25 °C) optimum levels of MAA in the shell phase copolymer were seen for both low and high strain behaviour. A film with 2 wt% MAA in the shell phase gave the highest Young's modulus (425 MPa) observed for any soft-soft nanocomposite coating, and a film with 3.5 wt% MAA had the highest extensibility of all higher core T_g films tested. Amounts of methacrylic acid in excess of 3.5 wt% in the shell phase appeared to be detrimental to the mechanical properties of the higher core T_g films. The unexpected trend in mechanical properties may be due to the pKa of the acid groups in the polymer, which was previously shown by Saunders *et al.* to decrease as the acid content increases²⁴⁴. This means that more of the acid groups would be ionised in the 5wt% MAA-containing film, increasing the degree of ionic crosslinking which restricts intermolecular chain diffusion and may lead to a lack of cohesion in the fully formed film.

The potential existence of an 'ionic shell' consisting of ionomerically crosslinked material around the surface of MAA-containing particles has been suggested in the literature, and may explain why the acid content has little significant effect upon the lower T_g films, as these

films form at above their T_g which, if it exists, dispels the interparticle diffusion-restricting membrane. However, this 'shell' could potentially still exist around the higher T_g particles with a greater concentration of MAA, as they film form below their T_g (~ 22 °C). This would result in the deterioration of mechanical properties during tensile testing, and the lack of cohesion that was seen from AFM images of the bulk film.

Also presented in Chapter 8 was a study regarding the effect of changing the type of neutralisation used. In the work discussed in Section 8.2, sodium hydroxide was used to neutralise MAA-containing soft-soft nanocomposite latexes, which would provide 'permanent' neutralisation due to its low volatility. Portions of a latex containing 2 wt% MAA were neutralised with ammonia, which would give 'temporary' crosslinking as it would evaporate during the coalescence stage of film formation. Comparison of the film and mechanical properties prepared in these different ways showed that lower Young's modulus values were observed for both temporarily (NH_3) and un-neutralised systems compared to the permanently (NaOH) neutralised equivalent, and was substantiated by a more reliable trend that was also seen in stress at 4% strain. AFM imaging of the three films showed little difference in film structure between the NH_3 and NaOH neutralised systems, but a more significant difference in the unneutralised film in which less evidence of retained particle morphology could be seen.

Chapter 9 presents a comparison of soft-soft nanocomposite coating films synthesised in this project with binder latexes utilised by AkzoNobel in commercial products. This showed that the soft-soft nanocomposite films were capable of competing with, and in some cases outperforming, existing acrylic systems. Plotting of Young's modulus against extension to break for a whole range of systems revealed that, by manipulating the core:shell ratio, T_g and crosslink density, soft-soft nanocomposite films are capable of behaving like a whole range of binder latexes, thus proving the high level of versatility that the soft-soft nanocomposite design theory affords and the suitability of these latexes for use as binders in paints and coatings.

11 Recommendations for further work

There are several areas of additional interest apparent from the work presented in this thesis that would be interesting to pursue in the future.

- The AFM-IR technique described in Section 3.4.2.5.1 became available as the experimental work for this project was coming to an end, so only an initial evaluation of its usefulness could be completed. As was shown in Section 5.4.3, it was potentially possible to resolve the distribution of crosslinked material in soft-soft nanocomposite films, by mapping the distribution of the C=N imine bond that results from the keto-hydrazide crosslinking reaction and is not present in any other component of the system. This represents a distinct possibility to gain more insight into the nature of the DAAM-ADH crosslinking reaction, and should be rigorously investigated in detail by examining films with varying DAAM contents and core:shell ratios. This may help rationalise the trends seen in Chapters 6 and 7, whereby an increasing concentration of crosslinks affected the high strain mechanical properties of the films and could potentially explain why the 80:20 core:shell ratio is consistently seen to be the optimum with regards to film properties. The effect of DAAM:ADH stoichiometry would also be interesting to probe using this technique, and may provide insights into the location and distribution of the imine groups in the percolating phase when a very low concentration of crosslinks is present.
- Also discussed in Chapter 5 was the use of an alternative method for calculating the Young's modulus of soft-soft nanocomposite films. Large inaccuracies were encountered at small strain values due to the unavoidable use of jaw separation as a measure of displacement, and a small study to investigate using a linear fit from strain values of 0.01-0.04 rather than a polynomial fit from strains of 0-0.04 showed that use of the linear method made analysis of the data more difficult. However, for systems where a larger difference in the calculated Young's modulus is seen this use of a linear fit should be more extensively investigated.
- The work regarding MAA-containing soft-soft nanocomposite films with core phase copolymer T_g of 25 °C (discussed in Chapter 8) showed that the acid content of the latexes had a significant effect on mechanical properties. Previous studies of MAA-containing particles reported in the literature suggested that this may be due to the

formation of an 'ionic membrane' around the particle surface, which varies in thickness according to the type of neutralisation used and restricts interparticle chain diffusion. Hence, studies of the film formation process, and specifically chain interdiffusion, could be carried out using techniques such as small angle neutron scattering (SANS)²⁶⁰ and direct energy transfer (DET)²⁶¹. For the purpose of these specific MAA-containing systems DET would probably be the more appropriate technique as it is more sensitive to chain diffusion in the early stages of film formation than SANS¹⁹, because generation of an 'ionic membrane' by ionomeric crosslinking will occur very quickly.

- The application potential of these soft-soft nanocomposite latexes was clearly demonstrated in Chapter 9. Preliminary experiments to utilise these systems as binders in paint formulations, which were conducted at AkzoNobel in Slough, indicated that the latex was not inherently shear stable, as flocculation of the particles was observed upon the addition of thickening agents. Adding additional non-ionic surfactant to the latexes helped to overcome this, so a full review of the surfactant systems used could be undertaken in order to see if the shear stability of these latexes can be increased without affecting the level of control gained during the polymerisation. A secondary, desirable effect of such a study may be to further reduce coagulum levels during the latex preparation process. Potential routes of investigation that could be considered include the use of alternative anionic and non-ionic surfactants, altering the ratio of anionic to non-ionic surfactant (currently 80:20) and using a monomer pre-emulsion feed rather than separate monomer and surfactant feeds during polymerisation. This will require rigorous testing of a wide range of latexes with differing core:shell ratios, crosslinker contents, core and shell T_g values and functional monomers to confirm that a decline in film properties does not occur.
- Also discussed in Chapter 9 was the Young's modulus-to-extension to break performance of selected soft-soft nanocomposite films relative to a whole range of other binder latexes. It can be seen from Figure 9.5 that it is possible to form soft-soft nanocomposite films with high modulus but poor extensibility, and low modulus but high extensibility. An optimum in either modulus or extensibility is often considered to come at the expense of the other property²⁶², and multiple strategies have been

suggested regarding the use of hybrid core-shell systems to attempt to overcome this technical problem and produce a film with both high extensibility and high modulus. Polyurethane/acrylic hybrids have been extensively investigated and found to provide many improvements in film properties, although an extension of the work regarding soft-soft nanocomposite PSAs that replaced the crosslinked acrylic shell phase with a polyurethane shell showed that an increased level of polyurethane component reduced the extensibility of the adhesive film²⁶³⁻²⁶⁵, which has also been observed for higher T_g polyurethane-acrylic systems²⁶⁶. However, studies concerning the addition of polysiloxane materials to acrylic latexes for external coating applications show that beneficial effects in terms of weather durability and extensibility are gained with the use of such systems²⁶⁷⁻²⁶⁹. It has previously been difficult to polymerise siloxanes in aqueous media due to the susceptibility of the alkoxy silane group to hydrolysis, but in 2014 Christopher *et al.* reported the synthesis, by seeded semi-batch emulsion polymerisation, of particles with a styrene-acrylic core and a polysiloxane shell phase²⁷⁰. These systems were found to have optimum extensibility when 10wt% polysiloxane was incorporated into the particles, as well as an associated increase in the hydrophobicity of the coating.

Hence, it is suggested that a low level of polysiloxane material be added to a soft-soft nanocomposite latex with a core phase T_g of 25 °C and 2 wt% MAA in the shell phase, to attempt to increase the extensibility of a film that has already been shown to have a high modulus. A secondary beneficial effect may result from the increased hydrophobicity of the polysiloxane, as the acrylic soft-soft nanocomposite contains DAAM-ADH crosslinks that are potentially susceptible to hydrolysis. Suggested strategies for achieving this are the addition of a subsequent shell of polysiloxane around the outside of the acrylic, DAAM-containing shell phase to create multilayer particles, or a 'blend-type' strategy whereby nanoparticles of the soft polysiloxane are blended with the soft-soft nanocomposite latex, similar to that used by Overbeek *et al.* which was discussed in more detail in Section 2.5.2¹³⁷.

12 References

1. Santos, F. D. d.; Fabre, P.; Drujon, X.; Meunier, G.; Liebler, L. *Journal of Polymer Science Part B: Polymer Physics* **2000**, 38, (23), 2989-3000.
2. VOC Solvents Emission Directive. In *1999/13/EC*, EU, Ed. 1999.
3. VOC Solvents Emission Directive. In *2004/42/CE*, EU, Ed. 2004.
4. Deplace, F.; Carelli, C.; Langenfeld, A.; Rabjohns, M. A.; Foster, A. B.; Lovell, P. A.; Creton, C. *Applied Materials & Interfaces* **2009**, 1, (9), 2021-2029.
5. Deplace, F.; Rabjohns, M. A.; Yamaguchi, T.; Foster, A. B.; Carelli, C.; Lei, C.-H.; Ouzineb, K.; Keddie, J. L.; Lovell, P. A.; Creton, C. *Soft Matter* **2009**, 5, 1440-1447.
6. Foster, A. B.; Lovell, P. A.; Rabjohns, M. A. *Polymer* **2009**, 50, (7), 1654-1670.
7. Pinprayoon, O.; Groves, R.; Lovell, P. A.; Tungchaiwattana, S.; Saunders, B. R. *Soft Matter* **2011**, 7, 247-257.
8. S.Tungchaiwattana; Musa, M. S.; Yan, J.; Lovell, P. A.; Shaw, P.; Saunders, B. R. *Soft Matter* **2014**, 10, 4725.
9. Tungchaiwattana, S.; Groves, R.; Lovell, P. A.; Pinprayoon, O.; Saunders, B. R. *Journal of Materials Chemistry* **2012**, 22, 5840-5847.
10. Stevens, M. P., *Polymer Chemistry: An Introduction*. 3rd ed.; OUP: New York, 1999.
11. Lovell, P. A.; El-Aasser, M. S., *Emulsion Polymerisation and Emulsion Polymers*. Wiley: Chichester, 1997.
12. Lovell, P. A., Free-radical Polymerisation. In *Emulsion Polymerisation and Emulsion Polymers*, Lovell, P. A.; Aasser, M. S. E., Eds. Wiley: Chichester, 1997; Vol. 1.
13. Nozaki, K.; Bartlett, P. D. *Journal of the American Chemical Society* **1946**, 68, (9), 1686-1692.
14. Nozaki, K.; Bartlett, P. D. *Journal of the American Chemical Society* **1946**, 68, (11), 2377-2380.
15. Flory, P. J. *Journal of the American Chemical Society* **1937**, 59, (2), 241-253.
16. Odian, G., *Principles of Polymerization*. 4th ed.; Wiley: 2004.
17. Young, R. J.; Lovell, P. A., *Introduction to Polymers (3rd Edition)*. 3rd ed.; CRC Press: Boca Raton, 2011.
18. Gottlob, K. A method for producing artificial caoutchouc. DRP 254672, 11th December 1912, 1912.
19. Taylor, J. W.; Winnik, M. A. *Journal of Coatings Technology Research* **2004**, 1, (3), 1-28.
20. El-Aasser, M. S.; Sudol, E. D., Features of Emulsion Polymerisation. In *Emulsion Polymerisation and Emulsion Polymers*, Lovell, P. A.; El-Aasser, M. S., Eds. Wiley: Chichester, 1997.
21. Capek, I.; Barton, J.; Karpatyova, A. *Die Makromolekulare Chemie* **1987**, 188, (4), 703-710.
22. Nomura, M.; Fujita, K. *Die Makromolekulare Chemie, Rapid Communications* **1989**, 10, (11), 581-587.
23. Nomura, M.; Yamada, A.; Fujita, S.; Sugimoto, A.; Ikoma, J.; Fujita, K. *Journal of Polymer Science Part A: Polymer Chemistry* **1991**, 29, (7), 987-994.
24. Daniels, E. S.; Sudol, E. D.; El-Aasser, M. S., *Polymer latexes: Preparation, characterisation and Applications*. ACS: Washington DC, 1992; Vol. 492.
25. Klein, A.; Daniels, E. S., Formulation components. In *Emulsion Polymerisation and Emulsion Polymers*, Lovell, P. A.; El-Aasser, M. S., Eds. Wiley: Chichester, 1997.
26. Schildknecht, C. E., *Polymer Processes*. Interscience: New York, 1956.
27. Harkins, W. D. *Journal of the American Chemical Society* **1947**, 69, (6), 1428-1444.
28. Smith, W. V.; Ewart, R. H. *Journal Of Chemical Physics* **1948**, 16, (6), 592-599.
29. Wessling, R. A.; Gibbs, D. S. *Journal of Macromolecular Science Part A: Chemistry* **1973**, 7, (3), 647-676.

30. Eckersley, S. T.; Rudin, A. *Journal of Applied Polymer Science* **2003**, 48, (8), 1369-1381.
31. Moad, G.; Solomon, D. H., *The Chemistry of Free Radical Polymerization*. 1st ed.; Elsevier: Oxford, 1995.
32. Fitch, R. M.; R.C.Watson. *Journal of Colloid and Interface Science* **1979**, 68, (1), 14-20.
33. Liu, B.; Zhang, M.; Liu, Y.; Tan, Z.; Zhou, C.; Zhang, H. *Journal of Macromolecular Science Part A: Chemistry* **2015**, 52, (2), 147-154.
34. Harada, M.; Nomura, M.; Kojima, H.; Eguchi, W.; Nagata, S. *Journal of Applied Polymer Science* **1972**, 16, (4), 811-833.
35. Nomura, M.; Tobita, H.; Suzuki, K. *Advances in Polymer Science* **2005**, 175, (Polymer Particles), 1-128.
36. Dobrowolska, M. E.; Esch, J. H. v.; Koper, G. J. M. *Langmuir* **2013**, 29, (37), 11724-11729.
37. Sood, A.; Lodhi, P. K. *Journal of Applied Polymer Science* **2011**, 122, 517-533.
38. Liu, B.; Zhang, M.; Zhou, C.; Ren, L.; Cheng, H.; Ao, Y.; Zhang, H. *Colloid and Polymer Science* **2013**, 291, (10), 2385-2398.
39. Liu, B.; Zhang, M.; Gui, Y.; Chen, D.; Zhang, H. *Colloids and Surfaces A: Physicochemical Engineering Aspects* **2014**, 452, 159-164.
40. Mason, T. G.; Wilking, J. N.; Meleson, K.; Chang, C. B.; Graves, S. M. *Journal of Physics: Condensed Matter* **2006**, 18, (41), R635-R666.
41. Ugelstad, J.; Hansen, F. K. *Rubber Chemistry and Technology* **1976**, 49, (3), 536-609.
42. Lovell, P. A., Batch and Semi-batch processes. In *Emulsion Polymerisation and Emulsion Polymers*, Lovell, P. A.; El-Aasser, M. S., Eds. Wiley: Chichester, 1997.
43. Durant, Y.; Sundberg, D. *Polymer Reaction Engineering* **2003**, 11, (3), 379-432.
44. Routh, A. F.; Keddie, J. L., *Fundamentals of Latex Film Formation: Processes and Properties*. Springer: 2010.
45. Dimonie, V. L.; Daniels, E. S.; Shaffer, O. L.; El-Aasser, M. S., Control of Particle Morphology. In *Emulsion Polymerisation and Emulsion Polymers*, Lovell, P. A.; El-Aasser, M. S., Eds. Wiley: Chichester, 1997.
46. Bates, F. S. *Science* **1991**, 251, (4996), 898-905.
47. Guo, T.-Y.; Tang, G.-L.; Hao, G.-J.; Song, M.-D.; Zhang, B.-H. *Journal of Applied Polymer Science* **2002**, 86, (12), 3078 - 3084.
48. Jonsson, J.-E.; Hassander, H.; Tornell, B. *Macromolecules* **1994**, 27, 1932-1937.
49. Chen, Y.-C.; Dimonie, V. L.; El-Aasser, M. S. *Macromolecules* **1991**, 24, 3779-3787.
50. Schuler, B.; Baumstark, R.; Kirsch, S.; Pfau, A.; Sandor, M.; Zosel, A. *Progress in Organic Coatings* **2000**, 40, 139-150.
51. Stubbs, J.; Karlsson, O.; Jonsson, J.-E.; Sundberg, E.; Durant, Y.; Sundberg, D. *Colloids and Surfaces A: Physicochemical and Engineering Aspects* **1999**, 153, 255-270.
52. Robeson, L. M., *Polymer Blends: A Comprehensive Review*. Hanser: 2007.
53. Cao, S.; Chen, J.; Hu, J. *Australian Journal of Chemistry* **2009**, 62, 1561-1576.
54. Ferguson, C. J.; Russell, G. T.; Gilbert, R. G. *Polymer* **2002**, 43, 4557-4570.
55. Borthakur, L. J.; Jana, T.; Dolui, S. K. *Journal of Coating Technology and Research* **2010**, 7, (6), 765-772.
56. Brandrup, J.; Immergut, E. H.; Grulke, E. A., *Polymer Handbook*. 4th ed.; Wiley: 1999.
57. Khan, A. K.; Ray, B. C.; J.Maiti; Dolui, S. K. *Pigment & Resin Technology* **2009**, 38, (3), 159-164.
58. Lovell, P. A. *Trends in Polymer Science* **1996**, 4, (8), 264-272.
59. Chen, Y.-C.; Dimonie, V. L.; Shaffer, O. L.; El-Aasser, M. S. *Polymer International* **1993**, 30, 185-194.
60. Sundberg, E. J.; Sundberg, D. C. *Journal of Applied Polymer Science* **1993**, 47, (7), 1277-1294.
61. Herrera, V.; Pirri, R.; Leiza, J. R.; Asua, J. M. *Macromolecules* **2006**, 39, 6969-6974.

62. Stubbs, J. M.; Sundberg, D. C. *Progress in Organic Coatings* **2008**, 61, 156-165.
63. Karlsson, L. E.; Karlsson, O. J.; Sunberg, D. C. *Journal of Applied Polymer Science* **2003**, 90, 905-915.
64. Stubbs, J. M.; Sundberg, D. C. *Journal of Applied Polymer Science* **2003**, 91, 1538-1551.
65. Wang, T.; Shi, S.; Yang, F.; Zhou, L. M.; Kuroda, S. *Journal of Material Science* **2010**, 45, 3392-3395.
66. Stubbs, J. M.; Sundberg, D. C. *Journal of Applied Polymer Science* **2006**, 102, 945-957.
67. Stubbs, J. M.; Sundberg, D. C. *Journal of Applied Polymer Science* **2006**, 102, 2043-2054.
68. Dillon, R. E.; Matheson, L. A.; Bradford, E. B. *Journal of Colloid Science* **1951**, 6, (2), 108-117.
69. Brown, G. L. *Journal of Polymer Science* **1956**, 22, 423-434.
70. Voyutskii, S. S. *Journal of Polymer Science* **1958**, 32, (125), 528-230.
71. Provder, T.; Winnik, M. A.; Urban, M. W., *Film Formation in Waterborne Coatings*. ACS: Washington DC, 1996.
72. Eckersley, S. T.; Rudin, A. *Progress in Organic Coatings* **1994**, 23, 387-402.
73. Winnik, M. A.; Feng, J. R. *Journal of Coatings Technology* **1996**, 68, (852), 39-50.
74. Carter, F. T.; Kowalczyk, R. M.; Millichamp, I.; Chainey, M.; Keddie, J. L. *Langmuir* **2014**, 30, 9672-9681.
75. Wang, T.; Canetta, E.; Weerakkody, T. G.; Keddie, J. L.; Rivas, U. *Applied Materials and Interfaces* **2009**, 1, (3), 631-639.
76. Armstrong, R. D.; Wright, J. D. *Corrosion Science* **1992**, 33, (10), 1529-1539.
77. Routh, A. F.; Russel, W. B. *Journal of the American Institute of Chemical Engineers* **1998**, 44, (9), 2088-2099.
78. Okubo, M.; Takeya, T.; Tsutsumi, Y.; Kadooka, T.; Matsumoto, T. *Journal of Polymer Science Part A: Polymer Chemistry* **1981**, 19, (1), 1-9.
79. Butt, H. J.; Kuroopka, R.; Christensen, B. *Colloid and Polymer Science* **1994**, 272, 1218-1233.
80. Butt, H.-J.; Gerharz, B. *Langmuir* **1995**, 11, 4735-4741.
81. Blackley, D. C., *Polymer Latices: Science and Technology (Volume 1: Fundamental Principles)*. 2nd ed.; Springer: 1997.
82. Paul, S. *Progress in Organic Coatings* **1977**, 5, (1), 79-96.
83. Vijayendran, B. R.; Bone, T.; Sawyer, L. C. *Journal of Dispersion Science and Technology* **1982**, 3, (1), 81-97.
84. Tongyu, C.; Yongshen, X.; Yunchen, S.; Fu, L.; Xing, L.; Yuhong, H. *Journal of Applied Polymer Science* **1990**, 41, 1965-1972.
85. Wang, Y.; Winnik, M. A. *Journal of Physical Chemistry* **1993**, 97, 2507-2515.
86. Routh, A. F.; Russel, W. B. *Industrial and Engineering Chemistry Research* **2001**, 40, 4302-4308.
87. Lepizzera, S.; Pith, T.; Fond, C.; Lambla, M. *Macromolecules* **1997**, 30, 7945-7952.
88. Winnik, M. A. *Journal of Coatings Technology* **2002**, 74, (925), 49-63.
89. Juhue, D.; Lang, J. *Macromolecules* **1995**, 28, 1306-1308.
90. Daniels, E. S.; Klein, A. *Progress in Organic Coatings* **1991**, 19, 359-378.
91. Devon, M. J.; Gardon, J. L.; Roberts, G.; Rudin, A. *Journal of Applied Polymer Science* **1990**, 39, (10), 2119-2128.
92. Zhang, X.; Liu, Y.; Huang, H.; Li, Y.; Chen, H. *Journal of Applied Polymer Science* **2011**, 123, (3), 1822-1832.
93. Flory, P. J.; Rehner, J. *Journal of Chemical Physics* **1943**, 11, 521-526.
94. Perez, E.; Lang, J. *Langmuir* **2000**, 16, 1874-1881.
95. Kessel, N.; Illsley, D. R.; Keddie, J. L. *Journal of Coatings Technology Research* **2008**, 5, (3), 285-297.

96. Joshi, R. G.; Provder, T.; Zeimer, P.; Mao, W.; Shen, W.; Jones, F. N. *Journal of Coatings Technology Research* **2009**, 6, (1), 47-65.
97. Horkay, F.; Craig, D. H. *Polymer Bulletin* **1998**, 41, 231-237.
98. Nic, M.; Jirat, J.; Kosata, B., *IUPAC Compendium of Chemical Terminology: Gold Book*. 2.2.3 ed.; 2014.
99. Threadingham, D.; Obrecht, W.; Wieder, W.; Wachholz, G.; Engelhausen, R., Rubber, 3. Synthetic Rubbers, Introduction and Overview. In *Ullman's Encyclopedia of Industrial Chemistry*, Wiley: 2011; Vol. 31.
100. Treloar, L. R. G., *The Physics of Rubber Elasticity*. 3rd ed.; Oxford University Press: Oxford, 2005.
101. Cook, W. D. *Journal of Applied Polymer Science* **1991**, 42, (5), 1259-1269.
102. Heatley, F.; Lovell, P. A.; McDonald, J. *European Polymer Journal* **1993**, 29, (2), 255-268.
103. Volfova, P.; Chrastova, V.; Cernakova, L.; Mrenica, J.; Kozankova, J. *Macromolecular Symposia* **2001**, 170, 283-290.
104. Tillet, G.; Boutevin, B.; Ameduri, B. *Progress in Polymer Science* **2011**, 36, 191-217.
105. Coleman, L. E.; Bork, J. F.; Wyman, D. P.; Hoke, D. I. *Journal of Polymer Science Part A: Polymer Chemistry* **1965**, 3, 1601-1608.
106. Koukiotis, C. G.; Karabela, M. M.; Sideridou, I. D. *Progress in Organic Coatings* **2012**, 75, 106-115.
107. Esser, R. J.; Devona, J. E.; Setzke, D. E.; Wagemans, L. *Progress in Organic Coatings* **1999**, 36, 45-52.
108. Thongnuanchan, B.; Ninjan, R.; Kaesaman, A.; Nakason, C. *Polymer Bulletin* **2015**, 72, 135-155.
109. Nakayama, Y. *Progress in Organic Coatings* **2004**, 51, 280-299.
110. Hirose, M.; Kadowaki, F.; Zhou, J. *Progress in Organic Coatings* **1997**, 31, 157-169.
111. Reck, B. In *Frontiers of Polymer Colloids: From Synthesis to Macroscale and Nanoscale applications*, Prague, Czech Republic, 2014; BASF: Prague, Czech Republic, 2014.
112. Clayden, J.; Greeves, N.; Warren, S.; Wothers, P., *Organic Chemistry*. OUP: Oxford, 2006.
113. Liu, X.; Zhang, C.; Xiong, T.; Chen, D.; Zhong, A. *Journal of Applied Polymer Science* **2007**, 106, 1488-1455.
114. Schroeder, W. F.; Liu, Y.; Tomba, J. P.; Soleimani, M.; Lau, W.; Winnik, M. A. *Polymer* **2011**, 52, 3984-3993.
115. Stubbs, J. M.; Sundberg, D. C. *Journal of Polymer Science Part B* **2011**, 49, (22), 1583-1589.
116. J.G.Tsavalas; Sundberg, D. C. *Langmuir* **2010**, 26, (10), 6960-6966.
117. Juhue, D.; Lang, J. *Macromolecules* **1994**, 27, (695-701).
118. Goikoetxea, M.; Reyes, Y.; Alarcon, C. M. d. I. H.; Minari, R. J.; Beristain, I.; Paulis, M.; Barandiaran, M. J.; Keddie, J. L.; Asua, J. M. *Polymer* **2012**, 53, 1098-1108.
119. Morgan, L. W. *Journal of Applied Polymer Science* **1982**, 27, (6), 2033-2042.
120. Keddie, J. L.; Jones, R. A. L.; Cory, R. A. *Faraday Discussions* **1994**, 98, 219-230.
121. Keddie, J. L.; Jones, R. A. L.; Cory, R. A. *Europhysics Letters* **1994**, 27, 59-64.
122. Price, K.; Wu, W.; Wood, K.; Kong, S.; McCormick, A.; Francis, L. *Journal of Coatings Technology and Research* **2014**, 11, (6), 827-839.
123. Dong, L.; Tong, Y.; An, Y.; Tang, H.; Zhuang, Y.; Feng, Z. *European Polymer Journal* **1997**, 33, (4), 501-503.
124. Gutierrez-Meija, A.; Herrera-Kao, W.; Duarte-Aranda, S.; Loria-Bastarrachea, M. I.; Canche-Escamilla, G.; Moscoso-Sanchez, F. J.; Cauich-Rodriguez, J. V.; Cervantes-Uc, J. M. *Materials Science and Engineering: C* **2013**, 33, 1737-1743.
125. Khan, I.; Poh, B. T. *Journal of Polymers and the Environment* **2011**, 19, 973-811.

126. Bellamine, A.; Degrandi, E.; Gerst, M.; Stark, R.; Beyers, C.; Creton, C. *Macromolecular Materials and Engineering* **2011**, 296, 31-41.
127. Urban, D.; Schoecker, P.; Kirsch, S.; Pietsch, I.; Kutschera, M.; Weiss, H.; Beyers, C. P. Adhesive film having at least two continuous phases. 2008.
128. Aymonier, A.; Papom, E.; Villenave, J.-J.; Tordjeman, P.; Pirri, R.; Gerard, P. *Chemical Materials* **2001**, 13, 2562-2566.
129. Sheu, H. R.; El-Aasser, M. S.; Vanderhoff, J. W. *Journal of Polymer Science Part A: Polymer Chemistry* **1990**, 28, (3), 629-651.
130. Majumder, A.; Ghatak, A.; Sharma, A. *Science* **2007**, 318, 258-261.
131. Wang, R.-M.; Wang, J.-F.; Wang, X.-W.; He, Y.-F.; Zhu, Y.-F.; Jiang, M.-L. *Progress in Organic Coatings* **2011**, 71, 369-375.
132. Mader, A.; Schiro, A.; Brischetto, M.; Pizzo, B. *Progress in Organic Coatings* **2011**, 71, 123-135.
133. Tamai, T.; Pinenq, P.; Winnik, M. A. *Macromolecules* **1999**, 32, 6102-6110.
134. Czech, Z. *Polymer International* **2003**, 52, 347-357.
135. Naderi, N.; Sharifi-Sanjani, N.; Khayyat-Naderi, B.; Agend, F. *Journal of Applied Polymer Science* **2007**, 106, (2), 1172-1180.
136. Houlton, S., *Chemistry World* March 2010.
137. Geurts, J.; Bouman, J.; Overbeek, A. *Journal of Coatings Technology and Research* **2008**, 5, (1), 57-63.
138. Warson, H.; Finch, C. A., *Applications of Synthetic Resin Latices, Volume 2: Latices in surface coatings - Emulsion paints*. Wiley: 2001; Vol. 2.
139. Harakawa, H.; Karasi, A.; Tominaga, A.; Yabuta, M. *Progress in Organic Coatings* **1998**, 34, 84-90.
140. Dwight, M. D.; Collins, M. J.; Lopez, P.; Taylor, J. W. Waterborne polymers having pendant allyl groups. US 5,869,590, 1996.
141. Frankel, L. S.; Jr, W. S.; Curen, J. V.; Winey, D. A. Multi-Stage binder for use in elastomeric coatings, caulks and sealants. US 6060532, 2000.
142. Emmons, W. D. Ambient or low-temperature curable coating compositions for coating rigid substrates. EP 0016518, 1980.
143. Kriessmann, I.; Awad, R.-R.; Gsoll, H.; Hirschmann, B.; Rossmann, K. Aqueous self-crosslinking copolymer dispersions, a process for preparing them and their use in binders for coating materials. US 6515042 B2, 2003.
144. Robinson, G. F.; Shemancik, R. C.; Speight, R. D.; Wong, P. T.; Zneidersic, K. M. Coating compositions and coatings formed therefrom US 6605359, 2003.
145. Mestach, D. Aqueous dispersions of particles of polymers with a glass transition temperature gradient. EP1125949-A1, 2001.
146. Krajnik, J. M.; Lam, V. H.; Sabo, L. O.; Camerson, J. M.; Mittleman, M. L.; Wise, K. M. Waterborne coating composition having improved crosslink density and uniform film formation and coating production. US 20020103278, 2002.
147. Schafheutle, M. Self Crosslinking Binders. EP 2025694 A1, 2009.
148. Moore, B. Polymer for extending the open time of water-borne architectural coatings. WO2012/087920, 2012.
149. Yang, S.-J.; Dandreux, G.; Sheerin, R. J. Ambient self-crosslinkable latex. US 2012/055883, 2012.
150. Mestach, D.; Thys, F.; Brinkhuis, R.; Egmond, R. v.; Roelofs, R.; Horst, R. v. d. A long shelf life aqueous coating composition. GB2503700, 2014.
151. Nabuurs, T.; Scheerder, J.; Buckmann, A. J. P.; Overbeek, G. C. Polymer composition comprising a polymer having a gradient polymeric morphology. EU 1434803, 2009.
152. Shen, M.; Bever, M. B. *Journal of Materials Science* **1972**, 7, 741-746.
153. Eian, G. L.; Ludwig, B. W.; Jr, M. H. A. Polymeric Compositions. EU 1208138, 2002.

154. Salomons, W.; Hofman, H. New protective colloids in latices with improved film formation at low temperatures. EU 965598, 1999.
155. Pecora, R. *Journal of Chemical Physics* **1964**, 40, (6), 1604-1614.
156. Tscharnuter, W., Photon Correlations Spectroscopy in Particle Sizing. In *Encyclopedia of Analytical Chemistry*, Meyers, R. A., Ed. John Wiley & Sons LTD: Chichester, 2000; pp 5469-5485.
157. Blanchard, R. Synthesis of Alkali Soluble Resins and their use as stabilisers in Emulsion Polymerisation. University of Manchester, 2005.
158. Small, H. *Journal of Colloid and Interface Science* **1974**, 48, (1), 147-161.
159. Streigel, A. M.; Brewer, A. K. *Annual Review of Analytical Chemistry* **2012**, 5, 15-34.
160. Suter, S. P.; Skalak, R. *Annual Review of Fluid Mechanics* **1993**, 25, 1-20.
161. McHugh, A. J.; Brenner, H. *Critical Reviews in Analytical Chemistry* **1984**, 15, (1), 63-117.
162. Lathe, G. H.; Ruthven, C. R. J. *Biochemical Journal* **1956**, 62, (4), 665-674.
163. Harris, D. C., *Quantitative Chemical Analysis*. W.H. Freeman & Co.: 1999.
164. Higson, S. P., *Analytical Chemistry*. Oxford University Press: Oxford, 2004.
165. Swallowe, G. M., *Mechanical Properties and Testing of Polymers*. Kluwer Academic Publishers: Dordrecht, 1999.
166. Meyers, M.; Chawla, K., *Mechanical Behaviour of Materials*. 2nd ed.; Cambridge University Press: Cambridge, 2009.
167. McCrum, N. G.; Buckley, C. P.; Bucknall, C. B., *Principles of Polymer Engineering*. 2nd ed.; Oxford Science Publications: 1997.
168. Roylance, D., *Engineering Viscoelasticity*. MIT: Cambridge, MA, 2001.
169. Lin-Vien, D.; Colthup, N. B.; Fateley, W. G.; Grasselli, J. G., *The Handbook of Infrared and Raman Characteristic Frequencies of Organic Molecules*. Elsevier: 1991.
170. Harwood, L. M.; Claridge, T. D. W., *Introduction to Organic Spectroscopy*. Oxford University Press: 1997.
171. Binnig, G.; Quate, C. F.; Gerber, C. *Physical Review Letters* **1986**, 56, (9), 930-934.
172. Rugar, D.; Hansma, P. *Physics Today* **1990**, 43, (10), 23-30.
173. Albrecht, T. R.; Akamine, S.; Carver, T. E.; Quate, C. F. *Journal of Vacuum Science and Technology A* **1990**, 8, 3386.
174. Zhong, Q.; Inniss, D.; Kjoller, K.; Elings, V. B. *Surface Science Letters* **1993**, 290, 688-692.
175. Gross, L.; Mohn, F.; Moll, N.; Liljeroth, P.; Meyer, G. *Science* **2009**, 325, (5944), 1110-1114.
176. Kaemmer, S. B., Introduction to Bruker's ScanAsyst and PeakForce Tapping AFM Technology. In http://www.bruker.com/fileadmin/user_upload/8-PDF-Docs/SurfaceAnalysis/AFM/ApplicationNotes/Introduction_to_Brukers_ScanAsyst_and_PeakForce_Tapping_Atomic_Force_Microscopy_Technology_AFM_AN133.pdf, Division, B. N. S., Ed. Bruker Corporation: Santa Barbara CA, USA, 2011.
177. Young, T. J.; Monclus, M. A.; Burnett, T. L.; Broughton, W. R.; Ogin, S. L.; Smith, P. A. *Measurement Science and Technology* **2011**, 22, 125703/1-125703/6.
178. Derjaguin, V. B.; Muller, V. M.; Toporov, Y. P. *Journal of Colloid and Interface Science* **1975**, 53, (2), 314-326.
179. Dazzi, A.; Prazeres, R.; Glotin, F.; Ortega, J. M. *Optics Letters* **2005**, 30, (18), 2388-2390.
180. Seidel, W.; Foerstendorf, H.; Heise, K. H.; Nicolai, R.; Schamlott, A.; Ortega, J. M.; Glotin, F.; Prazeres, R. *European Physical Journal - Applied Physics* **2004**, 25, (1), 39-43.
181. Dazzi, A.; Prazeres, R.; Glotin, F.; Ortega, J. M. *Infrared Physics and Technology* **2006**, 49, 113-121.
182. AnasysInstruments <http://www.anasysinstruments.com/products/nanoir2/>

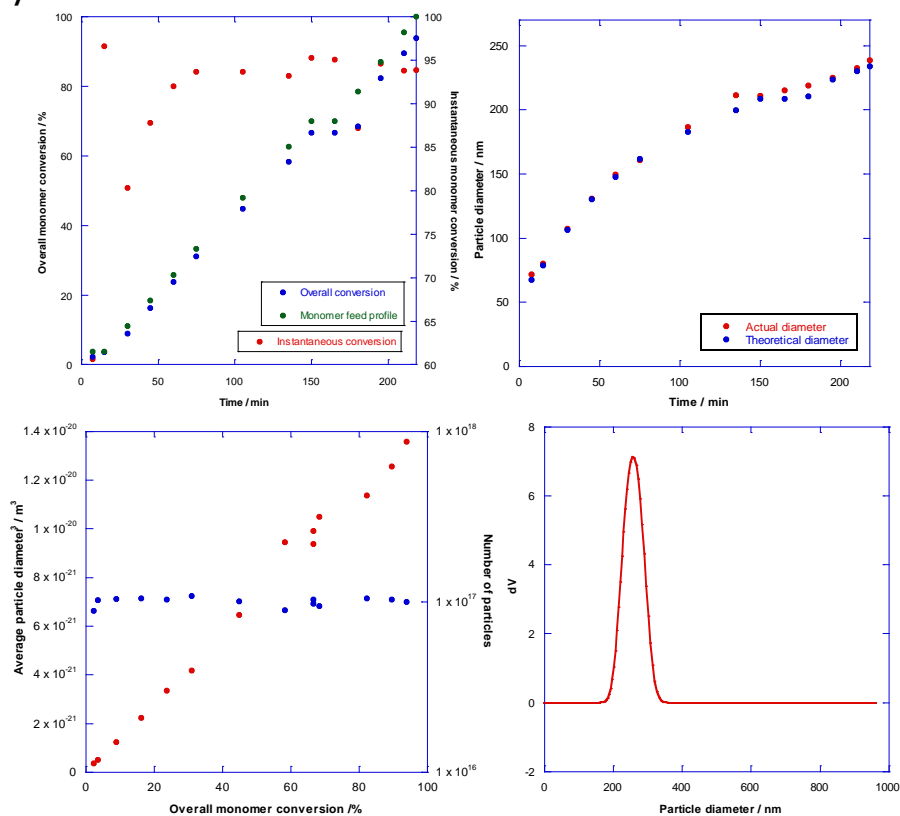
183. ISO, Determination of white point temperature and minimum film-forming temperature. 2011; Vol. ISO 2115-1997.
184. ASTM, Standard Test Method for Minimum Film Formation Temperature (MFFT) of Emulsion Vehicles. Vol. ASTM 2354-98.
185. Höhne, G.; Hemminger, E.; Flammersheim, H.-J., *Differential Scanning Calorimetry*. Springer: 2003; Vol. 2.
186. Smith, G. D.; Bedrov, D. *Journal of Polymer Science Part B: Polymer Physics* **2007**, 45, 627-643.
187. Aymonier, A.; E.Papom; Castelein, G.; Brogly, M.; Tordjeman, P. *Journal of Colloid and Interface Science* **2003**, 268, 341-347.
188. Benedek, I., *Pressure-Sensitive Adhesives and Application*. CRC press: 2004.
189. Koleske, J. V., *Paint and Coating Testing Manual: 15th Edition of the Gardner-Sward handbook*. ASTM: 2012.
190. Ishikawa, Y.; Katoh, Y.; Ohshima, H. *Colloids and Surfaces B: Biointerfaces* **2005**, 42, 53-58.
191. Piirma, I.; Chang, M. *Journal of Polymer Science Part A: Polymer Chemistry* **1982**, 20, (2), 489-498.
192. Kawaguchi, S.; Odrobina, E.; Winnik, M. A. *Macromolecular Rapid Communications* **1995**, 16, (11), 860-868.
193. Gibson, C. M. University of Manchester, 2013.
194. Kan, C. S. *Journal of Coatings Technology* **1999**, 71, (896), 89-99.
195. Soleimani, M.; Haley, J. C.; Lau, W.; Winnik, M. A. *Macromolecules* **2010**, 43, 975-985.
196. Andersen, F. A.; Cooper, C. G. *International Journal of Toxicology* **1994**, 13, (3), 154-156.
197. Corporation, H. *Technical Bulletin - Jeffamine EDR-148 Polyetheramine*; 2011.
198. Dokukin, M. E.; Sokolov, I. *Langmuir* **2012**, 28, 16060-16071.
199. Xu, G. H.; Dong, J.; Zhang, J.; Severtson, S. J.; Houtman, C. J.; Gwin, L. E. *Journal of Physical Chemistry: Part B* **2008**, 112, 11907-11914.
200. Arnold, C.; Klein, G.; Maaloum, M.; Ernstsson, M.; Larsson, A.; Marie, P.; Holl, Y. *Colloids and Surfaces A: Physicochemical Engineering Aspects* **2011**, 374, 58-68.
201. Aramendia, E.; Mallegol, J.; Jeynes, C.; Barandiaran, M. J.; Keddie, J. L.; Asua, J. M. *Langmuir* **2003**, 19, 3212-3221.
202. Williams, D. H.; Fleming, I., *Spectroscopic Methods in Organic Chemistry*. 3rd ed.; McGraw-Hill: UK, 1980.
203. Pretsch, E.; Buhlmann, P.; Badertscher, M., *Structure Determination of Organic Compounds: Tables of Spectral Data*. 4th ed.; Springer: Heidelberg, 2009.
204. Heuts, M. P. J.; Febre, R. A. I.; Hilst, J. L. M. v.; Overbeek, G. C., Influence of morphology on film formation of acrylic dispersions. In *Film Formation in Waterborne Coatings*, Provder, T.; Winnik, M. A.; Urban, M. W., Eds. American Chemical Society: 1996.
205. Meincken, M.; Sanderson, R. D. *Polymer* **2002**, 43, p4947-4955.
206. Koukiotis, C.; Sideridou, I. D. *Progress in Organic Coatings* **2010**, 69, 504-509.
207. Zhang, J.-D.; Yang, M.-J.; Zhu, Y.-R.; Yang, H. *Polymer International* **2006**, 55, 951-960.
208. Vanderhoff, J. W.; Hul, H. J. V. d.; Hamburg, R. D. *Polymer Preprints* **1975**, 16, (1), 155-160.
209. Kamel, A. A.; El-Aasser, M. S.; Vanderhoff, J. W. *Journal of Dispersion Science and Technology* **1981**, 2, (2-3), 183-214.
210. Stone-Masui, J.; Watillon, A. *Journal of Colloid and Interface Science* **1975**, 52, (3), 479-503.
211. Kawaguchi, S.; Yekta, A.; Winnik, M. A. *Journal of Colloid and Interface Science* **1995**, 176, 362-369.
212. Kim, H.-B.; Winnik, M. A. *Macromolecules* **1994**, 27, 1007-1012.

213. Gong, Y.-K.; Nakamasha, K.; Xu, R. *Langmuir* **2001**, *17*, (9), 2889-2892.
214. Vanderhoff, J. W.; Hul, H. J. V. d. *Journal of Electroanalytical Chemistry* **1972**, *37*, 161-182.
215. Dusek, K.; Prins, W. *Advances in Polymer Science* **1969**, *6*, (1), 1-102.
216. Vieira, R. A. M.; Sayer, C.; Lima, E. L.; Pinto, J. C. *Industrial and Engineering Chemistry Research* **2002**, *41*, 2915-2930.
217. Sayer, C.; Araujo, P. H. H.; Arzamendi, G.; Asua, J. M.; Lima, E. L.; Pinto, J. C. *Journal of Polymer Science Part A: Polymer Chemistry* **2001**, *39*, (20), 3513-3528.
218. Landel, R. F.; Nielsen, L. E., *Mechanical Properties of Polymers and Composites*. 2nd ed.; CRC Press: 1993.
219. Backfolk, K.; Holmes, R.; Ihalainen, P.; Sirvio, P.; Triantafillopolous, N.; Peltonen, J. *Polymer Testing* **2007**, *26*, 1031-1040.
220. Aklonis, J. J. *Journal of Chemical Education* **1981**, *58*, (11), 892-897.
221. Steward, P. A.; Hearn, J.; Wilkinson, M. C. *Advances in Colloid and Interface Science* **2000**, *86*, 195-267.
222. Khan, A. K.; Ray, B. C.; Dolui, S. K. *Progress in Organic Coatings* **2008**, *62*, (1), 65-70.
223. Hasanzadeh, I.; Mahdavian, A. R.; Salehi-Mobarakeh, H. *Progress in Organic Coatings* **2014**, *77*, 1874-1882.
224. Karlsson, O. J.; Hassander, H.; Columbini, D. *Comptes Rendus Chimie* **2003**, *6*, 1233-1244.
225. Kimber, J. A.; Gerst, M.; Kazarian, S. G. *Langmuir* **2014**, *30*, 13588-13595.
226. Bierwagen, G. P. *Journal of Coatings Technology* **1979**, *51*, (658), 117-126.
227. Lambourne, R.; Strivens, T., *Paint and Surface Coatings: Theory and Practice*. 2nd ed.; Elsevier: 1999.
228. Kast, H. *Die Makromolekulare Chemie* **1985**, *10*, (Supplement 10/11), 447-461.
229. Yoh, A. Y. C.; Mange, S.; Bothe, M.; Leyrer, R. J.; Gilbert, R. G. *Polymer* **2006**, *47*, 1159-1165.
230. Vorwerg, L.; Gilbert, R. G. *Macromolecules* **2000**, *33*, 6693-6703.
231. Ortega-Vinuesa, J. L.; Martin-Rodriguez, A.; Hidalgo-Alvarez, R. *Journal of Colloid and Interface Science* **1996**, *184*, 259-267.
232. Charmont, D.; D'Allest, J. F.; Dobler, F. *Polymer* **1996**, *37*, (23), 5237-5245.
233. Zhao, Y.; Urban, M. W. *Macromolecules* **2000**, *33*, 8426-8434.
234. Guo, T.-Y.; Liu, J.-C.; Song, M.-D.; Zhang, B.-H. *Journal of Applied Polymer Science* **2007**, *104*, (6), 3948-3953.
235. Montesinos-Gomez, R.; Reynoso, R.; Rodriguez-Gomez, F. J.; Reyes-Mercado, Y.; Vazquez, F. *Journal of Applied Polymer Science* **2009**, *113*, 553-557.
236. Taenghom, T.; Pan, Q.; Rempel, G. L.; Kiatkamjornwong, S. *Colloid and Polymer Science* **2013**, *291*, 1365-1374.
237. Snuparek, J.; Kaska, M.; Baghaffar, G.; Quadrat, O. *Macromolecular Symposia* **2002**, *179*, 89-103.
238. Klein, G.; Houerou, V. L.; Muller, R.; Gauthier, C.; Holl, Y. *Tribology International* **2012**, *53*, 142-149.
239. Pedraza, E. P.; Soucek, M. D. *Polymer* **2005**, *46*, 11174-11185.
240. Bas, S.; Soucek, M. D. *Reactive and Functional Polymers* **2013**, *73*, 291-302.
241. Lu, D.; Xie, J.; Shen, L.; Zhao, Q.; Yuan, T.; Guan, R. *Journal of Applied Polymer Science* **2012**, *125*, 2807-2813.
242. Kim, B.; Peppas, N. A. *Journal of Biomaterials Science, Polymer Edition* **2002**, *13*, (11), 1271-1281.
243. Tungchaiwattana, S.; Liu, R.; Halacheva, S.; Shahidan, N. N.; Kells, A.; Saunders, B. R. *Soft Matter* **2013**, *9*, (13), 3547-3557.
244. Pinrayoon, O.; Groves, R.; Saunders, B. R. *Journal of Colloid and Interface Science* **2008**, *321*, (2), 315-322.

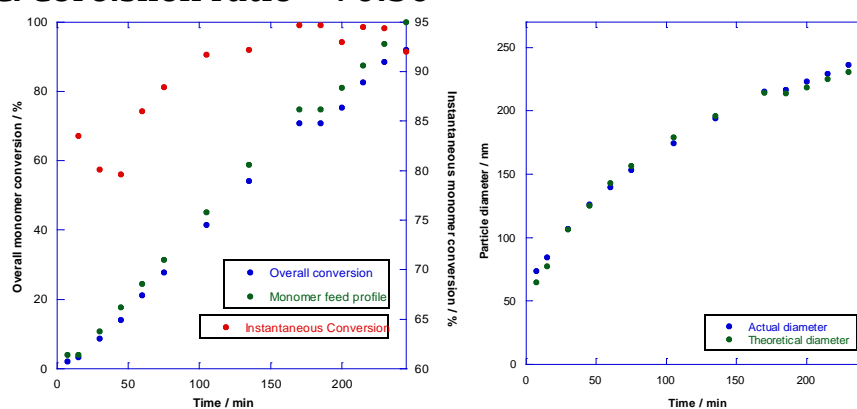
245. Phillipova, O. E.; Hourdet, D.; Audebert, R.; Khokhlov, A. R. *Macromolecules* **1997**, *30*, (26), 8278-8285.
246. Kim, H.-B.; Wang, Y.; Winnik, M. A. *Polymer* **1994**, *35*, (8), 1779-1786.
247. Distler, D.; Kanig, G. *Colloid and Polymer Science* **1978**, *256*, (11), 1052-1060.
248. Richard, J. *Polymer* **1992**, *33*, (3), 562-571.
249. Kanig, G.; Neff, I. *Colloid and Polymer Science* **1975**, *253*, (1), 29-31.
250. Richard, J.; Mignaud, C.; Wong, K. *Polymer International* **1993**, *30*, 431-439.
251. Adelnia, H.; Gavvani, G. N.; Riazi, H.; Bidsorkhi, H. C. *Progress in Organic Coatings* **2014**, *77*, 1826-1833.
252. Hellgren, A.-C. *Progress in Organic Coatings* **1998**, *34*, 91-99.
253. Andersson, C.; Backfolk, K. *Progress in Organic Coatings* **2008**, *63*, 63-71.
254. Ricci, D.; Braga, P. C., Recognising and Avoiding artefacts in AFM imaging. In *Atomic Force Microscopy - Biomedical methods and applications*, Braga, P. C.; Ricci, D., Eds. Humana Press: Totowa, NJ, 2004.
255. DowConstructionChemicals *Technical Data Sheet for Europe, Middle East and Africa - Primal (TM) AC337 ER Acrylic Emulsion Polymer*; 2012.
256. Bell, P., New One-Pack Crosslinking Polymers. *Paint & Coatings Industry* October 1, 2001, 2001.
257. Buckmann, F.; Overbeek, A.; Nabuurs, T., Self-crosslinking surfactant free acrylic dispersions for high performance coatings applications. In *Nuremburg Congress 2001 - Creative Advances in Coatings Technology*, Nuremburg, 2001.
258. Buckmann, A. J. P.; Nabuurs, T.; Overbeek, G. C., Self-crosslinking polymeric dispersants and their use in Emulsion polymerisation. In *International Waterborne, High Solids and Powder Coatings Symposium*, New Orleans, LA, USA, 2002.
259. Tan, B.-H. Linoleic acid functionalised amphiphilic block copolymers application in waterborne coatings. University of Twente, 2007.
260. Hahn, K.; Ley, G.; Schuller, H.; Oberthur, R. *Colloid and Polymer Science* **1986**, *264*, (12), 1092-1096.
261. Liu, Y. S.; Feng, J.; Winnik, M. A. *Journal of Chemical Physics* **1994**, *101*, (10), 9096-9103.
262. Holten-Andersen, N.; Fantner, G. E.; Hohlbauch, S.; Waite, J. H.; Zok, F. W. *Nature Materials* **2007**, *6*, 669-672.
263. Lopez, A.; Degrandi-Contraires, E.; Canaletta, E.; Creton, C.; Keddie, J. L.; Asua, J. M. *Langmuir* **2011**, *27*, 3878-3888.
264. Degrandi-Contraires, E.; Udagama, R.; Borgeat-Lami, E.; McKenna, T.; Ouzineb, K.; Creton, C. *Macromolecules* **2011**, *44*, 2643-2652.
265. Degrandi-Contraires, E.; Udagama, R.; McKenna, T.; Bourgeat-Lami, E.; Plummer, C. J. G.; Creton, C. *International Journal of Adhesion and Adhesives* **2014**, *50*, 176-182.
266. Kim, B. K.; Lee, J. C. *Journal of Applied Polymer Science* **1995**, *58*, 1117-1124.
267. Mayer, H. *Surface Coatings International* **1998**, *2*, 89-94.
268. Park, H.-S.; Yang, I.-M.; Wu, J.-P.; Kim, M.-S.; Hahm, H.-S.; Kim, S.-K.; Rhee, H.-W. *Journal of Applied Polymer Science* **2001**, *81*, (7), 1614-1623.
269. Park, H.-S.; Kim, S.-R.; Park, H.-J.; Kwak, Y.-C.; Hahm, H.-S.; Kim, S.-K. *Journal of Coatings Technology* **2003**, *75*, (936), 55-64.
270. Christopher, K. R.; Pal, A.; Mirchandani, G.; Dhar, T. *Progress in Organic Coatings* **2014**, *77*, 1063-1068.

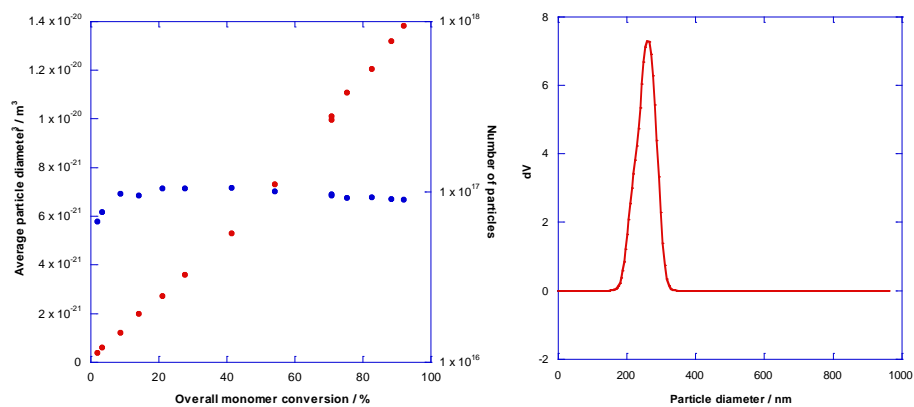
Appendix (i) – Characterisation plots for soft-soft nanocomposite latexes discussed in Chapter 4

a) Poly[(BA)-*co*-(BMA)] core and shell copolymers with $T_g = 0/-20$ °C. Core:shell ratio = 70:30

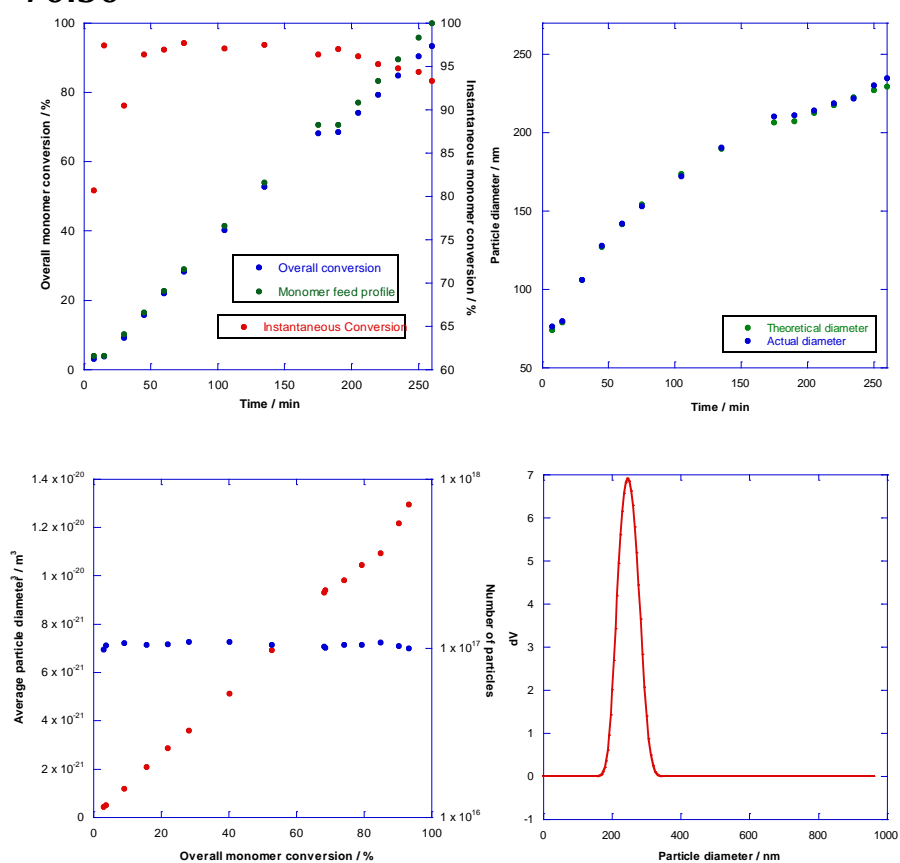


b) Poly[(BA)-*co*-(BMA)] core and shell copolymers with $T_g = 0$ °C. Core:shell ratio = 70:30

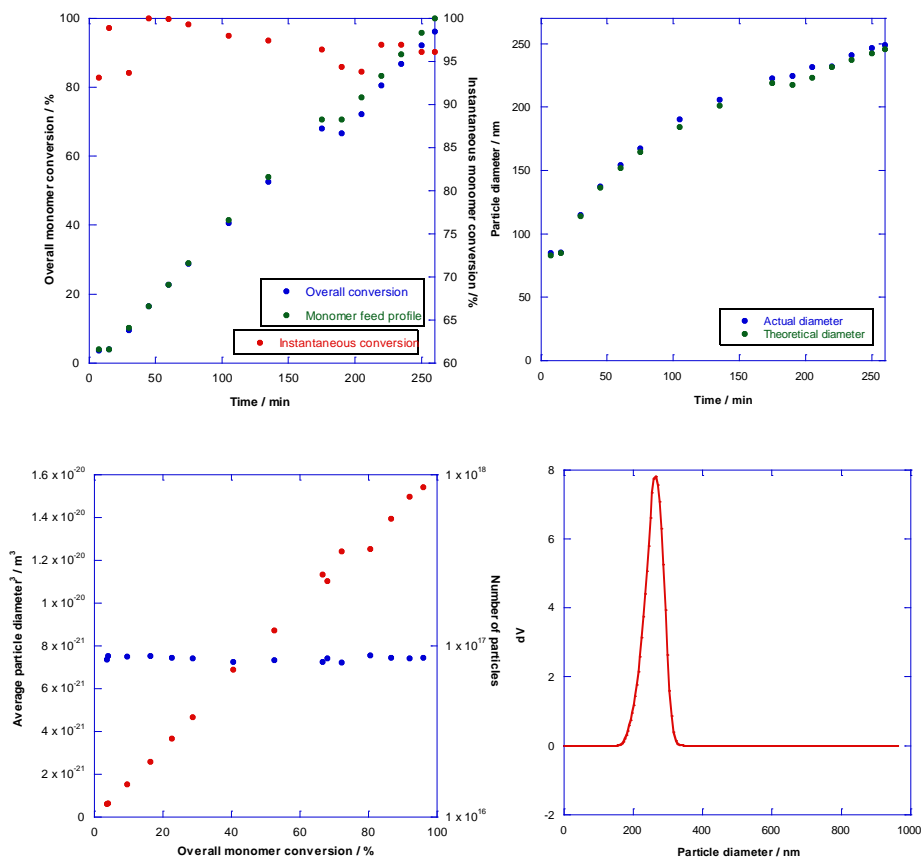




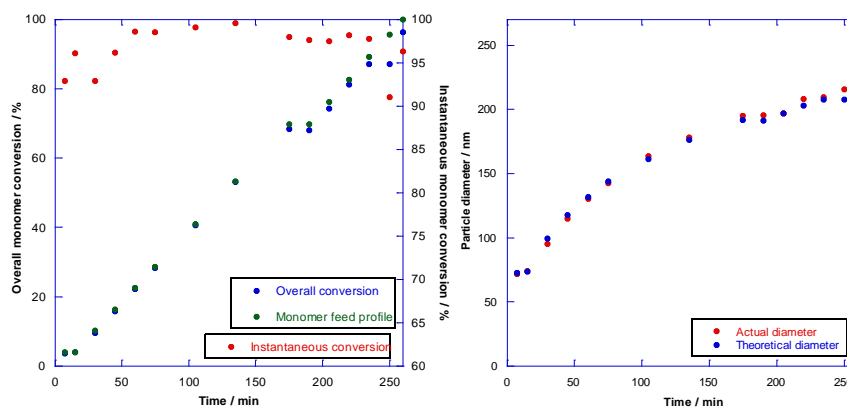
c) Poly[(BA)-*co*-(BMA)] core and poly[(BA)-*co*-(BMA)-*co*-(MAA)] shell copolymers with $T_g = 0/-20$ °C. Core:shell ratio = 70:30

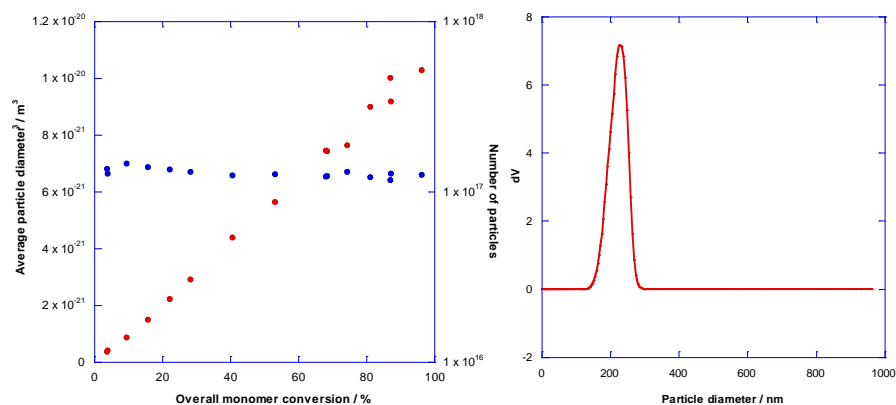


d) Poly[(BA)-*co*-(BMA)] core and poly[(BA)-*co*-(BMA)-*co*-(MAA)] shell copolymers with $T_g = 0$ °C. Core:shell ratio = 70:30



e) Poly[(BA)-*co*-(BMA)] core and poly[(BA)-*co*-(BMA)-*co*-(MAA)-*co*-(DAAM)] shell copolymers with $T_g = 0/-20$ °C. Core:shell ratio = 70:30

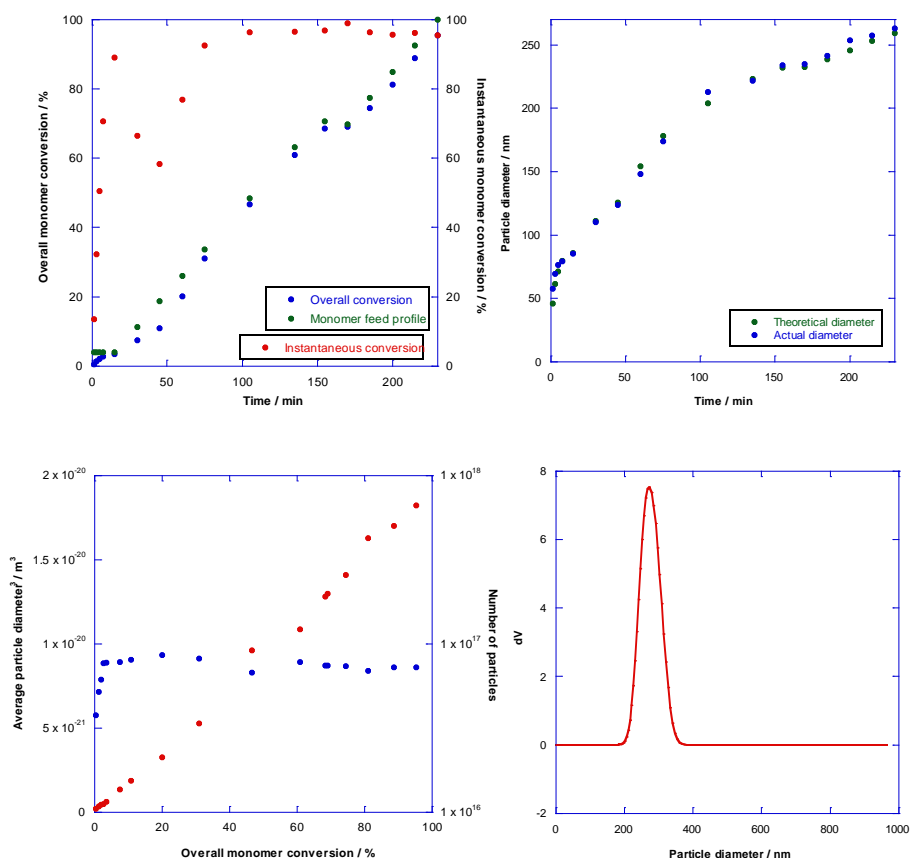




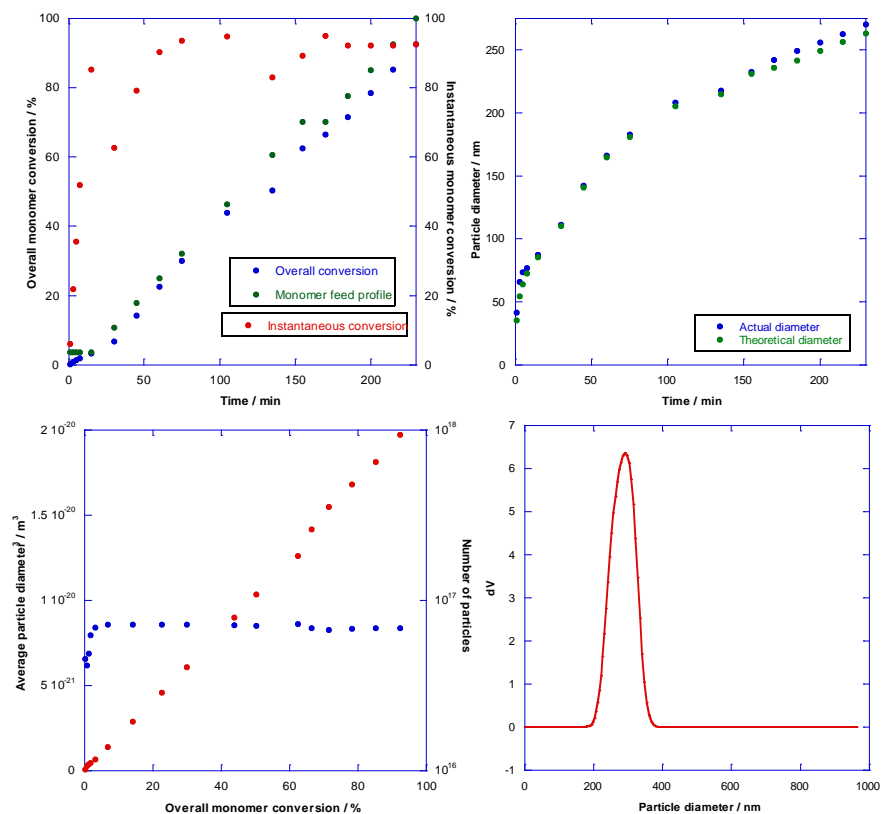
f) Poly[(BA)-*co*-(BMA)] core and shell copolymers with $T_g = 0$ °C; Lutensol T07 added to surfactant feeds. Core:shell ratio = 70:30

[See Figure 4.11]

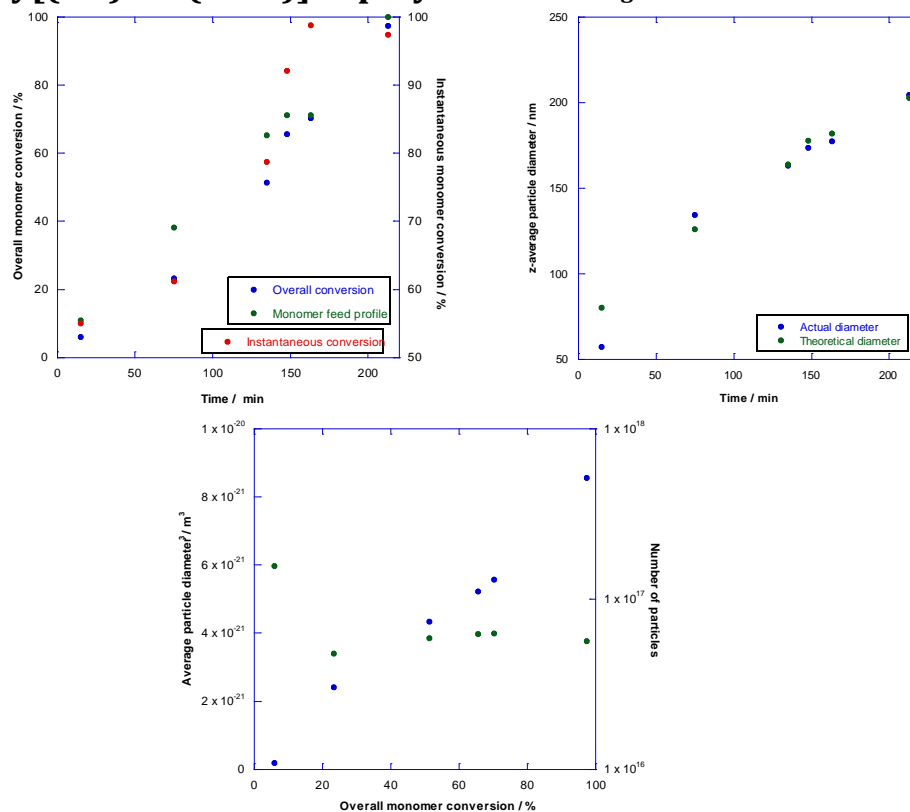
g) Poly[(BA)-*co*-(BMA)] core and poly[(BA)-*co*-(BMA)-*co*-(MAA)-*co*-(DAAM)] shell copolymers with $T_g = 0$ °C; Lutensol T07 added to surfactant feeds. Core:shell ratio = 70:30



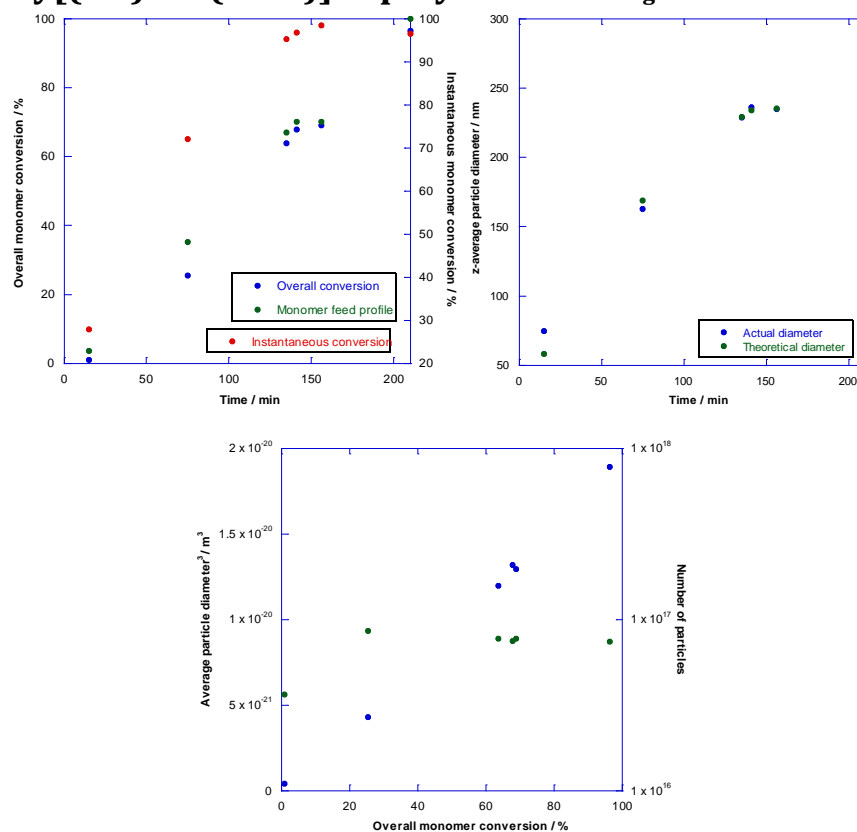
h) Poly[(BA)-*co*-(BMA)] core and poly[(BA)-*co*-(BMA)-*co*-(DAAM)] shell copolymers with $T_g = 0\text{ }^\circ\text{C}$; Lutensol T07 added to surfactant feeds. Core:shell ratio = 70:30



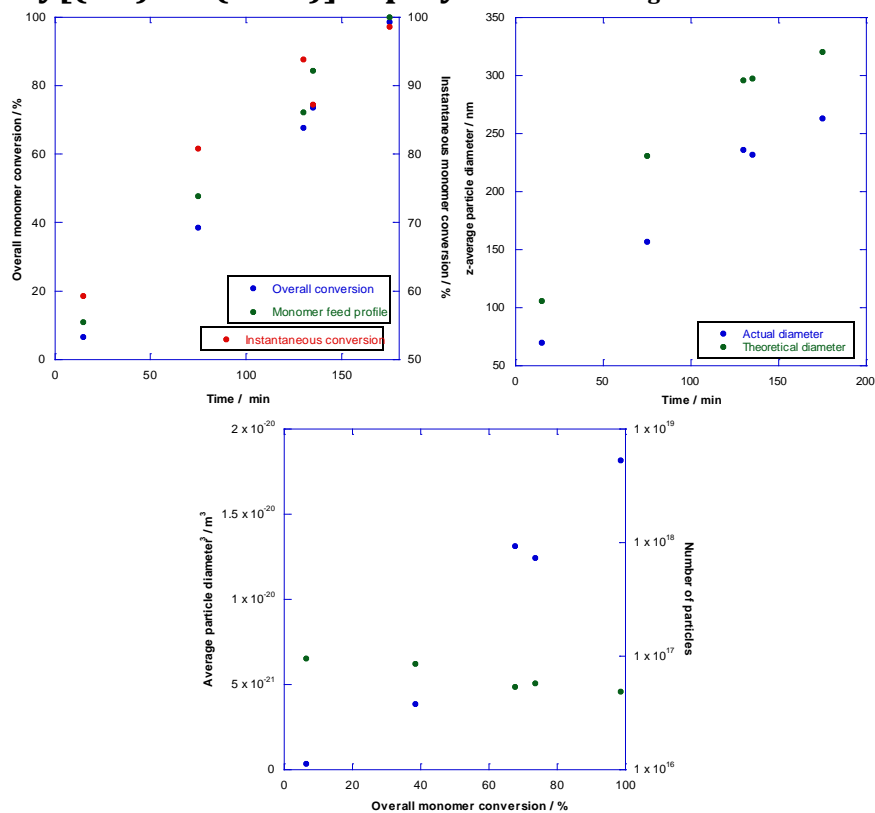
i) Poly[(BA)-*co*-(BMA)] copolymer with $T_g = 10\text{ }^\circ\text{C}$



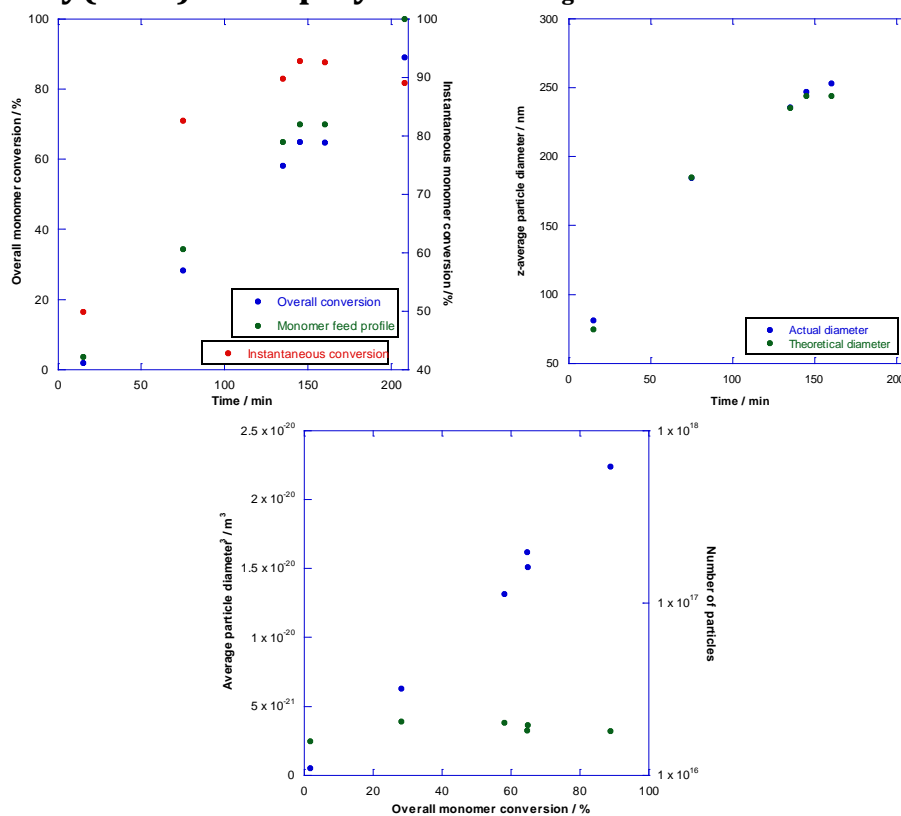
j) Poly[(BA)-*co*-(BMA)] copolymer with $T_g = 20\text{ }^\circ\text{C}$



k) Poly[(BA)-*co*-(BMA)] copolymer with $T_g = 30\text{ }^\circ\text{C}$

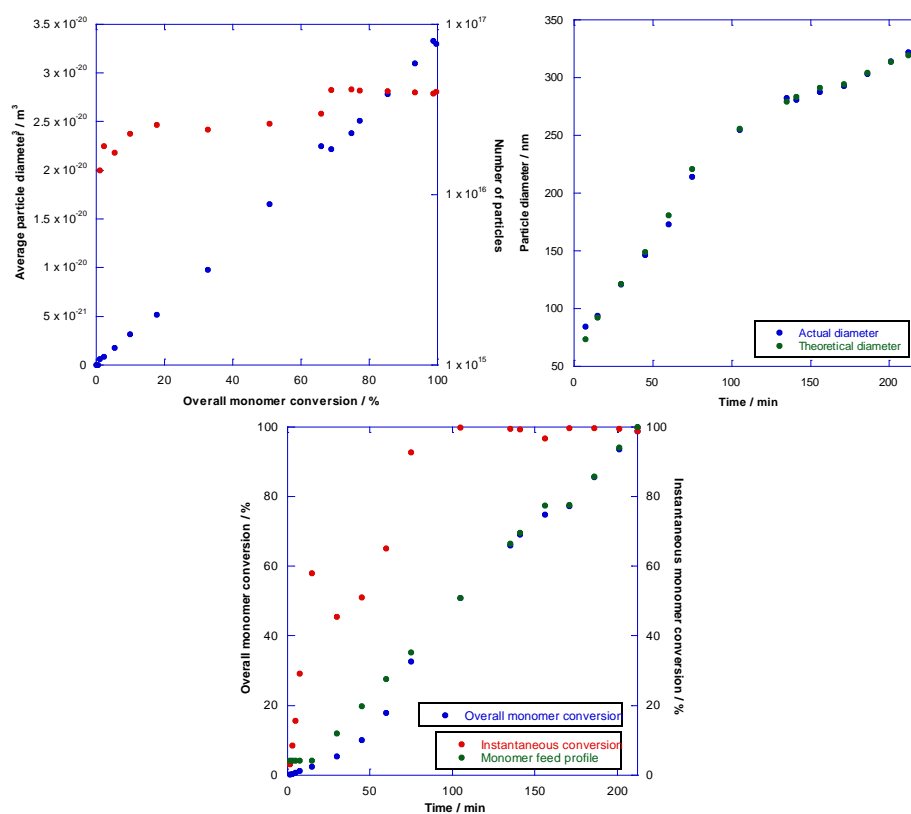


1) Poly(BMA) homopolymer with $T_g = 36\text{ }^\circ\text{C}$

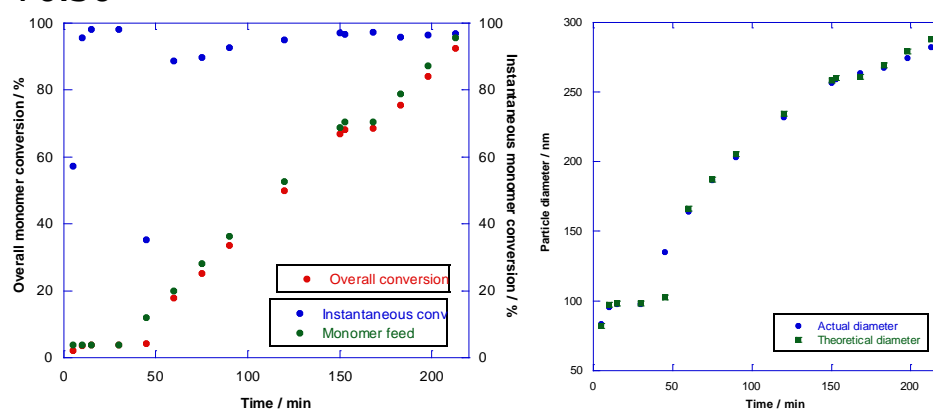


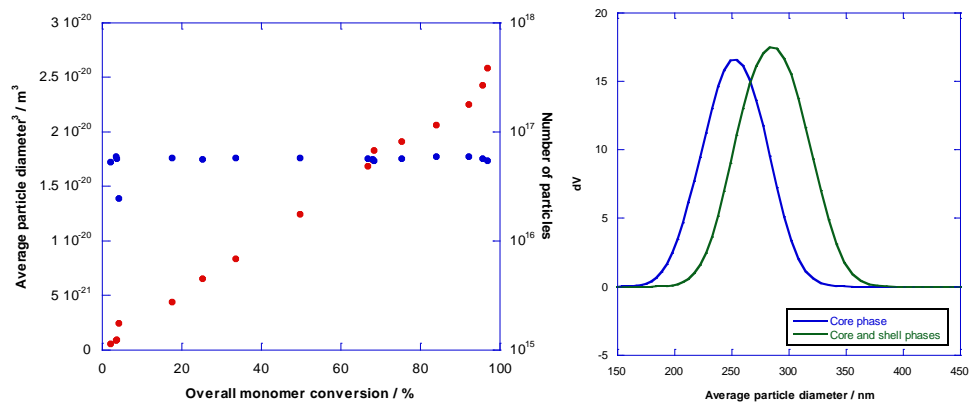
Appendix (ii) – Characterisation plots for soft-soft nanocomposite latexes discussed in Chapter 5

a) Poly[(BA)-*co*-(BMA)] core and shell copolymers with $T_g = 5\text{ }^\circ\text{C}$.
Core:shell ratio = 70:30



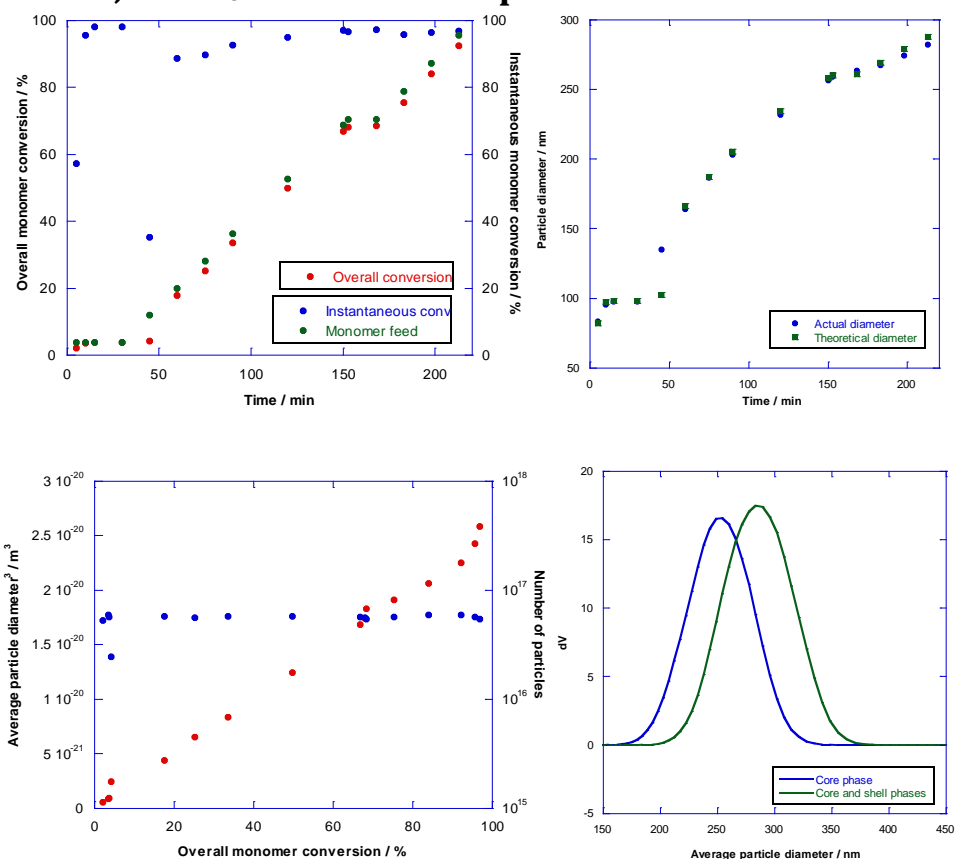
b) Poly[(BA)-*co*-(BMA)] core and poly[(BA)-*co*-(BMA)-*co*-(DAAM)] shell copolymers with $T_g = 5\text{ }^\circ\text{C}$. Core:shell ratio = 70:30



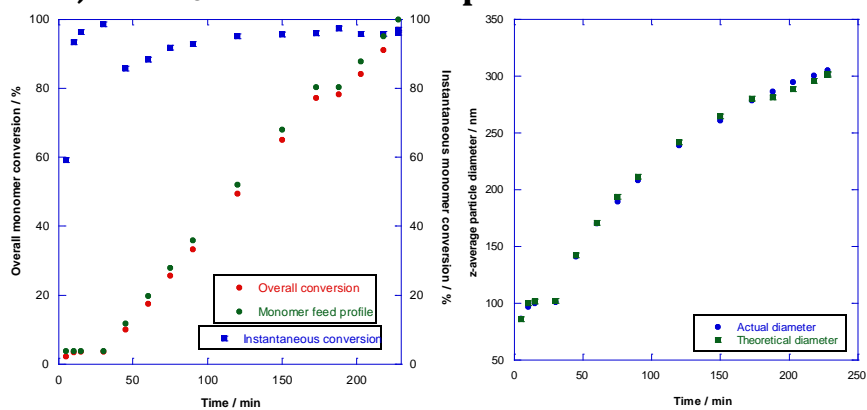


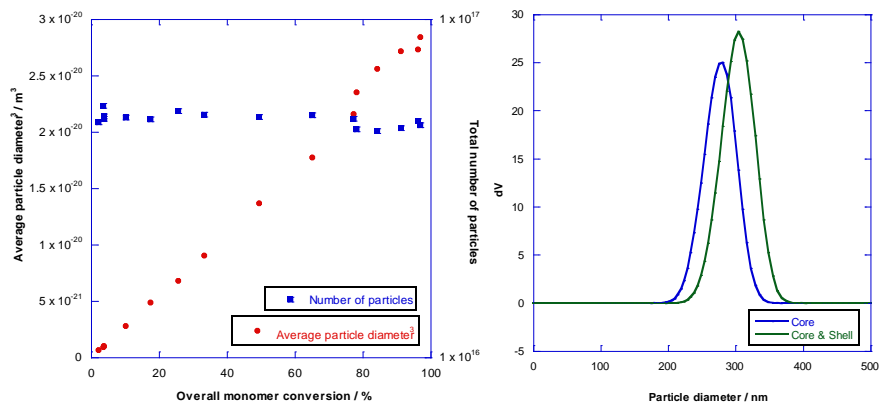
Appendix (iii) – Characterisation plots for soft-soft nanocomposite latexes discussed in Chapter 6

a) Poly[(BA)-*co*-(BMA)] core and poly[(BA)-*co*-(BMA)-*co*-(DAAM)] shell copolymers with $T_g = 5\text{ }^\circ\text{C}$. Core:shell ratio = 70:30; 2 wt% DAAM in shell phase

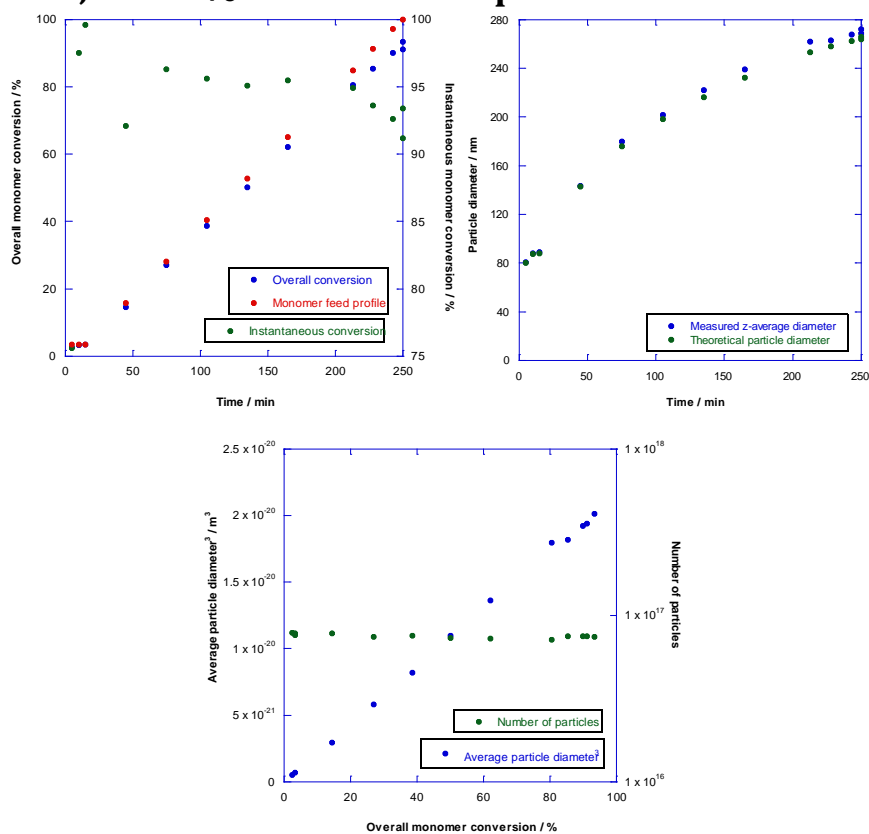


b) Poly[(BA)-*co*-(BMA)] core and poly[(BA)-*co*-(BMA)-*co*-(DAAM)] shell copolymers with $T_g = 5\text{ }^\circ\text{C}$. Core:shell ratio = 80:20; 3 wt% DAAM in shell phase

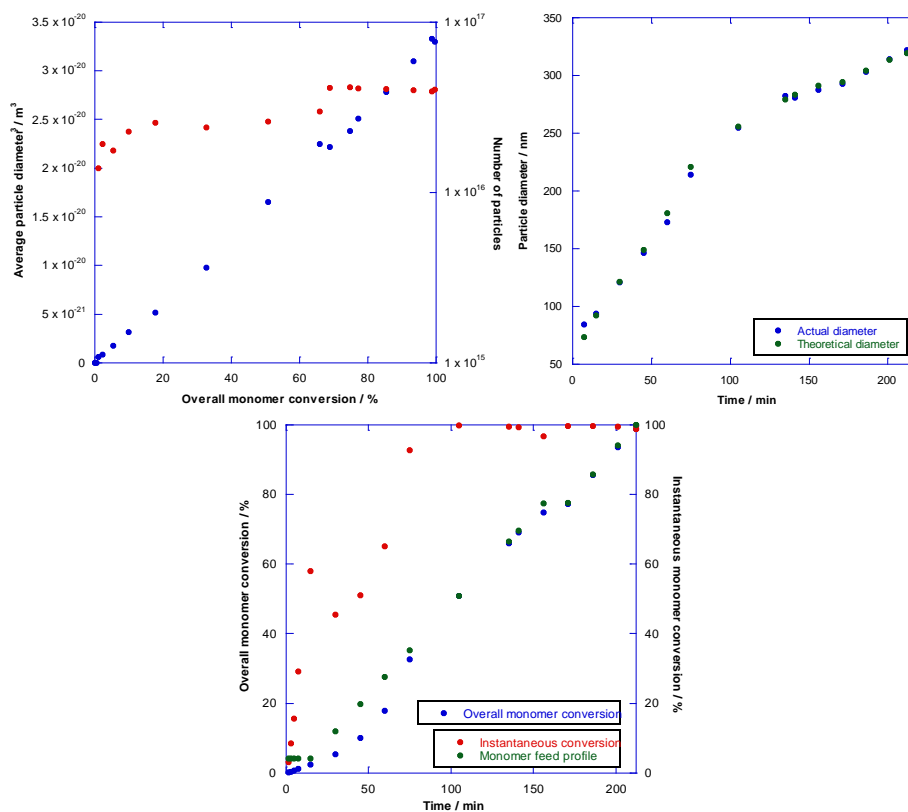




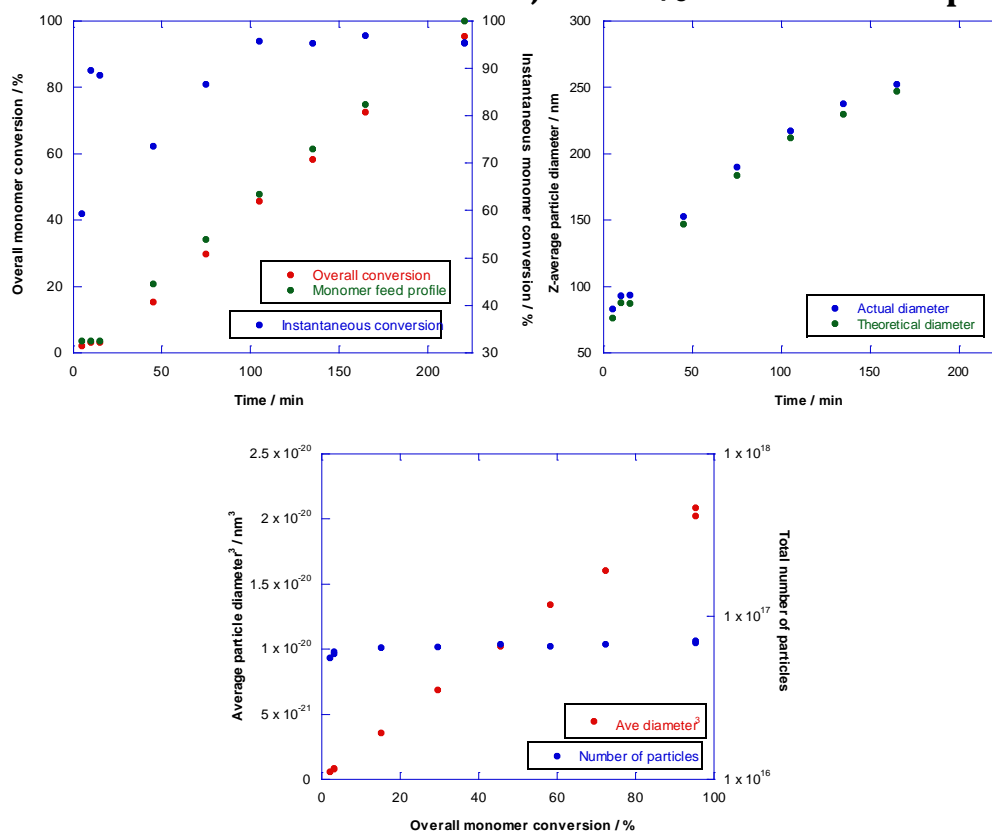
c) Poly[(BA)-*co*-(BMA)] core and poly[(BA)-*co*-(BMA)-*co*-(DAAM)] shell copolymers with $T_g = 5\text{ }^\circ\text{C}$. Core:shell ratio = 90:10; 5.8 wt% DAAM in shell phase



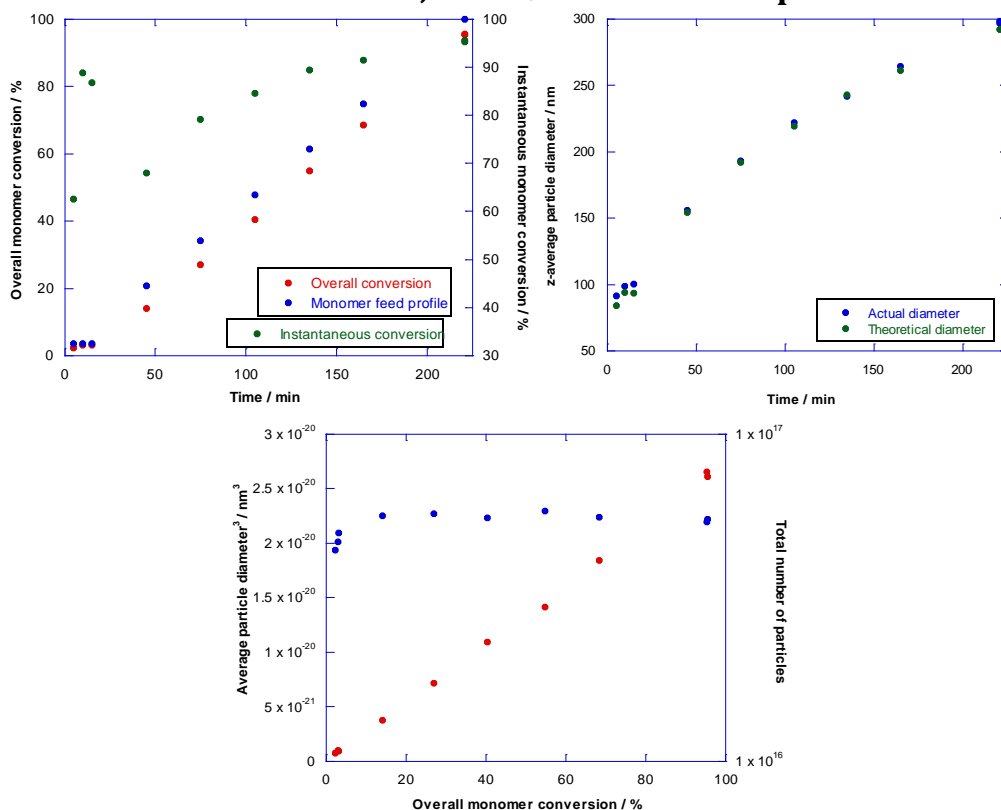
**d) Poly[(BA)-*co*-(BMA)] core copolymer with $T_g = 5\text{ }^\circ\text{C}$.
Core:shell ratio = 100:0**



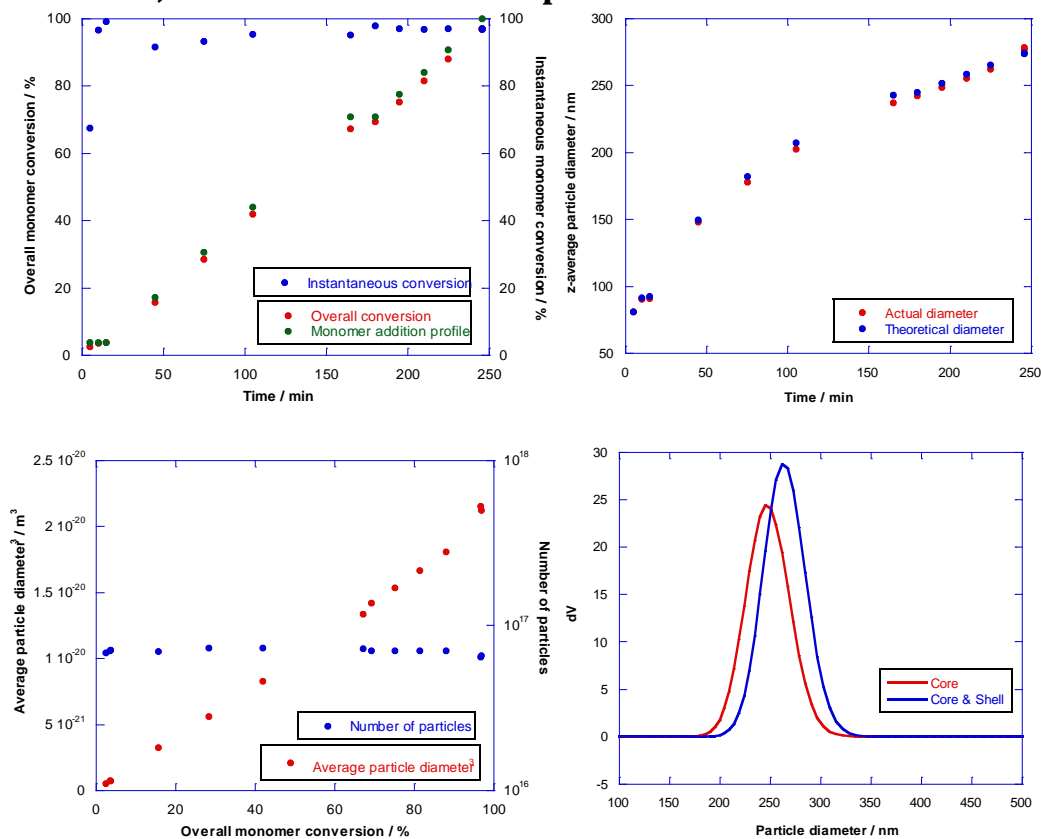
e) Poly[(BA)-*co*-(BMA)-*co*-(DAAM)] shell copolymer with $T_g = 5\text{ }^\circ\text{C}$. Core:shell ratio = 0:100; 0.4 wt% DAAM in shell phase



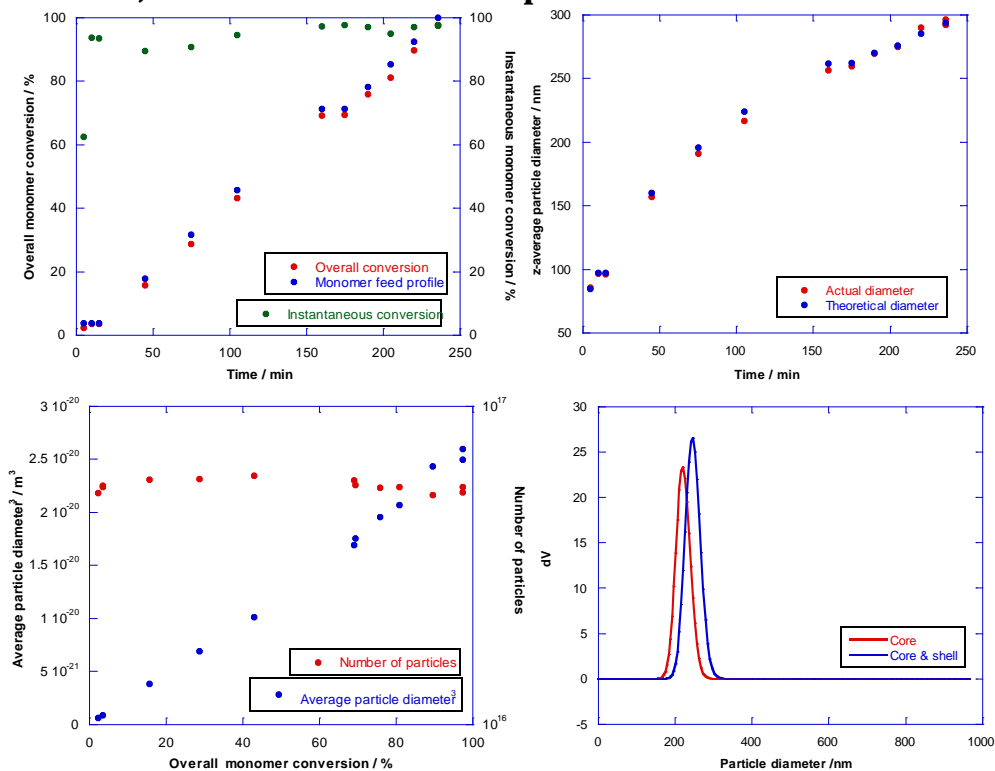
**f) Poly[(BA)-co-(BMA)-co-(DAAM)] shell copolymer with $T_g = 5\text{ }^\circ\text{C}$.
Core:shell ratio = 0:100; 2 wt% DAAM in shell phase**



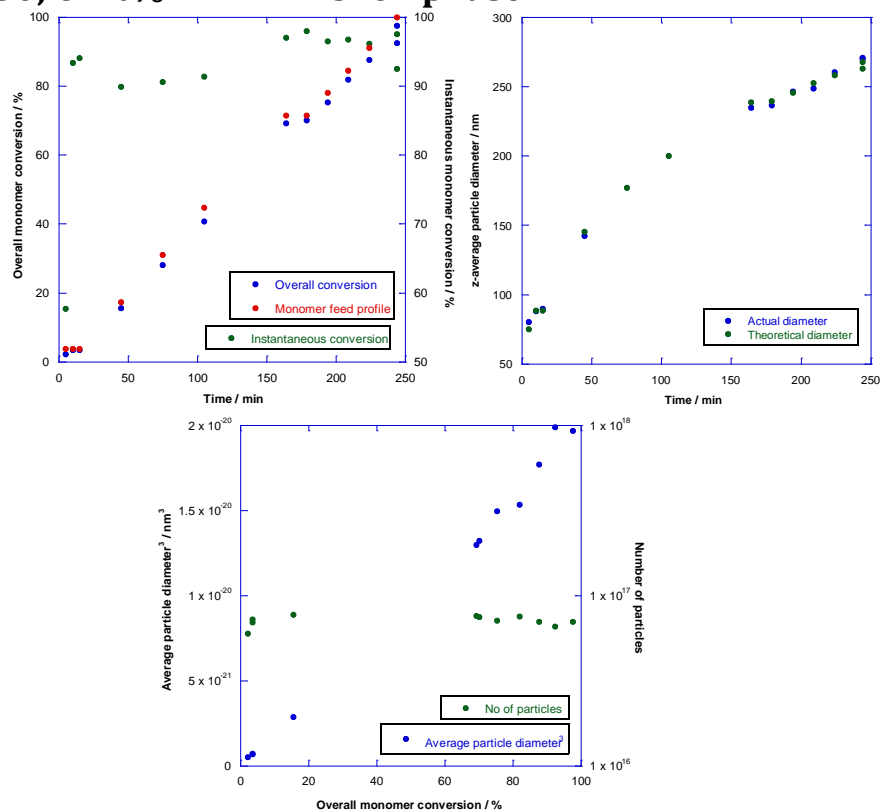
g) Poly[(BA)-co-(BMA)] core and poly[(BA)-co-(BMA)-co-(DAAM)] shell copolymers with $T_g = 5\text{ }^\circ\text{C}$. Core:shell ratio = 70:30; 3 wt% DAAM in shell phase



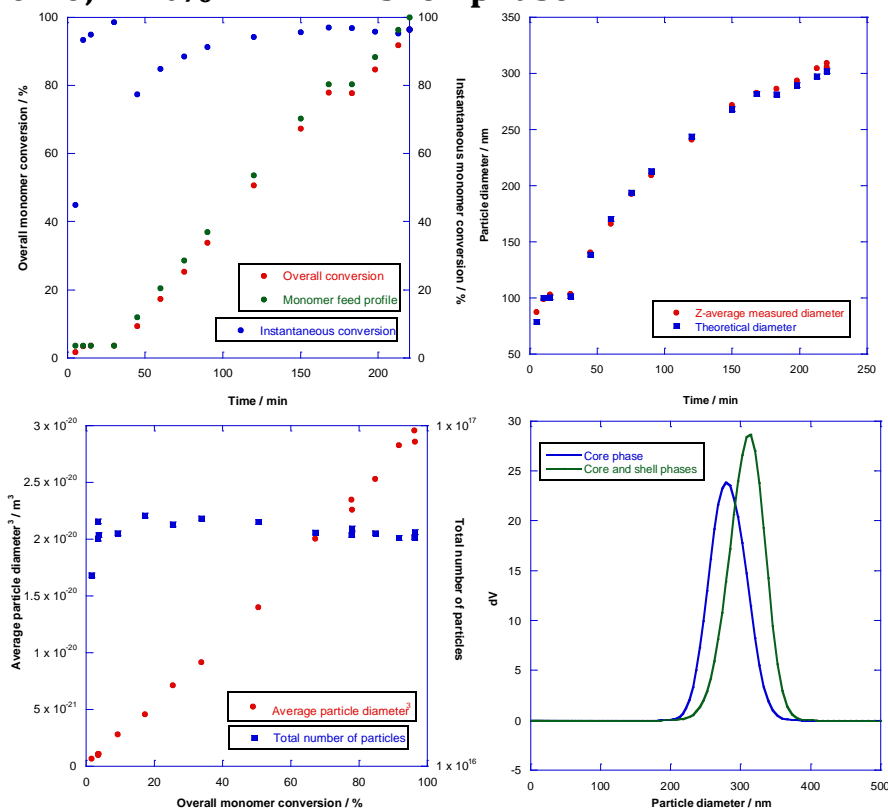
h) Poly[(BA)-*co*-(BMA)] core and poly[(BA)-*co*-(BMA)-*co*-(DAAM)] shell copolymers with $T_g = 5\text{ }^\circ\text{C}$. Core:shell ratio = 70:30; 5 wt% DAAM in shell phase



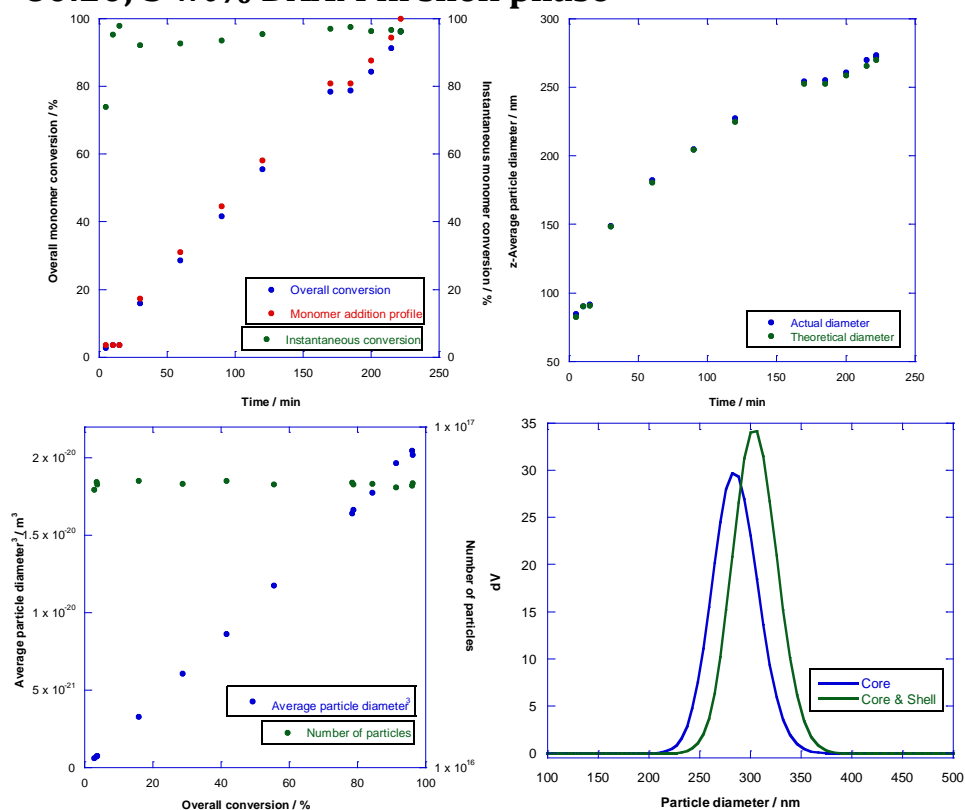
i) Poly[(BA)-*co*-(BMA)] core and poly[(BA)-*co*-(BMA)-*co*-(DAAM)] shell copolymers with $T_g = 5\text{ }^\circ\text{C}$. Core:shell ratio = 70:30; 6 wt% DAAM in shell phase



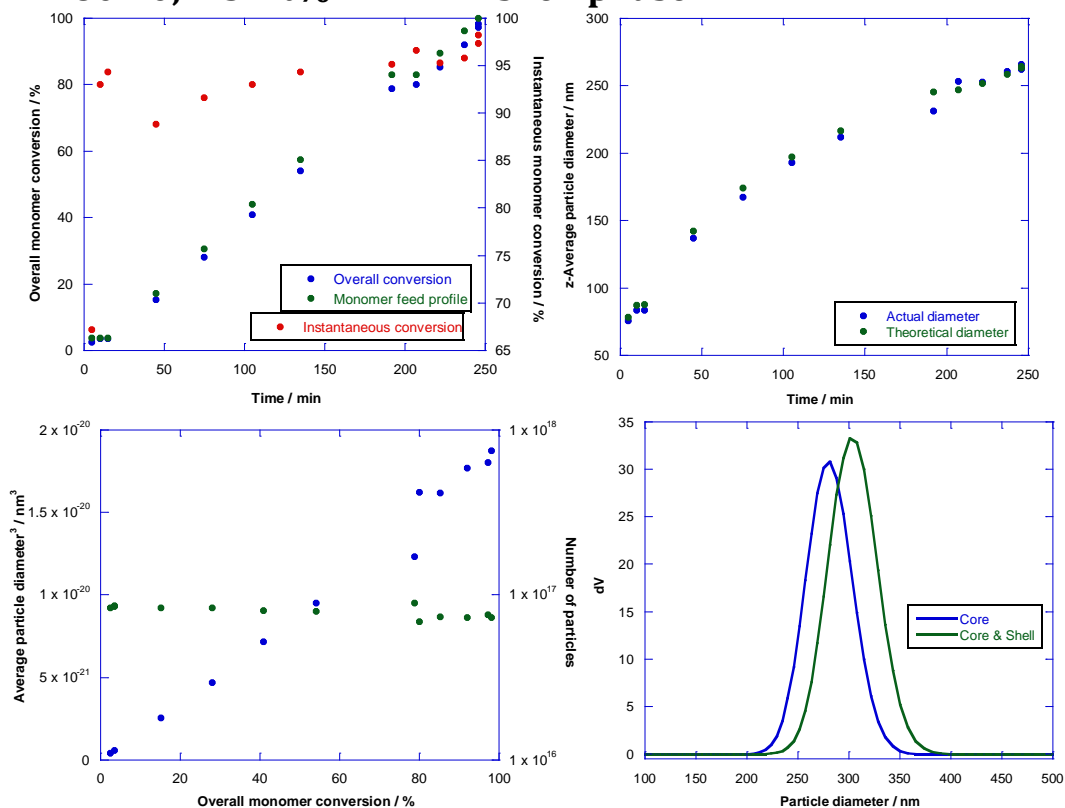
j) Poly[(BA)-co-(BMA)] core and poly[(BA)-co-(BMA)-co-(DAAM)] shell copolymers with $T_g = 5\text{ }^\circ\text{C}$. Core:shell ratio = 80:20; 2 wt% DAAM in shell phase



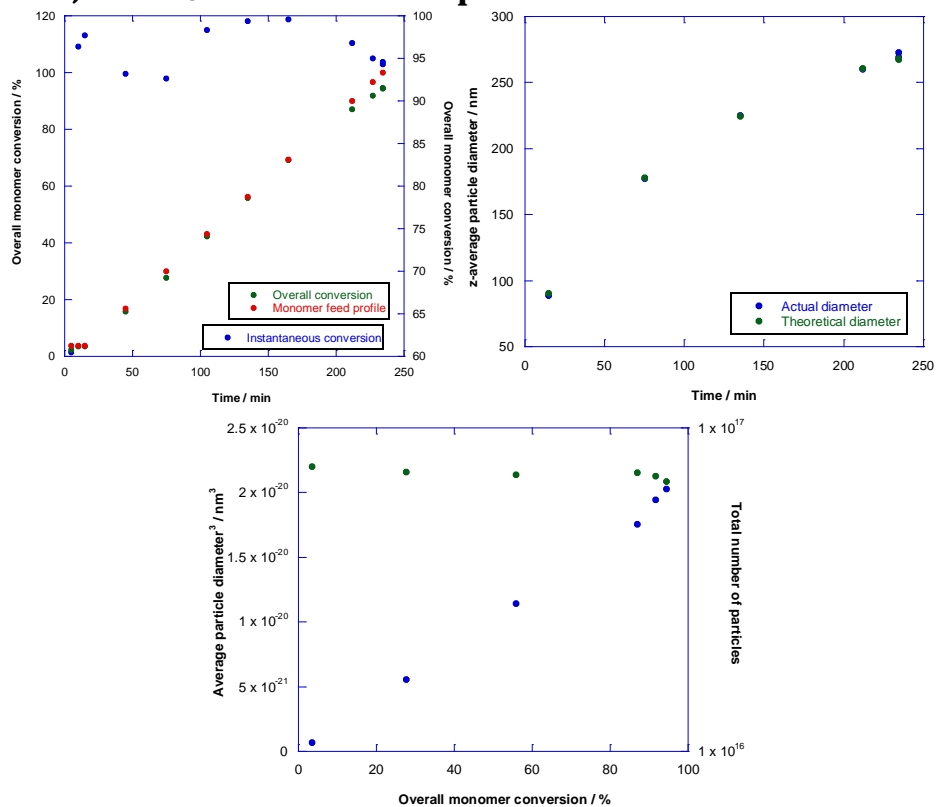
k) Poly[(BA)-co-(BMA)] core and poly[(BA)-co-(BMA)-co-(DAAM)] shell copolymers with $T_g = 5\text{ }^\circ\text{C}$. Core:shell ratio = 80:20; 5 wt% DAAM in shell phase



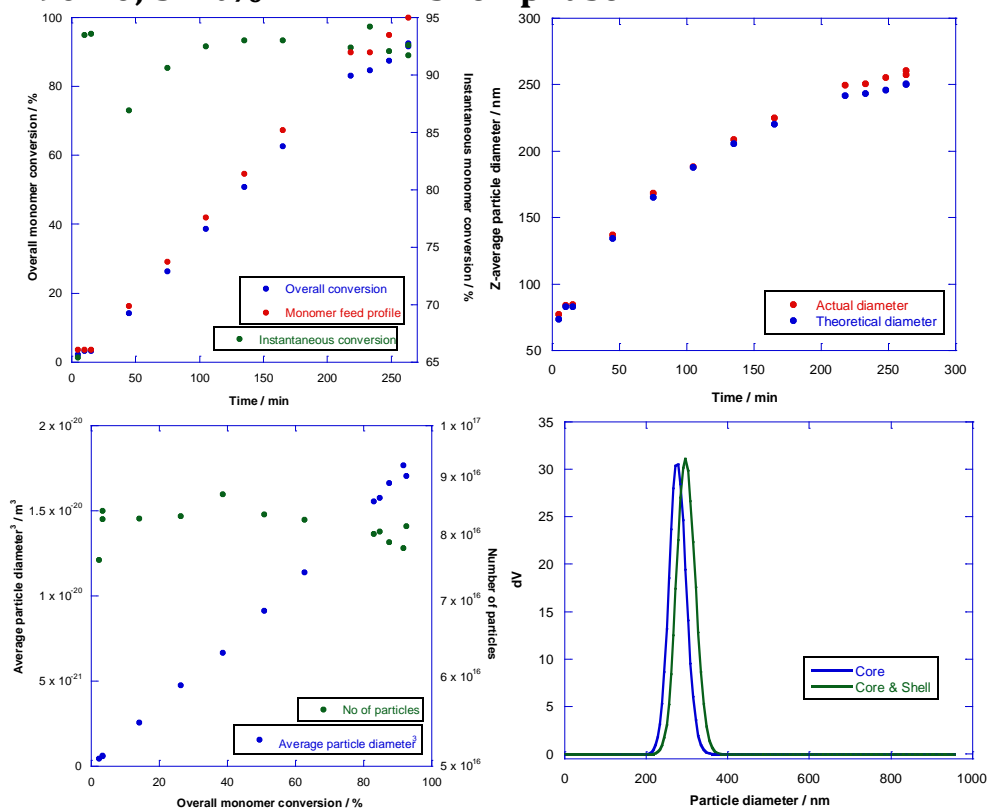
l) Poly[(BA)-*co*-(BMA)] core and poly[(BA)-*co*-(BMA)-*co*-(DAAM)] shell copolymers with $T_g = 5\text{ }^\circ\text{C}$. Core:shell ratio = 80:20; 7.5 wt% DAAM in shell phase



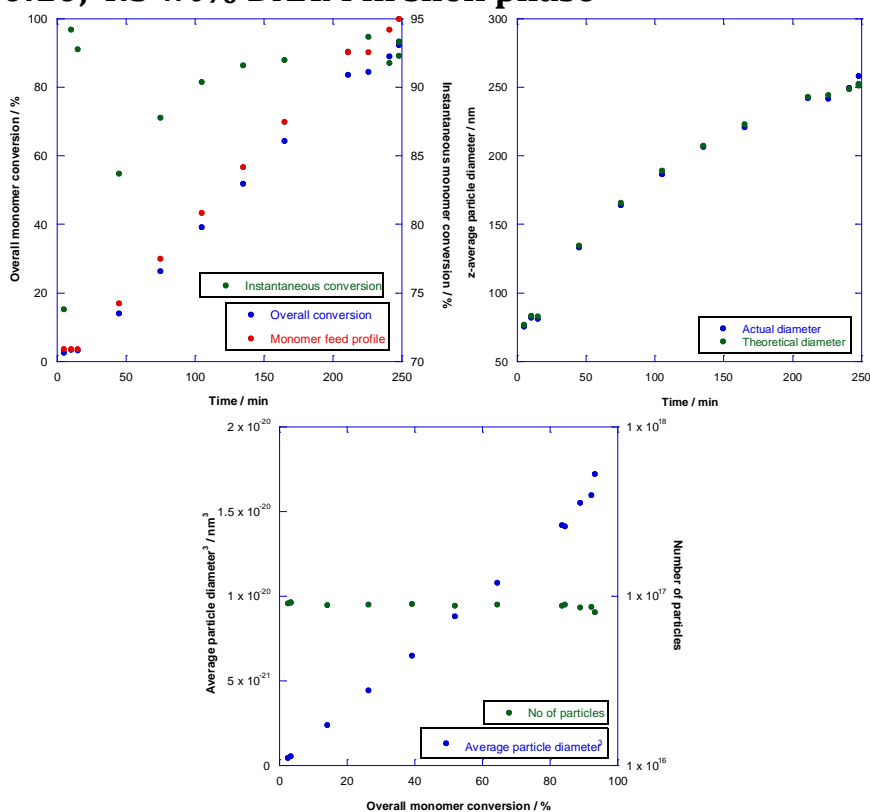
m) Poly[(BA)-*co*-(BMA)] core and poly[(BA)-*co*-(BMA)-*co*-(DAAM)] shell copolymers with $T_g = 5\text{ }^\circ\text{C}$. Core:shell ratio = 90:10; 2 wt% DAAM in shell phase



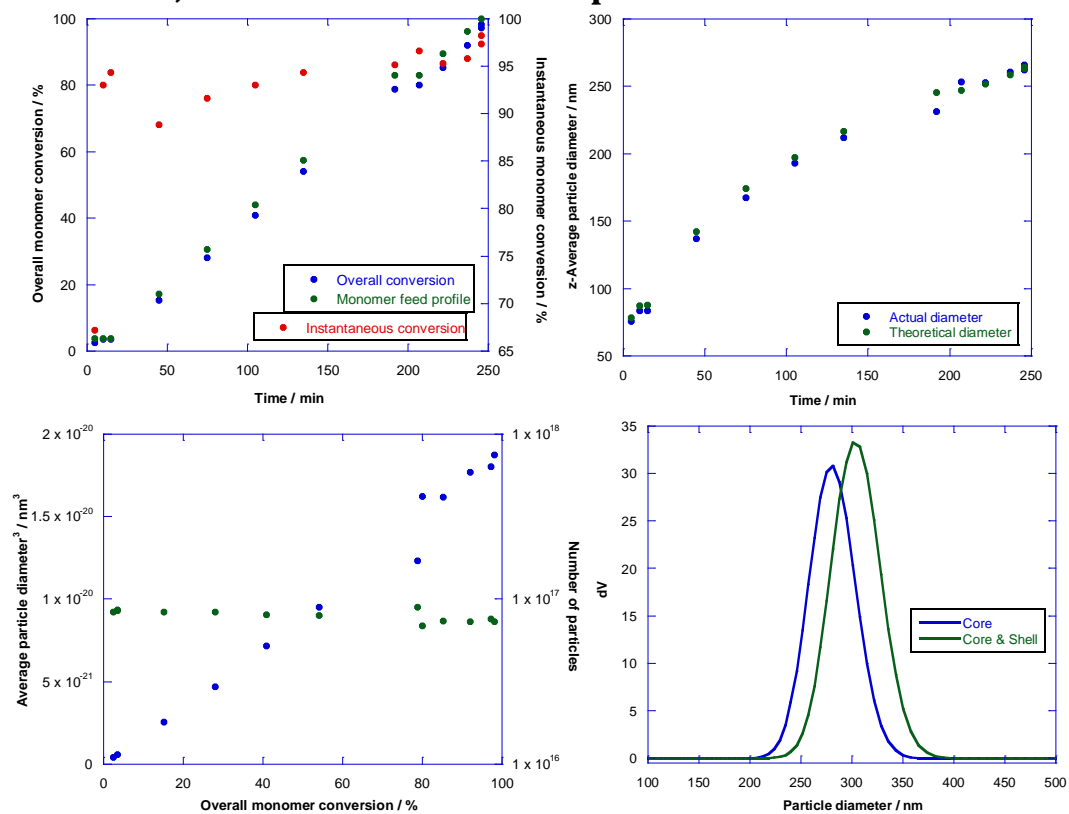
n) Poly[(BA)-*co*-(BMA)] core and poly[(BA)-*co*-(BMA)-*co*-(DAAM)] shell copolymers with $T_g = 5\text{ }^\circ\text{C}$. Core:shell ratio = 90:10; 3 wt% DAAM in shell phase



o) Poly[(BA)-*co*-(BMA)] core and poly[(BA)-*co*-(BMA)-*co*-(DAAM)] shell copolymers with $T_g = 5\text{ }^\circ\text{C}$. Core:shell ratio = 90:10; 4.5 wt% DAAM in shell phase

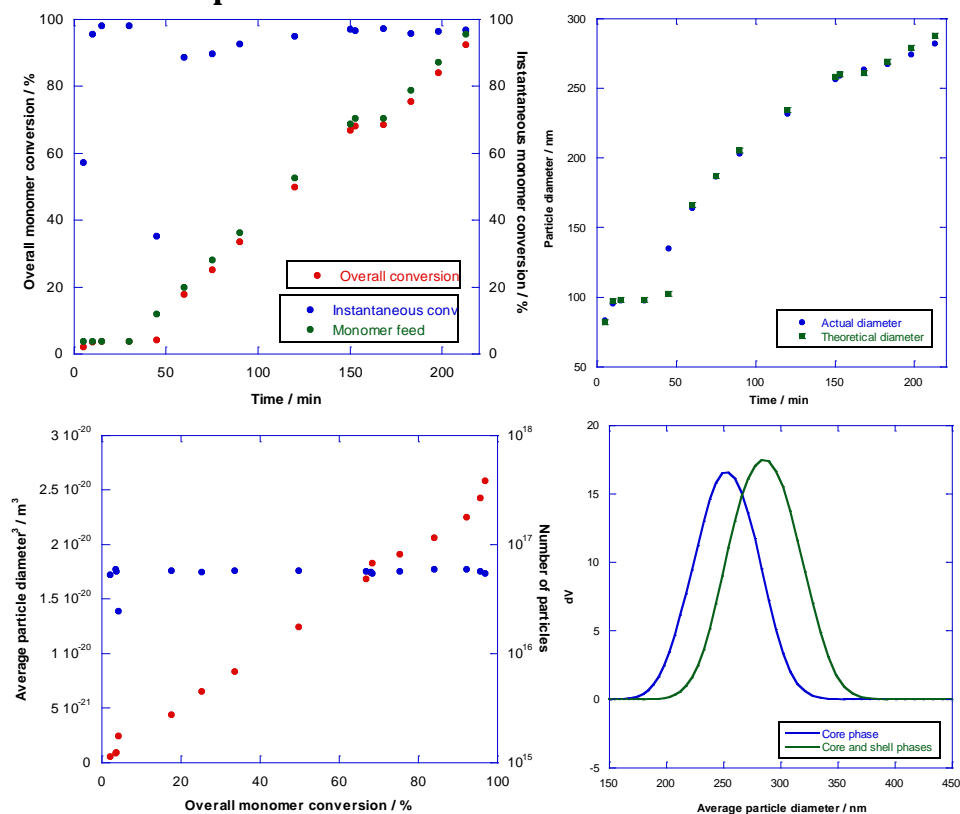


p) Poly[(BA)-*co*-(BMA)] core and poly[(BA)-*co*-(BMA)-*co*-(DAAM)] shell copolymers with $T_g = 5\text{ }^\circ\text{C}$. Core:shell ratio = 90:10; 7.5 wt% DAAM in shell phase

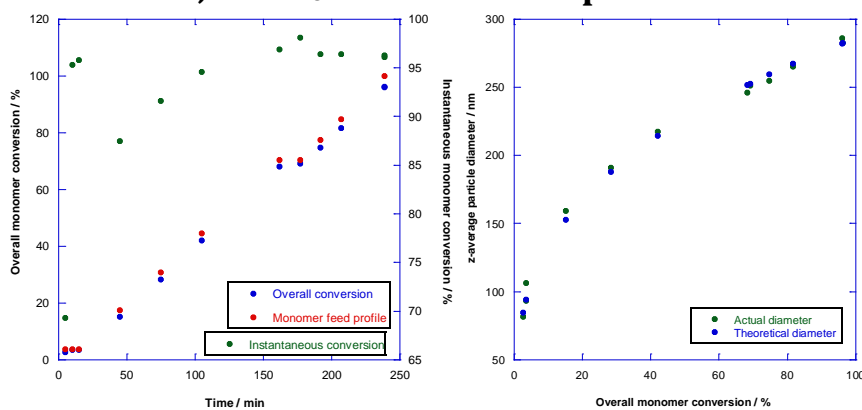


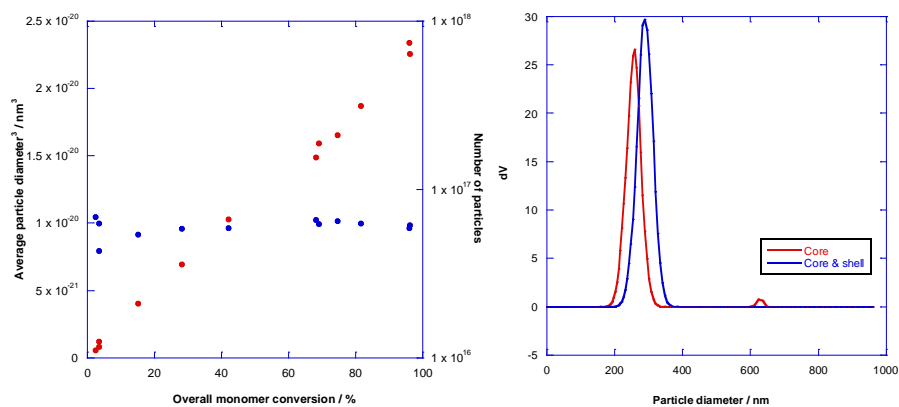
Appendix (iv) – Characterisation plots for soft-soft nanocomposite latexes discussed in Chapter 7

- a) Poly[(BA)-*co*-(BMA)] core and poly[(BA)-*co*-(BMA)-*co*-(DAAM)] shell copolymers with $T_g = 5$ °C. Core:shell ratio = 70:30; 2 wt% DAAM in shell phase

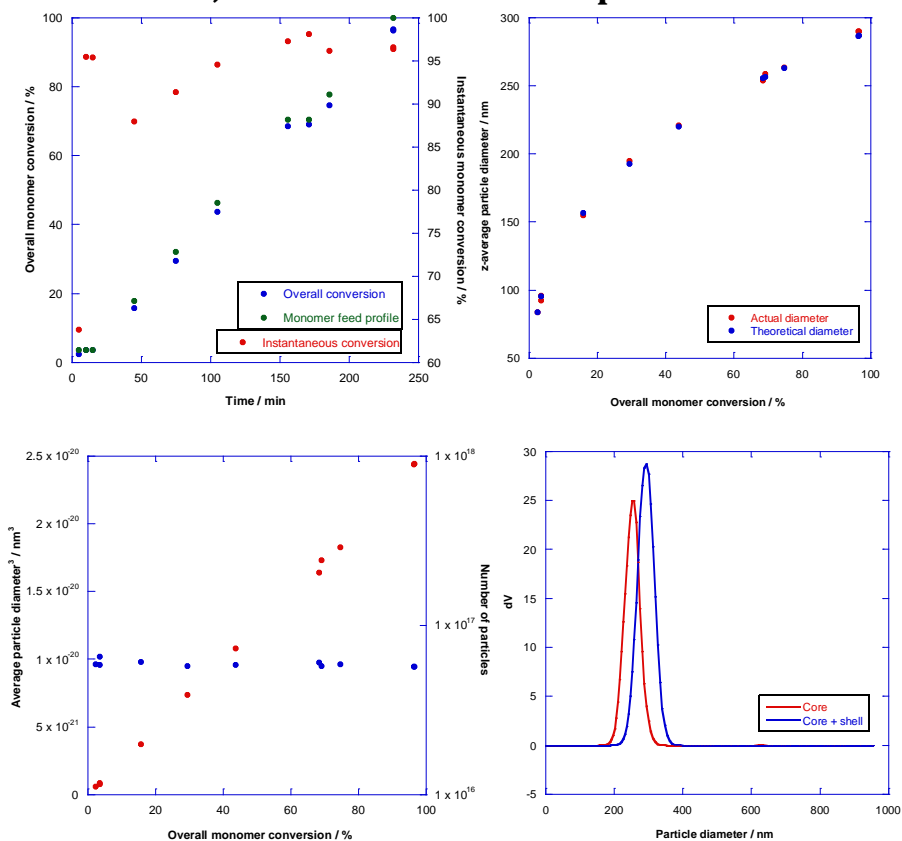


- b) Poly[(BA)-*co*-(BMA)] core and poly[(BA)-*co*-(BMA)-*co*-(DAAM)] shell copolymers with $T_g = 10/5$ °C. Core:shell ratio = 70:30; 2 wt% DAAM in shell phase

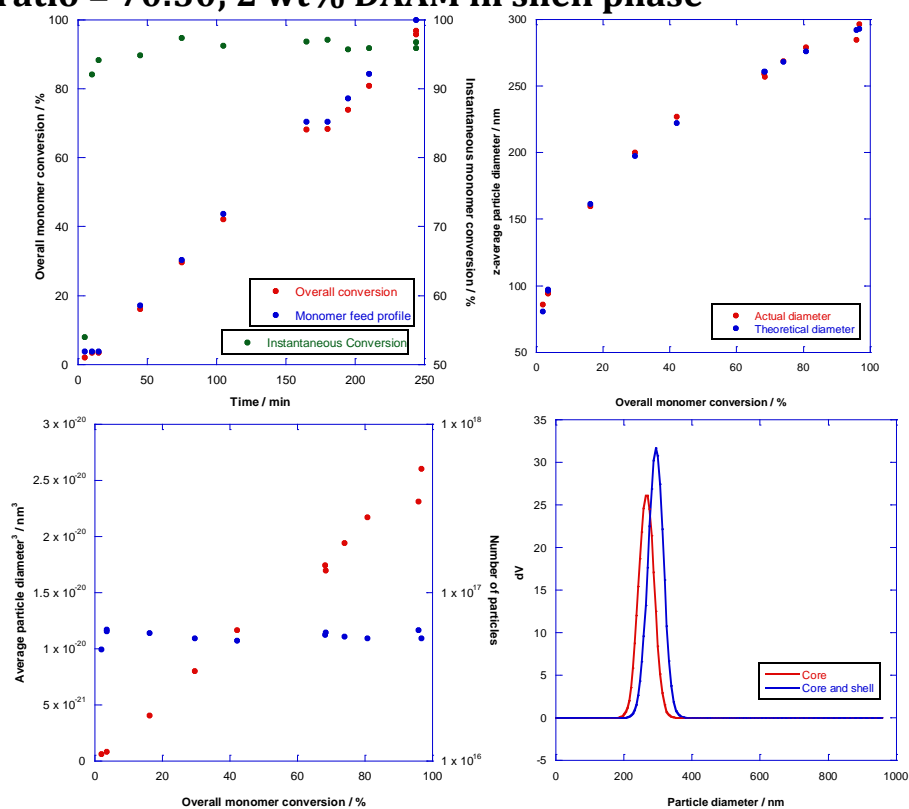




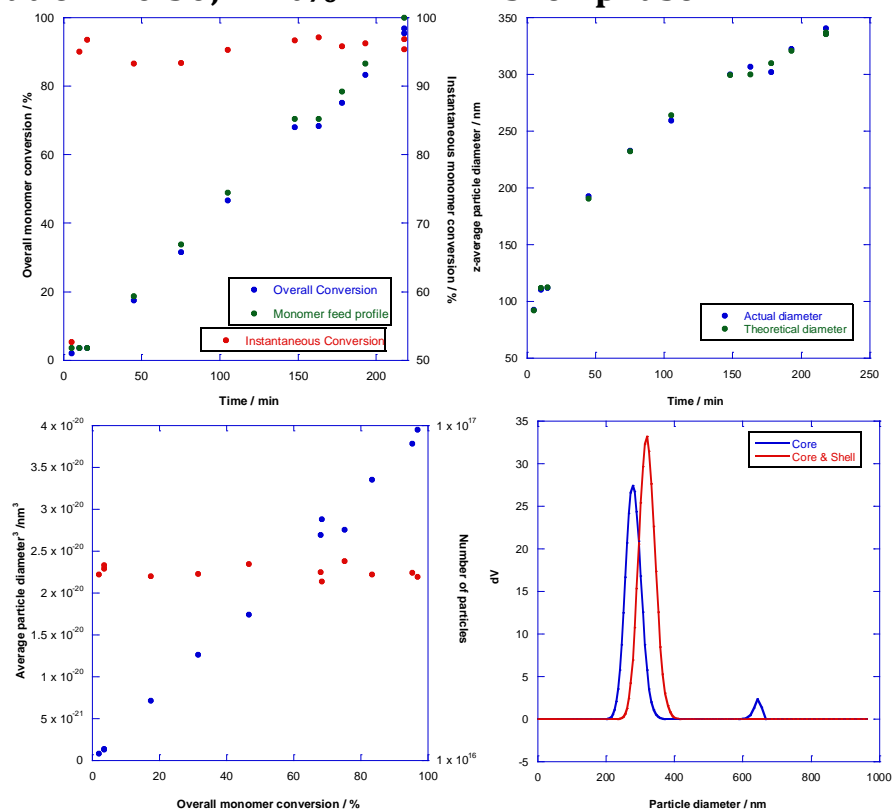
c) Poly[(BA)-*co*-(BMA)] core and poly[(BA)-*co*-(BMA)-*co*-(DAAM)] shell copolymers with $T_g = 15/5$ °C. Core:shell ratio = 70:30; 2 wt% DAAM in shell phase



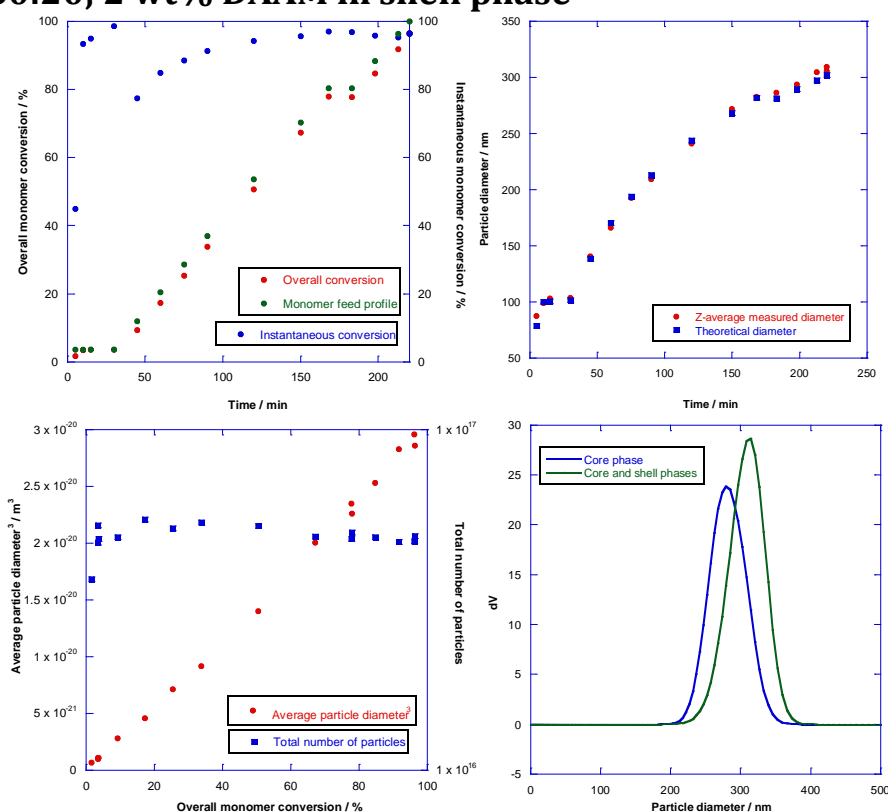
d) Poly[(BA)-*co*-(BMA)] core and poly[(BA)-*co*-(BMA)-*co*-(DAAM)] shell copolymers with $T_g = 20/5$ °C. Core:shell ratio = 70:30; 2 wt% DAAM in shell phase



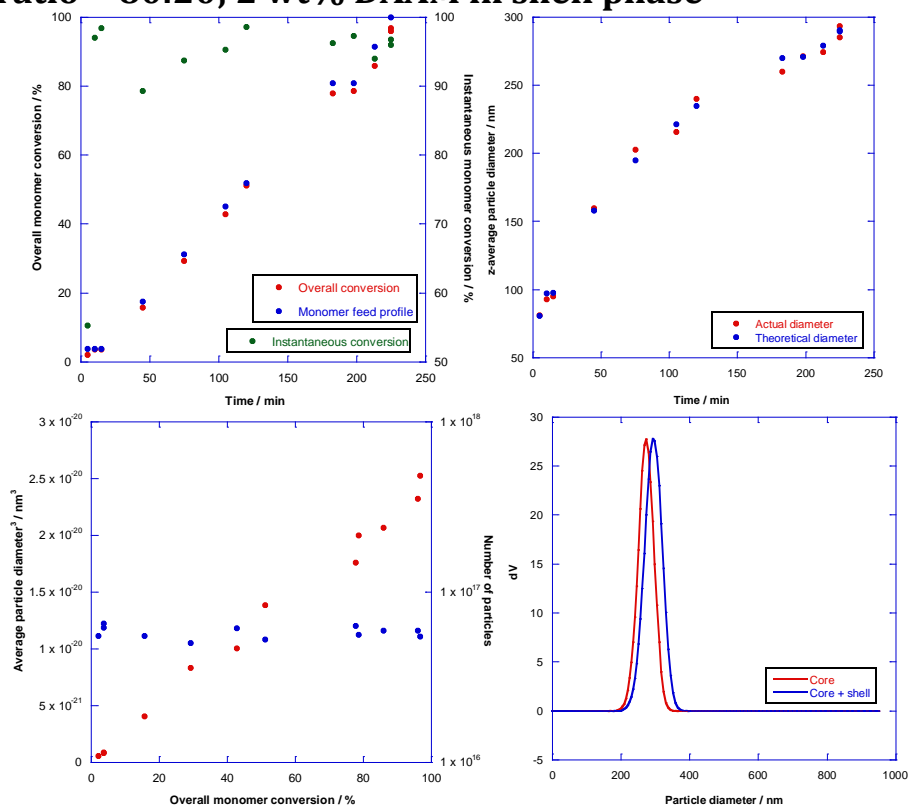
e) Poly[(BA)-*co*-(BMA)] core and poly[(BA)-*co*-(BMA)-*co*-(DAAM)] shell copolymers with $T_g = 25/5$ °C. Core:shell ratio = 70:30; 2 wt% DAAM in shell phase



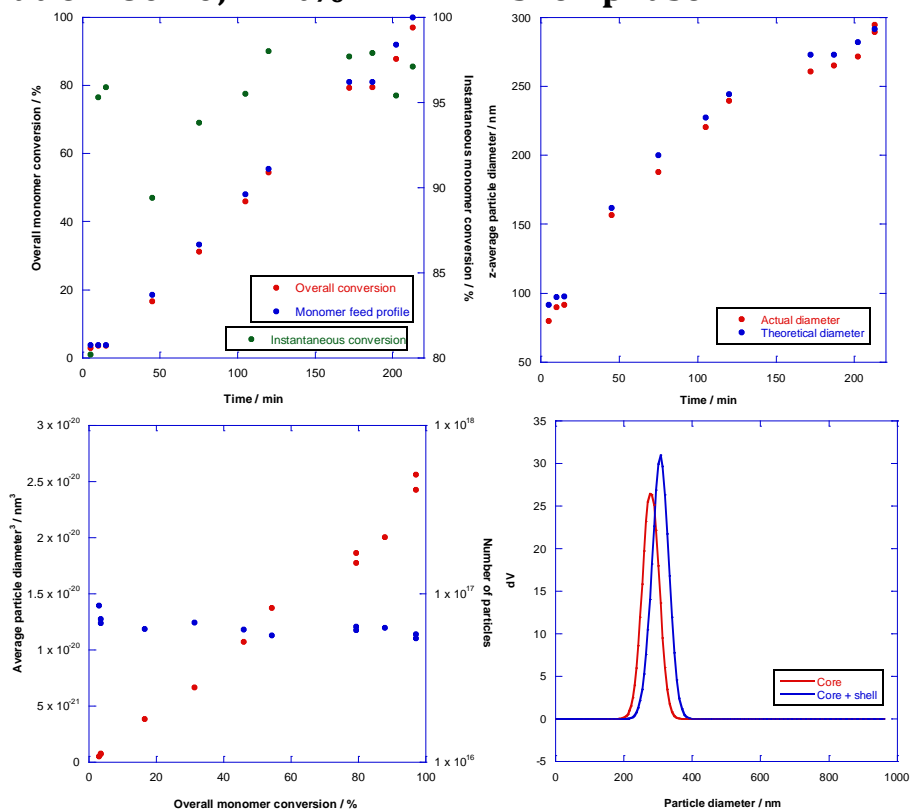
f) Poly[(BA)-*co*-(BMA)] core and poly[(BA)-*co*-(BMA)-*co*-(DAAM)] shell copolymers with $T_g = 5\text{ }^\circ\text{C}$. Core:shell ratio = 80:20; 2 wt% DAAM in shell phase



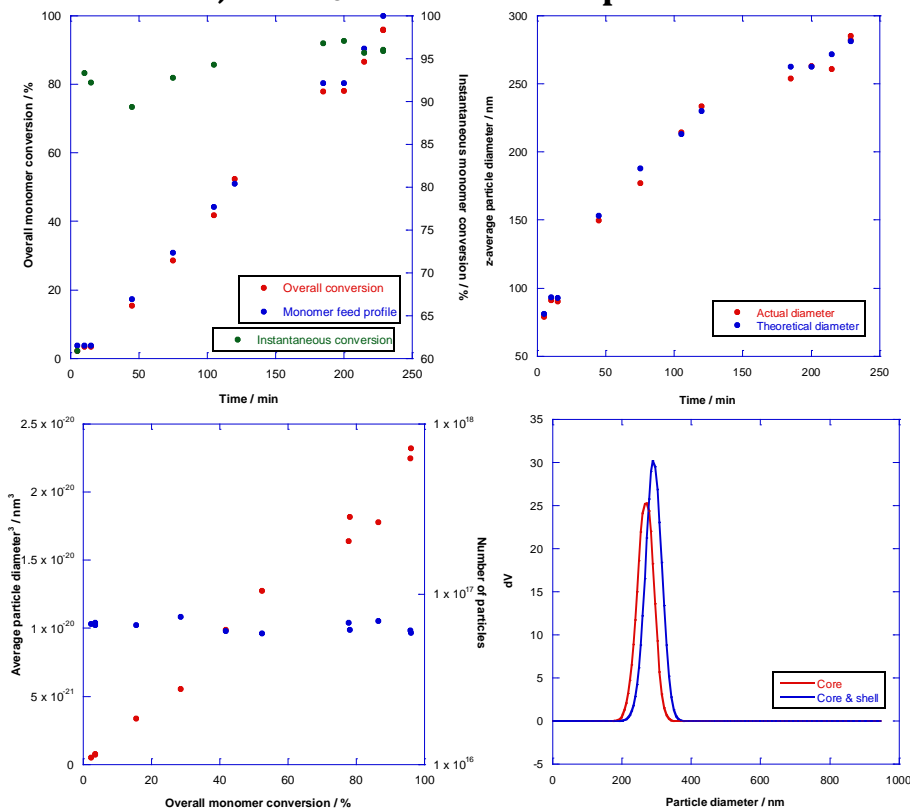
g) Poly[(BA)-*co*-(BMA)] core and poly[(BA)-*co*-(BMA)-*co*-(DAAM)] shell copolymers with $T_g = 10/5\text{ }^\circ\text{C}$. Core:shell ratio = 80:20; 2 wt% DAAM in shell phase



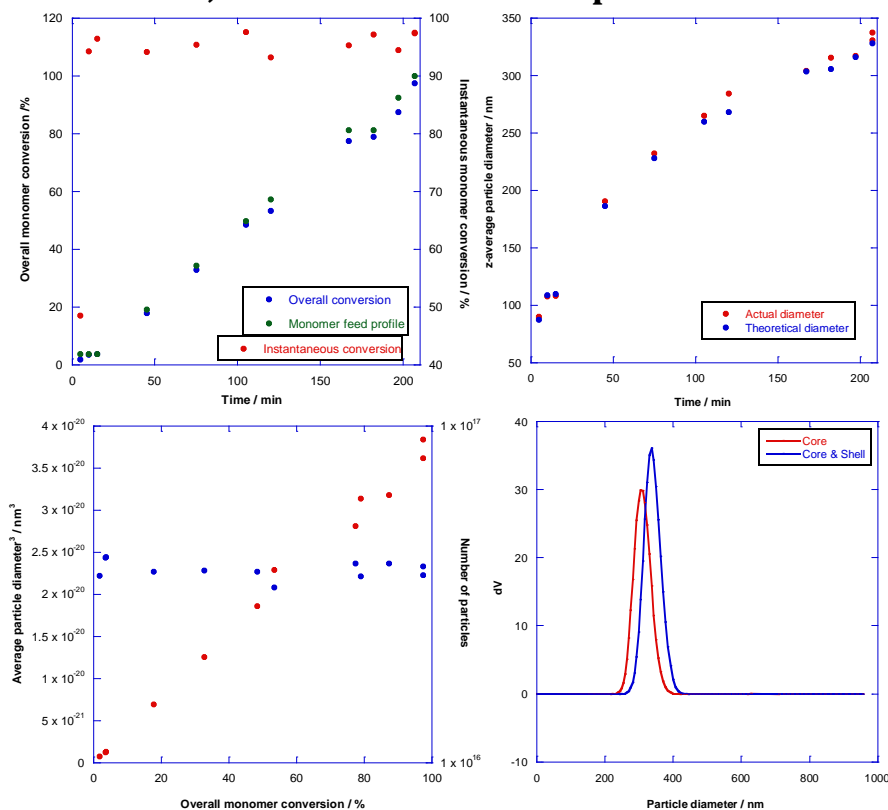
h) Poly[(BA)-*co*-(BMA)] core and poly[(BA)-*co*-(BMA)-*co*-(DAAM)] shell copolymers with $T_g = 15/5$ °C. Core:shell ratio = 80:20; 2 wt% DAAM in shell phase



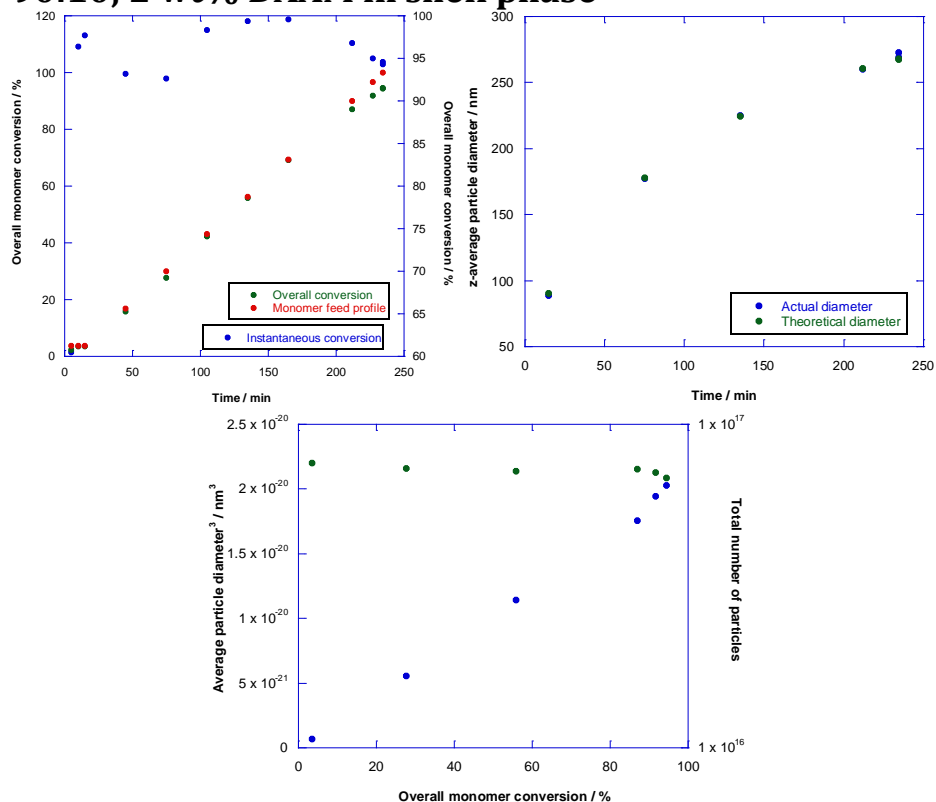
i) Poly[(BA)-*co*-(BMA)] core and poly[(BA)-*co*-(BMA)-*co*-(DAAM)] shell copolymers with $T_g = 20/5$ °C. Core:shell ratio = 80:20; 2 wt% DAAM in shell phase



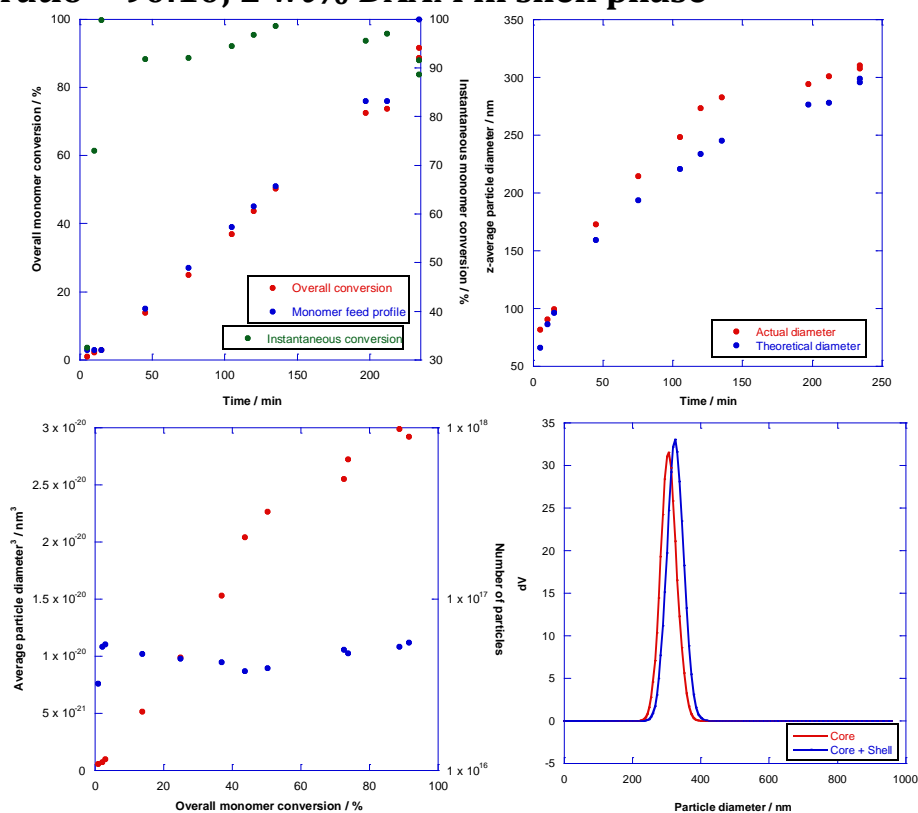
j) Poly[(BA)-*co*-(BMA)] core and poly[(BA)-*co*-(BMA)-*co*-(DAAM)] shell copolymers with $T_g = 25/5$ °C. Core:shell ratio = 80:20; 2 wt% DAAM in shell phase



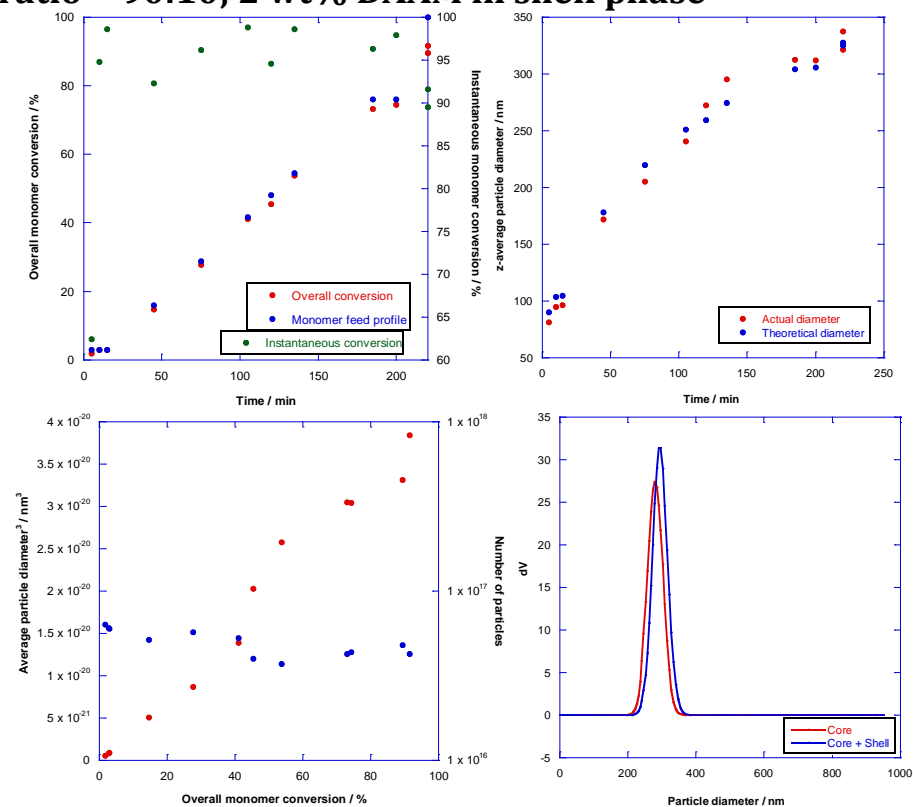
k) Poly[(BA)-*co*-(BMA)] core and poly[(BA)-*co*-(BMA)-*co*-(DAAM)] shell copolymers with $T_g = 5$ °C. Core:shell ratio = 90:10; 2 wt% DAAM in shell phase



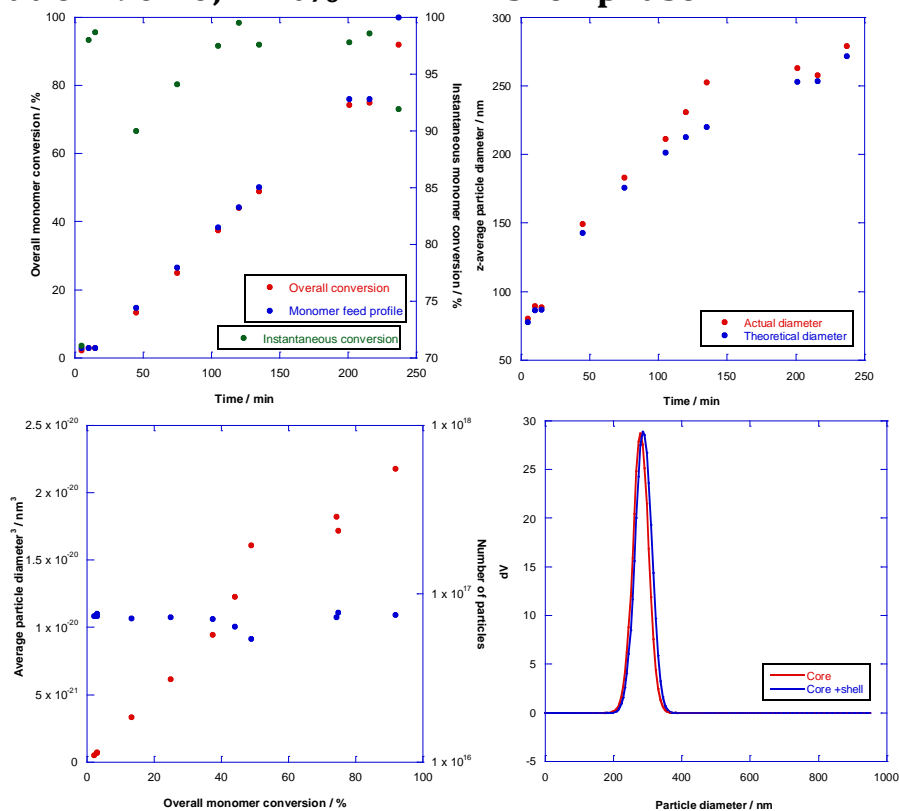
l) Poly[(BA)-*co*-(BMA)] core and poly[(BA)-*co*-(BMA)-*co*-(DAAM)] shell copolymers with $T_g = 10/5$ °C. Core:shell ratio = 90:10; 2 wt% DAAM in shell phase



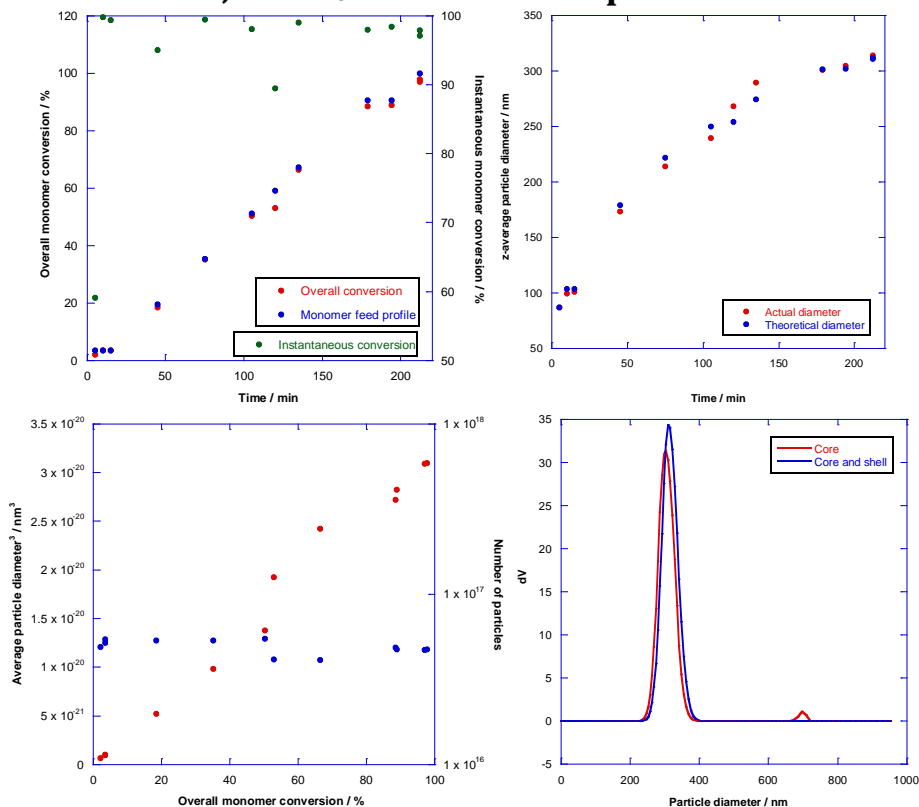
m) Poly[(BA)-*co*-(BMA)] core and poly[(BA)-*co*-(BMA)-*co*-(DAAM)] shell copolymers with $T_g = 15/5$ °C. Core:shell ratio = 90:10; 2 wt% DAAM in shell phase



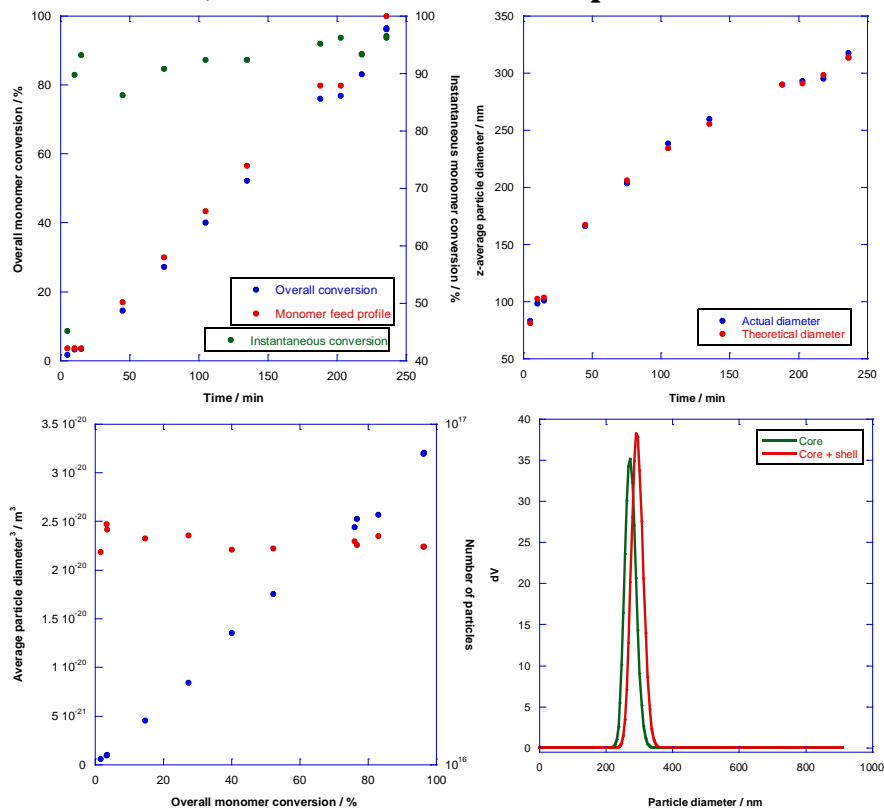
n) Poly[(BA)-*co*-(BMA)] core and poly[(BA)-*co*-(BMA)-*co*-(DAAM)] shell copolymers with $T_g = 20/5$ °C. Core:shell ratio = 90:10; 2 wt% DAAM in shell phase



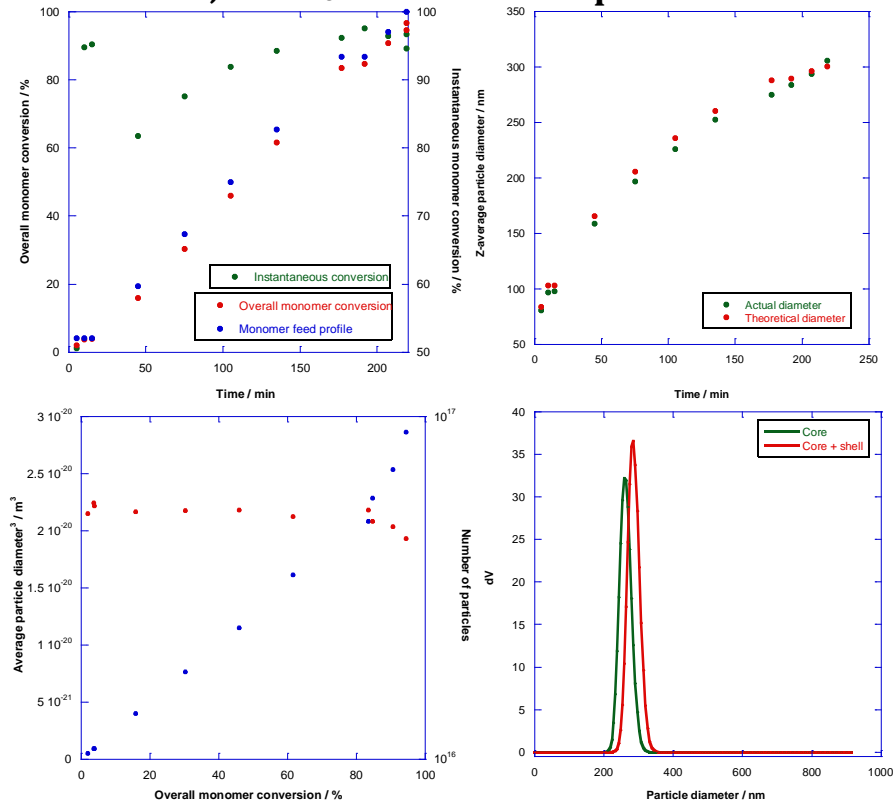
o) Poly[(BA)-*co*-(BMA)] core and poly[(BA)-*co*-(BMA)-*co*-(DAAM)] shell copolymers with $T_g = 25/5$ °C. Core:shell ratio = 90:10; 2 wt% DAAM in shell phase



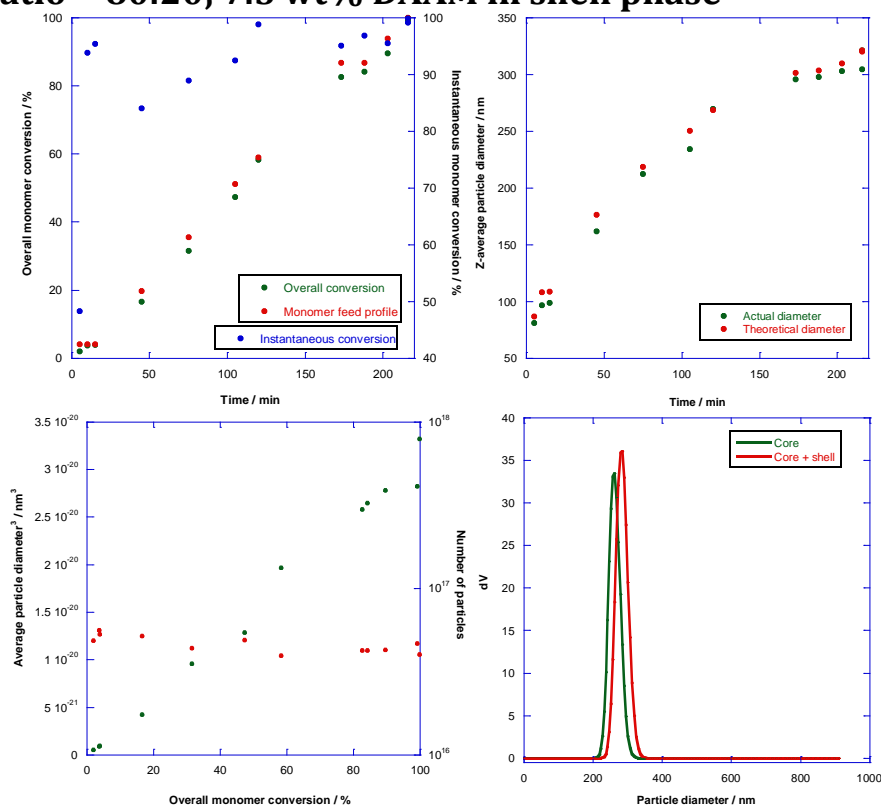
p) Poly[(BA)-*co*-(BMA)] core and poly[(BA)-*co*-(BMA)-*co*-(DAAM)] shell copolymers with $T_g = 20/5$ °C. Core:shell ratio = 80:20; 3 wt% DAAM in shell phase



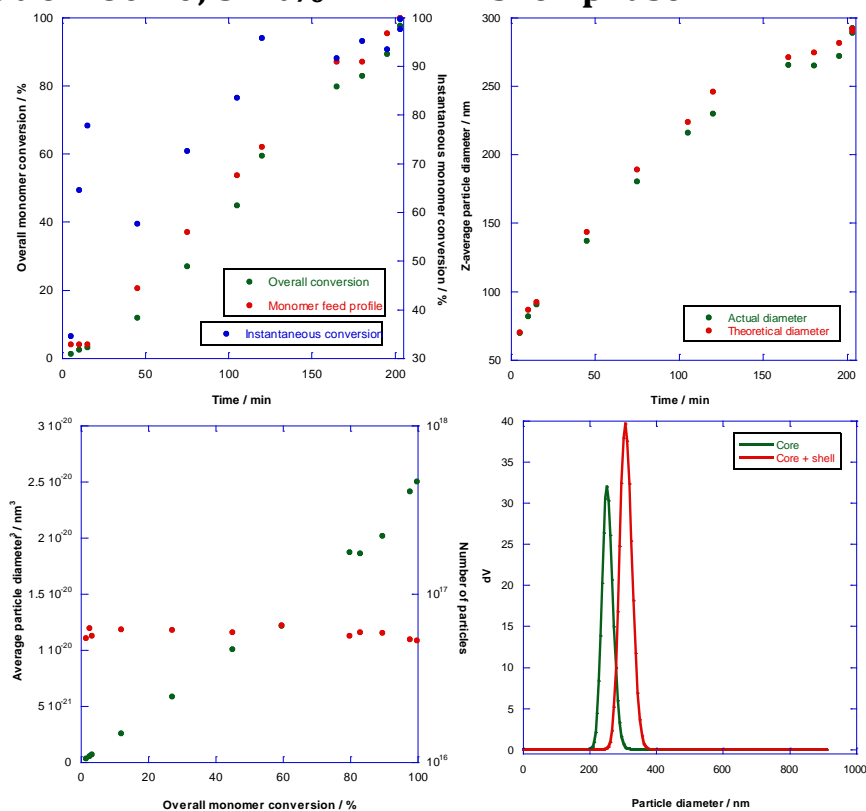
q) Poly[(BA)-*co*-(BMA)] core and poly[(BA)-*co*-(BMA)-*co*-(DAAM)] shell copolymers with $T_g = 20/5$ °C. Core:shell ratio = 80:20; 5 wt% DAAM in shell phase



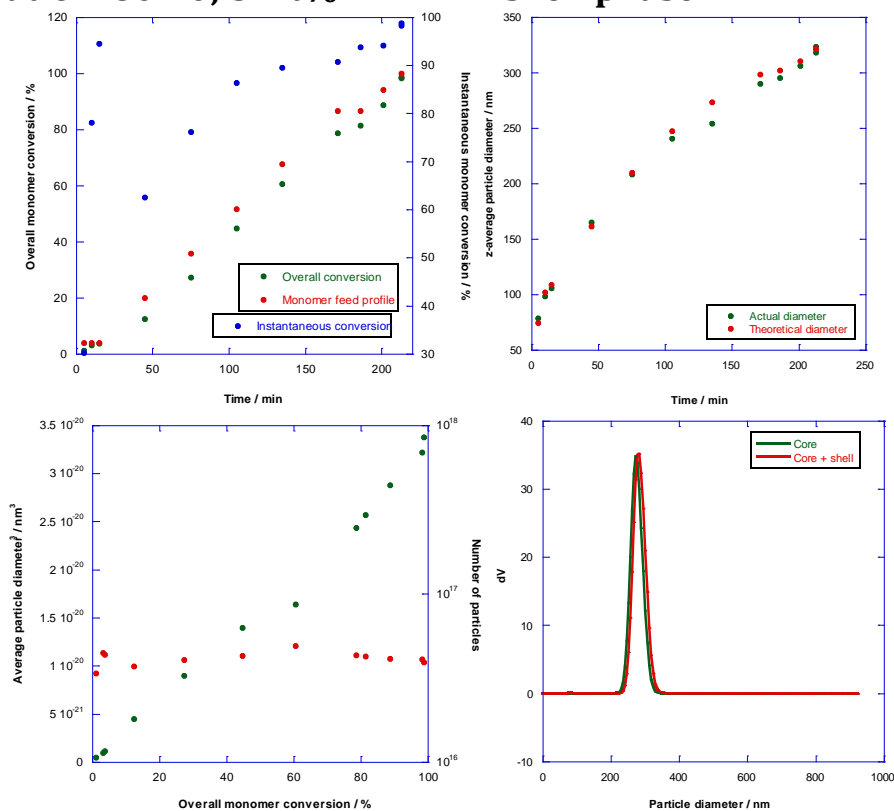
r) Poly[(BA)-*co*-(BMA)] core and poly[(BA)-*co*-(BMA)-*co*-(DAAM)] shell copolymers with $T_g = 20/5$ °C. Core:shell ratio = 80:20; 7.5 wt% DAAM in shell phase



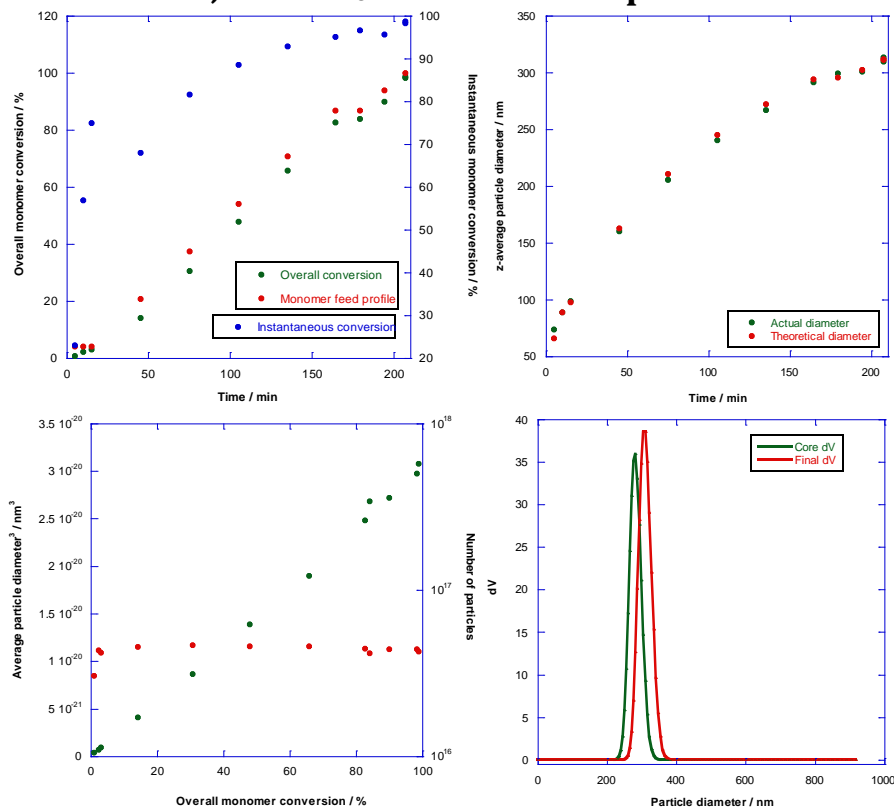
s) Poly[(BA)-*co*-(BMA)] core and poly[(BA)-*co*-(BMA)-*co*-(DAAM)] shell copolymers with $T_g = 25/5$ °C. Core:shell ratio = 80:20; 3 wt% DAAM in shell phase



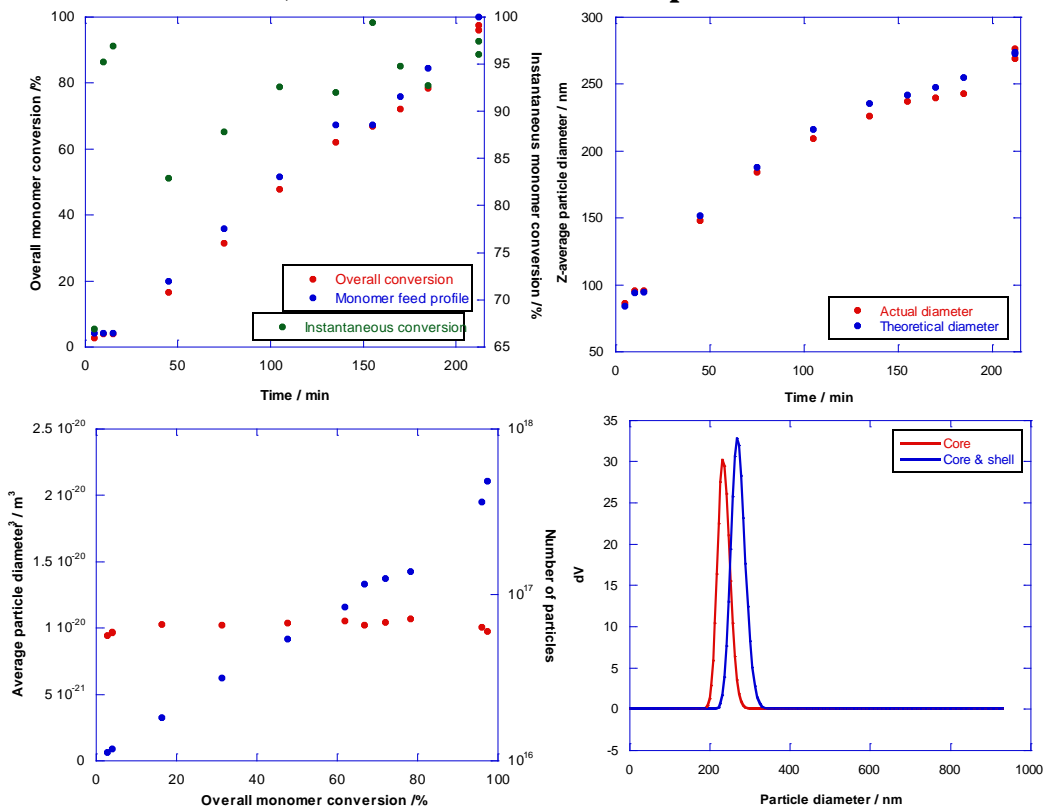
t) Poly[(BA)-*co*-(BMA)] core and poly[(BA)-*co*-(BMA)-*co*-(DAAM)] shell copolymers with $T_g = 25/5$ °C. Core:shell ratio = 80:20; 5 wt% DAAM in shell phase



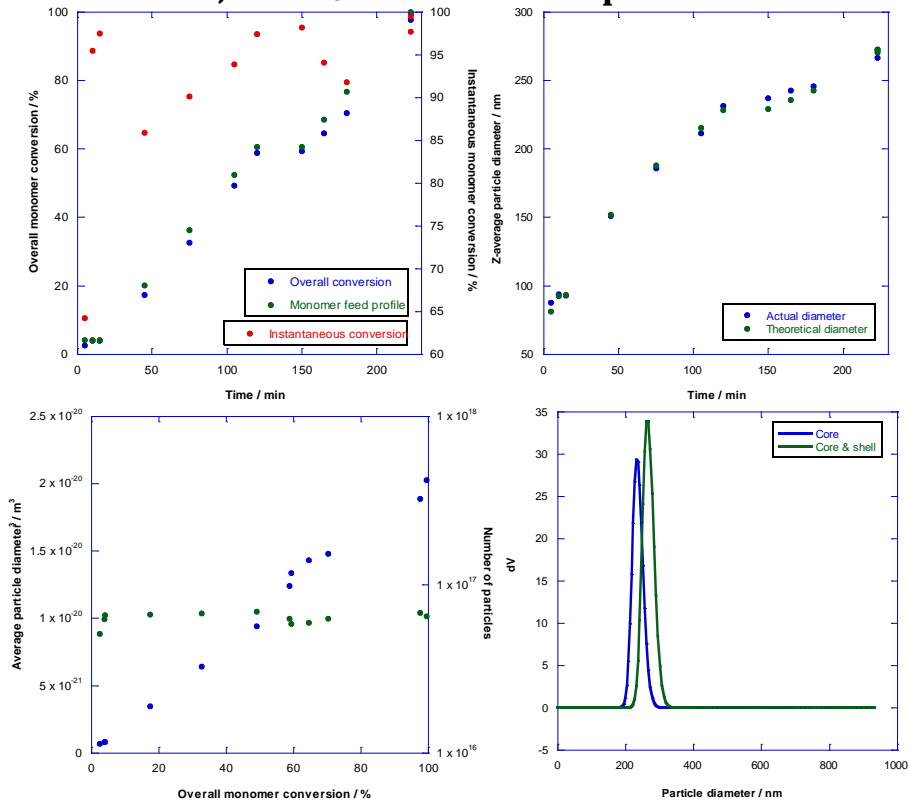
u) Poly[(BA)-*co*-(BMA)] core and poly[(BA)-*co*-(BMA)-*co*-(DAAM)] shell copolymers with $T_g = 25/5$ °C. Core:shell ratio = 80:20; 7.5 wt% DAAM in shell phase



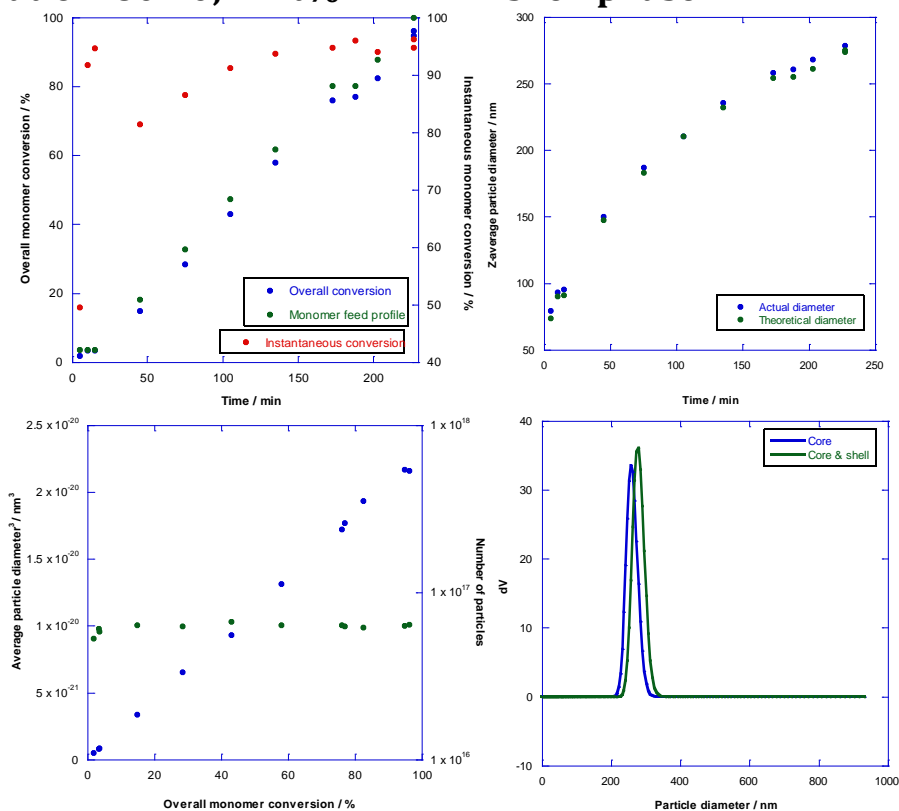
v) Poly[(BA)-*co*-(BMA)] core and poly[(BA)-*co*-(BMA)-*co*-(DAAM)] shell copolymers with $T_g = 10/10$ °C. Core:shell ratio = 70:30; 2 wt% DAAM in shell phase



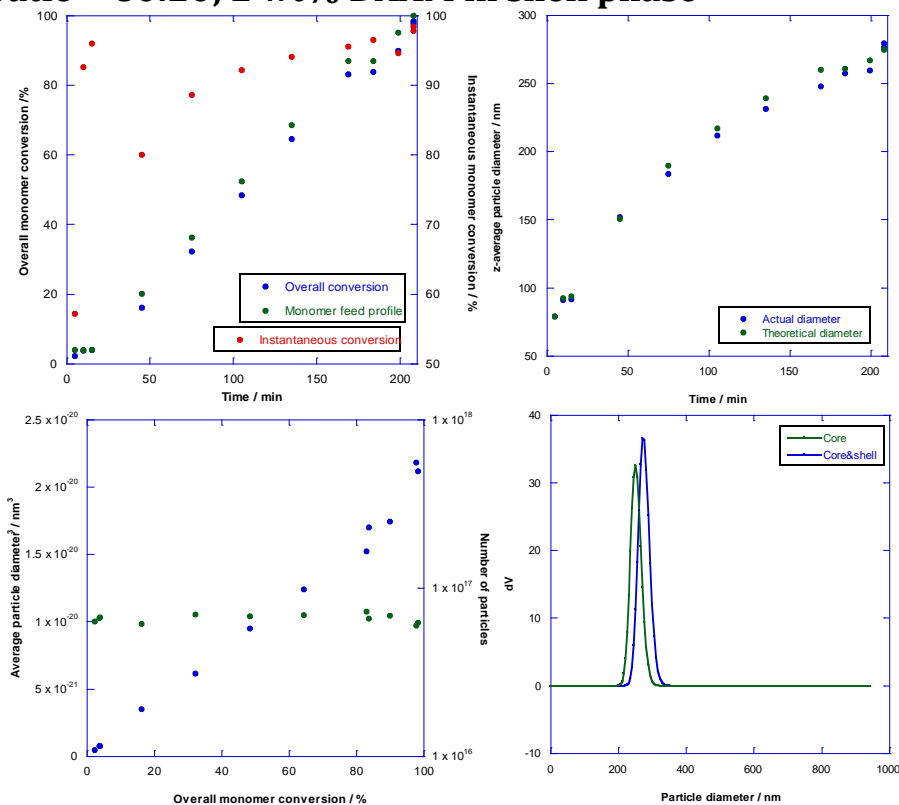
w) Poly[(BA)-*co*-(BMA)] core and poly[(BA)-*co*-(BMA)-*co*-(DAAM)] shell copolymers with $T_g = 10/15$ °C. Core:shell ratio = 70:30; 2 wt% DAAM in shell phase



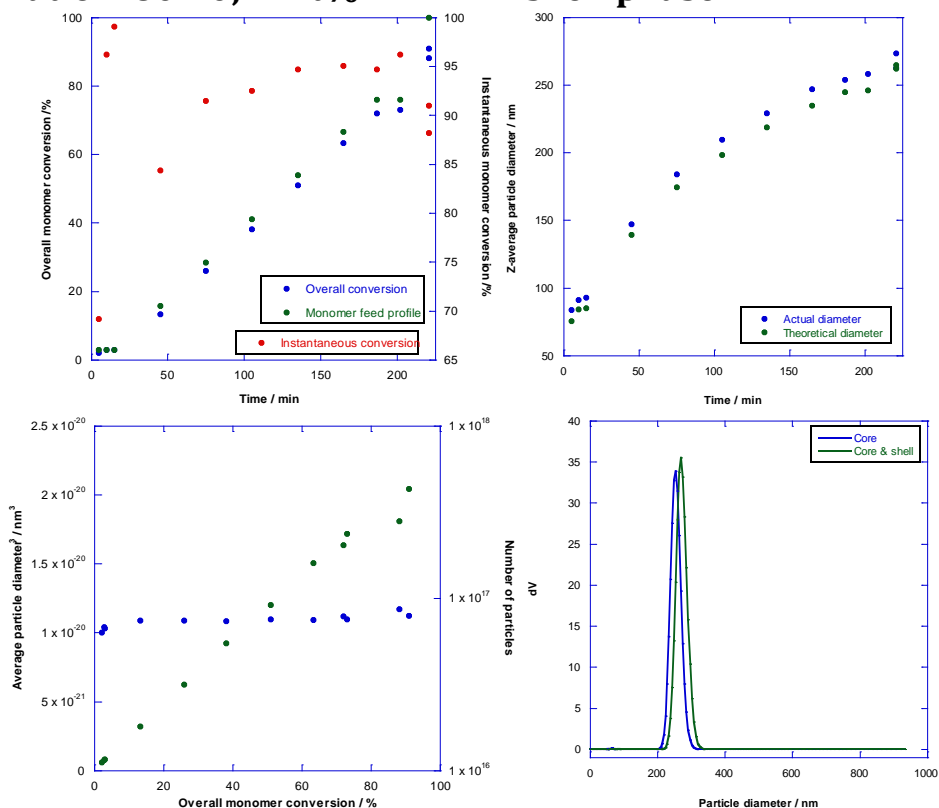
x) Poly[(BA)-co-(BMA)] core and poly[(BA)-co-(BMA)-co-(DAAM)] shell copolymers with $T_g = 10/10$ °C. Core:shell ratio = 80:20; 2 wt% DAAM in shell phase



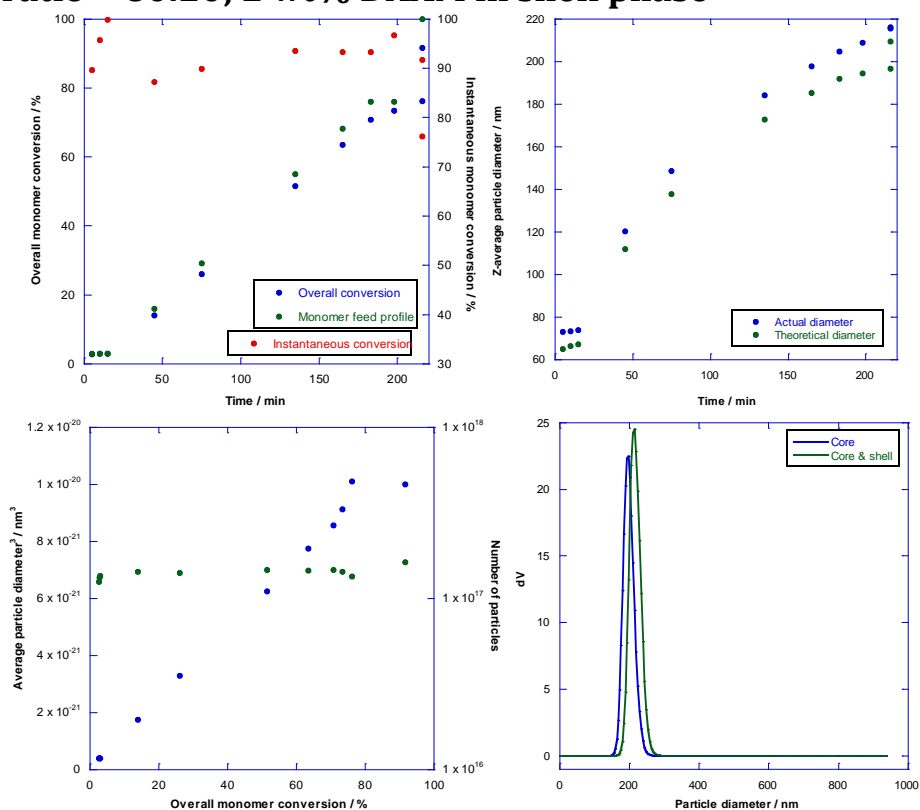
y) Poly[(BA)-co-(BMA)] core and poly[(BA)-co-(BMA)-co-(DAAM)] shell copolymers with $T_g = 10/15$ °C. Core:shell ratio = 80:20; 2 wt% DAAM in shell phase



z) Poly[(BA)-co-(BMA)] core and poly[(BA)-co-(BMA)-co-(DAAM)] shell copolymers with $T_g = 10/10$ °C. Core:shell ratio = 80:20; 2 wt% DAAM in shell phase

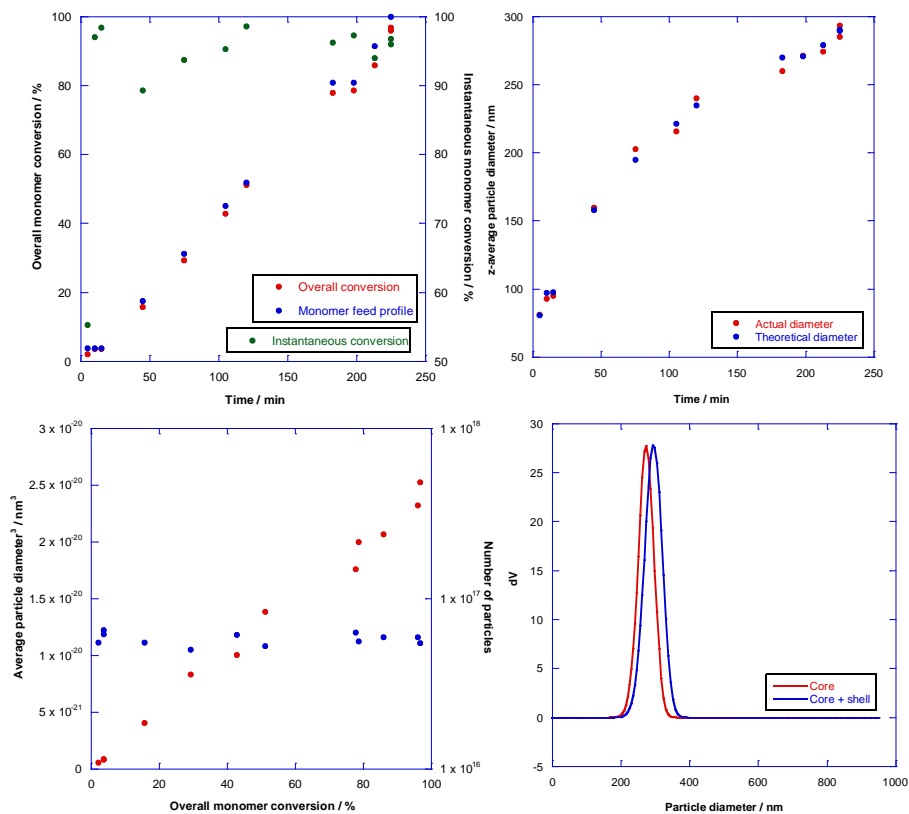


aa) Poly[(BA)-co-(BMA)] core and poly[(BA)-co-(BMA)-co-(DAAM)] shell copolymers with $T_g = 10/15$ °C. Core:shell ratio = 80:20; 2 wt% DAAM in shell phase

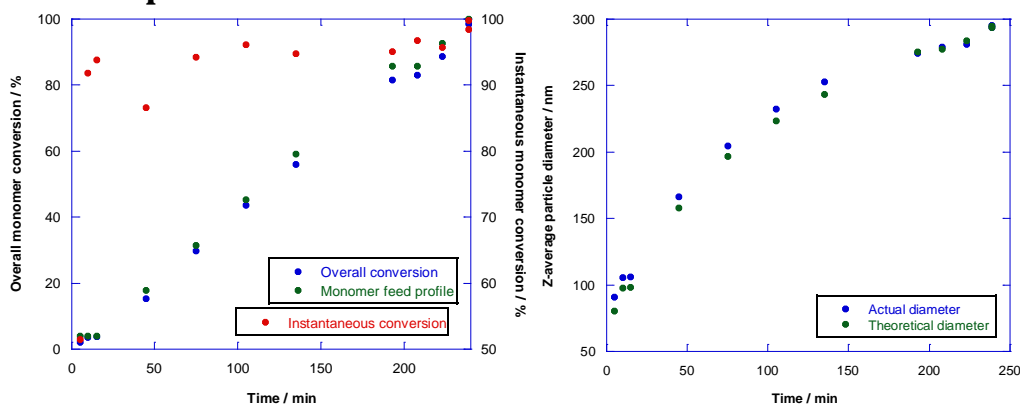


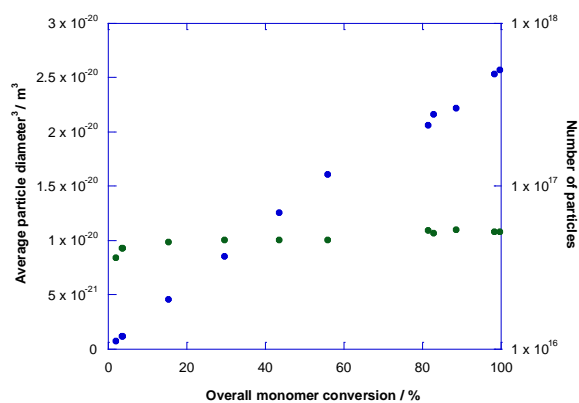
Appendix (v) – Characterisation plots for soft-soft nanocomposite latexes discussed in Chapter 8

- a) Poly[(BA)-*co*-(BMA)] core and poly[(BA)-*co*-(BMA)-*co*-(DAAM)-*co*-(MAA)] shell copolymers with $T_g = 10/5$ °C. Core:shell ratio = 80:20; 2 wt% DAAM in shell phase

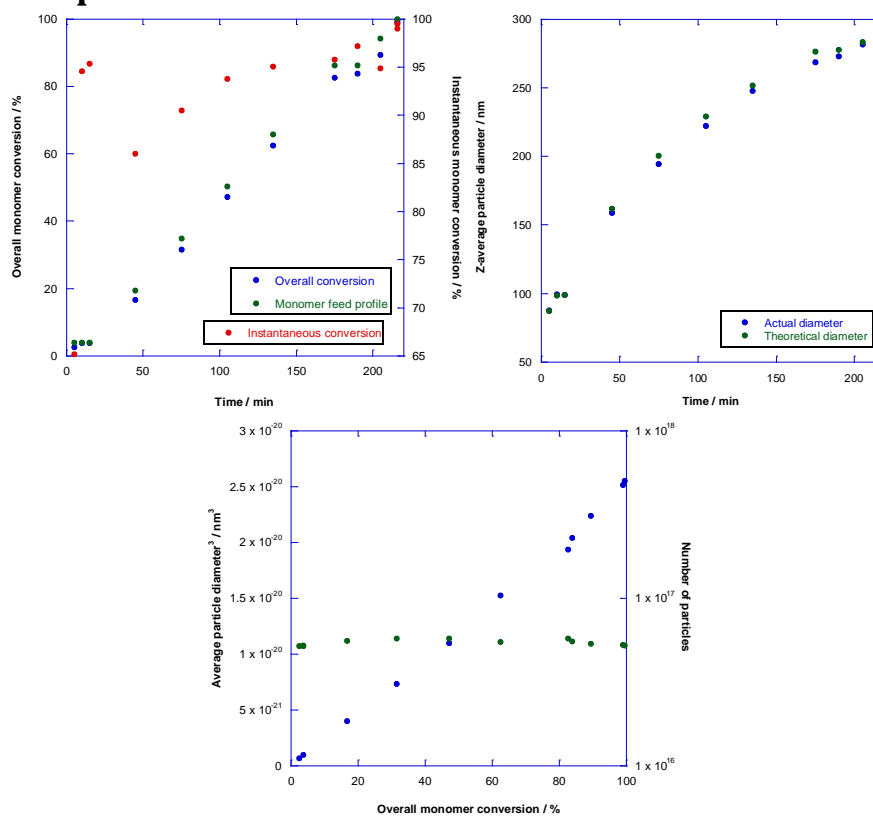


- b) Poly[(BA)-*co*-(BMA)] core and poly[(BA)-*co*-(BMA)-*co*-(DAAM)-*co*-(MAA)] shell copolymers with $T_g = 10/5$ °C. Core:shell ratio = 80:20; 2 wt% DAAM and 2 wt% MAA in shell phase

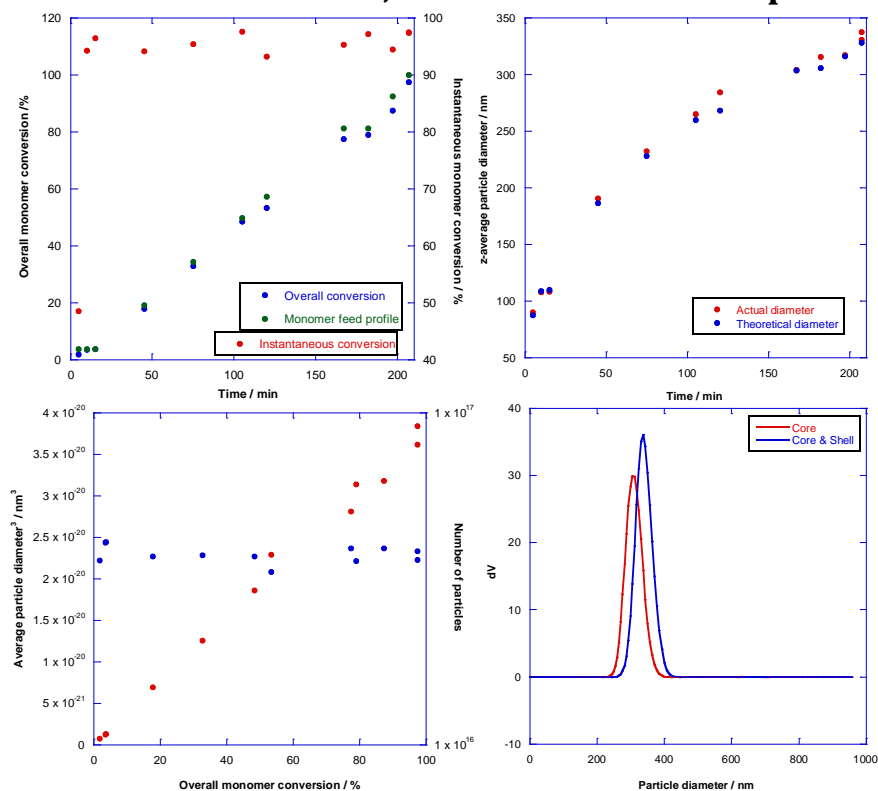




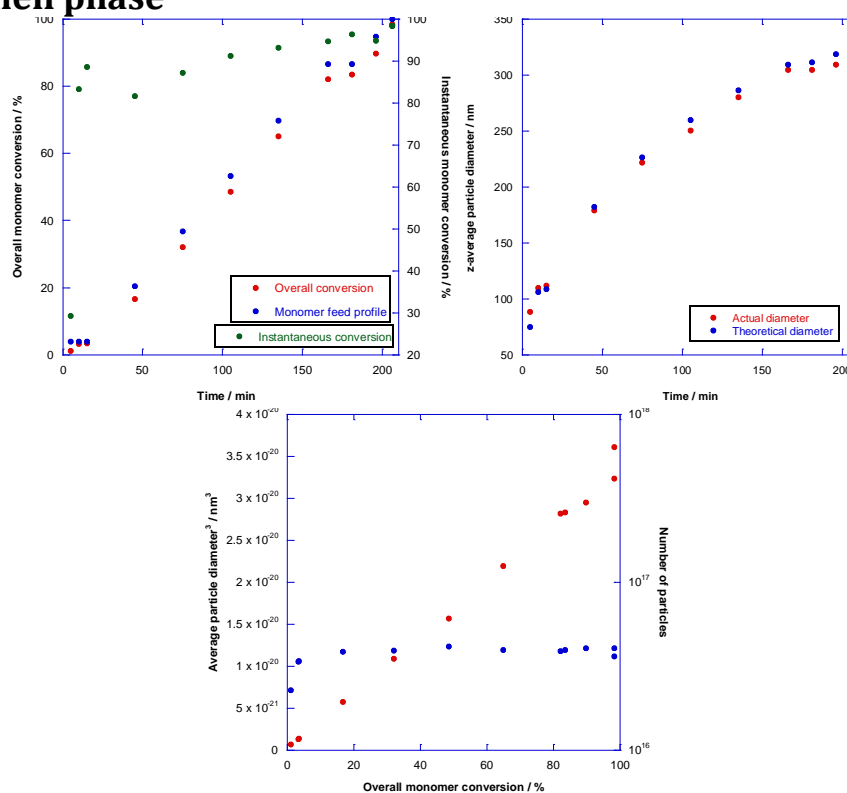
c) Poly[(BA)-*co*-(BMA)] core and poly[(BA)-*co*-(BMA)-*co*-(DAAM)-*co*-(MAA)] shell copolymers with $T_g = 10/5$ °C. Core:shell ratio = 80:20; 2 wt% DAAM and 5 wt% MAA in shell phase



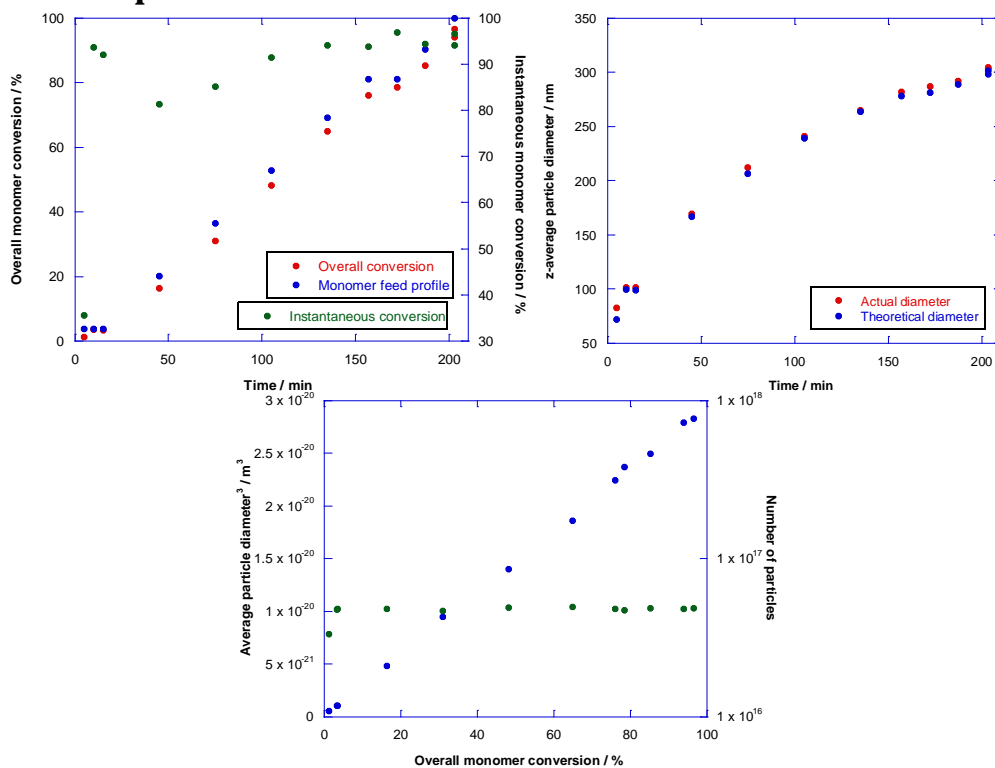
d) Poly[(BA)-co-(BMA)] core and poly[(BA)-co-(BMA)-co-(DAAM)-co-(MAA)] shell copolymers with $T_g = 25/5$ °C. Core:shell ratio = 80:20; 2 wt% DAAM in shell phase



e) Poly[(BA)-co-(BMA)] core and poly[(BA)-co-(BMA)-co-(DAAM)-co-(MAA)] shell copolymers with $T_g = 25/5$ °C. Core:shell ratio = 80:20; 2 wt% DAAM and 2 wt% MAA in shell phase



f) Poly[(BA)-*co*-(BMA)] core and poly[(BA)-*co*-(BMA)-*co*-(DAAM)-*co*-(MAA)] shell copolymers with $T_g = 25/5$ °C. Core:shell ratio = 80:20; 2 wt% DAAM and 3.5 wt% MAA in shell phase



g) Poly[(BA)-*co*-(BMA)] core and poly[(BA)-*co*-(BMA)-*co*-(DAAM)-*co*-(MAA)] shell copolymers with $T_g = 25/5$ °C. Core:shell ratio = 80:20; 2 wt% DAAM and 5 wt% MAA in shell phase

